HAROKOPIO UNIVERSITY OF ATHENS, GREECE

School of Environment, Geography and Applied Economics

Department of Geography

Master on Applied Geography and Spatial Planning,

Sector: Geoinformatics

# Use of Hyperion spectral signatures and Sentinel-1 Polarimetric backscatter for lava flow differentiation in Mt. Etna, Sicily

Master Thesis

**Aikaterini Karagiannopoulou**

**Athens, 2017**

# HAROKOPIO UNIVERSITY OF ATHENS, GREECE

School of Environment, Geography and Applied Economics

Department of Geography


Master on Applied Geography and Spatial Planning,

Sector: Geoinformatics

**Three-member examining committee**


**Is. Parcharidis (Supervisor)**

**Assistant Professor, Department of Geography, Harokopio University of Athens**

**Dr. O. Sykioti (2nd Supervisor)**

**Researcher, Institute of Astronomy, Astrophysics, Space Applications & Remote Sensing, National Observatory of Athens**

**P. Artelaris**

**Lecturer (under appointment), Department of Geography, Harokopio University of Athens**

Aikaterini Karagiannopoulou

I hereby declare that:

1. I am the owner of this master thesis and under my knowledge I don't calumniate other people and their copyrights. All citations quoted from publications in this thesis are labeled as such.
2. I accept that the university library could dispose my thesis in electronic form and keep more than one copies for maintenance and security reasons.

## Acknowledgements

I would like to thank my supervisor Dr. Olga Sykioti for introducing me to the marvelous science of hyperspectral, improve all the time my knowledge, correct my mistakes, providing me hints and new insights and steering me on the right track to completing this master thesis. I also thank Prof. Issaak Parcharidis, who is my second supervisor, for helping me understand the science of SAR and answering any question about the analysis of these data.

Moreover, I would like to thank Dr. Salvatore Giammanco for giving me the geological map of Mt. Etna, which plays one of the most important roles in my thesis. I appreciate and thank very much the Dr. Maurizio Poscolieri, who gave me the digital elevation model of Etna volcano with 10m spatial resolution, which was used for the extraction of the topographic variables (slope and aspect). Moreover, I am very thankful to the PhD candidate Manoli Proestaki, who provides me the MODIS data, which include the aerosol optical depth and cloud fraction values, in order to investigate the contribution of the atmosphere to the reflectance responses on the 2007 image.

Last but not least, I would like to thank my dearest friend, Vicky Pegiou (Post Graduated student), who support me all the time and didn’t get bored or mad of me, even if I was talking continuously about my thesis and of course for providing me her help in the script on MATLAB. Also, the biggest thank you is ascribed to my mother, who is always by my side, support my decisions and give me courage to continue.

## Table of Contents

## Abstract

Mount Etna (eastern Sicily, Italy) is one of the most active basaltic composite stratovolcanoes in the world and it has the ability to change its land field rapidly, vigorously and continuously. It is capable of producing both brief paroxysmal episodes and long-standing, relatively milder eruptions. During the last 100 years Mt. Etna has produced on average $10^7$ $m^3$ of new lava per year, both from its summit craters and from its flank areas.

The aim of this study is to investigate the capabilities of the hyperspectral spectral signatures and polarimetric backscatter coefficient values on the discrimination of the different volcanic products (lava flow, pyroclastic and scoria deposits), which belong to different effusive and explosive episodes within both the Mongibello (Torre del Filosofo formations: 122BC-1669AD, 1669AD-1971AC, 1971AD-2007) and Ellitico (Portella Giumenta, Monte Calvario, Piano Provenzana, Pizzi Deneri formations) volcanic supersystems, *(Branca et al, 2011)*. Furthermore, we investigate the potential relations between backscatter coefficient ($\sigma^0$) variations to topographic (aspect and slope) settings.

For this purpose, we analyzed three EO-1 Hyperion scenes, L1R and L1T acquired on 9/7/2007, 8/10/2009 and 14/7/2012, and two Sentinel-1A scenes, GRD (Level-1), IW in single (VV) and cross (VH) polarization both in ascending and in descending geometry, acquired on 22/8/2016 and 16/8/2016. Pre-processing steps for hyperspectral data include the destriping algorithm, the atmospheric correction, the band reduction, the img-to-img cooregistration and the noise and dimension reduction (PCA), whereas for polarimetric SAR datasets it included the radiometric calibration ($\sigma^0$), the orthorectification and the despeckle filtering.

Vegetation masking was performed on hyperspectral datasets using the NDVI map. Training sets for each lava flow were collected from chronologically different units according to the most recent geological map of Etna volcano (scale 1:50,000) (Branca et al., 2011). In the studied area, four main lithostratigraphic units are present. For each formation, the mean spectral signature and the standard deviation were also retrieved from the three hyperspectral datasets. For the same training sets, both the mean backscatter coefficient and the standard deviation were calculated for the single and cross polarizations, both for ascending and descending geometry. Correlation coefficient is calculated between the backscatter coefficient and the topographic variables (slope and aspect). Finally, the surface roughness contribution is estimated, when the moisture and topographic variables are immutable.

Primary results on the spectral signatures have shown that the temporal change was discriminated more accurately, while the discrimination of the volcanic products seems more difficult. The reflectance response increase from the youngest volcanic formation (MF1) to the oldest (Ellitico). However, the reflectance response isn't always increased, according to the recorded age of the volcanic products.

Pyroclastic and scoriae deposits always reveal lower reflectance response, compared with the lava flows. The endmembers derived from 2007 image have always higher reflectance responses, probably due to sensor's artifacts. Reflectance response of the endmembers of the 2009 image is usually lower than in 2012. Various endmembers are characterized by chlorophyll (0.7μm) and water (1.14μm) absorption and iron (0.9-1.3μm) and magnesium (2.3μm) presence. Alteration presence is also potentially occurred.

On the other hand, the results on the mean backscatter coefficient values have depicted that VV polarization reveals always higher backscatter coefficient values, regardless the satellite acquisition geometry. In ascending acquisition, the backscatter coefficient values increase from the Ellitico formation to the MF1 formation, while the opposite occurs in descending pass. Pyroclastic and scoriae volcanic products have lower backscatter coefficient values, in both polarizations and in satellite orbits. The potential presence of foreshortening and shadowing effects is depicted in MF1, MF2 and Ellitico formations.

The topography variables don't show strong linear correlation with the backscatter coefficient. The backscatter values are more affected by the roughness in Ellitico, in higher slopes ($30^{o}$-$45^{o}$) and East aspect. The backscatter coefficient values of the MF1, MF2 and MF3 formations are influenced more by the topography. Maybe, roughness affects more the North and South slopes orientations. Probably, the volcanic products can be discriminated in a more effective way in VH polarization and in descending pass, due to lower variance in their values.

**Keywords:** Hyperspectral, reflectance, SAR, backscatter coefficient, Mt. Etna, volcanic formations

## Acronyms & Abbreviations

| | |
|---|---|
| HSI | Hyperspectral imaging |
| MSI | Multispectral imaging |
| SFF | Spectral feature fitting |
| VIS | Visible |
| NIR | Near Infrared |
| VNIR | Visible Near Infrared |
| SWIR | Short-wave Infrared |
| EMS | Electromagnetic Spectrum |
| LULC - LULCC | Land Use / Land Cover<br>Land Use / Land Cover Change |
| EO-1 | Earth Observation 1 |
| NASA | National Aeronautics and Space Administration |
| SAR | Synthetic Aperture Radar |
| INGV | Istituto Nazionale di Geofisica e Vulcanologia |
| SNR | Signal-to-Noise Ratio |
| MODTRAN | MODerate resolution TRANsmission model |
| FFT | Fast Fourier Transform |
| ENVI | ENvironment for Visualizing Images |
| ALI | Advanced Land Imager |
| LAC | Atmospheric corrector |
| UTM | Universal Transverse Mercator |

| | |
|---|---|
| WGS | World Geodetic System |
| HDF | Hierarchical Data Format |
| DEM | Digital Elevation Model |
| FOV | Field of View |
| EM | Electromagnetic Radiation |
| HH | Horizontal transmit and horizontal receive |
| VV | Vertical transmit and vertical receive |
| HV | Horizontal transmit and vertical receive |
| VH | Vertical transmit and horizontal receive |
| LOS | Line of Sight |
| RCS | Radar Cross Section |
| $\sigma^0$ | Sigma naught |
| dB | Decibel |
| EC | European Commission |
| ESA | European Space Agency |
| SM | Stripmap |
| IW | Interferometric Wide swath |
| EW | Extra Wide swath |
| WV | Wave |
| SLC | Slant Range, Single Look Complex |
| GRD | Ground Range, Multi-Look, Detected Products |
| LiDAR | Light Detection and Ranging |
| HyspIRI | Hyperspectral and Infrared Imager |

| | |
|---|---|
| ASTER | Advanced Spaceborne Thermal Emission and Reflection Radiometer |
| InSAR | Interferometric Synthetic Aperture Radar |
| MNF | Minimum Noise Fraction |
| VOR | Voragine crater |
| BN | Bocca Nuova crater |
| NEC | Northeast Crater |
| SEC | Southeast Crater |
| NSEC | New Southeast Crater |
| VdB | Valle del Bove |
| GLOVIS | Global Visualization Viewer |
| USGS | United States Geological Survey |
| S-1A | Sentinel 1A |
| MF1, 2, 3 | Mongibello Torre del Filosofo formation 1, 2, 3 |
| EPG | Ellitico Portella Giumenta |
| EC | Ellitico Monte Calvario |
| EPD | Ellitico Pizzi Deneri |
| EP | Ellitico Piano Provenzana |
| ESC | Ellitico Serra delle Concazze |
| CNR | Istituto di Acustica e Sensoristica |
| BOA | Bottom of the atmosphere |
| PCA | Principal Component Analysis |
| NDVI | Normalized Vegetation Index |
| FWHM | Full width at half maximum |

| | |
|---|---|
| FLAASH | Fast Line-of-sight Atmospheric Analysis of Spectral Hypercubes |
| BSQ | Band Sequential |
| BIL | Interleaved by Line |
| sr | Steradian |
| ASCII | American Standard Code for Information Interchange |
| NOAA | National Oceanic and Atmospheric Administration |
| GCP | Ground Control Point |
| RMS error | Root Mean Square error |
| ROI | Region of interest |
| DN | Digital Number |
| PDF | Portable Document Format |
| PPI | Pixel Purity Index |
| AMEE | Automated Morphological Endmember Extraction |
| GIS | Geographical Information Systems |
| MATLAB | Matrix Laboratory |
| 1:1 | One-to-one relationship |
| SQL | Structured Query Language |
| DBMS | Database Management System |
| AOD | Aerosol Optical Depth |
| MODIS | Moderate-resolution imaging spectroradiometer |
| r | correlation coefficient |

# Introduction

Remote sensing is indicated as the science, in which information about the surface (from Earth or other planets) can be detected from sensors that are not in contact with objects that might be recorded. The usage of different regions of the electromagnetic spectrum (from visible to microwave) gives us the opportunity to analyze the surface materials and its texture. In particular, each individual region from 0,3μm to 2,5μm is sensitive to different electronic and vibrational processes based on the physiochemical properties. Hyperspectral imaging (HSI) has enabled a variety of applications in Earth studies, providing significant improvements on spectral measurement capabilities over conventional systems. It contributes to the identifications and mapping of different materials, especially in retrieving, identifying and quantifying their chemical and structural characteristics as well as their temporal and spatial changes. For example, the usage of Hyperspectral techniques (e.g. spectral linear unmixing, SFF, spectral classification etc) provide information about the different volcanic materials, their existence and the possibility to detect the environmental variables (e.g. chemical and biological weathering and alteration) which change their spectral response, or potential a new lava flow deposition in the same area.

When spectra are measured and analyzed, additional features can be detected. For example, visible (VIS) and near infrared region (NIR) of the electromagnetic spectrum (EMS) are suitable to analyze the alteration of the volcanic deposits, *(Spinetti et al, 2009).* Moreover, mafic rocks are characterized by low reflectance in the VIS and NIR spectral range due to the presence of large amount of dark minerals *(Carmichael, 1982).*

On the other hand, microwave portion of the EMS covers the range from approximately 1cm to 1m and it is sensitive to topography and dielectric constant. The transmition pulses of the microwave energy towards to Earth's surface gives information about the surface's moisture content and rugosity, *(Ferretti, 2014).* Moreover, different polarizations are sensitive and affected to specific LULC structures (e.g. rock types) and to topography parameters. The combination of this knowledge is used in order to map the LULCC and to detect or quantify the range of the effect in the microwave signal due to the aforementioned parameters.

Volcanic activity has been characterized one the most crucial issues science because it has the ability to change its LULC area rapidly and rigorously over time. Many surveys have implemented using remote sensing technologies in order to identify, detect and mapping the various phenomena that occur; proving better information about it, risk management politics, civil protection etc.

Accept from the above perspectives, lots of others; containing field measurements such as spectrometers and GPS (stable and kinematic) are applied for the estimation, detection and mapping of a volcano's landscape dynamics.

The main goal of this study is the analysis of the temporal LULCC in the low active part of the Etna volcano, according to the recorded eruptions, from the Smithsonian institute and the INGV that occurred from 2007 up to 2012, using hyperspectral (EO-1 Hyperion) and SAR (Sentinel-1A) data. In addition, we categorize the volcanic materials into 4 groups according to the Geological Map, which was created by Branca et al (2011) and according to this segregation; we analyze the temporal change of the reflectance surface materials, the polarization and the acquisition mode sensitivity to the above categories and lastly we investigate the variables (e.g. topography), which could cause a surface change.

Following this introduction, an inclusive background (Chapter 1) on hyperspectral imagery, the science of spectroscopy and the atmospheric effects are described. Moreover, it gives extended information about the hyperspectral sensor (EO-1 Hyperion) that is used for this research. Chapter 2 analyzes the principal theories of SAR imagery and the sensor (Sentinel 1) that will be use, correspondingly. A brief presentation of the researches on lava flow detection and differentiation on Mt. Etna and other volcanoes, will be described in Chapter 3. The presentation of the study area and resent studies on volcanic deposits is analyzed on Chapter 4. Furthermore, the data, the approaches and methods section (Chapter 5) explains the analysis steps of this study. The next section (Chapter 6) presents and compares the results from the particular analysis individually for each sensor type. Finally, the research is summarized and conclusions are offered (Chapter 7) on the benefits of the hyperspectral and SAR imageries, in the lava flow differentiation. Suggestions for future enquiry are shown in this chapter also.

# Chapter 1: Hyperspectral Imaging

## Background

This section introduces the vast field and the capabilities of the hyperspectral imagery. For the initial understanding of this subject it is crucial to review the principals of the reflectance spectroscopy theory and its atmospheric effects. Lastly, the sensor Hyperion (EO-1) and its utility are depicted.

## 1.1. Introduction in Spectroscopy

Reflectance Spectroscopy is the technique that investigates the material properties according to their interaction of the sun radiation (electromagnetic radiation – EMR) with matter, *(Green, 1998)*. Each substance interacts with its own way and this is the reason of light absorption in some wavelengths regions, while light reflection or transmition in others, *(van der Meer & de Jong, 2011)*. This technique analyzes the spectral data in VIS and NIR region to identify different materials, based on the spectral signature definition; i.e. t absolute reflectance as a function of solar radiation wavelength (reflectance curve), acquired under specific environmental conditions. Each spectral signature or spectral profile refers to a specific target structure, *(van der Meer & de Jong, 2011)*.

### 1.1.1. Radiance

Radiance is defined as the radiance flux per unit solid angle per unit of the projected area of the ground viewed by the sensor at that instance, *(Berk et al 1989; Olsen, 2014; Rees, 2013; Salvaggio, et al, 2011; van der Meer & de Jong, 2011)*. This measurement is indicative of how much power radiated, by a reflective or emitting surface, will be received by an optical instrument looking at the surface from a specified angle.

Radiance, L in units $\frac{\mathrm{Watts}}{\mathrm{m}^2 * \mu * \mathrm{ster}}$ is defined as: $\mathrm{L} = \frac{2\mathrm{hc}^2}{\lambda^5} * \frac{1}{e^{\frac{\mathrm{hc}}{\lambda \mathrm{KT}}} - 1}$ (1)

Where:

- L  = Spectral radiance
- T = Absolute temperature
- $k_B$ = Boltzmann constant, 1,38 * $10^{-23}$, $\frac{m^2 * kg}{s^2 * K}$
- h = Plank constant, 6,62 * $10^{-34}$, J*s
- c = Speed of light in the vacuum, 3 * $10^{8}$, $\frac{m}{s}$

### 1.1.1. Reflectance

Reflectance is the proportion of the radiation reflected off a surface to the radiation striking it, *(Van der Meer & de Jong, 2011)*. Reflectance spectroscopy is the analysis of the sun radiation as a function of wavelength that has been reflected or scattered from the surface materials. As photons enter a material, some are reflected from the surface, some pass through the surface and other are absorbed. Primary reflectance features are seen in VNIR and SWIR wavelength regions.

More specifically, concerning mineral detection, using spectroscopy techniques, various applications can implement such data mining (manmade or natural), gold exploration, mine drainage materials identification, tourmaline group minerals, volcanic materials or even minerals that indicate of hydrothermal alteration, such as kaolinite, dickite, illite and ammonium-illite etc.

Spectral features occurring in the VNIR wavelength region from 0.4 to 1.0 micrometers are caused by electronic processes. Electronic processes include crystal field effects, charge transfer, conduction band absorption, and color centers *(Van der Meer & de Jong, 2011)*. A common electronic process is seen in healthy vegetation, which has an absorption feature at approximately 0.68 micrometers from the presences of chlorophyll *(Elvidge, 1990)*.

Features occurring in the SWIR wavelength region from 1.0 to near 2.5 micrometers are the result of molecular vibrational processes. Rocks and soils have absorption features that depend on the specific molecules and the types of molecular bonds present in the substance *(Goetz, 1985)*. For instance, some lava flows can have a similar chemical/mineralogical composition but dissimilar spectral behavior due to the different grain size, surface texture and presence of weathering. The main components of igneous rocks do not display any peculiar spectral features in the visible and near infrared spectral range. In the case of basalts, the only spectral feature commonly found is an absorption peak, due to iron, located around 1000 nm *(Carmichael, 1982; Clark & Roush, 1984)*. However, in the case of hydrothermal alteration, hydroxyl bearing minerals show distinctive absorption features in 2000–2500 nm *(Hellman & Ramsey, 2004)*.

## 1.2. Introduction to Hyperspectral Imaging (HSI)

Passive sensors (Optical) are classified into three main categories; the Panchromatic (one band, visible region of EMS), the Multispectral (tens of bands, many region of EMS, usually from visible till infrared) and the Hyperspectral (hundreds of continuous spectral bands and each of it covers a small range of the EMS), usually 5-10 nm, (Figure 1.2.1).

Hyperspectral refers to the multidimensional character of spectral data including the aforementioned definition; *(Goetz et al, 1985)*. Chein (2003), Grahn & Geladi (2007) support that the hyperspectral sensors collect and analyze data in tens or hundreds narrows of the spectral bands. These continuous measurements make possible the production of a continuous spectrum for each pixel of the image. These particular spectral profiles, which combine an image (dataset), can be compared respectively with laboratory spectral signatures, in order to potentially identify the minerals of each study area. The greater number of bands enables more accurate measurements of physical quantities at Earth's surfaces, such as upwelling radiance, reflectance, emissivity and temperature *(van der Meer & de Jong, 2011)*. The ability to identify materials using HSI differs from MSI systems because the band widths are narrower and more closely spaced (Figures 1.2.1 & 1.2.2.).

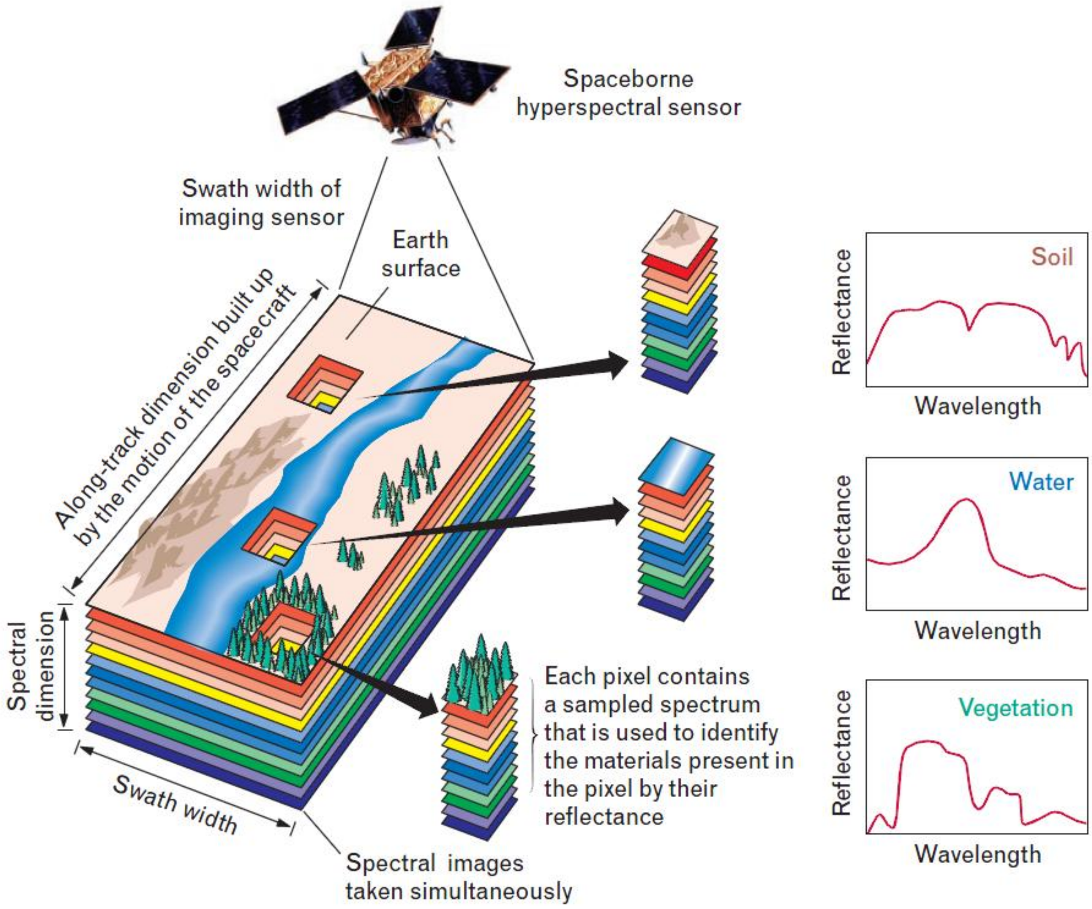


***Figure 1.2.1: The imaging spectroscopy concept (Shaw & Burke, 2003)***

The HSI has the ability to reduce its own spectral dimension or to be removed, due to atmospheric and solar effects for direct comparison with spectra measured in the field or in a laboratory setting *(van der Meer & de Jong, 2011)*. High spectral resolution also allows the identification and the discrimination of different surface materials (Figure 1.2.2). MSI sensors with higher spatial resolution are suitable to segregate different land use/land cover (LULC) categories, but with coarser spectral resolution lose the ability to distinguish and map the spectral detail.

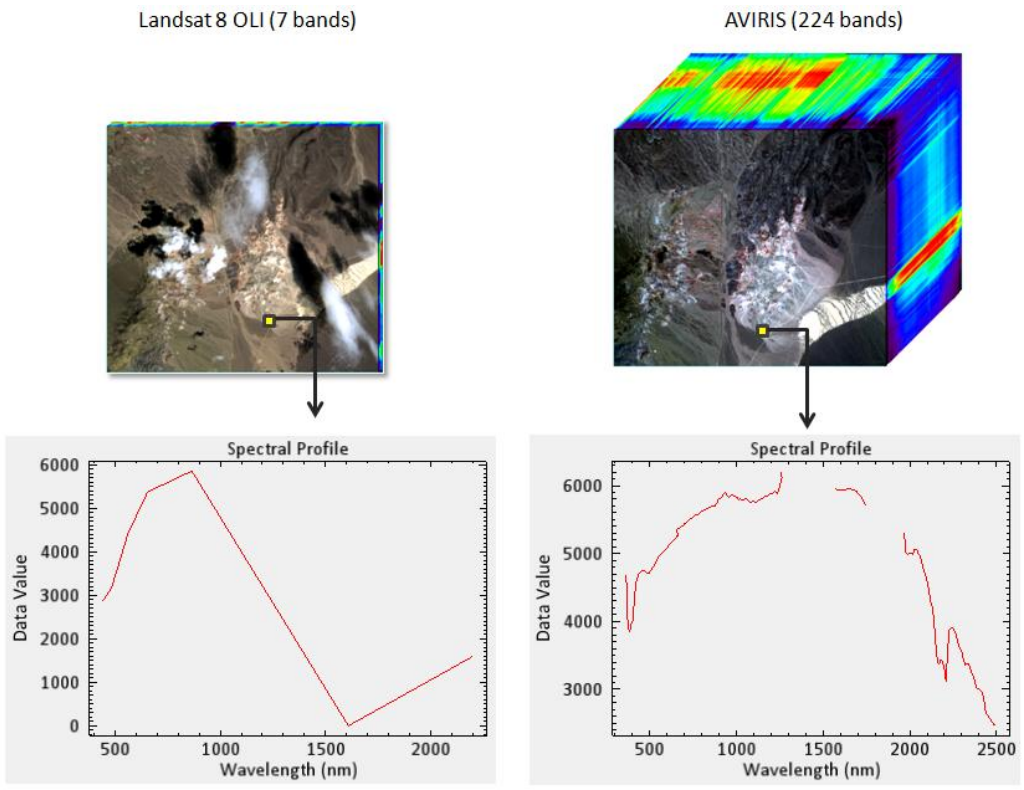


***Figure 1.2.2: Comparison of MSI (left) and HSI (right) spectral signatures, (source: [https://www.harrisgeospatial.com](https://www.harrisgeospatial.com))***

As it is mentioned before, hyperspectral sensors collect information as the aggregate of "images" and this is called dataset. The combination of them designs a 3-dimensional (x, y, λ) hypercube (Figure 1.2.2, right), where x and y represent the spatial dimensions and the λ the spectral dimension, which includes a specific spectral ranges.

Spatial scanning, spectral scanning, non-scanning (snapshot) and spatiospectral scanning are the techniques that are used for the hyperspectral cube recording. There have been designed four different technologies for the receiving of the 3D (x, y, λ) data. Each of them has a particular usage and variable advantages and drawbacks, *(Lu & Fei, 2013)*. Hypercubes are produced from satellite (EO-1) and airborne (AVIRIS) sensors, *(Schurmer, 2003)*. The accuracy of these sensors depends on the spectral resolution. For example, if the scanner detects a large number of spectral bands, it will be possible to identify different materials, only in a few pixels. However, spatial resolution is another crucial factor of accuracy. For instance, lower spatial resolution can have the abundance of different materials in a single pixel. On the contrary, if the spatial resolution increases, then the consuming energy will be lower in proportion with the signal-to-noise ratio (SNR).

## 1.3. Introduction to Atmospheric Effects

Interaction between electromagnetic radiation and earth's surface change the characteristics of the radiation. This modulated radiation, reflected from the earth's surface serves as the signal that is sensed by the optical airborne and satellite remote sensing systems. Atmosphere is often considered as impediment for remote sensing data. To exclude the atmospheric effect from the Hyperspectral imaging system various algorithms have been designed.

### 1.3.1. Atmospheric effects

The atmospheric gases, aerosols and clouds scatter and absorb solar radiation and can modulate the reflected radiation from the Earth. This phenomenon affects the intensity and spectral composition of the radiation, *(Lillesand & Kiefer, 1999)*. The "direct effect" is caused due to the atmospheric scattering, absorption, gas molecules, aerosols and dust particles. The net warming effect of atmosphere varies with the path length that the radiation has to travel from source to sensor and also varies with the magnitude of the energy signal being sensed.

Atmospheric absorption causes an effective loss on energy to atmospheric constituents. Aerosols, carbon dioxide, ozone and water vapor are the most effective gas molecules, *(Lillesand & Kiefer, 1999; Olsen, 2014)*. Absorption affects Hyperspectral sensors operate within the absorption regions of these gases. Sensors receive the energy (flux) leaving from each pixel of the image, (Figures 1.3.1.1 & 1.3.1.2). The water vapor features in the SWIR region of the EMS are commonly found at approximately 1.4 and 1.9 μm. In regions all the energy is absorbed by the atmosphere and no remote sending data can be received. In the 2.5, 4.4, 5-8 and beyond 14 μm are also affected from similar atmospheric features (water vapor, carbon dioxide, ozone), which defined the atmospheric windows, (Figures 1.3.1.1 & 1.3.1.2).

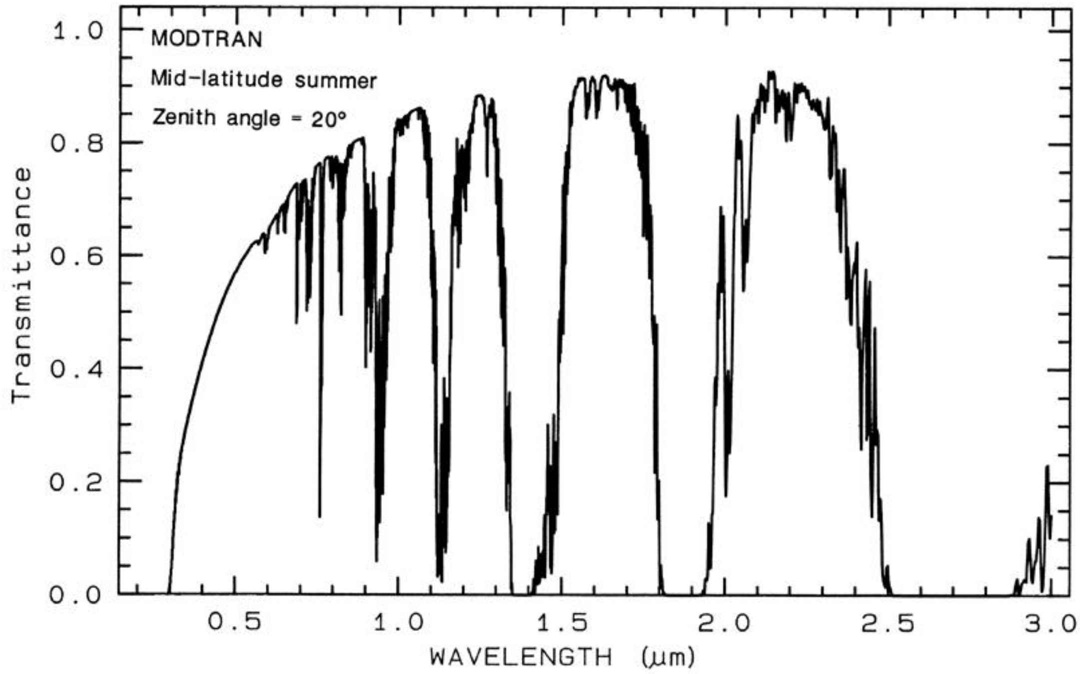


***Figure 1.3.1.1: Atmospheric transmition plot of VNIR and SWIR, (Berk et al, 1989).***

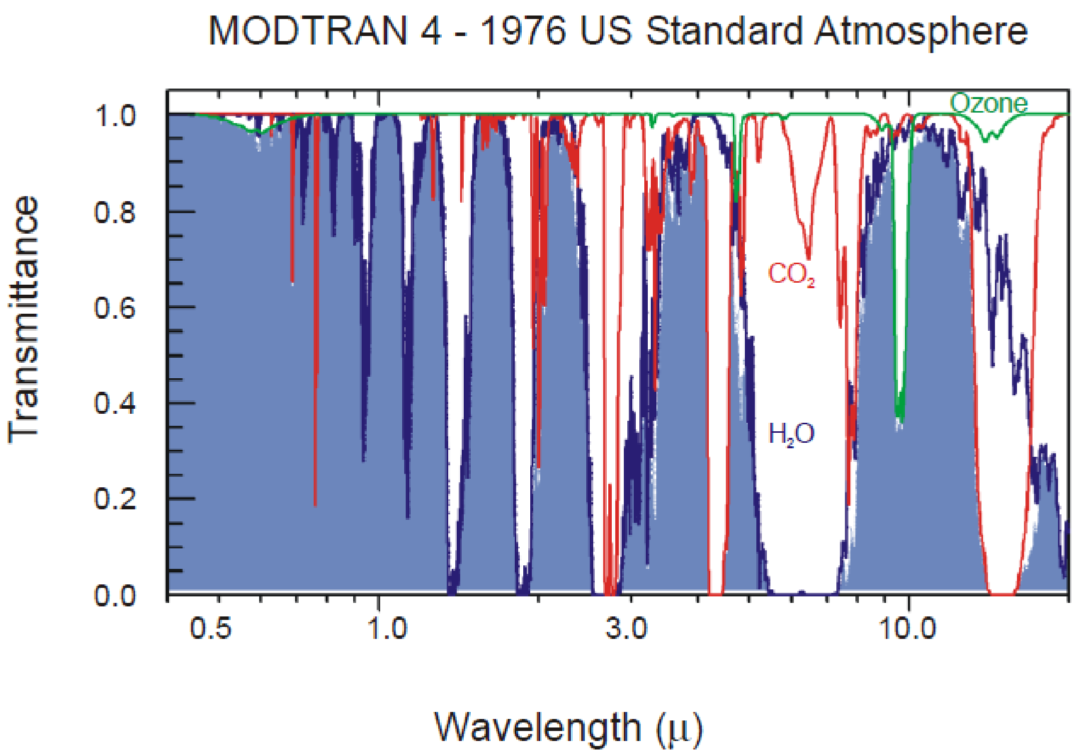


***Figure 1.3.1.2: MODTRAN plot displaying the atmospheric transmition bands, (Olsen, 2014).***

On the other hand, atmospheric scattering is created by collisions between the photon and scattering agents that include molecules, suspended particles and clouds, *(Olsen, 2014)*, (Figure

1.3.1.3). Gas molecules ($O_3$, $O_2$, $CO_2$, $CH_4$ etc.) and haze create Rayleigh scattering, which inverse the power of the wavelength. Mie scattering primarily, is caused by larger size particles such as water vapor and small dust particles. Non-selective scattering is the most significant and variable atmospheric effect, which is produced by the aerosols (water droplets), whose size is much larger than the wavelength energy (visible to mid infrared) is sensed. Scattering by the atmospheric particles is the dominant mechanism that concludes to radiometric distortions in the dataset and to sensor's malfunction effects, *(Lillesand & Kiefer, 1999).*

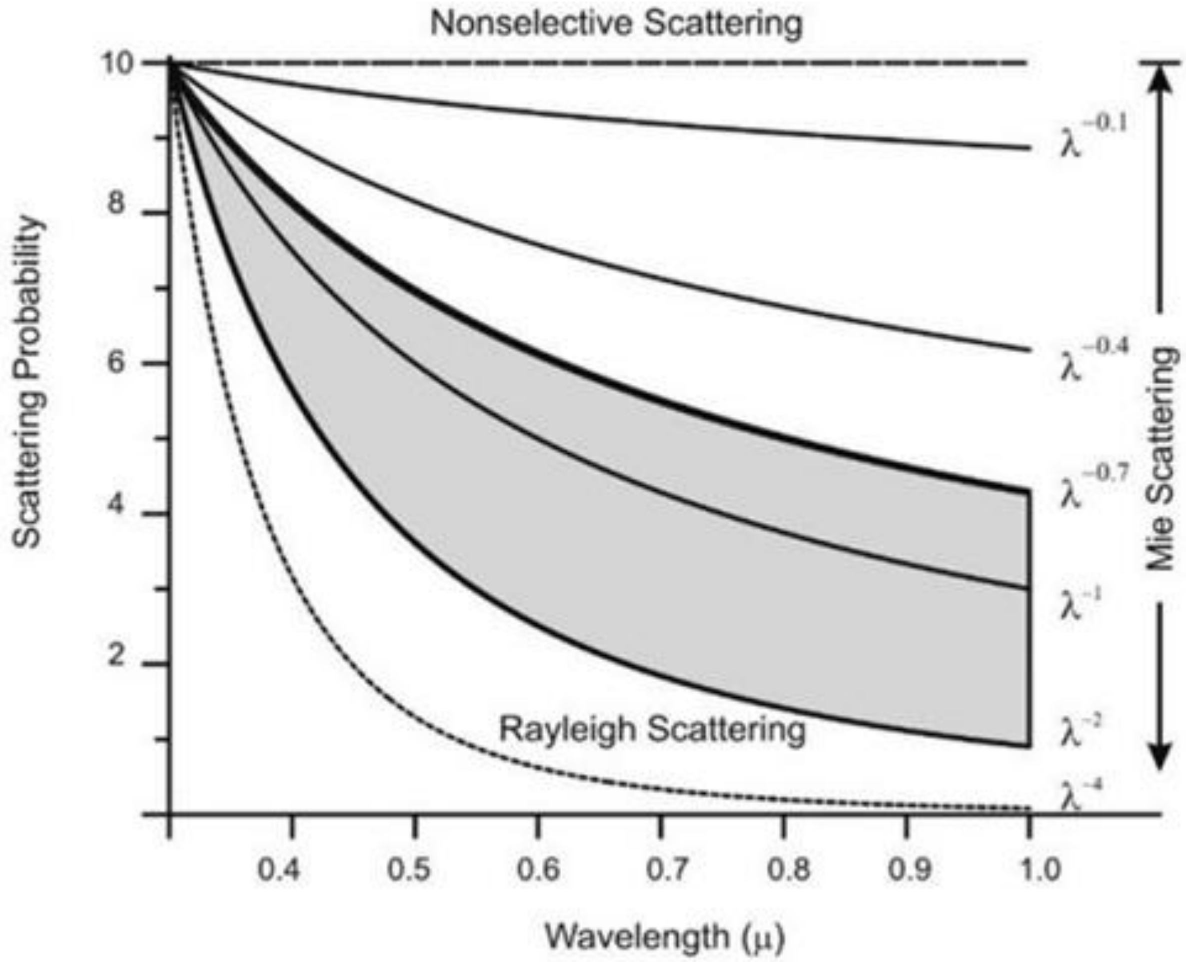


***Figure 1.3.1.3: Atmospheric scattering effects caused by the size of the scattering agent, (Olsen, 2014).***

The last environmental effect, which restricts the flux transmition, is turbulence. Turbulence is caused by fluctuations in the temperature and density of the atmosphere, *(Olsen, 2014)*, (Figure 1.3.1.4).

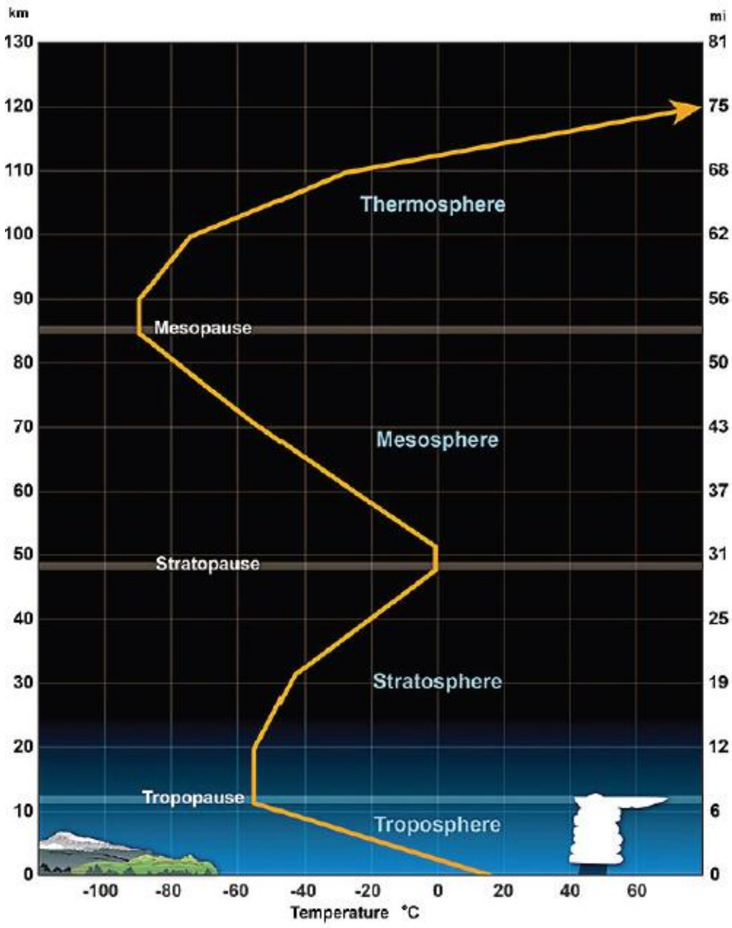


***Figure 1.3.1.4: Temperature profile of the standard atmosphere as a function of height. Layers of the atmosphere are denoted on the figure along with transition layers. (NOAA, National Weather Service, 2013).***

## 1.4. Striping Noise reduction in Hyperspectral Data

In pushbroom sensors, the striping noise is an effect perceived such as columns in the vertical direction, visually apparent and pronounced well in almost all bands of Hyperion (EO-1) sensor. An ideal destriping method should be able to eliminate the stripes without altering the information of the original image, and pixels values not affected by stripes should not be changed after destriping process to preserve the original data. Several methods were proposed such as histogram matching and spectral filtering. Moreover, it is suggested matching the gain and offset of each sensor to typical values used an inverse regression to reduce striping in Landsat TM band-6 data, *(Datt & Jupp, 2004; Jarecke & Yokoyama, 2000)*. On the other side, Nishii et al *(Chen et al, 2003)* applied univariate Bayesian regressions for spatial smoothing. Another method was developed to destripe EO-1 Hyperion hyperspectral imagery locally or globally, *(Kerola et al, 2009)*. Moreover, spectral model was also constructed to correct airborne imaging spectrometer data, *(Jupp, 2001)*. A similar algorithm was modified to deal with the spaceborne EO-1 Hyperion data, *(Önder & Dogan, 2013)*.

These algorithms involved in adjusting gray values column by column or line by line for all spectral bands according to a calculated offset relative to the average of the entire scene, thus also requiring through scene examination and intensive computation. The spectral filtering was also used to reduce striping noise *(Kawishwar, 2007)*. For example, Fast Fourier transform (FFT)-based semiautomatic filtering was also used to eliminate striping patterns in Landsat-7 Enhanced TM plus image pairs for better imageodesy analysis *(Münch et al, 2009)*, wavelet analysis and spline interpolation. Among the ideas proposed, the simplest is statistical balancing using the means or the means and variances of the columns of the data image. A vertical stripe is said to occur where the statistics indicate that the image information is likely to be valid (that is, the pixel is not "bad") but with significantly modified gain and offset. A general approach to removing vertical stripes with these characteristics is then similar to methods used in the past to balance horizontal stripes in mirror scanner images by histogram equalization or to flatten images affected by limb brightening or to balance detectors in airborne pushbroom sensors *(Goetz et al, 1985)*. Figure 1.4.1 depicts a typical example of the striping effect and the results after using destriping ENVI-SPEAR-Tools, Vertical Stripe Removal algorithms and global and local approaches.

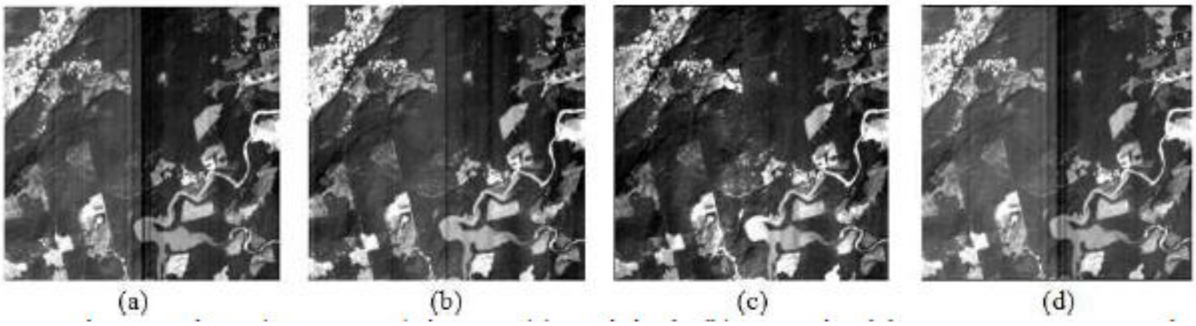


***Figure 1.4.1: Destriping results of the Hyperion Band 28 (630.94 nm) image. (a): Original. (b): Destriped by ENVI-SPEAR-Tools, Vertical Stripe Removal. (c), Destriped by the global approach. (d): Destriped by the local approach***

## 1.5. Earth Observing 1 (EO-1) Satellite and the Hyperspectral sensor, Hyperion

### 1.5.1. Earth Observing 1 (EO-1) Satellite

Earth Observing Satellite was launched on 21st of November in 2000, from the Vandenberg air force base, with one year mission. It was part of NASA's, New Millennium Program (NMP), which was an initiative to demonstrate advanced technologies for dramatically reducing the cost and improving the quality of instruments and spacecrafts for future space missions. Under this program, missions were intended to validate new technologies in flight and to provide useful scientific data to the user community. The primary demonstrations were oriented towards remote sensing and spacecraft technologies that would be used in defining future Landsat type missions. The technology categories were divided into three main axes. Category I technologies were mandatory and the missions would be delayed or restructured to properly flight-validate these technologies. Category II technologies were important but risky in terms of their maturity such that a conventional technology was carried in parallel should the new technology not mature as required for the mission. Category III technologies were flight opportunities. They were designed with interfaces such that their absence or failure cannot adversely affect the successful flight-validation of the Category I or II technologies.

However, the first goals were oriented to the remote sensing technologies, because they wanted to improve the LULC mapping and understanding better the planet. EO-1 is a combination of three systems; Hyperion (hyperspectral sensor), ALI (Advanced Land Imager, multispectral sensor) and LAC (atmospheric corrector). The first three months of the mission life were focused on instrument activation and performance verification.

The EO-1 has a sun-synchronous orbit with an altitude of 705km and a 10.01 am descending node. The orbit inclination is 98.2 degrees, the orbital period is 98.9 minutes and its equatorial crossing time is one minute behind Landsat-7. The velocity of the EO-1 nadir point is 6.74 km/sec. Figure 1.5.1.1 shows the information flying capability of the EO-1 spacecraft. Also, it is depicted the overlay of the swath width for the different instruments.

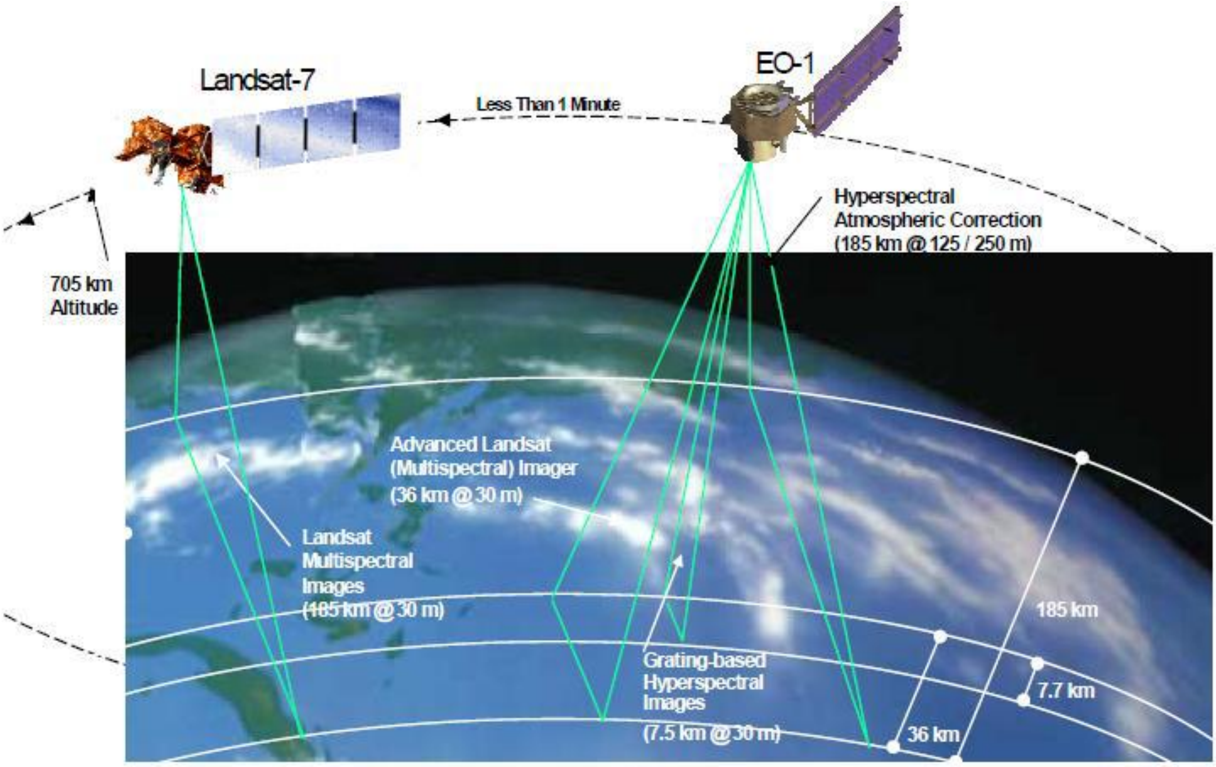


***Figure 1.5.1.1: Schematic of the satellite constellation. This figure shows the overlap and dimensions of the ground tracks for Landsat 7 and the three EO-1 instruments, Hyperion, Advanced Landsat Imager, and the Atmospheric Corrector. Note that EO-1 follows one minute behind Landsat in the Landsat orbit, (EO-1 Users Guide).***

The EO-1 data are projected to the WRS-2 Universal Transverse Mercator coordinate system (UTM). The coordinates for each dataset are divided into path and row. The first refers to the satellite trajectory and the second to the geometric centroid of the detected images. The most important EO-1's capability is the data acquition from three different viewing angles, allowing receiving images decides of the current satellite path. The first is the overhead path, with revisiting time of 16 days and angle range of ± 5.975$^{o}$. The second is the west path, which is implemented 7 days after the overhead acquition, with viewing range angle from 5.975 to 17.433

degrees and final; the east path, which is implemented 9 days after the overhead acquition, with viewing range angle from -17.433 to -5.975, (Figure 1.5.1.2).

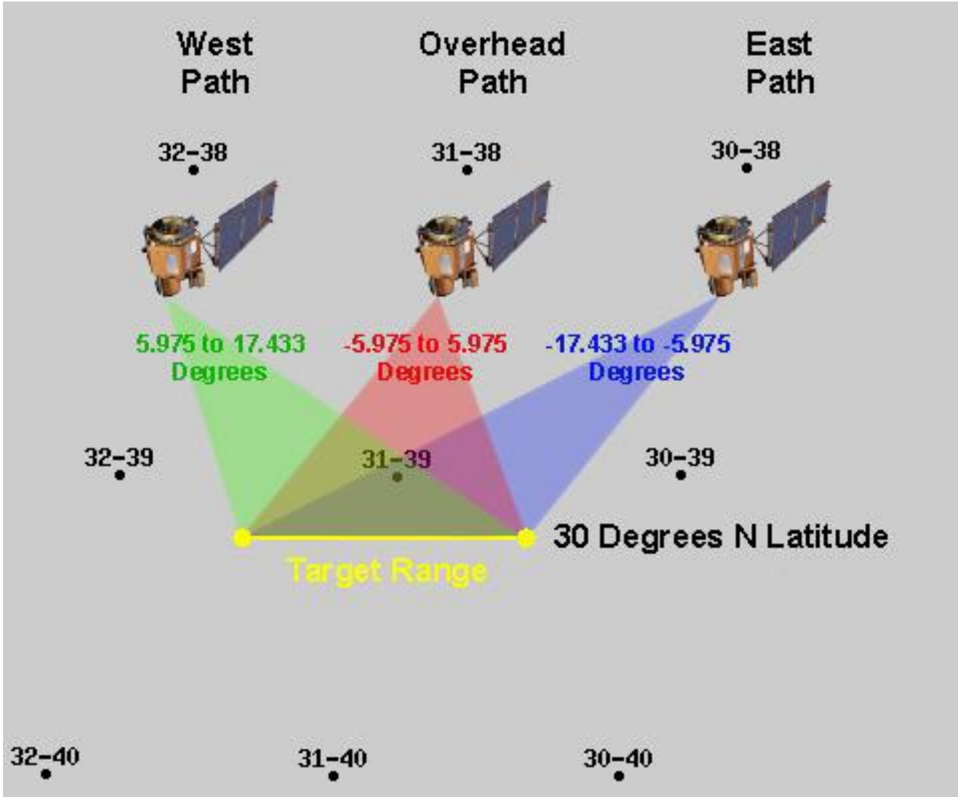


***Figure 1.5.1.2: The different viewing angle acquitions, from the EO-1 satellite, (source: USGS)***

## 1.5.2. Hyperion sensor

The Hyperion instrument was built by TRW, Inc. (now Northrop Grumman Space Technology) with strong support from key sensor subsystem organizations. The Hyperion project had a fast-track schedule and was delivered to NASA Goddard Flight Center (GSFC) for spacecraft integration in less than 12 months. The Hyperion pushbroom instrument was designed to provide radiometrically calibrated data with high quality, which are able to support; hyperspectral application evaluations and future earth observation space missions. With Hyperion, each pushbroom image frame captured the spectra from an area 30m, along track by 7.7km cross-track. The forward motion of the satellite creates a sequence of frames that are combined into a two-dimensional spatial image with a third dimension of spectral information (3D data cube).

The pushbroom technology introduced new operations and performance characteristics in comparison to traditional scanning sensors. Scanning sensors such as Landsat 7 ETM+ used linear detector arrays and a mirror that scans in the cross track direction in order to create multi-band, 2D images. Hyperion has a single telescope and two spectrometers; one in visible/near infrared (VNIR) and one in short-wave infrared (SWIR). The VNIR (356 - 1000 nm) and SWIR (900 – 2577 nm) of the EMS detect with pushbroom technology and receive data, line by line for each frame. Likewise, it offers a high quality spectral mapping due to the 220 spectral bands, with high radiometrical resolution. A narrow spatial line that is depicted in a specific time is divided into spectral components before reaching the sensors arrays. In sensor's 2D, the usage of the first dimension is for the spectral discrimination and the second for the spatial discrimination. Although, the second usage is for the surface scanning during sensor's moving. The result is either a 2D image for each spectral band or a continuous spectrum for each pixel, respectively. It is also consisted by three physical units; the Hyperion Electronics Assembly (HEA), the Cryocooler Electronics Assembly (CEA) and the Hyperion Sensor Assembly (HSA). These units are placed on nadir deck of spacecraft with the viewing direction along the major axes of the spacecraft.

Additionally, there is a specific area (852 – 1058 nm) between VNIR and SWIR spectrometers, in which the aforementioned two are overlapping, while the result is the noise production in data. Moreover, from the 242 spectral bands only the 220 of them are radiometrically calibrated, due to the low sensors' sensitivity. According to this phenomenon, pre-processing steps in each data are crucial for the noise deduction. So, the final number of the remaining spectral bands is 196, which corresponds to 8 (497nm) – 57 (925nm) in VNIR region and to 77 (918nm) – 224 (2395nm) on SWIR region. The rest of them are characterized as "bad bands". Each dataset is represented in HDF (Hierarchical Data Format) file format, with radiance values (Watt/m2*str*μm), in 16-bit radiometric scale, *(Datt et al, 2003)*.

***Table 1.5.2.1: Brief presentation of Hyperion's characteristics***

| Hyperion System | |
|---|---|
| Construction corporation | NASA |
| Platform | EO-1 |
| Orbit inclination | 98.2 degrees |
| Orbital period | 98.9 minutes |

| | |
|---|---|
| Number of bands | 242 (220 radiometrically calibrated) |
| Spatial resolution | 30m |
| Swath width | 7.5 (7.7) * 100 (120) km |
| Temporal resolution | 16 days |
| Orbit Altitude | 705 km |
| Spectral resolution | 10 nm |
| Equatorial crossing time | 10.00-10.15 a.m. |
| Spectral range | 355.59 - 2577.08 nm |
| Mass | 370 kg |
| Launched day | 21/11/2000 |
| File format | HDF |

### 1.5.3. Data Cube Structure

A typical Hyperion image has the dimensions of 256*6925*242. The first number represents the number of pixels that span the field of view. The span of the field-of-view defines the swath width. One entire swath width of data is obtained for each frame. The total number of frames is represented by the second dimension and defines the swath length. The instantaneous field of view (iFOV) for each pixel and the frame rate, 223.4 Hz, define the dimensions of ground being imaged. Each pixel location images approximately a 30 m by 30 m region of the ground. The swath width for each focal plane is comprised of 256 pixel locations corresponding to 7.7 km. There is a 1- pixel shift between the VNIR and SWIR cross track co-registration, resulting in a 255 VNIR - SWIR coincident field-of-view locations. For each pixel location, 242 spectral channels of data are obtained. Spectral channels from 1-70 are collected from the VNIR and channels 71-242 are collected from the SWIR. Due to low signal for some channels, and to reduce duplication in the VNIR-SWIR overlap region, some of these spectral channels are not calibrated. The uncalibrated channels are set to zero. The “zero-ed” channels are not removed from the file so the final data set is the same size as the initial data set.

There are three versions of the Hyperion Level 1 data product, suffixes .L1, .L1_A and .L1_ B, so the header and the data file extension should be reviewed to determine which data product is being analyzed, *(Datt et al, 2003)*.

- **Original level 1:** The data is an unsigned integer. The data is presented as calibrated radiance (W/m$^2$-sr-μm) times a factor of 100 for both the VNIR and the SWIR. The calibrated data file has the extension .L1.
- **Revision A:** The data is a signed integer. A scaling factor has been applied to the calibrated radiance (W/m$^2$-sr-μm). A factor of 40 was applied to spectral bands 1-70, and a factor of 80 was applied to spectral bands 71-242. To obtain data in units of (mW/cm$^2$-sr-μm), the data should be multiplied by 10-1. The extension to the calibrated data file is .L1_A. The header file will also indicate the version of the processing code as well as the factors used for the VNIR and SWIR bands.
- **Revision B:** The SWIR and VNIR components of the data have been spatially co-registered in the cross-track and along-track dimensions. An additional metadata file, a text file with the extension .aln.log, indicates the source file and the output file names for the final co-registered data product, .L1_B.

In particular, the available level processing data are the below:

- **Level 0R (L0R):** Data that have no corrections applied
- **Level L1_R:** These data are radiometrically corrected to compensate for variations due to detector sensitivity but not geometrically corrected and they are designed from EPGS (EO-1 Product Generation System). This processing level is only available for Hyperion data. L1R products are provided in HDF format.
- **Level 1Gst (L1Gst):** Radiometric and systematic geometric corrections derived from spacecraft ephemeris data have been applied while employing a 90-meter Digital Elevation Model (DEM) for topographic accuracy. L1Gst scenes are provided in GeoTIFF format.
- **Level 1T (L1T):** Radiometric and systematic geometric corrections incorporating ground control points have been applied while employing a 90-meter Digital Elevation Model (DEM) for topographic accuracy. Geodetic accuracy of the product depends on the accuracy of the ground control points and is expected to be within 2 pixels. Scenes that do not have adequate ground control are processed to the best level of correction (L1Gst). L1T scenes are provided in GeoTIFF format, *(Barry et al, 2001)*.

# Chapter 2: Principal theories of Synthetic Aperture Radar (SAR)

## Background

Synthetic Aperture Radar (SAR) has been widely used for Earth remote sensing for more than 30 years. It is a microwave imaging system, which covers the range from approximately 1cm to 1m of the EMS. These relatively long wavelengths are independent of atmospheric scattering and can penetrate through clouds, dust, fog, water vapor particles or even dense rainfall. Active sensors supply its own source of energy, which illuminate the target (surface). The advantage of these sensors is the possibility to acquire data day and night, *(Vanko, 2015 & Ferretti, 2014)*. Also, with high spatial resolution is suitable for various applications extending from geoscience and climate change research, environmental monitoring, 2D and 3D LULC mapping and change detection, 4D mapping (temporally and spatially), risk assessment and management up to planetary exploration. Nowadays, more than 15 spaceborne SAR systems have been designed for innumerous applications, *(Moreira et al, 2013)*.

## 2.1. Introduction to SAR

The word radar is an acronym for Radio Detection and Ranging. As its name implies, radar was developed as the meaning of using radio waves for object detection and for the determination of their distance and sometimes their angular position. The process entails transmitting short bursts, or pulses, of microwave energy in the right side of looking imaging geometry of the interest and recording the strength and origin of “echoes” received from objects within the sensor’s field of view (FOV), *(Lillesand et al, 2008 & Moreira et al, 2013)*.

SAR transmits pulses of the microwave energy with high power towards Earth’s surface and detects portion of it as a reflected backscatter from each target, in a sequential way. The returning signal can be received from the same antenna (monostatic radar) or from a different one (bi- or multi-static radar), *(Moreira et al, 2013)*. The received backscattered signals are separated into two components, which are carrying information about the amplitude and the phase of the returning signal. Information about the location of a target can be gathered by recording the amplitude of the echoed signal (the backscattered illuminating beam) and the delay between the transmitted and received signals, *(Ferretti, 2014)*. Amplitude depends on target properties (structure and dielectric properties) and on physical properties (geometry, roughness).

Although, it should be noted that each band can burst more than one frequency of energy. So, to be able to transmit signals of specific frequency bands, the radar pulse should modulate a specific central frequency: i.e. the signal should be multiplied by a sinusoidal function, often referred as the carrier. The spectrum of the transmitted signal is identical to that of the original pulse, but centered on the carrier frequency. In particular, it is hypothesized that the received signal as a certain time (t) is due to the echo of a target, is x meters distant from the radar antenna. If the shape of the transmitted pulse is a rectangular function modulating the amplitude of a sinusoid (Figure 2.1.1), the received signal will be, *(Ferretti, 2014)*:

$$s_r(t) = Acos\left[2\pi f_0 t - \frac{2\pi}{\lambda}\,2x\right] = Acos[2\pi f_0 t - \varphi] \qquad (2)$$

Phase is a function of the distance between the sensor and the target as well as target properties, *(Vanko, 2015)*. Relative phase is defined as the timing of the one EM wave component relative to another, specifying whether the vertically polarized component reaches its peak when the horizontal is near its minimum. The timing difference contains information about the structure and the composition of the target. The phase's equation is very crucial because it shows how the phase of the carrier is proportional to the target distance x *(Ferretti, 2014)*:

$$\Phi = \frac{2\pi}{\lambda}\,2x = \frac{2\pi}{\lambda/2}x = \frac{4\pi}{\lambda}x \qquad (3)$$

Together they form a complex number (Equation 4), where the sum is the overall scattering centers. To create an image, the returning signal of a single pulse is sampled and these samples are stored in an image line. As radar platforms moves forward, recording and processing of the backscattered signals build a 2D image, *(Lee & Pottier, 2009)*.

$$z = Ae^{j\varphi} = \sum z_i = \sum Real\left[A_i e^{j\varphi i}\right] + \sum Imag\left[A_i e^{j\varphi i}\right] \qquad (4)$$

SAR systems were developed to overcome the limitations of Real Aperture Radar (RAR) systems. SAR synthetically increases electronically the antenna's size to achieve a better resolution. On the other hand, RAR systems have their physical constraints due to the length of the antenna that is positioned on the aircraft or satellite.

Depending on the frequency band, considerable penetration can occur so that the imaged objects and media must be modeled as a volume (e.g. vegetation, ice, snow, dry soil etc.). More penetration will occur with longer wavelengths, which have an accentuated volume contribution in the backscattered signal. The frequencies that are commonly in use in SAR systems are depicted in Table 2.1.1.

*Table 2.1.1: Commonly used frequencies in SAR systems. The bolded bands are the most frequency used.*

| ***Frequency Band*** | ***Ka*** | ***Ku*** | ***X*** | ***C*** | ***S*** | ***L*** | ***P*** |
|---|---|---|---|---|---|---|---|
| ***Frequency (GHz)*** | *40-25* | *17.6-12* | *12-7.5* | *7.5-3.5* | *3.75-2* | *2-1* | *0.5-0.25* |
| ***Wavelength (cm)*** | *0.75-1.2* | *1.7-2.5* | *2.5-4* | *4-8* | *8-15* | *15-30* | *60-120* |

- P, L band: For foliage penetration, subsurface imaging and biomass estimation
- L, C, S, X band: Agriculture, ocean, ice or subsidence monitoring
- X and Ku band: Snow monitoring
- X and Ka band: Very high resolution imaging

## 2.2. Detected SAR image

Each SAR system measures the amplitude of the radiation backscattered toward the radar by objects (scatters) contained in each SAR resolution pixel, *(Ferretti et al, 2007)*. The detected amplitude depends on how the energy interacts with the surface, which based on several variables, (Figure 2.2.1). These parameters include the radar characteristics (viewing geometry, frequency, polarization), while the surface characteristics (land cover type, topography, relief, etc). Generally the dominant factor in determining the color tones in radar images is surface roughness. For instance, targets with high backscattered signal are identified as bright spots in the radar images and flat smooth surfaces are representing as dark areas, since the radiation is reflected away from the radar. Amplitude images are displaying by means of grey scale levels.

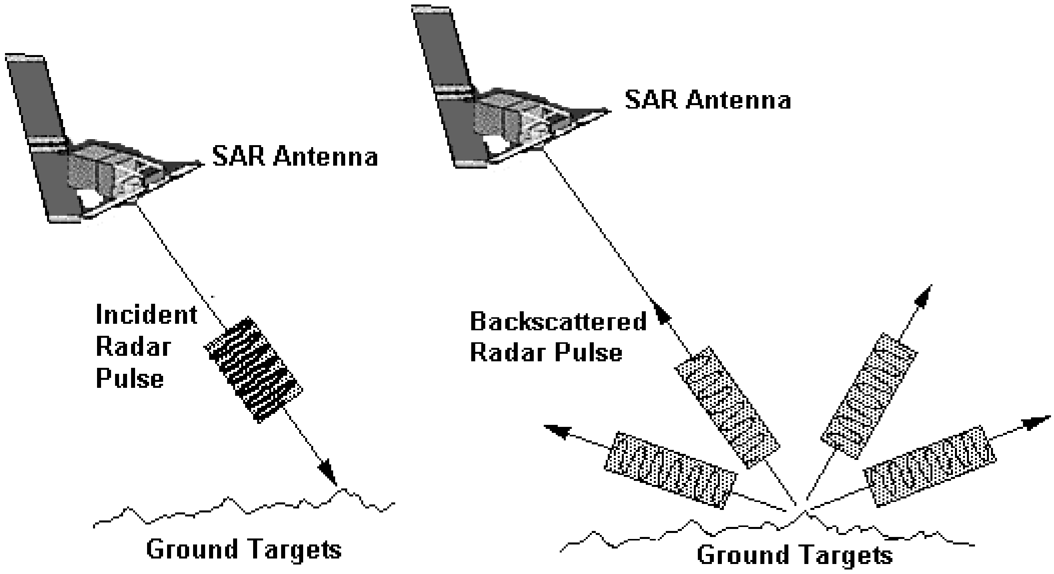


***Figure 2.2.1: A radar pulse is transmitted from the antenna to the ground (left). The radar pulse is scattered by the ground targets back to the antenna (right), (CRISP, 2001).***

## 2.3. SAR Polarization

The main problem for the quantitative estimation of different materials (soil moisture, surface roughness etc) from SAR data lies in the separation of their individual effects on the backscatter signal. SAR polarizations play an important role as it allows either a direct separation or a parameterization of roughness and moisture effects within the scattering disability.

Polarization is a characteristic of all EM radiation. Any EM wave, regardless of which part of the spectrum it occupies, propagates through vacuum as a transverse wave. The electric and magnetic field of the wave are directed perpendicular to one another and lie in a place perpendicular to the direction of propagation, *(Ockert, 2011)*. It is the direction of these fields and how they vary with time and space that define the polarization state of the wave. While the length of the vector represents the amplitude of the wave, and the rotation rate of the vector represents the frequency of the wave, polarization refers to the orientation and shape of the pattern traced by the tip of the vector, *(Stetten & Mc Laughlin, 1999)*.

The waveform of the electric field strength (voltage) of an EM wave can be predictable (the wave is polarized) or random (the wave is unpolarized), or a combination of both. In the latter case, the degree of polarization describes the ratio of polarized power to total power of the wave.

Polarimetric radar systems use multiple antennas and switches that allow a complete characterization of the reflected echo while allowing variation in the transmitted polarization as well. Especially, a fully polarimetric system can determine the echo for any combination of transmit and receive polarizations using only a small number (at most 4) of chosen measurements. An example of a fully polarized wave would be a monochromatic sine wave, with a single, constant frequency and stable amplitude.

- Linear horizontal
- Linear vertical
- Left-hand circular
- Right-hand circular

Furthermore, the polarization types are described, (Figure 2.3.1).

- **Vertical polarization:** It occurs when the electrical field of an antenna is perpendicular to the Earth's surface. The Vertical signal oscillates from top to bottom. Signals are transmitted in all directions. The usage of the vertical polarization is deposited for ground-wave transmition, allowing the wave to travel a considerable distance along the ground surface with minimum depreciation.
- **Horizontal polarization:** It occurs when the electrical field of an antenna is parallel to the Earth's surface. The Horizontal signal oscillates from left to right. While Earth is a good conductor at low frequencies; some frequencies travelling very fast.
- **Circular polarization:** This type is more used on satellites. The signal is rotating. Due to the Earth's position, it has many geometric differences. The advantage of circular polarization is that it keeps the signal constant regardless of the anomalies, *(Ockert, 2011; Kanakaki, 2016).*

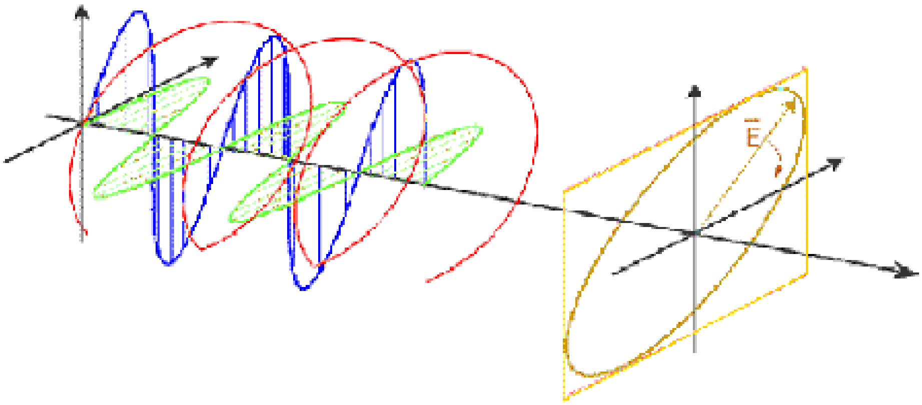


***Figure 2.3.1: Example of horizontal, vertical & circular polarizations of a plane electromagnetic wave, (source: http://latex-community.org/forum/viewtopic.php?t=24290)***

The Coherence is another thing that is required in radar polarimetric systems. The determination of the polarization of an EM wave requires details about their relative magnitudes of the EM field components and their relative phases. Radar is coherent if it can measure the relative phase and the magnitude, of the received echoes; so the polameritric radars must be coherent. Relative phase is also crucial if the responses of a target to an arbitrary combination of transmit and receive polarizations is to be mathematically synthesized, rather than directly measured. This process is called polarization synthesis. A small set of coherent measurements utilizing the orthogonal polarizations (vertical or horizontal). Polarization synthesis computes the radar cross section of the given target for any desired combination and receives polarizations. With these radars, there can be four combinations of transmit and receive polarizations:

- HH - for horizontal transmit and horizontal receive
- VV - for vertical transmit and vertical receive
- HV - for horizontal transmit and vertical receive, and
- VH - for vertical transmit and horizontal receive.

The first two polarization combinations are referred to as "like-polarized" because both polarizations are the same. The last two combinations are referred to as "cross-polarized" because the transmit polarization is orthogonal to the receive polarization, *(Stetten & Mc Laughlin, 1999).*

Radar systems can have one; two or all four of these transmit/receive polarization combinations. Note that "quadrature polarization" and "fully polarimetric" can be used as synonyms for "polarimetric". Examples include the following types of radar systems:

- Single polarized: HH or VV (or possibly HV or VH)
- Dual polarized: HH and HV, VV and VH, or HH and VV
- Alternating polarization: HH and HV, alternating with VV and VH
- Fully polarimetric or Quadrature polarization: HH, VV, HV, and VH

## 2.4. Mathematical Approach

### 2.4.1. Representation of Polarized Electromagnetic Waves

**Completely Polarized Waves:** As it was mentioned, the polarization state of an EM wave is determined by the relative magnitudes and the phases of its electric field components. Assume, an EM wave is propagated along the z-axis of a right-handed coordinate system. The electric field lies in the x-y plane and it is defined according to the 5 equation.

$$\delta^{o} = E_x^0 \cos(\omega t - kz + a_x)\, x^{\wedge} + E_y^0 \cos\left(\omega t - kz + a_y\right) y^{\wedge} \quad (5)$$

Where:

- $\omega = 2\pi f$ (radian frequency)
- $k = 2\pi/\lambda$ (wavenumber)
- $\lambda$ = wavelength
- t = time
- x & y = unit vectors in the x, y directions, respectively
- $\alpha_x$ & $\alpha_y$ = the phases of each component
- $E_x$ & $E_y$ = the corresponding magnitudes

Moreover, when the wave is **linearly polarized**, $\alpha_x = \alpha_y = \alpha$. In this case the two components are in phase with one another and equation 5 can be simplified to:

$$\delta^{o} = \cos(\omega t - kz + a) * \left(E_x^0 + E_y^0\right) = \cos(\omega t - kz + a) * e^{\wedge} \quad (6)$$

Where:

$$\delta^{0} = \sqrt{\left(E_x^0 + E_y^0\right)^2}, \quad (2.4.3) \quad e^{\wedge} = {\left(E_x^0 + E_y^0\right)}\Big/{E^0}, \quad (7)$$

In this case, the field is always parallel to the unit vector $e^{\wedge}$ (Figure 2.4.1.1). As the magnitude and sign of field vary with time and/or position, the tip of the field vector traces out a straight line parallel to$e^{\wedge}$.

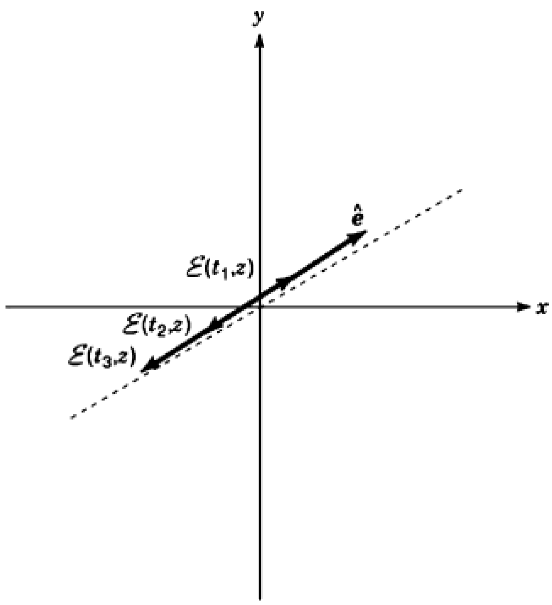


***Figure 2.4.1.1: Electric field at three instants in time for a linearly polarized EM wave. The electric field vector is always parallel to a line defined by the vectore^. The direction of e^ depends on the relative magnitudes of the x and y components of the field, (Stetten & Mc Laughlin, 1999).***

On the contrary, when $\alpha_x \neq \alpha_y$, the wave is elliptical polarized. In more general it occurs when, the two components are not in phase and the direction of the electric field is not constant. The tip of the electric field vector at any point in space (value of z) traces out an ellipse as time progresses. This can be clarified by the evaluation of the Equation 5 at a particular value of z, for example z=0.

$$\delta_{(z=0)} = E_x^0 \cos(\omega t + a_x\ )\, x^\wedge + \ E_y^0 \cos\left(\omega t + a_y\ \right) y^\wedge \quad (8)$$

The ellipse is displayed in Figure 2.4.1.2. The ellipse is characterized by its orientation angle ψ and ellipticity angle χ. in terms of the original x and y amplitudes and phases, ψ and χ are given by:

$$\tan(2\psi) = \tan(2\xi) * \cos(\delta)\ \&\ \sin(2\chi) = \sin(2\xi) * \sin\ (\delta) \quad (9)$$

Where:

$$\tan(\xi) = \left. E_y^o \middle/ E_x^o \right. \ (2.4.1.6) \quad \& \quad \delta = \alpha_y - \alpha_x \quad (10)$$

Note that ψ is defined as the smallest angle between the x axis and the major axis of the ellipse. The ellipticity angle can be related to the major and minor axes of the ellipse, $2E_{x\prime}^o$, & $E_{y\prime}^o$, respectively, through the expression.

$$\tan(x) = \pm \left. E^{o}_{y'} \middle/ E^{o}_{x'} \right. \qquad (11)$$

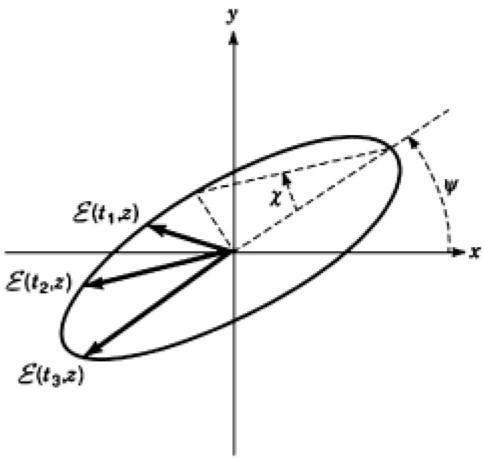


***Figure 2.4.1.2: Electric field at three instants in time for an elliptically polarized EM wave. The tip of the electric field vector traces out an ellipse as time progresses. The ellipse is characterized by its orientation angle ψ and its ellipticity angle χ, (Stetten & Mc Laughlin, 1999).***

With these definitions, the limits of χ are −45◦≤χ≤45◦ while ψ spans the range −90◦≤ψ≤90◦. The direction of rotation of the electric field vector about the ellipse is specified by the sign of χ. The left-hand elliptical polarization is specified by χ>0, while right-hand rotation is denoted by χ<0. Note that if |χ| = 45◦, the ellipse degenerates to a circle. This special case is referred to as circular polarization, (Stetten & Mc Laughlin, 1999).

**Vertical and Horizontal Polarization:** In the most radar applications, the polarized waved are presented in spherical, rather than rectangular, coordinate system. The aforementioned is more suitable, because the electric and magnetic fields that propagate in vacuum and transverse to the direction of the propagation is not always lies in a convenient fixed plane, (Figure 2.4.1.3). The direction of propagation of the wave (z^) is denoted by the k^ unit vector, while transverse coordinate unit vectors (x^ & y^) and $v^{\wedge}$ and h^. The coordinate system (k^, $v^{\wedge}$, h^) is defined such that it coincides with the standard spherical system (r^, θ^, φ^). The letters v and h define the vertical and the horizontal polarization, with the fact the angle between them is $\theta^{o} = 90^{o}$, $v^{\wedge}$ contains a vertically oriented component while h^ the horizontal, respectively. In the particular coordinate system, the spherical wave can be expressed as

$$E = \left(E_v v^{\wedge} + E_h h^{\wedge}\right) \frac{e^{jkk^{\wedge}r}}{r}, \quad (12)$$

Where r = rˆr and r is the distance from the coordinate system origin. Sufficiently far from the origin and over a small enough range of angles about the direction ˆk, this spherical wave can be considered to be a plane wave. All the expressions derived above for a plane wave propagating in the z direction are then still valid with the x and y subscripts interchanged with "v" and "h", respectively. Note that with this transformation, the orientation angle, ψ, is defined relative to the vertical axis, *(Stetten & Mc Laughlin, 1999)*.

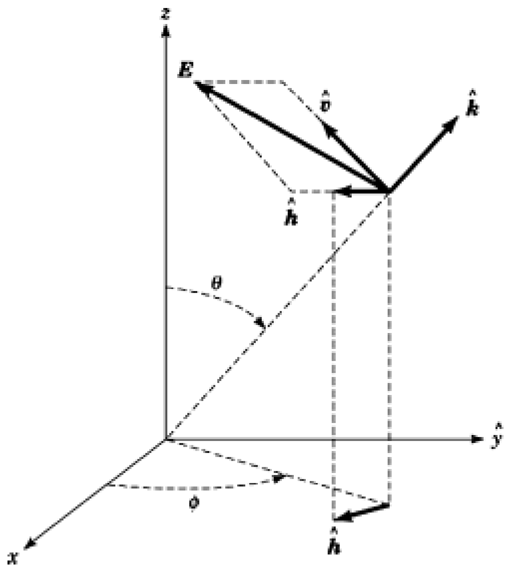


***Figure 2.4.1.3: Diagram indicating the decomposition of the electric field E(t,z) into vertically and horizontally polarized components. The direction of propagation, denoted by the unit vector ˆk, and the vertically and horizontally polarized unit vectors, ˆv and ˆh, respectively, from a right-handed coordinate system coincident with the standard spherical coordinate system (ˆr,ˆθ,ˆφ). The terms "vertical" and "horizontal" arise from the fact that ˆh is always parallel to the horizontal (ˆθ = 90◦) plane while ˆv has a component in the vertical (ˆz) direction, (Stetten & Mc Laughlin, 1999).***

## 2.5. SAR Acquisition Geometry

SAR sensors direction of transmition is orthogonal to their flight direction, (Figure 2.5.1). More recent sensors transmit and receive the microwave beams both at right-looking and left-looking (usually right), but they cannot have both directions at the same time. The inclination of the antenna on nadir viewing is referred as off-nadir or look angle (θ). Most satellites' look angle is between 20-50 degrees. It should be noted that due to the Earth's curvature, the incidence angle of the radiation (α) on a flat horizontal terrain is larger than the off-nadir angle. The direction alongside the sensor Line of Sight (LOS) is defined as the slant-range direction. The off-nadir angle is always nonzero, since the radar would receive the echoes from the detected targets at nearly the same time, making possible to create an image. The antenna receives radar echoes while moving at a few km/sec and so it is in different locations compare to where it had transmitted each pulse, *(Feretti, 2014).*

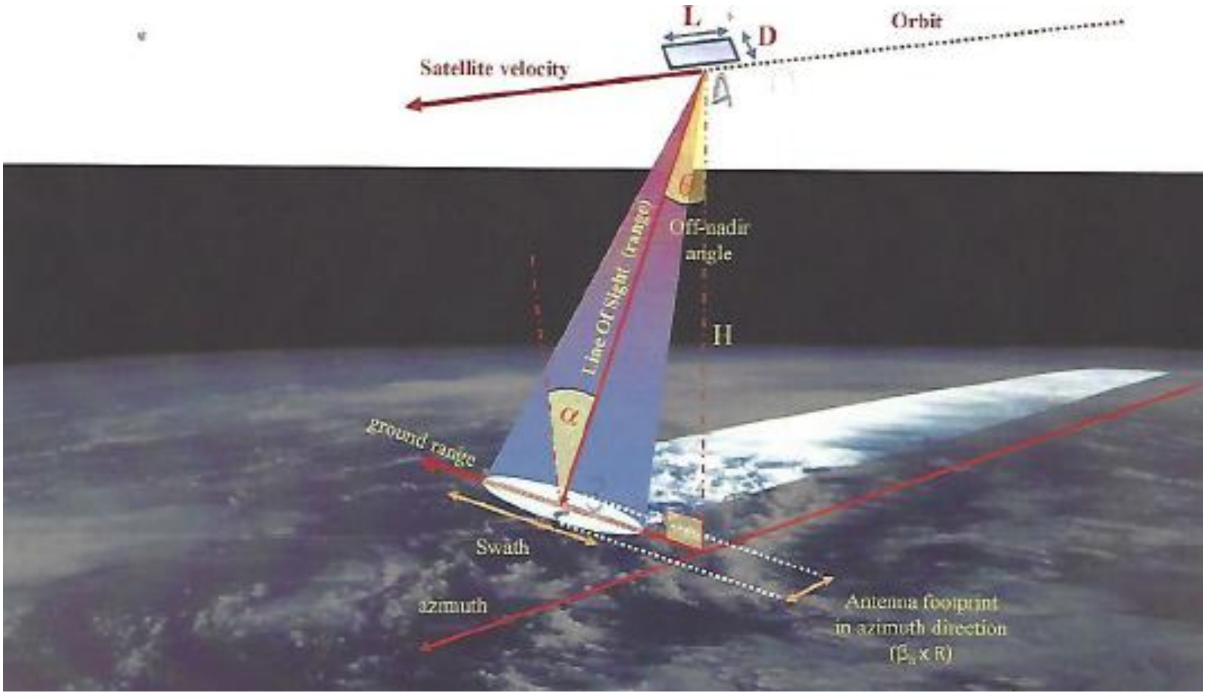


***Figure 2.5.1: The direction of a SAR platform, (Ferretti, 2014)***

The dimensions of an area in radar geometry depend on the dimensions of the antenna and its attitude. If D and L are the width and the length of the antenna, respectively, the angular beamwidth is $\beta_r \sim \lambda/D$ in across-track and $\beta_r \sim \lambda/L$ in along-track direction *(Curlander & McDonough, 1991).*

## 2.6. Backscatter measurements

The measurement of the received signal of a SAR antenna (backscatter) can vary for a multiple conditions such as; the acquisition geometries (observation angles), size of the scatterers, surface roughness and orientation, dielectric constant (in particular moisture content) of the object, wavelength and polarization of the radar signal. Radar backscatter is measured in units of area, according to the Radar Cross Section (RCS), which defined the degree of visibility of an object. According to the aforementioned parameters; backscatter can be reduced or enhanced, compared to that of a sphere of a similar size.

Bright pixels in the amplitude SAR image correspond to objects having high RCS. Radar intensity values ($I = A^2$) proportional to RCS values. A radar intensity image is radiometrically corrected when its values have been scaled, so that they can correspond to the RCS values of the radar targets, while they depend on the resolution of the radar system and the size of the resolution cell. In order to obtain measurement, which are independent of the aforementioned parameters, the concept of the normalized radar cross is used in radar remote sensing. The value in decibels (dB) is called sigma naught ($\sigma^0$).

$$\sigma^0 = 10\log_{10}\frac{\text{RCS}}{\text{Area}} \quad (13)$$

The $\sigma^0$ values (often referred to as the radar backscatter coefficient) can vary from -40 to +5 dB or even more, spanning five orders of magnitude. Typically, the reference area, according to the equation 2.5.1 is a flat terrain and its values can change from near-range to far-range pixels as a function of the local incidence angle of the illuminating beam, *(Ferretti, 2014)*.

## 2.7. Speckle noise Reduction

Speckle noise or “Salt & Pepper” is a phenomenon in all coherent imaging systems like SAR imagery etc. The source of this noise is attributed to random interference between the coherent returns, issued from the numerous scatterers present on a surface, on the scale of a wavelength of the incident radar wave (i.e. a resolution of a pixel), *(Lee et al, 1994; Goodman, 1976; Arsenault & April, 1976; Lim & Nawab, 1981)*. These bright and dark pixels result in a SAR image that fails to have a constant mean radiometric level in homogeneous areas. If there were a single large dominant scatter in the pixel, such as a corner reflector or a building, then the returned signal would be largely determined by the response of that dominant element, and any scattering from the background would be negligible. More often, though the pixel will be a sample of very large number of incremental scatters; their returns combine to give the resultant received signal for that pixel, (Figure 2.7.1), *(Richards, 2009)*.

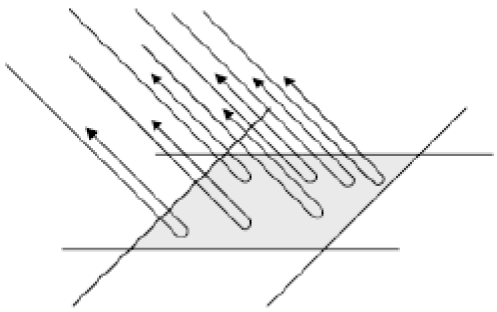

***Figure 2.7.1: Generation of speckle through the interference of a very large number of rays scattered from within a pixel, (Richards, 2009)***

Radar speckle noise has a standard deviation linearly related to the mean and is often modeled as a multiplicative process, (Equation 14). This means that the higher the signal strength the higher the noise. As a result, more speckle noise is commonly present near brighter pixel areas *(North and Wu, 2001)*. According to Hervet et al. (1998) and Schulze & Wu (1995), the statistics of the speckle noise are well known. The noise of single-look SAR amplitude imagery often has a Rayleigh distribution, whereas that of single-look intensity imagery has a negative exponential distribution. Multi-look SAR imagery usually follows a gamma distribution, assuming the looks are independent *(Lee, 1986; April & Harvy, 1991)*.

$$g(x, y) = f(x, y) * u(x, y) \quad (14)$$

Where:

- $g(x, y)$ is the observed amplitude image with speckle
- $f(x, y)$ is the image of the true radiometric values
- $u(x, y)$ is the speckle noise
- $(x, y)$ is the pixel location

The presence of speckle may decrease the utility of SAR imagery by reducing the ability to detect ground targets and obscuring the recognition of spatial patterns *(Sheng and Xia, 1996)*.

Consequently, it not only complicates visual image interpretation, but also makes automated digital image classification a difficult problem. Therefore, speckle noise in radar data must often be reduced before the data can be used for further analysis or information extraction. Dozens of despeckle filters have been proposed such as: Frost filter *(Mansourpour et al, 2006);* Gamma or maximum a posteriori (MAP) filter, *(Shanthi & Valarmathi, 2013)*; Lee filter *(Lee, 1981)* etc., in order to remove multiplicative speckle noise. Despeckle filters with good noise removal capabilities often tend to degrade the spatial and radiometric resolution of an original image and cause the loss of image detail. This may be acceptable for applications involving large scale image interpretation or mapping. However, in many cases where the retention of the subtle structures of the image is important, the performance of noise suppression must be balanced with the filter's effectiveness in order to preserve fine detail *(Xiao et al, 2003)*.

## 2.8. Geometric Distortions & Satellite Orbits

In previous sections, we discuss various variables that affect the microwave wave signal. Although, it should be noted that it also affected by the acquisition geometry and the geometric distortions, which are related to the target point, local slope and range direction. Furthermore, the geometrical distortions are described.

- **Shadowing:** It occurs, when the terrain slopes face the sensor. Then they "compressed" into few samples, while a much higher data sampling is obtained along the opposite slope.
- **Foreshortening:** When slopes with different extension on the terrain, facing the sensor the backscatter signal is very high (bright pixels). This occurs because the resolution pixel could hundred meters of ground range. In contrary, slopes facing the opposite direction appear dark.
- **Layover:** It affects in mountain and urban areas. When radar faces these particular features the beam reaches the top and reflects back, without getting receiving information until the top of the surface. The result is that the top is depicted towards the radar from its true position and "lays-over" the base, *(Ferretti, 2014)*.

One of SAR's advantages is it can detect the Earth's surface by two different acquisition geometries; the descending and the ascending. All satellites equipped with SAR sensors have a near-polar orbit according to Earth's relative orbit, while their angle is in the range of ten degrees. By combining Earth's rotation and satellite's orbital paths, the entire Earth's surface can illuminate by two different satellite geometries. Descending orbit describes the north to south sensor's travelling with westward looking (in right looking mode), while the opposite occurs in ascending mode.

## 2.9. Sentinel 1 SAR satellite

The Sentinel-1 mission is the European Radar Observatory for the Copernicus joint initiative of the European Commission (EC) and the European Space Agency (ESA). Copernicus, previously known as GMES, is a European initiative for the implementation of information services dealing with environment and security. It is based on observation data received from Earth Observation satellites and ground-based information.

The Sentinel-1 is a Synthetic Aperture Radar (SAR) instrument. It operates C-Band in four exclusive imaging modes with different resolution (down to 5 m) and coverage (up to 400 km). It provides dual polarization capability, very short revisit times and rapid product delivery. The instrument is based on a deployable planar phased array antenna carrying Transmit/Receive Modules. The antenna features both azimuth and elevation beam steering facilities, allowing SAR data acquisition in four different modes. For each observation, precise measurements of spacecraft position and attitude are available. The mission is composed of a constellation of two satellites, SENTINEL-1A and SENTINEL-1B, sharing the same orbital plane.

Sentinel-1 (Figure 2.8.1) is designed to work in a pre-programmed, conflict-free operation mode, imaging all global landmasses, coastal zones and shipping routes at high resolution and covering the global ocean with vignettes. This ensures the reliability of service required by operational services and a consistent long term data archive built for applications based on long time series, *(Sentinel-1 Handbook Documentation, 2013)*.


***Figure 2.8.1: Sentinel -1 sensor, (Sentinel-1 Handbook Documentation, 2013)***

***Table 2.8.1 summarizes the characteristics of the platform and SAR instrument.***

| System's Parameters | Value |
|---|---|
| Radar Carrier Frequency | 5.405 GHz |
| RF Peak Power | 4.141 kW |
| Incidence Angle Range | $20^o$ – $46^o$ |
| Look Direction | Right |
| Antenna Length | 12.3m |
| Azimuth Beam Width | $0.23^o$ |
| Azimuth Beam Steering Range | $-0.9^o$ to $+0.9^o$ |
| Antenna width | 0.82m |
| Elevation Beam Width | $3.43^o$ |
| Elevation Beam Steering Range | $-13.0^o$ to $+13.0^o$ |
| Maximum Range Bandwidth | 100 MHz |

| | |
|---|---|
| Pulse Repetition Frequency (PRF) Range | 1000 Hz – 3000 Hz |
| Polarization Options | Single (HH, VV), Dual (HH+HV, VV+VH) |
| Attitude Steering | Zero-Doppler Steering and Roll Steering |

The SENTINEL-1 Synthetic Aperture Radar (SAR) instrument may acquire data in four exclusive modes (Figure 2.8.2) and it is also capable of operating with duty cycles of 25 minutes per orbit in the SM, IW or EW acquisition modes, *(Sentinel-1 Product Definition, 2011)*.

- **Stripmap (SM):** This is a standard SAR stripmap imaging mode where the ground swath is illuminated with a continuous sequence of pulses and with the antenna beam pointing to a fixed azimuth and elevation angle.
- **Interferometric Wide swath (IW):** Data is acquired in three swaths using the Terrain Observation with Progressive Scanning SAR (TOPSAR) imaging technique. In IW mode, bursts are synchronized from pass to pass to ensure alignment of interferometric pairs.
- **Extra Wide swath (EW):** Data is acquired in five swaths using the TOPSAR imaging technique. EW mode provides very large swath coverage at the expense of spatial resolution.
- **Wave (WV):** Data is acquired in small stripmap scenes called 'vignettes', situated at regular intervals of 100 km along track. The vignettes are acquired by alternating; acquiring one vignette at a near range incidence angle while the next vignette is acquired at a far range incidence angle, *(Sentinel-1 Product Definition, 2011)*.

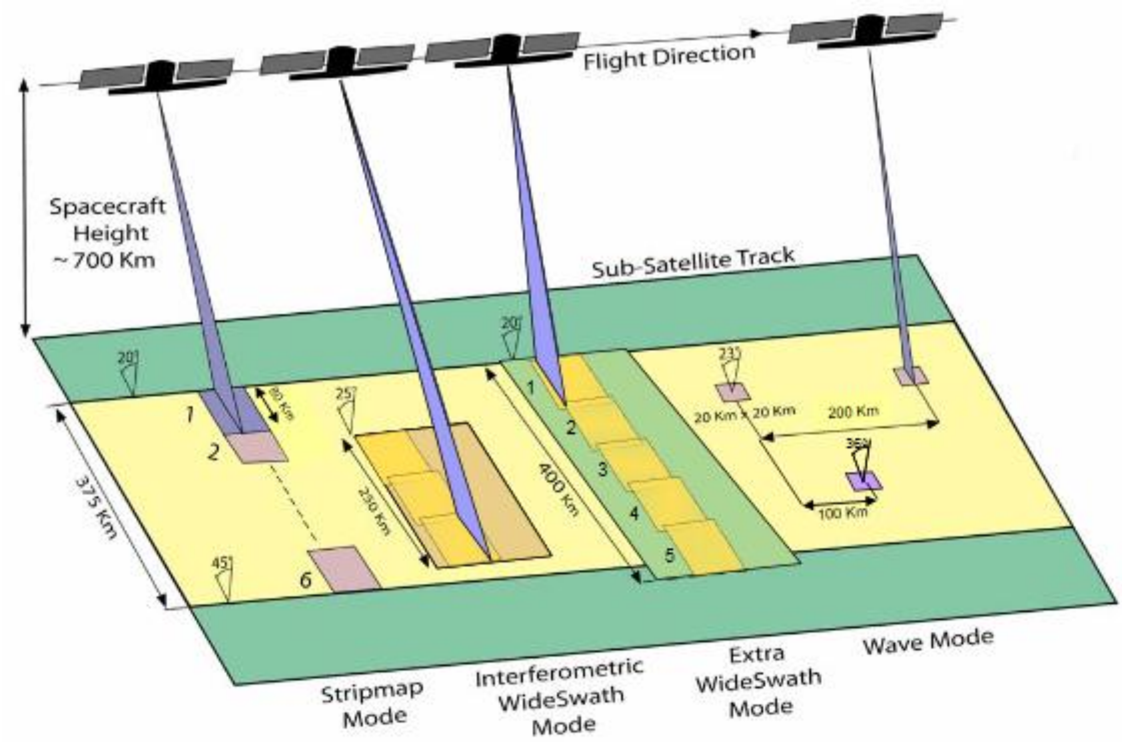


*Figure 2.8.2: Sentinel-1 Acquisition Modes, (Sentinel-1 Product Definition, 2011)*

### 2.9.1. Sentinel-1 Product Types

For the Sentinel-1 acquisition modes, the following types of L1 (Table 2.8.1) products are provided:

- **Slant Range, Single Look Complex (SLC)**

SLC products are images in the slant range by azimuth imaging plane, in the image plane of satellite data acquisition. Each image pixel is represented by a complex (I and Q) magnitude value and therefore contains both amplitude and phase information. The processing for all SLC products results in a single look in each using orbit and attitude data from the satellite. SLC images are produced in a zero Doppler geometry.

- **Ground Range, Multi-Look, Detected Products (GRD)**

GRD products lie in the ground range by azimuth surface, with image coordinates oriented along ground range and flight direction. The standard GRD products are detected, multi-look products, with approximately square resolution cells and square pixel spacing. To convert from imaging slant range coordinates to ground range coordinates, a slant to ground projection is performed onto an ellipsoid (typically the WGS84 ellipsoid) corrected using terrain height, which varies in azimuth and is constant in range.

GRD images are produced in a zero Doppler geometry. The principle of generating GRD products is the same for all acquisition modes. However, for the TOPSAR modes, the multi-looking is performed on each burst individually, while for the SM mode multi-looking is performed on entire blocks of azimuth data.

For the IW and EW GRD products, as opposed to the SLC products, all the bursts in all sub-swaths are seamlessly merged to form a single, contiguous, ground range, detected image. Therefore, the IW and EW GRD products, like the SM products, contain one image per polarization channel (i.e. either one or two images), *(Sentinel-1 Product Definition, 2011)*.

| Acq. Mode | Product Type | Resolution Class | Resolution [1, 2] [Rng x Azi] [3] [m] | Pixel Spacing [2] [Rng x Azi] [m] | No. Looks [Rng x Azi] | ENL[4] |
|---|---|---|---|---|---|---|
| SM | SLC | | 1.7 x 4.3 to 3.6 x 4.9 | 1.5 x 3.6 to 3.1 x 4.1 | 1 x 1 | 1 |
| | GRD | FR | 9 x 9 | 4 x 4 | 2 x 2 | 3.9 |
| | | HR | 23 x 23 | 10 x10 | 6 x 6 | 34.4 |
| | | MR | 84 x 84 | 40 x 40 | 22 x 22 | 464.7 |
| IW | SLC | | 2.7 x 22 to 3.5 x 22 | 2.3 x 17.4 | 1 | 1 |
| | GRD | HR | 20 x 22 | 10 x 10 | 5 x 1 | 4.9 |
| | | MR | 88 x 87 | 40 x 40 | 22 x 5 | 105.7 |
| EW | SLC | | 7.9 x 43 to 15 x 43 | 5.9 x 34.7 | 1 x 1 | 1 |
| | GRD | HR | 50 x 50 | 25 x 25 | 3 x 1 | 2.9 |
| | | MR | 93 x 87 | 40 x 40 | 6 x 2 | 12.7 |
| WV | SLC | | 2.0 x 4.8 and 3.1 x 4.8 | 1.7 x 4.1 and 2.7 x 4.1 | 1 x 1 | 1 |
| | GRD | MR | 52 x 51 | 25 x 25 | 13 x 13 | 139.7 |

***Table 2.8.1: The resolution pixel, spacing and multi-look characteristics of the GRD and SLC products, (Sentinel-1 Product Definition, 2011).***

# Chapter 3: Previous Work: Spectral and SAR analysis

## Background

This section gives a brief summary of some approaches, in identification, mapping and temporal discrimination of lava deposits using SAR and Hyperspectral spaceborne sensors. Furthermore, it is interesting to review the capabilities of the RS imagery in detection the different materials or texture in Mt. Etna or in other active volcanoes.

## 3.1. Hyperspectral Imagery

Hyperspectral imaging is often used for the identification of different materials by mapping the LULC and theirs temporal change. As it was mentioned before, there are some specific regions of the EMS where particular elements can be recognized, due to their spectral conduct (reflectance or absorption). Moreover, the characterization of surface reflectance by HSI is constrained by the spectral range and resolution (i.e. number of spectral bands) as well as by the spatial resolution of the imagery. Hyperspectral analysis of lava flows, especially in the visible and shortwave infrared regions, is rare and limited to a few volcanoes, *(Li et al, 2015)*.

**Lombardo & Buongiorno (2003)** investigate the several fractures that opened on Mt. Etna southern flank generating different lava flows spreading both in Valle del Bove towards Nicolosi at 17-18 July in 2001. This work focuses on the thermal mapping of lava flows, taking advantage of MIVIS sensor high technical performances. Moreover it focuses on the evaluation of the energy flux by means of remote-sensing techniques. Surface temperature analysis is performed on distinct lava flows using the dual band technique. These quantities are compared with the integrated temperatures retrieved using the MIVIS thermal infrared bands. The influence of topography is also considered in the flux calculation using a Digital Elevation Model (DEM) of Mt. Etna.

**Spinetti et al (2009)** characterize the air-fall deposits, recent and old lava flows, based on their spectral reflectance properties and on the textural characteristics (grain size) of the pyroclastic deposits of Mt. Etna, using field spectrometer (ADS FieldSpecPro instrument) combined with hyperspectral satellite (EO-1 Hyperion) and airborne LiDAR (Light Detection and Ranging) data, according to the 2002-2003 eruption. The spectral analysis shows that air-fall deposits are characterized by low reflectance values besides variations in grain size. This distinguishes them from other surface materials. Old lava flows show highest reflectance values due to weathering and vegetation cover. The spectral data set derived from the field survey, has been compared to corrected satellite hyperspectral data in order to investigate the Hyperion capabilities to differentiate the surface cover using the reflectance properties. This allows identifying the 2002–2003 air-fall deposits in a thematic image just few months after their emplacement. Moreover, the observed differences in the field spectra of volcanic surfaces are compared with differences in the signal intensity detected by airborne LiDAR survey showing the possibility to include information on the texture of volcanic surfaces at Mt. Etna.

**Abrams et al (2013)** use Hyperspectral and Infrared Imager (HyspIRI) mission in order to provide global observations of surface attributes at local and landscape spatial scales (tens of meters to hundreds of kilometers) to map volcanic gases and surface temperatures, which are identified as indicators of impending volcanic hazards, as well as plume ejects which pose risks to aircraft and people and property downwind. The particular project creates precursor HyspIRI data sets for volcanological analyses, which combine with the existing 28 EO-1 Hyperion data acquisitions, and 12 near-coincident ASTER data acquisitions, covering six eruptive periods between 2001 and 2010 over Mt. Etna. These datasets allow the examination of the temporal sequences of several Etnaean eruptions.

**Amici et al (2014)** compare the spectral measurements of the ADS FieldSpecPro instrument with the EO-1 Hyperion spectral in order to prove that spaceborne sensors can provide information about the spectral characterization of lava flows on Mt. Etna. They also represent reflectance spectra of lava flows of different ages and different materials. Validation results show a good agreement between the aforementioned two.

**Karagiannopoulou et al (2016)** detect LULCC that occurred between 2009 and 2012 using hyperspectral imaging (EO-1 Hyperion). For this purpose, the volcano is discriminated into three main land cover types: dense vegetation, urban and semi-urban areas and bare lava areas. For each area, a change detection map is produced. For the bare lava areas, two classification maps are produced based on (i) reflectance differences and (ii) chronology as proposed in bibliography. Results show changes in all three land cover types. In particular, for the bare lava areas, the most significant lava changes are observed in the northern and central part of the volcano, where several lava flows occurred during the 3-year study period.

**Amici & Pieri (2010)** try to evaluate the geological information that can be retrieved from RS hyperspectral (EO-1 Hyperion) and multispectral (ASTER) sensors and mapping the volcanic products for the Teide Volcano (Tenerife, Canary Islands). To account for the enhanced information content these sensors provide, hyperspectral analysis methods, incorporating for example Minimum Noise Fraction-Transformation (MNF) for data quality assessment and noise reduction as well as Spectral Angle Mapper (SAM) and Support Vector Machine (SVM) for supervised classification, were applied. Ground Truth reflectance data were obtained with FieldSpecPro Pro measurements.

**Li et al (2015)** explore the impact of the environmental factors on the spectral characteristics of the lava surfaces on Volcano (Tenerife, Canary Islands), using field, HSI and MSI spectroscopy. They report on spectral reflectance measurements of basaltic lava flows on the volcano. Lava flow surfaces of different ages, surface roughness and elevations are systematically measured using a field spectroradiometer operating in the range of 350–2500 nm. Surface roughness, oxidation and lichen coverage are documented at each measured site. Spectral properties vary with age and morphology of lava. Pre-historical lavas with no biological coverage show a prominent increase in spectral reflectance in the 400–760 nm range and a decrease in the 2140–2210 nm range. Pahoehoe surfaces have higher reflectance values than ‘a’a ones and attain a maximum reflectance at wavelengths < 760 nm. Lichen-covered lavas are characterized by multiple lichen-related absorption and reflection features.  They demonstrate that oxidation and lichen growth are two major factors controlling spectra of Tenerife lava surfaces and, therefore, propose an oxidation index and a lichen index to quantify surface alterations of lava flows: (1) the oxidation index is based on the increase of the slope of the spectral profile from blue to red as the field-observed oxidation level strengthens; and (2) the lichen index is based on the spectral reflectance in the 1660–1725 nm range, which proves to be highly correlated with lichen coverage documented in the field. The two spectral indices are applied to Landsat ETM+ and Hyperion imagery of the study area for mapping oxidation and lichen coverage on lava surfaces, respectively. Hyperion is shown to be capable of discriminating different volcanic surfaces, i.e., tephra vs. lava and oxidized lava vs. lichen-covered lava.

## 3.2. SAR Imagery

Nowadays, SAR data are using in various fields of research, including the LULCC identification and mapping as an alternative way, in order to overcome the atmospheric problems. Geographical analysis *(Weeks et all, 1997)*, surface flow pattern mapping *(Vieux et al, 2002)*, vegetation types mapping *(Simard et al, 2002)*, mangrove forest mapping *(Trisasongko, 2009)*, the volcano mapping *(Weissel et al, 2004)* are some aspects in which SAR data can be used. Recently, radar utilization is also used to identify lava deposit trough the characterization of two objects in associated with aspect of geomorphology, *(Handayani et al, 2015)*. Here below some bibliographic examples of lava deposits analysis using SAR data are presented.

**Stevens et al (2001)** investigate the surface movements of emplaced lava flows measured by Synthetic Aperture Radar (SAR) Interferometry (InSAR). In particular, they specify that Lava flows continue to move after they have been emplaced by flow mechanisms. This movement is largely vertical and can be detected using differential SAR Interferometry. The main components of their research are: (i) movement of surface scatterers, resulting in radar decorrelation, (ii) measurable subsidence of the flow surface due to thermal contraction and clast repacking and (iii) time-dependent depression of the flow substrate. These effects act in proportion to the thickness of the lava flow decay with time, although there is a time lag before the third component becomes significant. The exploration of these effects was analyzed by using SAR data from the ERS satellites over the Etna volcano.

**Dierking & Haack (1998)** investigate the L-band Polarimetric signatures of lava flows in the Northern Volcanic Zone (Iceland), using EMISAR airborne imaging radar data. Studies of radar scattering signatures are suitable of the interpretation of the volcanic terrain and the establishment of the usage of SAR for geological mapping. Intensity images with a high spatial resolution are suitable for geological interpretation, both in the discrimination of lava flows from the surrounding terrain and in the recognition of different morphologic types within a flow. The largest contrasts were observed at cross-polarization. The phase difference between the VV- and HH-channels provides information about a vegetation cover on the lava. The radar signal scattered from lava deposits is dominated by surface scattering contributions with a comparatively large fraction of multiple scattering.

**Solikhin et al (2015)** use L-band ALOS-PALSAR images, acquired before, during and after the 2010 Merapi eruption to classify and map the pyroclastic deposits emplaced during the VEI-4 event. They characterize the deposits using direct-polarized and cross-polarized L-band SAR data and by combining the information of amplitude evolution with temporal decorrelation. Changes in amplitude of the radar signal enable them to map the pyroclastic density currents and tephra-fall deposits.

**Handayani et al (2015)** use SAR full polarimetric data for the Geomorphology analysis of lava flow of Mt. Guntur in West Java, in order to minimize the adverse effects of the volcanic eruptions. This research analyze geomorphologicaly and identify the lava flows using high-resolution optical imagery through characterization (signature) landforms and L-band SAR polarimetry backscattering in combination with decision tree classification techniques using the

QUEST algorithm (Quick, Unbiased, Efficient Statistical Trees). Moreover, the accuracy of the classification results is calculated using matrix analysis accuracy and Kappa coefficient calculation. In addition, the characterization is also performed using analysis of spectral separation. The analysis showed that the geomorphological analysis can be used for volcanic landforms mapping based on their morfocronologic aspect. The identification of the image depends on the spatial resolution of the image. The objects are identified using IKONOS imagery, Google Earth, and PALSAR imagery. The results show that the HV and VV polarization serves as the best combination to identify the lava flows.

## 3.3. Hyperspectral and SAR Imagery

**Saepuloh & Koike (2010)** present a simple solution for field mapping activity in the Torrid Zone by analyzing SAR and hyperspectral data. by the combination of two types of satellite images, they detect the geothermal paths by identifying the alteration zone named A-zone. The main purpose of their study is to discriminate the alteration of the pyroclastic flow deposits and estimate their alteration degree by selecting Mt. Merapi in central Java, Indonesia as a study site and targeting the eruptions during May-June 2006. To delineate the A-zone, they apply an image fusion technique using a ratio image of RADARSAT-1 SAR $\beta^0$ data and an MNF transformation of Hyperion image data. The acquisition dates of these images are almost the same to reduce large different change in the image characteristics. In addition, a field survey is carried out to check the usefulness of the image fusion results. The A-zone is found to extend in the eastern flanks by 1.5 $km^2$ which are covered mainly by the old pyroclastic flow deposits. This area can be interpreted as an ascent flow zone of hydrothermal fluids beneath the summit.

# Chapter 4: Study Area

## Background

Mt. Etna is a young volcano and one of the most active around the world. It gives both summit and flank eruptions, but the first are occurring more frequently. Moreover, this chapter describes the principal characteristics of the volcano, its evolution history and the eruptive activity from 2007 to 2012.

### 4.1. Introduction to Etna volcano

Mt Etna is located on the eastern coast of Sicily (Italy). It is a basaltic ($SiO^2 < 50\%$) complex stratovolcano with an elevation of 3328m, which was created after the 1994 eruption *(Corsaro & Miraglia, 2014; Branca et al, 2011)*, with basic perimeter of 140km *(Murray, 1990)* and maximum base diameter of 1.200km$^2$ (47 km N-S x 38 km E-W), which was created about 20 ka ago, *(Branca et al, 2011)*.

Three main structural units characterize the area (Figure 4.1.1): the Apennine Chain to the north, the Hyblean foreland to the south and the foredeep deposits in between, *(Lentini, 1982)*. To the east these units are shorten by the Malta escarpment, a N-S extensional feature corresponding to a lithospheric boundary which confines to the east the subduction of the Ionian oceanic lithosphere beneath the Aeolian *(Corsaro et al, 2002; Spinetti et al, 2009)*.

During the 20$^{th}$ century, it was responsible for brief eruptive episodes at its summit vents with the production of large scoria cones. In particular, in Voragine crater (1945) and Bocca Nuova crater (1968) were produced and the first is the main summit crater, *(Neri et al, 2011; Clocchiatti et al, 2004)*. In May 1911, the Northeast Crater (NEC) was performed by a collapse at the northeast base of the summit cone at 3100m, *(Ponte, 1920; Behncke et al, 2013)*. The NEC became a site of intense activity between 1955 and 1981. Also, it is the highest point of Etna, at 3350m *(Tanguy & Patane, 1984; Chester et al, 1985)*, though later collapse of its crater rims reduced its height to 3329m *(Neri et al, 2008)*. In the same way, the youngest and presently the most active of Etna's summit craters, named Southeast Crater (SEC), was formed in May 1971 at the southeast base of the summit cone *(Calvari et al, 1994; Alparone et al, 2003; Behncke et al, 2006, 2008)*.

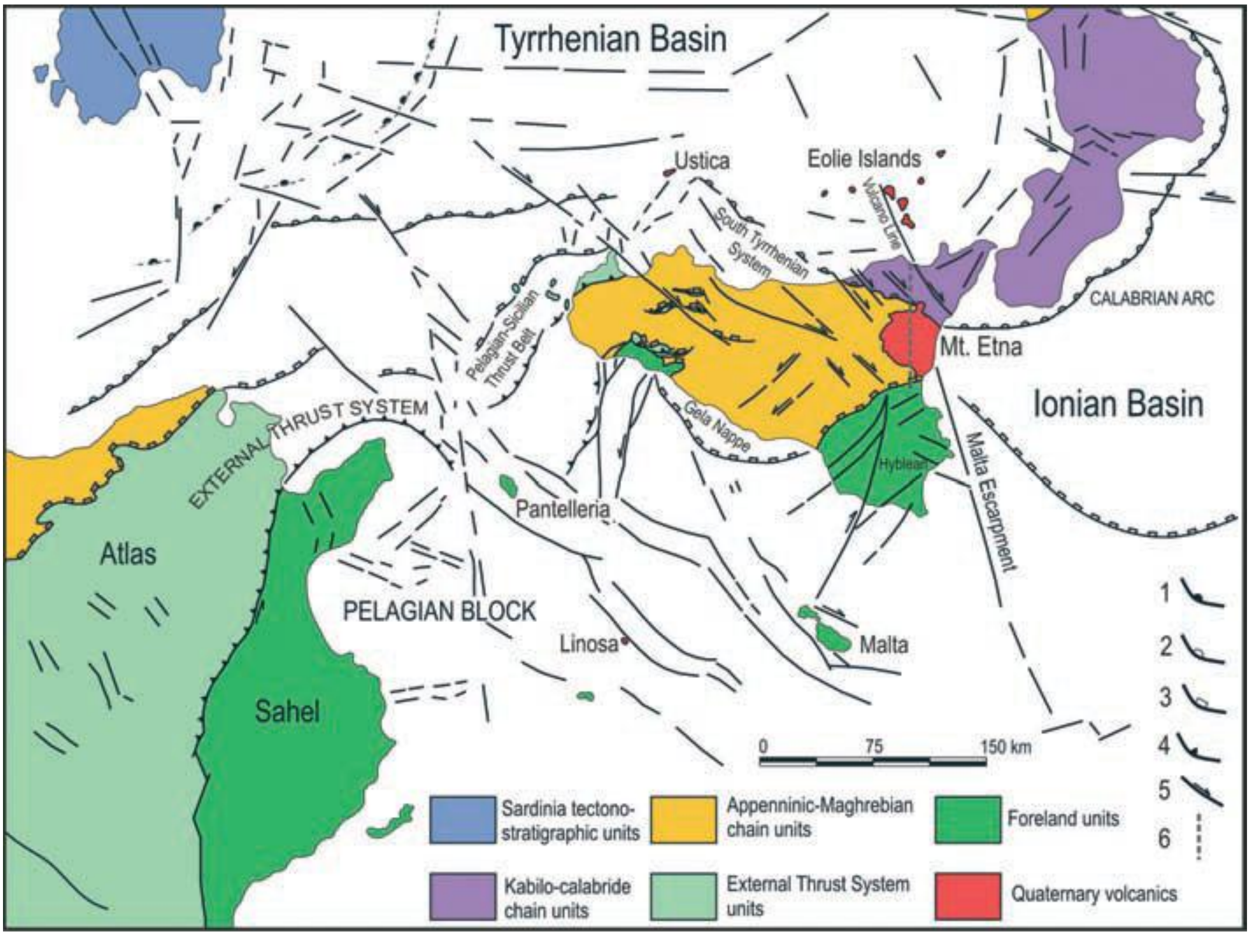


***Figure 4.1.1: Structural edifice of central Mediterranean Sea (modified by Lentini et al, 2006). 1) Regional over thrust of the Sardinia-Corsica block upon Calabride units; 2) Regional over thrust of the Kabilo-Calabride units upon the Apenninic-Maghrebian chain; 3) External front of the Apenninic-Maghrebian chain upon the Foreland units and the External Thrust System; 4) Thrust front of the External Thrust System; 5) Main normal and strike-slip faults;***

The eruptive activity of the SEC has involved numerous and relatively closed-spaced vents, pyroclastic cones began to build up within this pit, around the main vent of the SEC. On November of 2009, a small elliptical pit (P3a) opened on the lower eastern lip of the P3 pit; which two years after was occupied by a large pyroclastic cone informally named “New Southeast Crater cone – NSEC cone”, *(Behncke et al, 2014).*

## 4.2. History of Etna Volcano

Many researches (De Beaumont, 1836; Gemmellaro, 1858 & Lyell, 1859) according to their initial observations defined that Etna has a complex evolutionary history created by the superimposition of two main eruptive centers in time and space. They recognized the presence of an ancient center in the south-western side of the Valle del Bove. The feeder system of this volcano was inferred to be on the Trifoglietto plain from which it took its name. The present volcanic center, called Mongibello, was recognized as overlying it, (Figure 4.2.1).

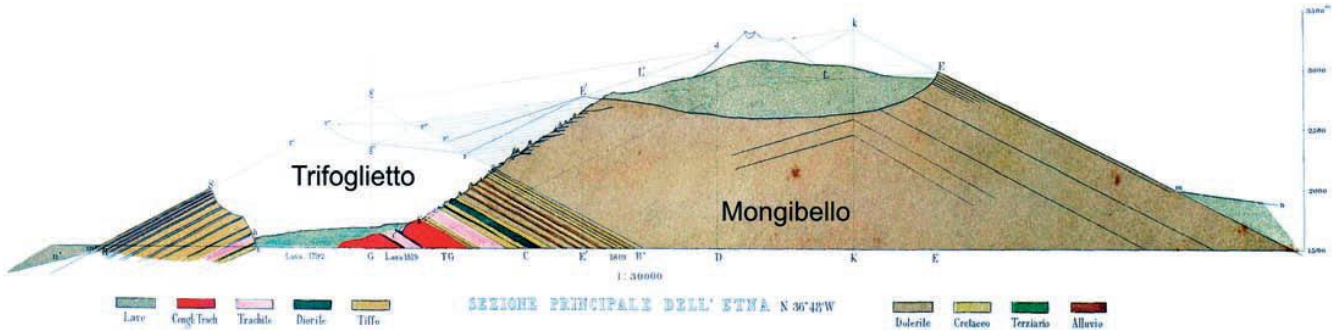


***Figure 4.2.1: Geological cross-section of Waltershausen that evidences the polygenetic structure of Etna edifice characterized by the superimposition between Trifoglietto and Mongibello volcanoes (modified from Waltershausen, 1880).***

From the 19th till the present, many researchers focused on the stratigraphy of the volcano, including the Valle del Bove area. Table 4.2.1 presents the different stratigraphic reconstruction approaches. In this point, it is needed to be mentioned that for this thesis, the latest approach is used, (Figure 2.4.2).

***Table 4.2.1: Stratigraphy framework approaches from different researchers since 19th century, (Branca et al, 2011)***

| Waltershausen 1844-1859 | Rittman 1973 | Romano 1982 | Chester et al, 1985 | Kieffer & Tanguy, 1993 | Branca et al, 2004a | Branca et al, 2011 |
|---|---|---|---|---|---|---|
| Lave Moderne | Mongibello | Recent Mongibello | Recent Mongibello | Mongibello Moderne | Stratovolcano phase | Stratovolcano Supersynthem |
| | | | | | | Il Piano Synthem |
| Lave del Medioevo | | Ancient Mongibello | Ancient Mongibello | Mongibello Recent | Mongibello volcano | |
| Lave senza epoca (Mongibello) | | Leone volcano | Leone volcano | | | Mongibello volcano |
| | | Ellitico volcano | Ellitico volcano | Mongibello Ancient | Ellitico volcano | |
| | | | Belvedere volcano | | | Concazze Synthem |
| | | | Cunigghiuni volcano | | | Ellitico volcano |
| | | | Vavalaci volcano | | | |

| | | | | | | |
|---|---|---|---|---|---|---|
| Formazione Centrale (Trifoglietto) | Trifoglietto II<br>volcano | Trifoglietto Unit<br>Serra Giannicola Piccola volc.<br>Vavalaci-Belvedere vol<br>Zoccolaro volc.<br>Trifoglietto II volc. | Trifoglietto:<br>Trifoglietto II lavas<br>Trifoglietto II pyroclastic | Cunigghiuni<br>Vavalaci<br>Zoccolaro<br>Trifoglietto II<br>Effusive series<br>Trifoglietto II<br>Pyroclastic series | Valle del Bove (central phase)<br>Cunigghiuni volc.<br>Salifizio volc.<br>Giannicola volc.<br>Trifoglietto volc.<br>Rocche volc.<br>Tanderia volc. | Valle del Bove Supersynthem<br>Zappini Syntthem<br>Cunigghiuni Salifizio, Giannicola,<br>Monte Cerasa volcanoes<br>Croce Menza Synthem<br>Trifoglietto, Rocche, Tanderia volcanoes |
| | Trifoglietto I volcano<br>Calanna volcano | Ancient Alkaline Centers<br>Trifoglietto I volc.<br>Calanna volcano<br>Monte Po vol. | Pre-Trifoglietto:<br>Trifoglietto I volcano<br>Calanna volcano<br>Terdaria volcano | Trifoglietto I<br>Calanna<br>Ancient Etna | Timpe phase | Timpe Supersynthem<br>S. Alfio Synthem<br>Acireale Synthem |
| Basalti | Pre-Etnean volcanic activity | Basal Subalkaline Lavas | Basal Tholeitic<br>Volcanic | Premieres Etna's eruptions | Basal Tholeitic<br>phase | Basal Tholeitic Supersynthem<br>Adrano Synthem<br>Aci Trezza Synthem |

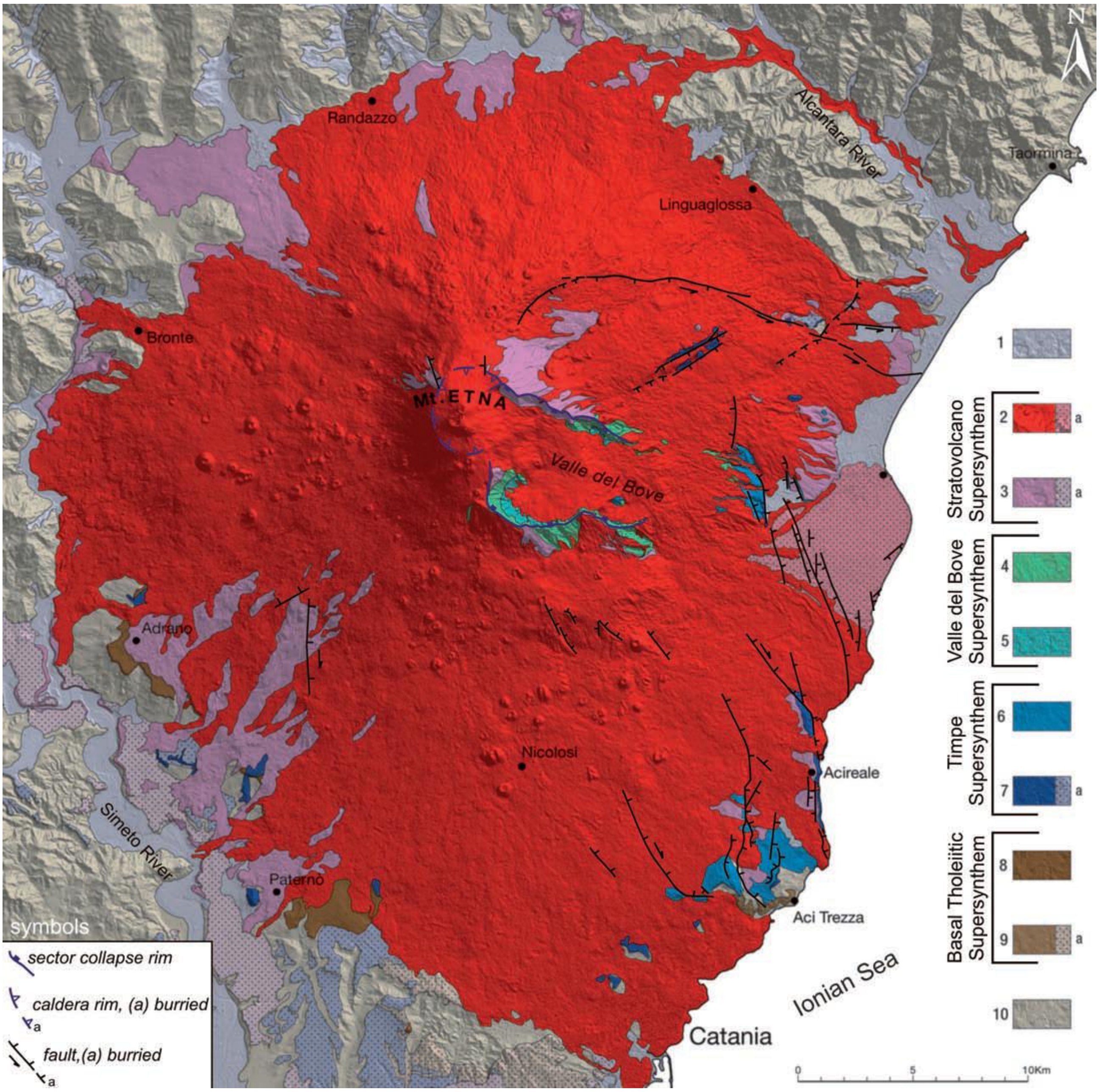


*Figure 2.4.2: The stratigraphy of Mt. Etna, modified by Branca et al, 2011.*

## 4.3. Volcanic Activity

The present Etna is characterized by a central conduit system, located immediately west of a major collapse depression, the Valle del Bove, 7km * 5km wide and 1000m deep. Volcanic activity originates from the summit craters (more often) and flanks (from a few months to several decades), *(Acocella & Neri, 2003; Allard et al, 2006)*. The present activity is characterized by long-lived effusive and moderately explosive to brief, extremely high rate and violent paroxysmal summit eruptive episodes, accompanied by strong ground deformations most of them at the SEC, *(Calvari et al., 2002; Acocella et al., 2003; Neri et al., 2006, 2007; Behncke et al., 2005, 2006; Mazzarini et al., 2005; Neri & Acocella, 2006; Allard et al, 2006)*. It is recorded that the last 400 years it erupted over 60 times from vents on its flanks, while the summit activity was continuous, *(Behncke et al, 2005)*. Both of them are responsible for various destructions, such as human property and natural environment. Although, flank eruptions are more hazardous cause they occur closer to vulnerable areas. During the past 50 years, the area around the volcano has been rapidly developed, with an extensive system of lifelines and rapid growth of population centers, often in areas that have been covered by lava flows in the historical period and that are the main reasons of Etna being more vulnerable than it was before, *(Behncke et al, 2005)*.

The intense recent activity, (Figure 4.3.1) revealed the existence of two different types of eruptive cycles, *(Behncke & Neri, 2003a, b)*. The first type, named short-term, is extending over several decades and the other (long-term) lasting several centuries. A new short-term cycle was initiated in the spring of 1993, after a major flank eruption, where the magna drained from the shallow plumbing system. After this episode the eruption frequency and the lava flow production rate increased, *(Allard et al, 2006)*.

According to previous works, the future eruptions may occur nearly anywhere on Etna, although certain areas are more likely to produce eruptions than others. These areas are those of high vent density, such as the NE, S and W rift zones *(Kieffer et al, 1975; Garduno et al, 1997*). Guest and Murray (1979) stated that flank eruptions were most probably to occur within the range of 3km from the summit craters or on the rift zones and that lava flows would rarely extend below 900m elevation.

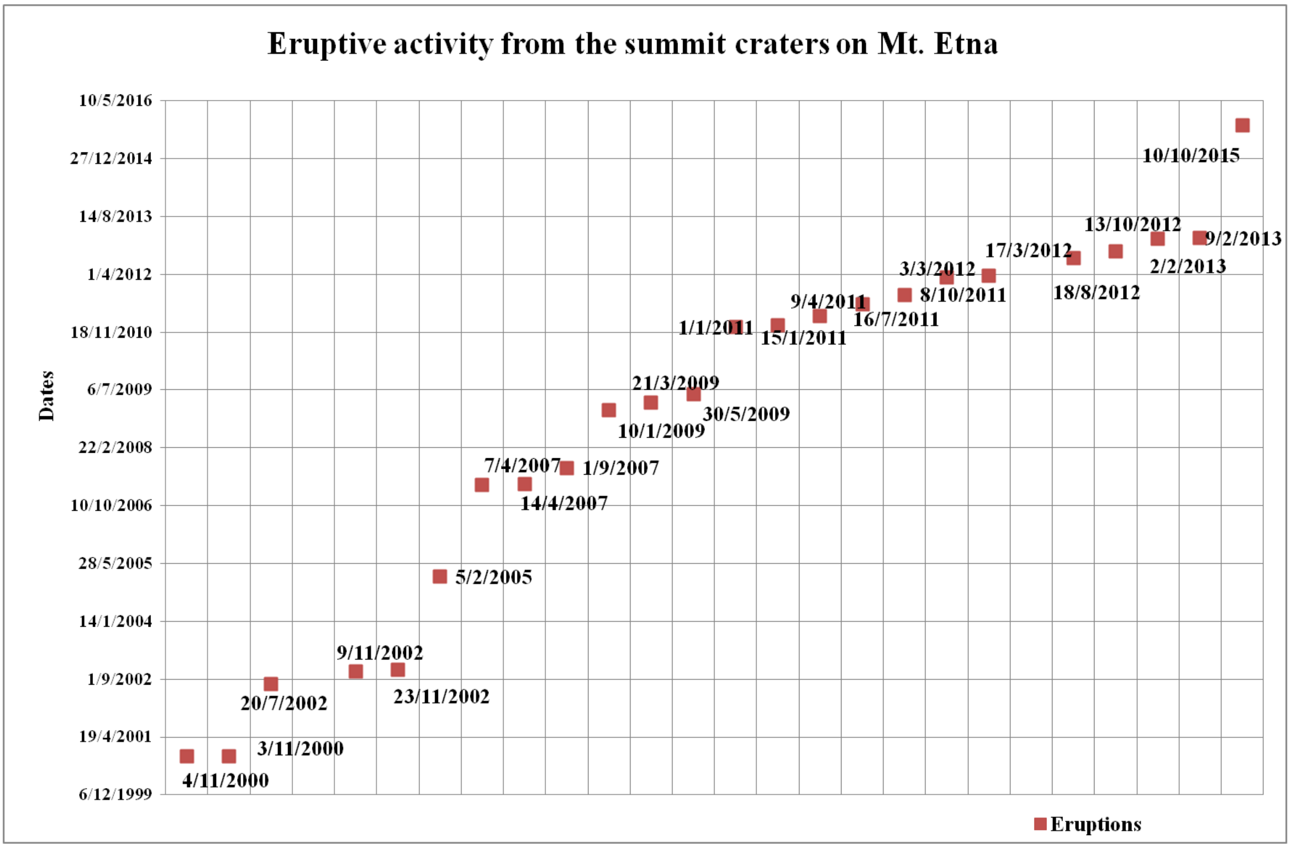


***Figure 4.3.1: The eruptive activity from each summit crater from 2000 to 2015.***

## 4.4. Volcanic Products

In general, lava is a fluid in motion under the influence of gravitational force; these lava flows are largely influenced by the local steepest descent paths. As a lava flow progresses, it also modifies the topography itself. Whatever the type of lava (e.g. pahoehoe of a'a), the flowing lava builds its own solid structures, such as levees or frozen flow units, and forms a new topography over which the newly emitted lavas will flow, *(Favalli et al, 2011)*. At Mount Etna, lava flows usually evolve into compound lava-flow *fields (Guest et al, 1987; Kilburn & Lopes, 1988; Calvari & Pinkerton, 2002)*. These fields are made of a number of flow units that form during the same effusive event, owing to a pulsed lava supply, to topography-induced bifurcations, to overflow etc. *(Lautze et al, 2004; Bailey et al, 2006)*. Flow units formed after the emplacement of previous flow units will encounter a topography that may have changed drastically with respect to the pre-eruption topography. Indeed, the emplacement of a compound lava flow field is deeply influenced by this fundamental parameter, the topography, which is intrinsically and continuously modified during the course of the emplacement itself.

According to their petrological and geochemical characteristics; the volcanic products (including the lava flows) were categorized into 14 units grouped into 6 main units; named Basal Subalkaline lavas, Ancient alkaline centers, Triglietto, Chiancone, Ancient Mongibello and Recent Mongibello, *(Branca et al, 2011).* In particular, concerning only the Recent Mongibello lava flows (3-5 ka); the prehistoric lava flows were divided into 2 units, according to their morphological state: (i) lavas scoria cones with degraded surface morphology and poorly defined flow boundaries, (ii) lava and scoria cones with well preserved surface morphology. Moreover, the historical lava flows are categorized into 5 units: (i) undated, (ii) 12$^{th}$ to 17$^{th}$ century's lava flow, (iii) 18$^{th}$ to 19$^{th}$ century lava flow, (iv) lava flows of 20$^{th}$ century up to 1974 eruption and (v) from 1974 up to 2007 eruption, *(Branca et al, 2011).*

## 4.5. Volcanic Eruptions (2007-2012) Mapping

The Volcanic activity of the Etna volcano is recorded since BC. In particular the most enormous volcanic eruptions damaged the Catania city with significant human losses. In particular, according to the latest records of Smithsonian Institute (***http://volcano.si.edu)*** and INGV, the map in Figure 4.5.1 depicts the points where a volcanic eruption with lava deposit, potentially occurred, from 2007 to 2012. The points indicate the range of the area of active lava flow centers suggesting that there are two sectors according to lava activity: a stable and an unstable sector.

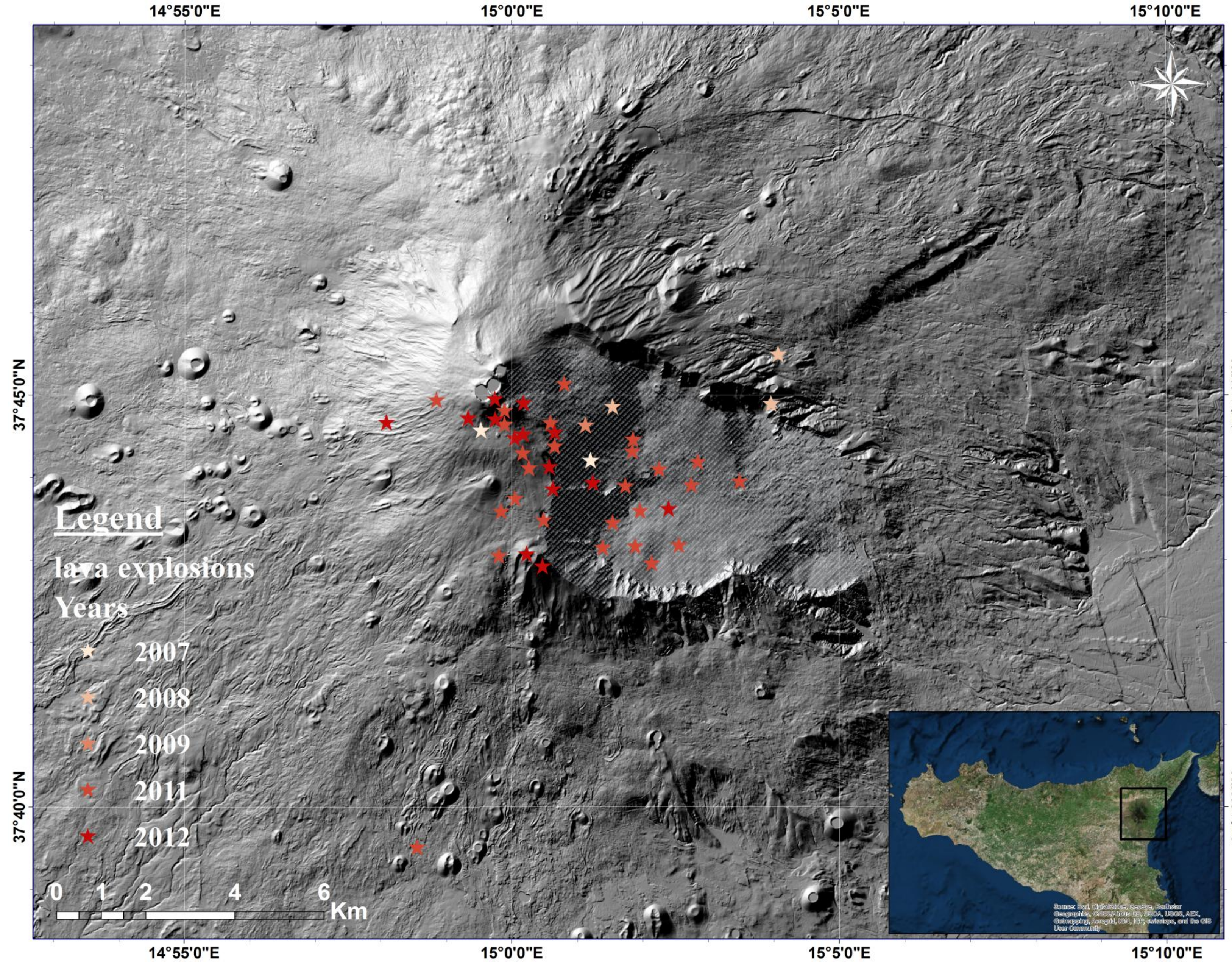


*Figure 4.5.1: Volcanic eruptions with lava deposits in Mt. Etna.*

# Chapter 5: Data & Methodology

## Background

This chapter is divided into two parts. The first part describes the datasets we used in this study and the second part the methodology.

The first one analyses both hyperspectral and SAR datasets that are used for this research. Moreover, we provide a short description of the Geological Map, in 1:50.000 scale, *(Branca et al, 2011)*, which is used as a reference map for the endmembers extraction and the Digital Elevation Model (DEM) with 10m resolution (3587236 pixels: 1894 rows and 1894 columns), from which the topographic information (aspect, slope) is extracted.

The methodology part describes: (i) the pre-processing steps for hyperspectral and SAR data. In hyperspectral pre-processing procedure, it is also included (ii) the NDVI mapping for vegetation masking and (iii) the segregation of the high and low active sections of the volcano, in order to investigate only the second area. Further up, the main processing step are (iii) Geological Map georeferencing, (iv) Training sets extraction, (v) Topographic information extraction and (vi) Statistical Approaches including the calculation of mean and standard deviation both for spectral reflectance and backscatter coefficient measurements, the temporal analyses and the quantative analysis with the topographic variables.

## 5.1. Data

This section describes the Hyperspectral, SAR and Reference data that are used.

### 5.1.1. Hyperspectral Data (EO-1 Hyperion)

The Hyperion data were downloaded from the GLOVIS (USGS) website, *(*http://glovis.usgs.gov/*)*. The chosen dates are 9/7/2007, 8/10/2009 and 14/7/2012. The selection criteria are mentioned below.

1. They include the summit crater of the volcano
2. The cloud coverage in smaller than 10% and it doesn’t cover the summit craters.

3. 2009 and 2012 datasets' look angle are between $-5^o$ and $+5^o$, (overhead path), in order to avoid the geometrical distortions. However, the 2007 image doesn't fulfill the above prerequisite.
4. We select both 1R and 1T level processing data. Level 1R data were used in order to correct the striping effect but the failure in atmospheric correction (negative values in various part of EMS) and the oblique viewing angle of 2007 (-22,323) dataset, rendered the dataset not reliable for further processing. Instead, we used Level 1T data (that includes radiometric and geometric corrections) for further analyses.
5. 2009 and 2012 datasets were chosen, according to the volcanic activity records, because between these dates, volcanic eruptions with lava deposits occurred, within a few months temporal range. On the other hand, the 2007 dataset was selected as the reference image since Amici et al (2014) use this dataset in their work.

Table 5.1.1.1 and figure 5.1.1.1 depict the Level 1T datasets, in pseudocolor RGB composition. The direction of all datasets is from NW to SE, with ~8km width, which cover the main section of the volcano as well as small urban, cultivated and forest areas (the Level 1R datasets cover the same geographic area). This particular area has a great scientific interest, due to the continuous volcanic activity and the ability to change the LULC environment rapidly and rigorously. The volcanic eruptions are responsible for various hazards in human and natural environment and lots of natural hazards management assessments politics have implemented for the avoidance of these destructions.

***Table 5.1.1.1: The main characteristics of the Hyperion datasets***

| | 2007 | 2009 | 2012 |
|---|---|---|---|
| Scene Name (Level 1R & 1T) | EO1H1880342007190110KF | EO1H1880342009281110PF | EO1H1880342012196110PF |
| Spatial Res. | 30m | | |
| Spectral Res. | 10nm | | |
| VNIR & SWIR calibrated bands | 8-55 (426-895nm)<br>77-224 (912-2396nm) | | |

| | | | |
|---|---|---|---|
| Site Latitude | 37 42 02.61 | 37 35 22.67 | 37 48 52.59 |
| Site Longitude | 14 59 25.86 | 14 57 19.85 | 15 01 08.82 |
| HYP Start Time<br><br>Stop | 09:10:21<br><br>09:14:39 | 09:19:58<br><br>9:24:17 | 09:14:24<br><br>09:18:43 |
| Cloud Coverage | 0-9 % | | |
| Look Angle | -22,323 | -5,4479 | -1,2394 |
| Map Projection & Datum | WGS ’85, UTM 33N | | |

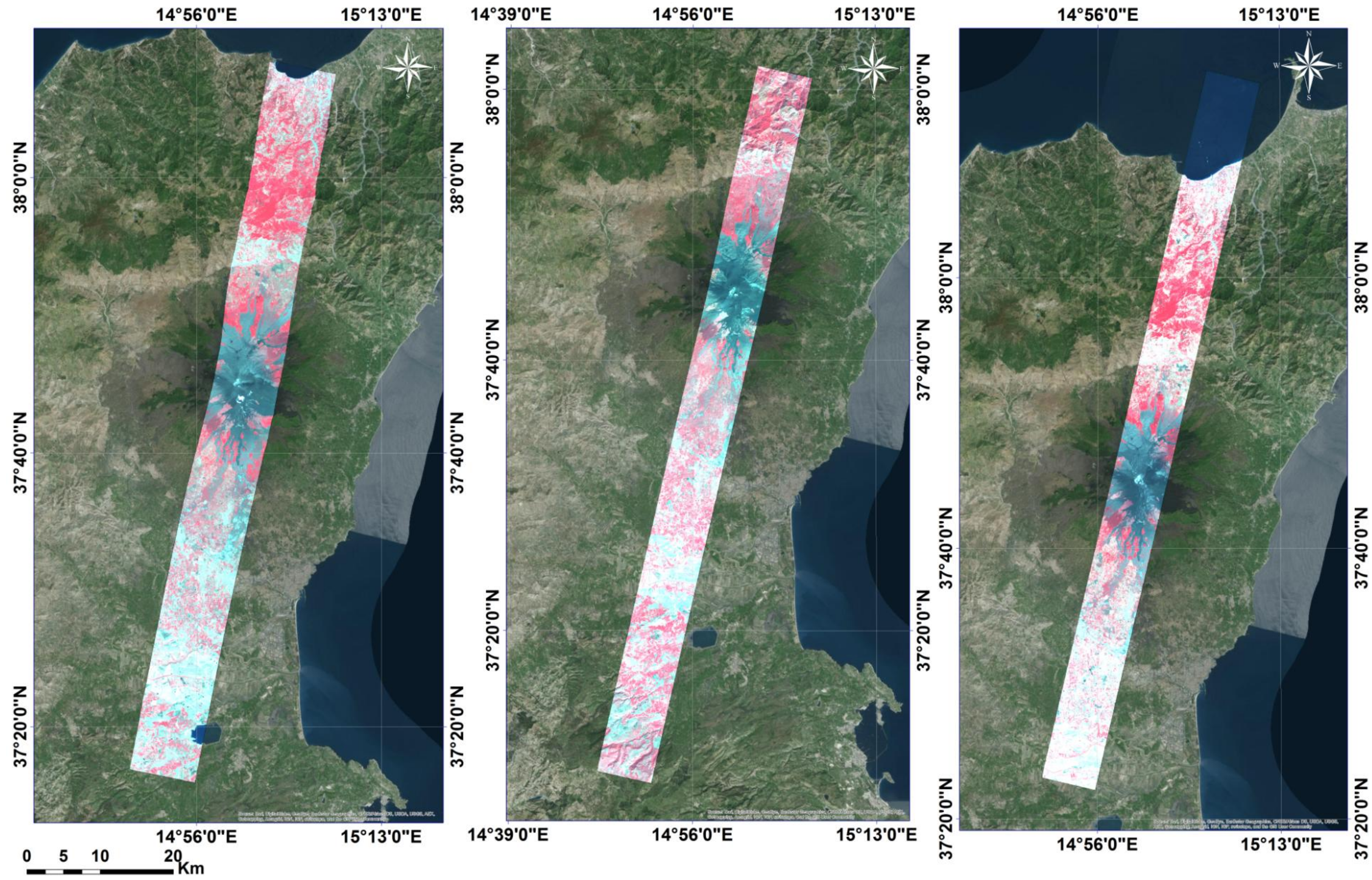


*Figure 5.1.1.1: The RGB composition (R: 782nm, G: 691nm, B: 599nm) of 2007 (left), 2009 (middle) and 2012 (right) Hyperion dataset*

### 5.1.2. SAR data (Sentinel-1)

In this study, two scenes are used; acquired from the Sentinel-1A SAR sensor. Data were retrieved from the Sentinels Scientific Data Hub (https://scihub.copernicus.eu/), one in ascending and the other in descending acquisition mode. The main criterion of selection was seasonality. The most suitable season was summer and especially August, where in general, the moisture percentages are low and is in accordance with the Hyperion and Sentinel-2 data acquisition dates. In Table 5.1.2.1 presents the main characteristics of the S-1A data and the visualization of the above is represented in Figure 5.1.2.1, respectively.

***Table 5.1.2.1: Characteristics of the Sentinel-1A datasets***

| Sentinel Sensor | 1A | |
|---|---|---|
| Date | 22.08.2016 | 16.08.2016 |
| Pass | Ascending | Descending |
| Acquisition Mode | IW | |
| Polarization | VV, VH | |
| Map Projection | WGS’ 84 (DD) | |
| Near Latitude<br>Near Longitude | 37.213<br>14.307 | 37.231<br>14.259 |
| Far Latitude<br>Far Longitude | 37.213<br>15.658 | 37.231<br>15.658 |
| Near Incidence Angle<br>Far Incidence Angle | 30.631<br>46.379 | 30.629<br>46.391 |

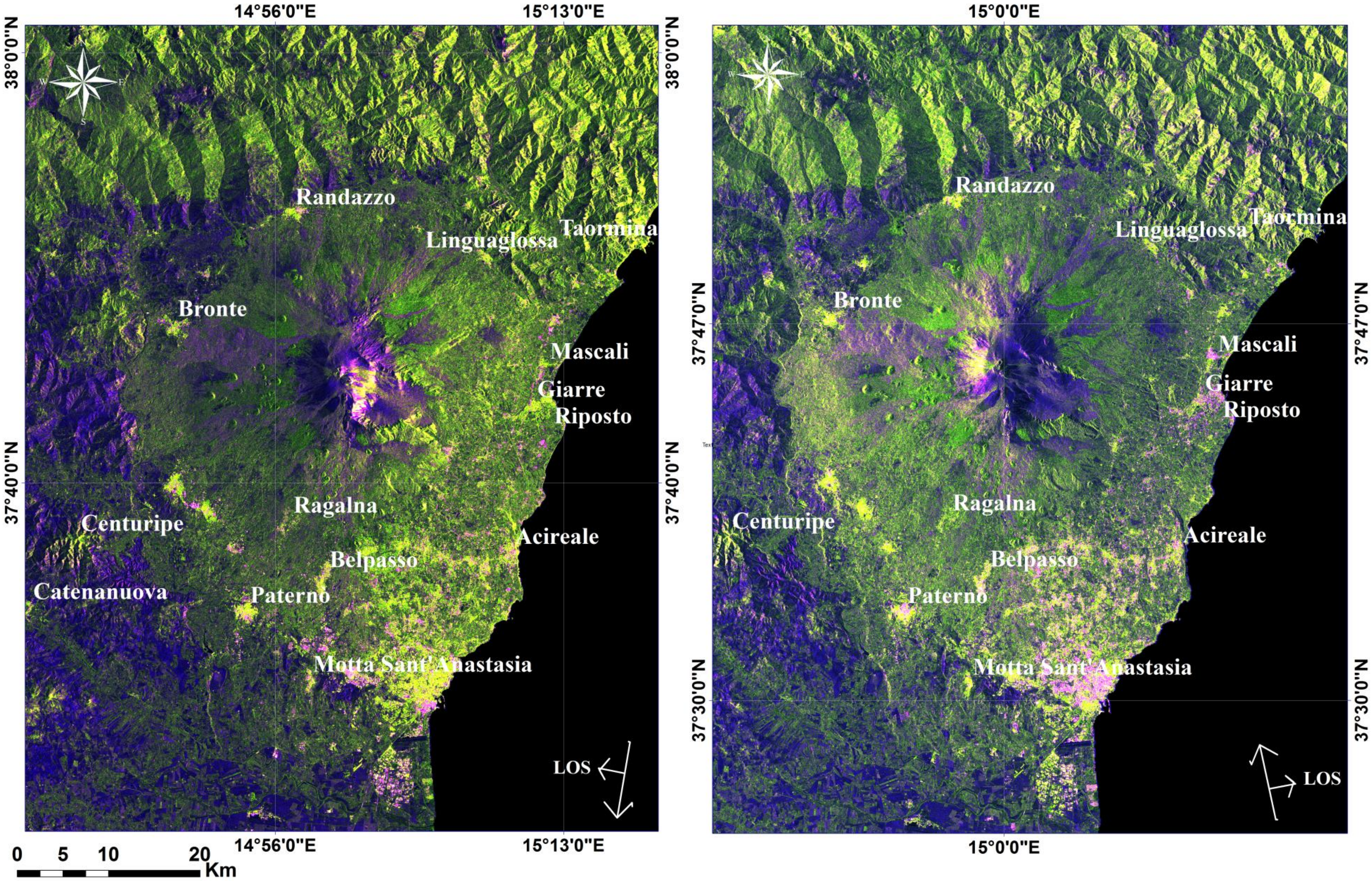


*Figure5.1.2.1: Dual-polarization and Single-polarization Sentinel 1A in ascending and descending geometry pseudocolor image R: VV, G: VH, B: VV/V*

### 5.1.3. Geological Map

The new Geological Map of Etna volcano at 1:50.000 scale, which was created from Branca et al (2011) and acquired from the INGV, is used in order to extract the training sets, which correspond to 4 different volcanic categories and their subdivisions. The differentiation of these groups accomplished by the detection of the deposits that were generated both in Il Piano Synthem (Mongibello Volcano) and in Concazze Synthem (Ellitico volcano), (see Chapter 4). More specifically, we divided the Mongibello's volcanic products into 3 sub-groups, which belong to Torre del Filosofo formation; (i) 1971-2007, (ii) 1669-1971 and (iii) 122 BC–1669 AD. The Ellitico volcanic products are assigned as a single entity. Figure 5.1.3.1 depicts the aforementioned Geological Map. A brief summary about the two main categories is represented below.

**Torre del Filosofo formation** was defined by the SERVIZIO GEOLOGICO D'ITALIA (2009a), consists mainly of lava flows and subordinate proximal and distal pyroclastic fall deposits covering almost entire Etna summit and the Valle del Bove and took place after Il Piano caldera collapse (122 BC) up to the present. On the whole, the most common litho type is characterized by a porphyritic texture containing phenocrysts of plagioclase (pl), pyroxenes (px) and olivine (ol) in highly variable amount and size. Lava composition ranges from basalt to mugearite *(Corsaro & Pompilio, 2004).* Lava flows are mainly compound lava flow fields with prevalent "a'a" morphology and/or a more complex mix of both "a'a" and "toothpaste". The morphology of the lava field rarely is pahoehoe. The eruptive fissures are formed by hornitos, spatter ramparts and single or coalescent scoria cones elongated according to the fissure trend. The scoria cone deposits are generally made of an alternation of scoriaceous lapili and bomb-rich layers. Volcanic products belonging to this formation are divided into three time intervals: (1) post- 122 BC plinian eruption-1669 AD eruption; (2) post 1669 AD eruption- pre 1971 AD eruption; (3) 1971 AD eruption-present (May 2007 eruption), while these categories are used as training sets, with the acronyms Mongibello Filosofo 3 (MF3), Mongibello Filosofo 2 (MF2) and Mongibello Filosofo 1 (MF1). The formation mainly covers the Pietracannone formation. The thickness is not determinable. Lava flows are described in the Digital Supplementary Materials.

**Ellitico formation** consists of the following lithostratigraphic units, which are described in Table 5.1.3.1. Also, this formation is used as a training set, named Ellitico.

*Table 5.1.3.1: The Lithostratigraphic units, which compose Ellitico lithosomatic unit. A and B code names represent the upper and lower members, correspondingly.*

| Formation | Acronym | Code | Description |
|---|---|---|---|
| **Portella Giumenta** | EPG | 25a,b | Complex pyroclastic succession subdivided into three members; (i) Osservatorio Etneo member (pyroclastic made of scoriaceous spatters that became reddish and partially welded), (ii) Ragabo member (rheomorphic lava flows often banded cropping out discontinuously), (iii) Biancavilla-Montalto ignimbrite member (pyroclastic flow deposits with at least four flow units. Pyroclastic are scoriae and ash flows including reomorphic spatters and lithic lava blocks. Radiometric ages: 15,420±60 ka, 15,050±70 ka |
| **Monte Calvario** | EC | 24 | Autoclastic lava breccia deposits, often hydrothermally altered, and lava flows. Lava composition is benmoreite, porphyritic texture. The thickness ranges from 20 to 100 m. |
| **Piano Provenzana** | EP | 22 | Lava flows, scoria cones and pyroclastic fall deposits. Lava composition ranges from hawaiite to benmoreite, aphyric to porphyritic texture, variable in quantity and size. Radiometric ages: 42.1± 10.4 ka, 40.9±14.4 ka, 32.9±10.6 ka, 30.8±21.2 ka, 28.7±12.6 ka. |
| **Pizzi Deneri** | EPD | 21a,b | Lava flow succession interbedded with volcaniclastic deposits, subdivided into two members. Lava composition ranges from hawaiite to mugearite. Radiometric ages: 32.5±17.8 ka, 29.1±10.6 ka |
| **Serra delle Concazze** | ESC | 20 | Pyroclastic flow and fall deposits interbedded with explosion breccia, epiclastic deposits, and lava flows. Lava composition ranges from hawaiite to benmoreite, subaphyric to high porphyritic texture. The thickness ranges from 100 m to 400 m. Radiometric ages: 41.3±6.2 ka, 56.6±15.4 ka. |

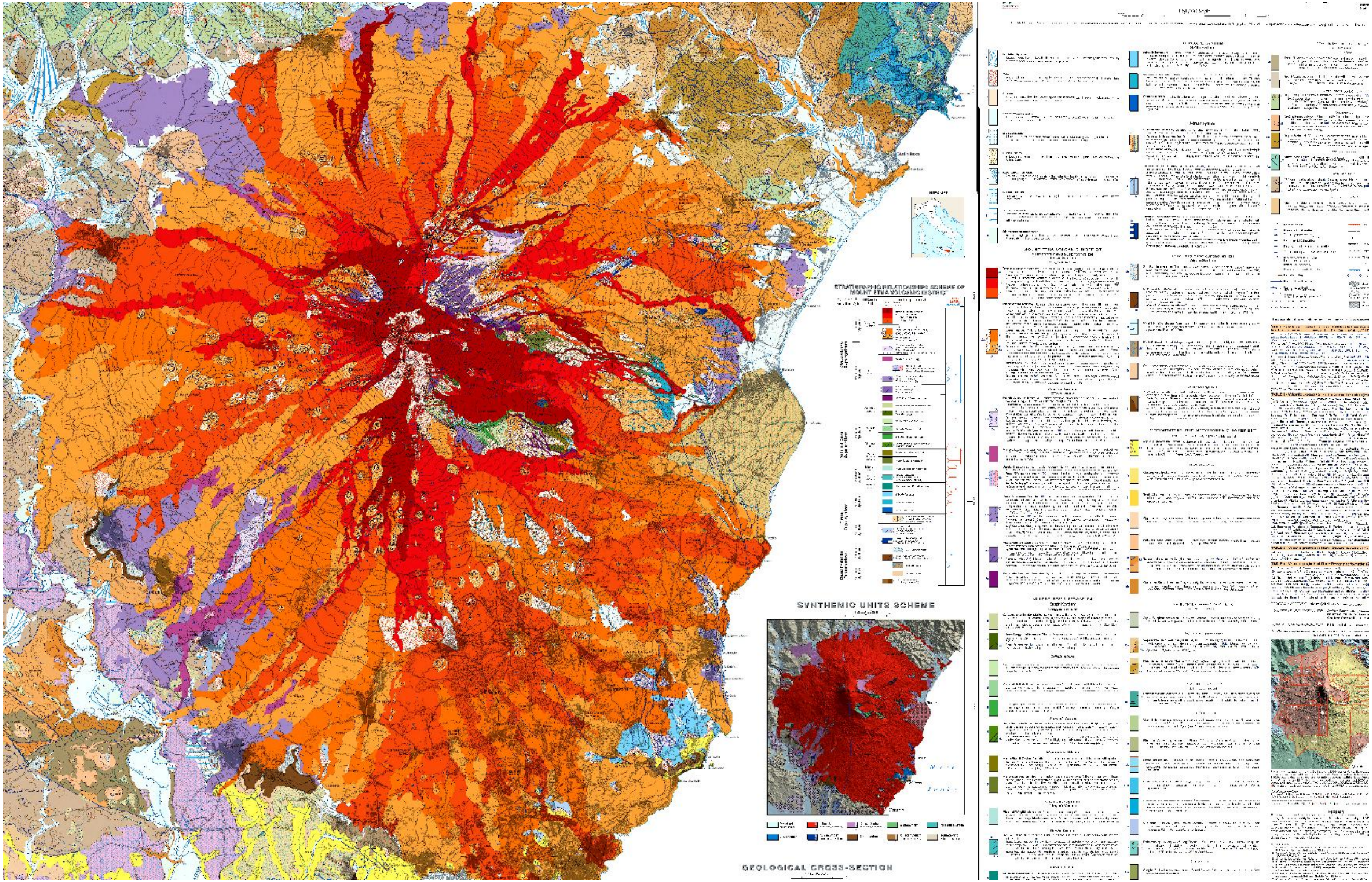

*Figure 5.1.3.1: The Geological Map of Etna Volcano, in 1:50.000 scale, (Branca et al, 2011)*

### 5.1.4. Digital Elevation Model (DEM)

In order to produce the topographic slope and aspect, a Digital Elevation Model was used, which was obtained from the CNR - Istituto di Acustica e Sensoristica (CNR-IDASC) "Orso Mario CORBINO". The aforementioned product was derived from LIDAR data acquired during ATA flights carried out during 2007-2008 campaigns on the behalf of Sicily region, for the Department of Land and Environment - Department city planning. This initial DEM has 2m spatial resolution, while its coordinate system is WGS84, UTM 33N. Figure 5.1.4.1 presents the hillshade product, which was created from the DEM, resampled in 10m spatial resolution. The resampled DEM is final layer which was used for further processing.

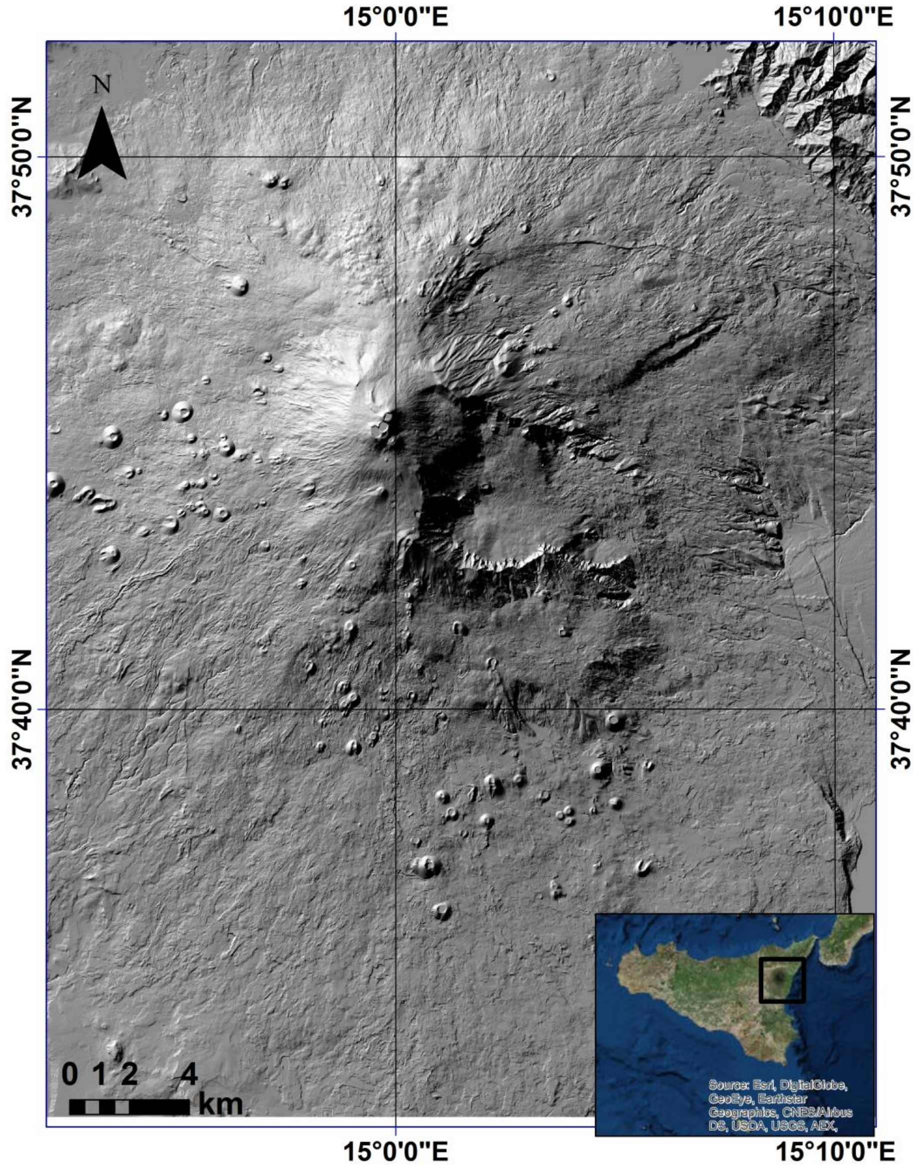


*Figure 5.1.4.1: The hillshade calculation, using the DEM (10m).*

## 5.2. Methodology

### 5.2.1. Pre-Processing Steps

This chapter presents the main preprocessing procedures applied to the hyperspectral (L1R & L1T) and SAR data. In particular, it concerns (i) the destriping algorithm to Hyperion L1R data (2007, 2009 and 2012), (ii) the elimination of the atmospheric effects and the conversion from radiance to reflectance (bottom of the atmosphere – BOA) values in both datasets, (iii) the data co-registration, in order to ensure a sub pixel spatial accuracy and (iv) the noise and dimensions reduction of L1T data using Principal Component Analysis (PCA). Moreover, this chapter includes the NDVI mapping and masking of vegetation and dynamic volcanic section. Correspondingly, the pre-processing steps for SAR data (ascending-22.08.2016 and descending-16.08.2016) are: (i) the radiometric calibration, which converts the radar intensity values into sigma 0 ($\sigma^0$) backscatter coefficient (in decibel (dB) values), (ii) the geometric correction by applying the range Doppler terrain correction operator and (iii) the despeckle filtering (Gamma-Map).

#### 5.2.1.1. Hyperspectral Pre-Processing Steps

Both L1R and L1T data include 242 spectral bands, from which only 155 were finally retained for further processing. From the excluded bands, (i) 44 are uncalibrated, (ii) 77 bands (912nm) and 78 (922nm) have high noise values (low signal to noise ratio), due to the overlay between VNIR and SWIR sensors and (iii) bands 120-132 (1346-1467nm), 165-182 (1800-1971nm) and 185-187 (2002-2022nm) due to intense atmospheric effects, (Pervez et al, 2015; Datt, 2003).

Furthermore, they include information about the wavelength, full width at half maximum (FWHM), gains offsets and irradiance. Figure 5.2.1.1.1 shows the flow charts of the L1R and L1T data preprocessing. The (pre-) processing procedures were performed using ENVI 5.2 & 5.3 software.

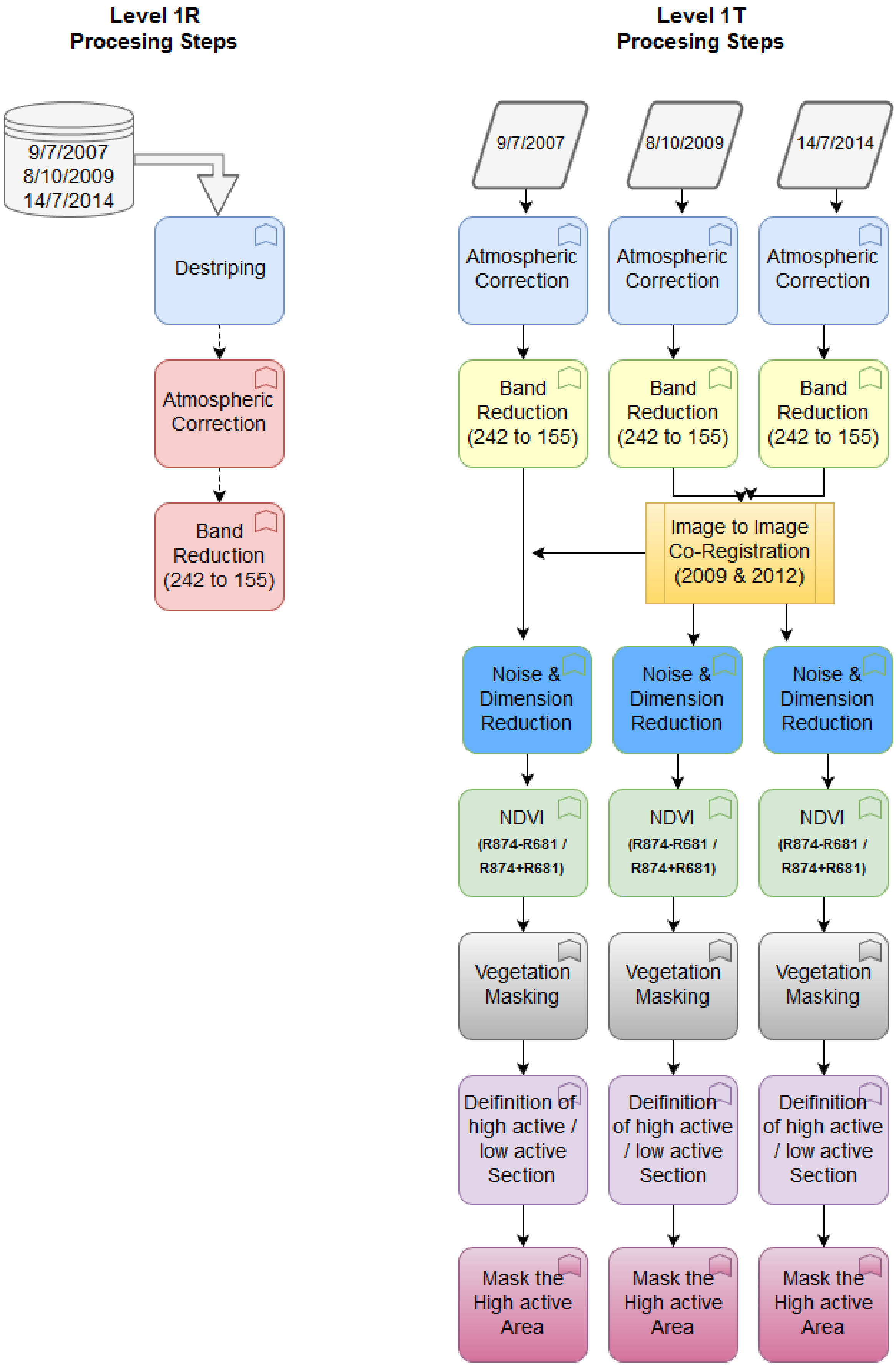


***Figure 5.2.1.1.1: L1R & L1T Pre-processing flow chart.***

### 5.2.1.1. (A)Destriping

Since every image column per band corresponds to the signal of the same Hyperion detector, the adjustment of the individual column statistics is possible in order to destripe the data. Such methods are based on global and local statistic algorithms implying that each individual column mean and/or standard deviations equaled to the global mean of the spectral band or to the statistics of adjacent columns. Other methods rely on a transformation of the dataset into the frequency domain and use the amplitudes of each image row to find and eliminate significant variations. Some destriping techniques adjust only predefined image columns, other methods use a threshold to identify image columns that have to be corrected; other methods are based on a recalculation of the whole image information, *(Scheffler & Karrasch, 2013)*.

In this study SPEAR-Vertical Stripe Removal and THOR-De-Striping techniques are tested, on the L1R Hyperion datasets. The bands 1-7, 58-76 and 225-242 have no corrected stripes since they do not contain any image signal. In Figure 5.2.1.1.2 an example of the correction results is shown for band 8 (427 nm), of the 2009 dataset. The THOR-De-Striping technique is finally retained for further processing because; it provides more accurate results and no batch errors in the atmospheric correction procedure. Examples of the destriping results, using the aforementioned spectral band for each one of the three dates between the original imagery and the destriped image are shown in Figure 5.2.1.1.3.

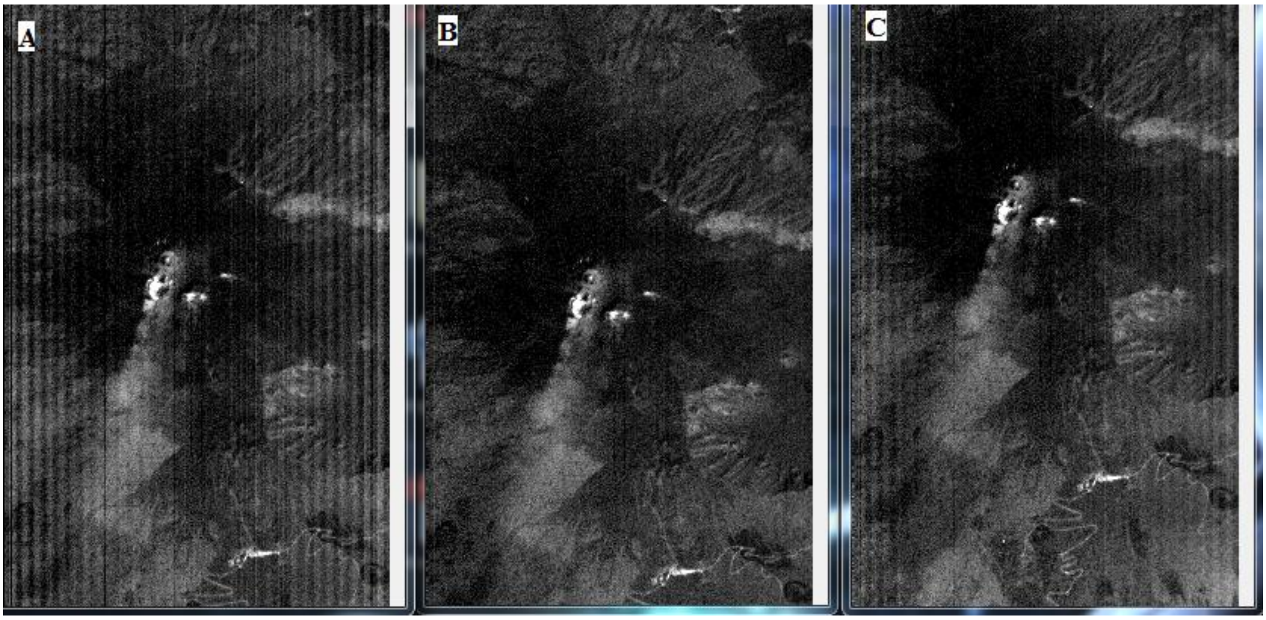


***Figure 5.2.1.1.2: Destriping results depending on the destriping techniques. (A) Uncorrected L1R data; (B) ENVI- THOR-De-Striping; (C) ENVI- SPEAR-Vertical Stripe Removal.***

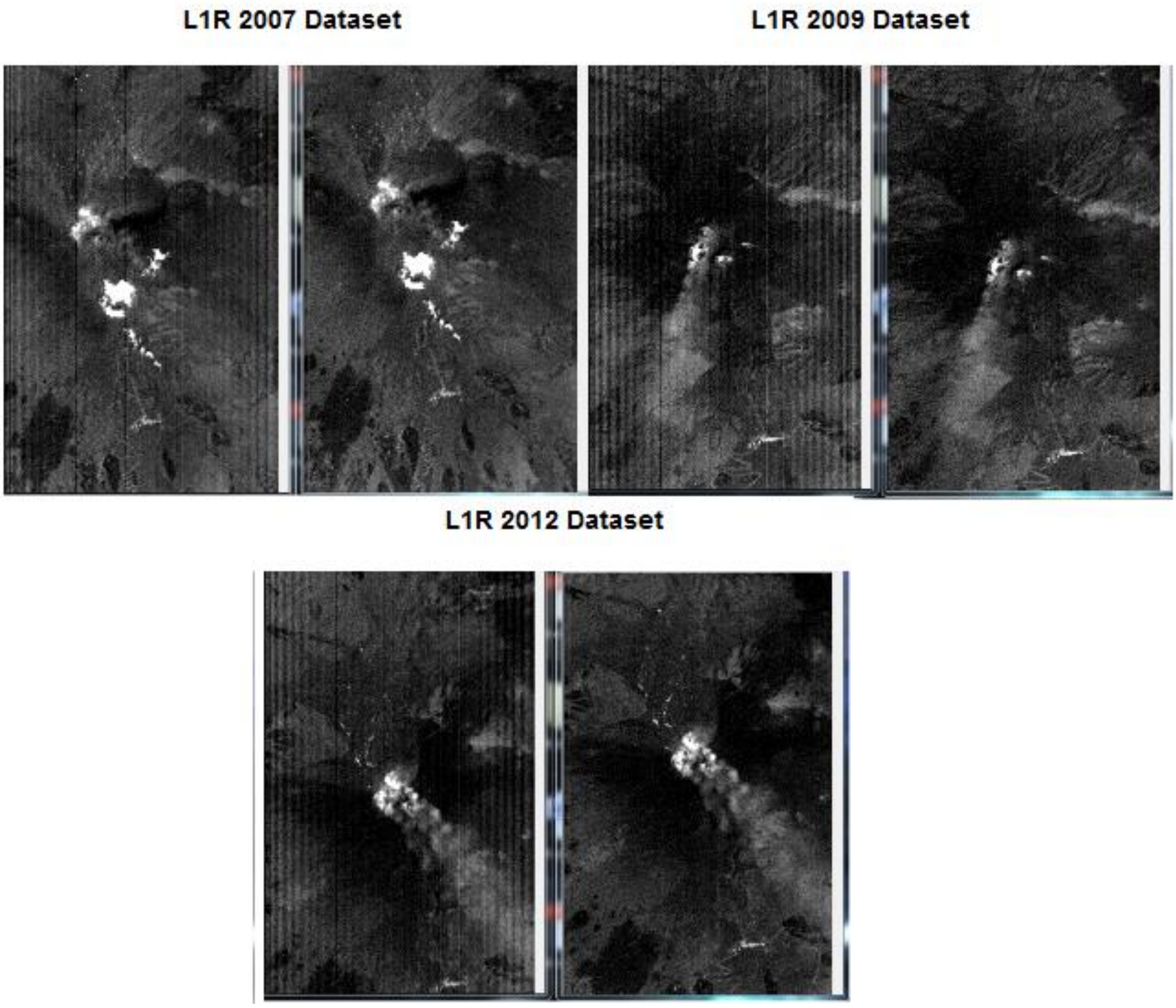


***Figure 5.2.1.1.3: Difference between the original datasets (left) and ENVI-THOR De-Striping technique (right).***

## 5.2.1.1.(B) Atmospheric Correction

The joint retrieval of atmospheric gas concentrations and ground reflectance is a major issue for numerous earth sciences studies exploiting hyperspectral data (e.g. geological, aquatic, ecological and atmospheric research).

Several techniques (FLAASH, ATCOR, ACORN, 5 & 6 S, HATCH, Sen2Cor etc) have been proposed in order to separate the contribution of the atmosphere from the one of the ground and most of them are based on MODTRAN-4 radiative transfer model, which was designed from the Spectral Sciences Inc. in collaboration with the US AIR FORCE, (source: http://www.spectral.com & http://modtran5.com). For this study, the Fast Line-of-sight Atmospheric Analysis of Spectral

Hypercubes (FLAASH) is applied and its equation (14) is described below. Also, Figure 5.2.1.1.4 shows the schematic flow of the FLAASH code.

$$L_e = \left(\frac{(A+B)\rho_e}{1-\rho_e S}\right) + L_a, \qquad (14)$$

Where:

- $\rho_e$ = The average surface reflectance for the pixel and a surrounding region
- $S$ = The spherical albedo of the atmosphere
- $La$ = The radiance back scattered by the atmosphere
- $Le$ = The averaged radiance image
- $A, B$ = The coefficients that depend on atmospheric and geometric conditions but not on the surface.

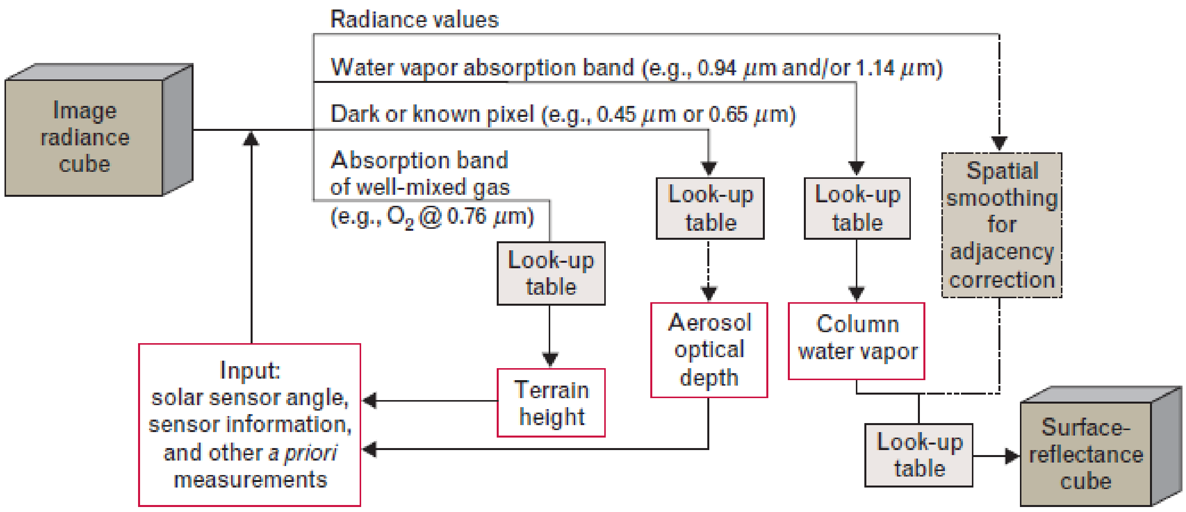


***Figure 5.2.1.1.4: Schenematic flow chart of the FLAASH code. The diagram defines the basic steps used to convert the sensor measured radiance to surface reflectance. Secondary products such as the column water vapor and the aerosol optical depth can also be obtained, (adapted from: Griffin & Burke, 2003)***

Each of these variables depends on the spectral channel; the wavelength index has been omitted for simplicity. However, this correction can result in significant reflectance errors at short wavelengths, especially under hazy conditions and when strong contrasts occur among the materials in the scene.

The values of A, B, S and $L_a$ are strongly dependent on the water vapor column amount, which is generally not well known and may vary across the scene. To account for unknown and variable column water vapor, the MODTRAN4 calculations are looped over a series of different column amounts, and then selected wavelength channels of the image are analyzed to retrieve an estimated amount for each pixel. Specifically, radiance averages are gathered for two sets of channels: an absorption set centered at a water band (typically 1130 nm) and a reference set of channels taken from just outside the band.

Spatial averaging is performed using a point-spread function that describes the relative contributions to the pixel radiance from points on the ground at different distances from the direct line of sight. For accurate results, cloud-containing pixels must be removed prior to averaging. The cloudy pixels are found using a combination of brightness, band ratio, and water vapor tests, as described by Matthew et al. (2000).

The FLAASH model includes a method for retrieving an estimated aerosol/haze amount from selected dark land pixels in the scene. The method is based on observations by Kaufman et al. (1997) of a nearly fixed ratio between the reflectance for such pixels at 660 nm and 2100 nm. FLAASH retrieves the aerosol amount by iterating Equation (1) over a series of visible ranges, for example, 17 km to 200 km. For each visible range, it retrieves the scene average 660 nm and 2100 nm reflectance for the dark pixels, and it interpolates the best estimate of the visible range by matching the ratio to the average ratio of ~0.45 that was observed by Kaufman et al. (1997). Using this visible range estimate, FLAASH performs a second and final MODTRAN4 calculation loop over water.

- **Input data Requirements**

Both L1R and L1T type storing data must converted from Band Sequential (BSQ) to Band Interleaved by Line (BIL). FLAASH requires input data to be floating-point values in units of $\mu W/cm^2$ * nm* steradian (sr). If the input radiance image is not already in floating-point format, the scale factors for the radiance conversion must satisfy the following relationship.

$$\left(\frac{\text{Integer radiance image}}{\text{Scale Factor}}\right) = \text{Floating point radiance image } [\mu W/(cm^2 * nm * sr]$$

For this purpose, we used the Hyperion Tool 2.0 to create an ASCII file, including the scale factors for each spectral band for L1R and L1T datasets, which are 400 for the VNIR and 800 for SWIR.

### 5.2.1.1.(B1) Atmospheric Correction on Hyperion datasets.

FLAASH atmospheric correction is applied, in order to eliminate the atmospheric effects and to obtain surface reflectance, in both L1R and L1T datasets. The same parameters are used for the two level processing data, according to the FLAASH tutorial, but a different atmospheric model was chosen for the 2007 dataset. The $CO_2$ values are determined, according to global $CO_2$ measurements, derived from Global Monitoring Division of NOAA/Earth System Research Laboratory, (https://www.esrl.noaa.gov/gmd/ccgg/trends/global.html). After the atmospheric correction, the reflectance values are also divided by 100, in order to represent the surface reflectance in each pixel in percentage values.

The evaluation of the atmospheric tests is performed using two conditions: (i) non-negative values in the whole spectrum range of each pixel, and (ii) the validation of the water vapor estimation according to the field measurements, which were retrieved from NASA's site; Aeronet (http://aeronet.gsfc.nasa.gov). For this method various combinations of parameters have been tested. Table 5.2.1.1.5 shows the parameters that gave the best results and tables 5.2.1.1.6 the validation with the field measurements for Level 1R dataset and Level 1T, correspondingly.

***Table 5.2.1.1.5: The best parameters combinations for Hyperion L1R and L1T datasets.***

| | **2007** | **2009** | **2012** |
|---|---|---|---|
| **Scene Center Location**<br>• **Latitude**<br>• **Longitude** | **37 42 02.61**<br>**14 59 25.86** | **37 35 22.67**<br>**14 57 19.85** | **37 48 52.59**<br>**15 01 08.82** |
| **Sensor Type** | **Hyperion** | | |
| **Sensor Altitude (km)** | **705** | | |
| **Average Ground Elevation (km)** | **1.5** | | |
| **Pixel size (m)** | **29,970** | | |
| **Flight Date** | **09/07/2007** | **08/10/2009** | **14/07/2012** |
| **Fight Time GMT** | **09:10:21** | **09:19:58** | **09:14:24** |

| | | | |
|---|---|---|---|
| **(H:M:S)** | | | |
| **Atmospheric Model** | **T** | **MLS** | **MLS** |
| **Water Retrieval** | **yes** | | |
| **Water Absorption Feature (nm)** | **1135** | | |
| **Aerosol Model** | **Rural** | | |
| **Aerosol Retrieval** | **2-Band Over Water** | | |
| **Initial Visibility (km)** | **40** | | |
| **Spectral Polishing** | **yes** | | |
| **Width (number of bands)** | **9** | | |
| **Wavelength Recalibration** | **no** | | |
| **Aerosol Scale Height (km)** | **1.50** | | |
| **$CO^2$ Mixing Ratio (ppm)** | **382.67** | **403** | **413** |
| **Use Square Slit Function** | **no** | | |
| **Use Adjacency Correction** | **yes** | | |
| **Reuse MODTRAN Calculations** | **no** | | |
| **MODTRAN Resolution:** | **5cm-1** | | |
| ***MODTRAN Multiscatter Model*** | ***Scaled DISORT*** | | |

| | |
|---|---|
| ***Number of DISORT streams*** | ***8*** |
| ***Zenith & Azimuth angle*** | ***180$^o$ & 0$^o$*** |
| ***Use Tile Processing:*** | ***no*** |

***Table 5.2.1.1.6: The atmospheric correction results and the corresponding field measurements for Water Vapor and Visibility, for L1R & L1T datasets.***

| **Level 1R Datasets** | | | | | | |
|---|---|---|---|---|---|---|
| | **Aeronet** | **2007** | **Aeronet** | **2009** | **Aeronet** | **2012** |
| **Water Vapor (cm)** | 1.42 | 1.37 | 1.581 | 1.70 | 1.52 | 1.49 |
| **Visibility (km)** | | 36.9 | | 300 | | 79 |
| **Level 1T Datasets** | | | | | | |
| | **Aeronet** | **2007** | **Aeronet** | **2009** | **Aeronet** | **2012** |
| **Water Vapor (cm)** | 1.42 | 1.38 | 1.581 | 1.70 | 1.52 | 1.52 |
| **Visibility (km)** | | 300 | | 300 | | 300 |

From the aforementioned results, it is shown that the most accurate results are those for the 2012 dataset. Moreover, the water vapor measurements, from the atmospheric corrected L1T data were closer to the field measurements than those from L1R data. Additionally, Figure 5.2.1.1.5 shows an example of surface reflectance profiles, from two different lava flows (A & B regions), close to the summit craters, from the L1R and L1T 2012 datasets. The lava flow land cover type is used because it is characterized by darker pixels, where the atmospheric model fails. The failure of the atmospheric correction in the L1R dataset is noticed by the presence of negative values in the blue visible region of the EMS.

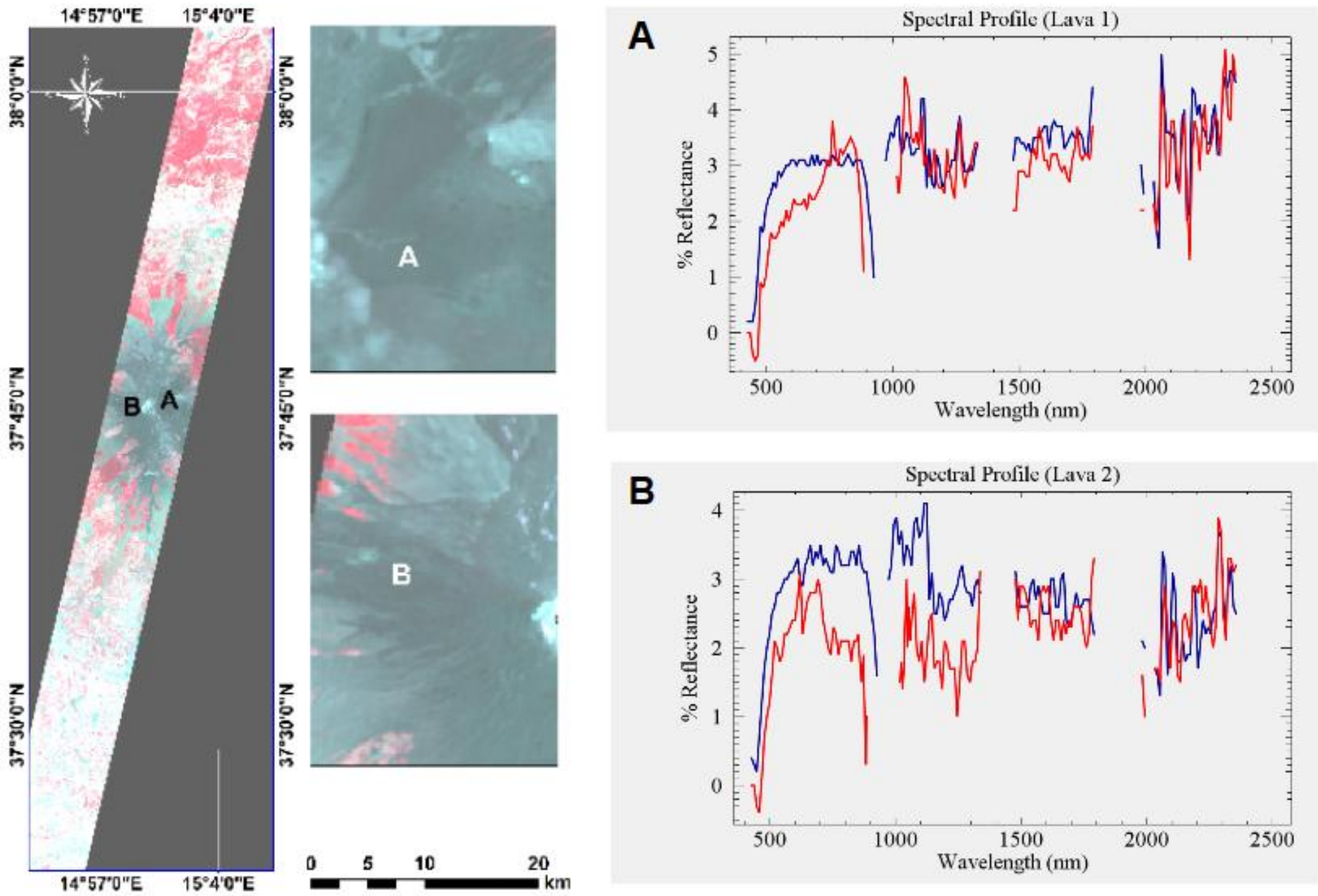


***Figure 5.2.1.1.5: The spectral profile from A and B regions, from L1R (red) and L1T (blue); 2012 datasets.***

## 5.2.1.1.(B2) Water Vapor and Cloud Mask products

After FLAASH atmospheric correction, three products are always created; (i) the surface reflectance image, (ii) the water vapor image and (iii) the cloud mask image. The first image refers to the retrieved column water vapor in units atm*cm, in the particular area and time when the dataset was acquired. Cloud mask image is a classified product, using by FLAASH in order to estimate ρe variable. The neighbor pixels are affected by the quantity of this variable. Table 5.2.1.1.7 describes the clouds categorization in the aforementioned image.

*Table 5.2.1.1.7: Cloud Mask classes*

| |
|---|
| No clouds |
| High Altitude clouds (Cirrus or Tall Cumulus) |
| Opaque clouds |
| Opaque and High Altitude clouds |
| Water retrieval error |
| Water retrieval error & High clouds |
| Water retrieval error & Opaque clouds |
| Water retrieval error & Both cloud types |

Figures 5.2.1.1.6 and 5.2.1.1.7 visualize for each dataset the water vapor and cloud mask image.

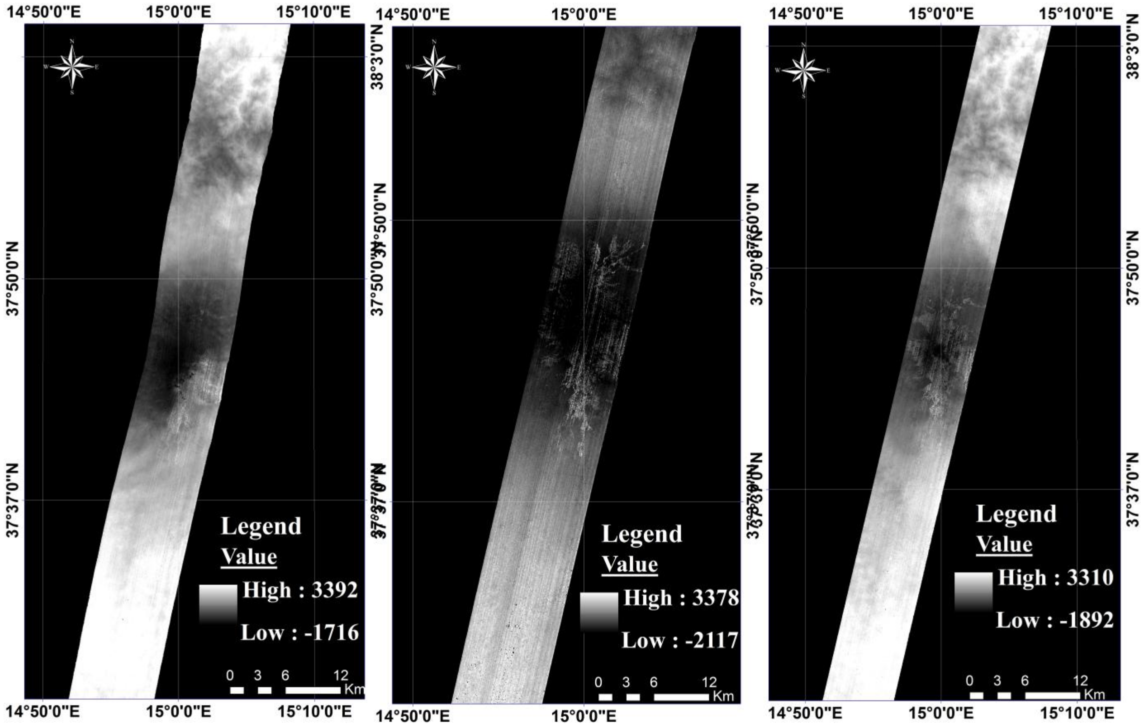


***Figure 5.2.1.1.6: Water vapor images for the 2007(left), 2009(middle) and 2012(right).***

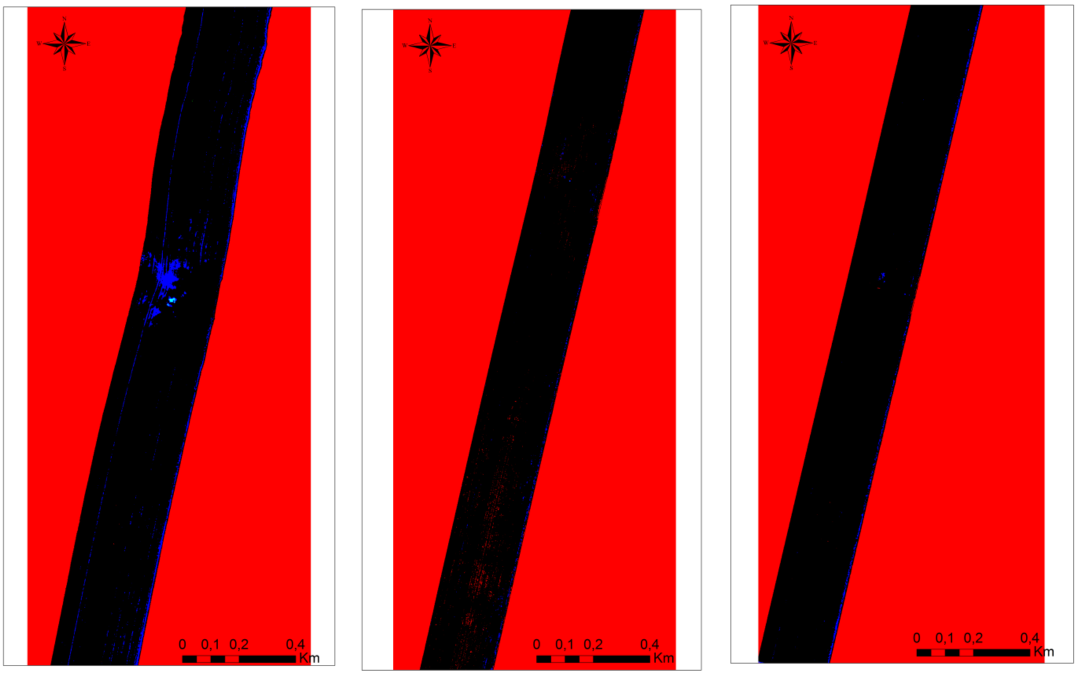


***Figure 5.2.1.1.7: Cloud mask images for the 2007(left), 2009(middle) and 2012(right).***

## 5.2.1.1. (C) Image to Image Co-Registration

After atmospheric correction, a geometric correction is applied to the Hyperion images, in order to eliminate the geometric distortions. For this study, the image-to-image co-registration is applied to 2009 and 2012 datasets, defining the 2007 dataset as the reference image. It should be noted that the orthorectification process requires parameters for the satellite camera and its position, which were not available. But, as aforementioned the L1T data are already orthorectified so, the use of the above method is adequate and can provide reliable results. For each dataset, 70 ground control points (GCP's) have been detected and the total RMS error, using a first polynomial equation, for the 2009 dataset is 0.397498 and for the 2012 dataset 0.317740.

## 5.2.1.1.(D) Noise and Dimension Reduction

The use of hyperspectral images brings new capabilities along with some difficulties in their processing and analysis. The large amount of data involved with hyperspectral imagery will dramatically increase processing complexity and time. The above phenomenon named redundancy produces spectral noise. Furthermore, the more spectral bands detecting an area, the most spectral information will be correlated. The reduction of the spectral noise and the correlated spectral information can be succeeded by the implementation of the Principal Components Analysis (PCA), *(Burgers et al, 2009).*

PCA is a statistical procedure that uses an orthogonal transformation to convert a set of observations of possibly correlated variables into a set of values of linearly uncorrelated variables called principal components, *(Joliffe 2002; Raiko et al, 2008).* The PCA employs the statistic properties of hyperspectral bands to examine bands dependency or correlation. All these transformations are based on the same mathematical principle known as eigenvalues decomposition of the covariance matrix of the hyperspectral image bands to be analyzed. The more correlated are the data the most repeated information will be reduced. Below is a brief formulation of the principle, *(Rodarmel & Shan, 2002).*

An image pixel vector is calculated as (Equation 15):

$$x_i = [x_1, \dots, x_N]_i^T \qquad (15)$$

While, all pixel values $x1...z_N$ correspond to pixel location of the hyperspectral image data. The dimension of the image vector is equal to the number of hyperspectral bands N, (Figure 5.2.1.1). For a hyperspectral image with *m* rows and *n* columns there will be M = m*n such vectors, namely i = 1… M. The mean vector of all image vectors is denotes and calculated as (Equation 16):

$$m = \frac{1}{M}\sum_{i=1}^{M}[x_1, \dots., x_N]_i^T, \qquad (16)$$

The covariance matrix of *x* is defined as (Equation 17):

$$Cov(x) = E\{(x - Ex)(x - Ex)^T\}, \quad (18),$$

Where:

- E = Expectation operator;
- T superscript = transpose operation;
- Cov = notation for covariance matrix

The covariance matrix is approximated by the following calculation (Equation 19):

$$C_x = \frac{1}{M}\sum_{i=1}^{M}(x_i - m)(x_i - m)^T, \quad (19)$$

The PCA, which is based on the eigenvalue decomposition of the covariance matrix, which takes the form of (Equation 20):

$$C_x = ADA^T \quad (20)$$

$$\text{Where,} D = diag\ (\lambda_1, \dots, \lambda_N), \quad (21)$$

Is the diagonal matrix composed of the eigenvalues $(\lambda_1, \dots, \lambda_N)$ of the covariance matrix Cx and A is the orthonormal matrix composed of the corresponding $N$ dimension eigenvectors $a_k$ $(k = 1,\dots, N$ of the $Cx$ as follows (Equation 22):

$$A = (a_1, \dots, a_N), \quad (22)$$

The total amount of the PCs is also expressed as the linear transformation of the initial data by the Equation 8, (Figure 5.2.1.1.6). *(Pervez, 2015)*:

$$y_i = A^T x_I, (I = 1,2, \dots, M), \quad (23)$$

The calculation of the components serves the compression of the useful information into fewer images. Usually, the PC1 expresses the 99% of the useful information and the latest contents only noise. All PCs must express the 100% of the uncorrelated information of the initial dataset, *(Rodarmel & Shan, 2002).*

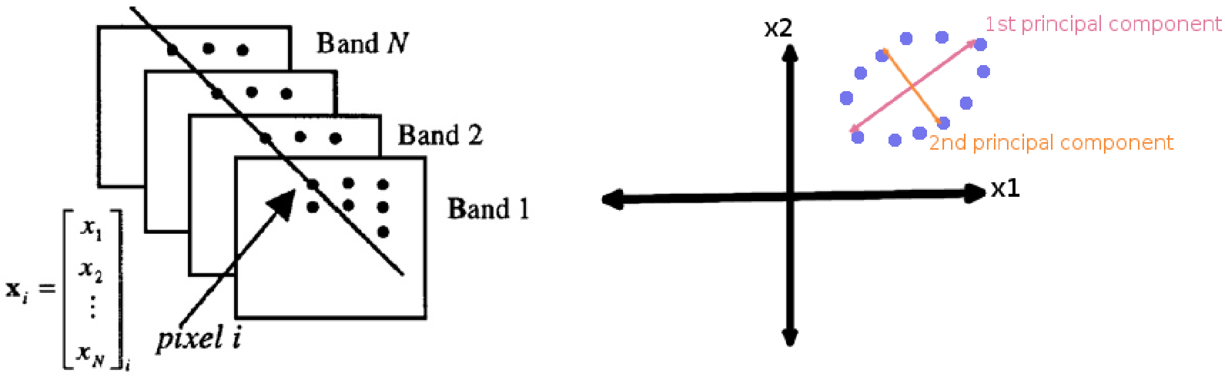


***Figure 5.2.1.1.6: Pixel vector in principal component analysis (left) and the Geometry of principal components [adapted from Gonzales & Woods (1993)].***

The PCA as and the inverse PCA is applied in all Hyperion L1T datasets, with 20 components. The first 4 components (Figures 5.2.1.1.7), include most of the information and are used for the Inverse PCA rotation. The inverse procedure is performed in order to transform the components to the initial dimensions, minimizing the spectral noise. Table 5.2.1.1.7 presents the PCs statistics, which show that the first component contains most of the useful information. Figure

5.2.1.1.8 shows the spectral profiles of 3 specific LULC types (vegetation, lava flows, urban-semi urban areas), from the initial data and after PC inversion. All spectra seem to be less noisy after inversion especially the lava flow spectral profile.

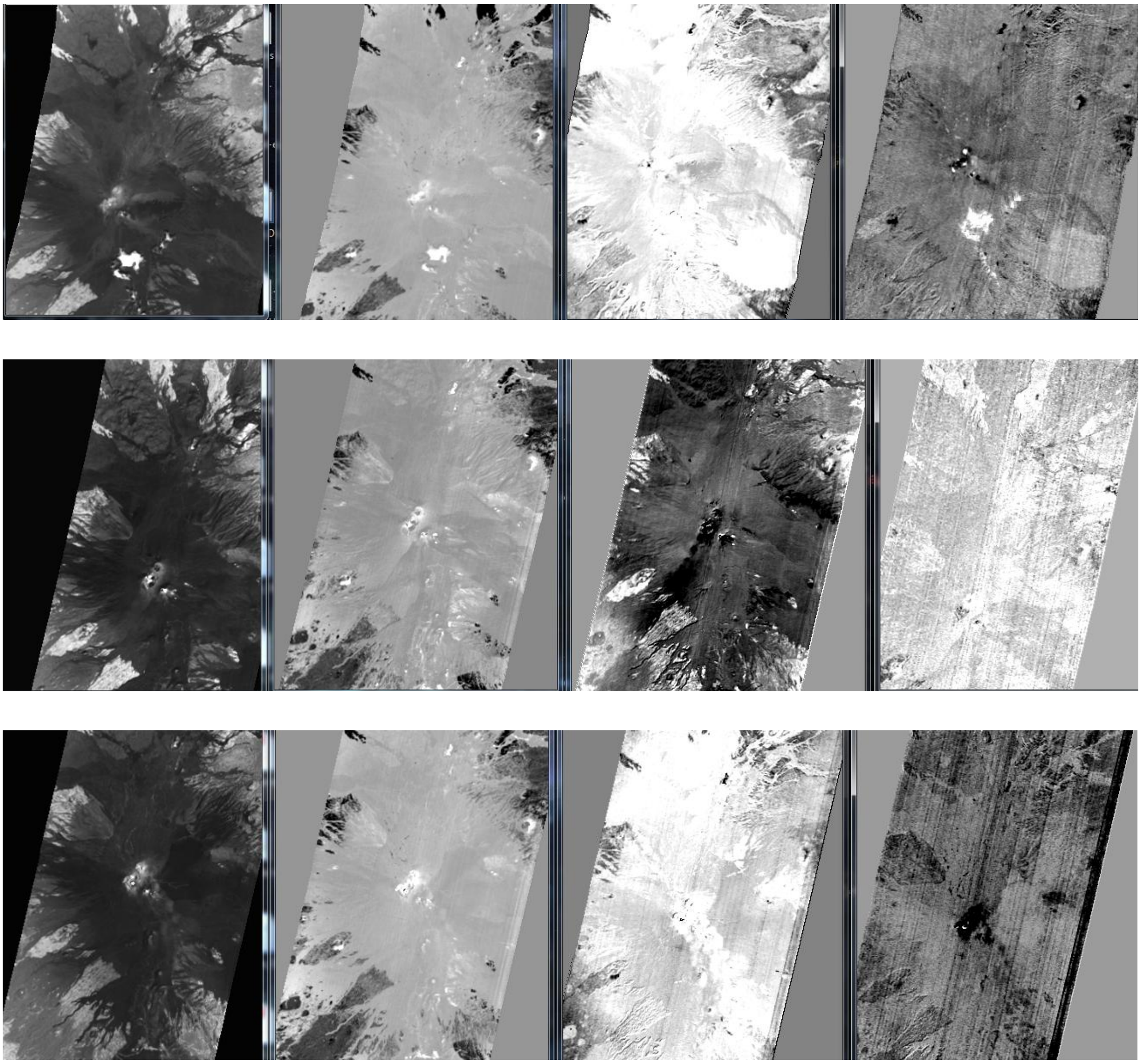

***Figure 5.2.1.1.7: PC1-PC4 components containing the most useful information from the (i) 2007, (ii) 2009 and (iii) 2012 datasets.***

***Table 5.2.1.1.7: The eigenvalues for each component***

| | 2007 | 2009 | 2012 |
|---|---|---|---|
| Components | Eigenvalues | Eigenvalues | Eigenvalues |

| | | | |
|---|---|---|---|
| 1 | 24119,56 | 8080,73 | 11696,01 |
| 2 | 1029,44 | 370,39 | 454,42 |
| 3 | 54,50 | 23,32 | 29,66 |
| 4 | 36,62 | 18,24 | 24,27 |
| 5 | 24,19 | 17,36 | 18,42 |
| 6 | 20,26 | 9,89 | 16,94 |
| 7 | 12,71 | 8,50 | 8,79 |
| 8 | 10,73 | 6,96 | 7,82 |
| 9 | 7,30 | 5,59 | 4,76 |
| 10 | 6,49 | 4,24 | 3,34 |
| 11 | 4,34 | 3,72 | 3,08 |
| 12 | 4,26 | 3,40 | 2,62 |
| 13 | 2,81 | 3,18 | 2,58 |
| 14 | 2,37 | 2,18 | 1,96 |
| 15 | 2,28 | 1,90 | 1,59 |
| 16 | 1,95 | 1,67 | 1,48 |
| 17 | 1,78 | 1,40 | 1,28 |
| 18 | 1,61 | 1,19 | 1,18 |
| 19 | 1,48 | 1,13 | 1,13 |
| 20 | 1,31 | 0,91 | 0,95 |

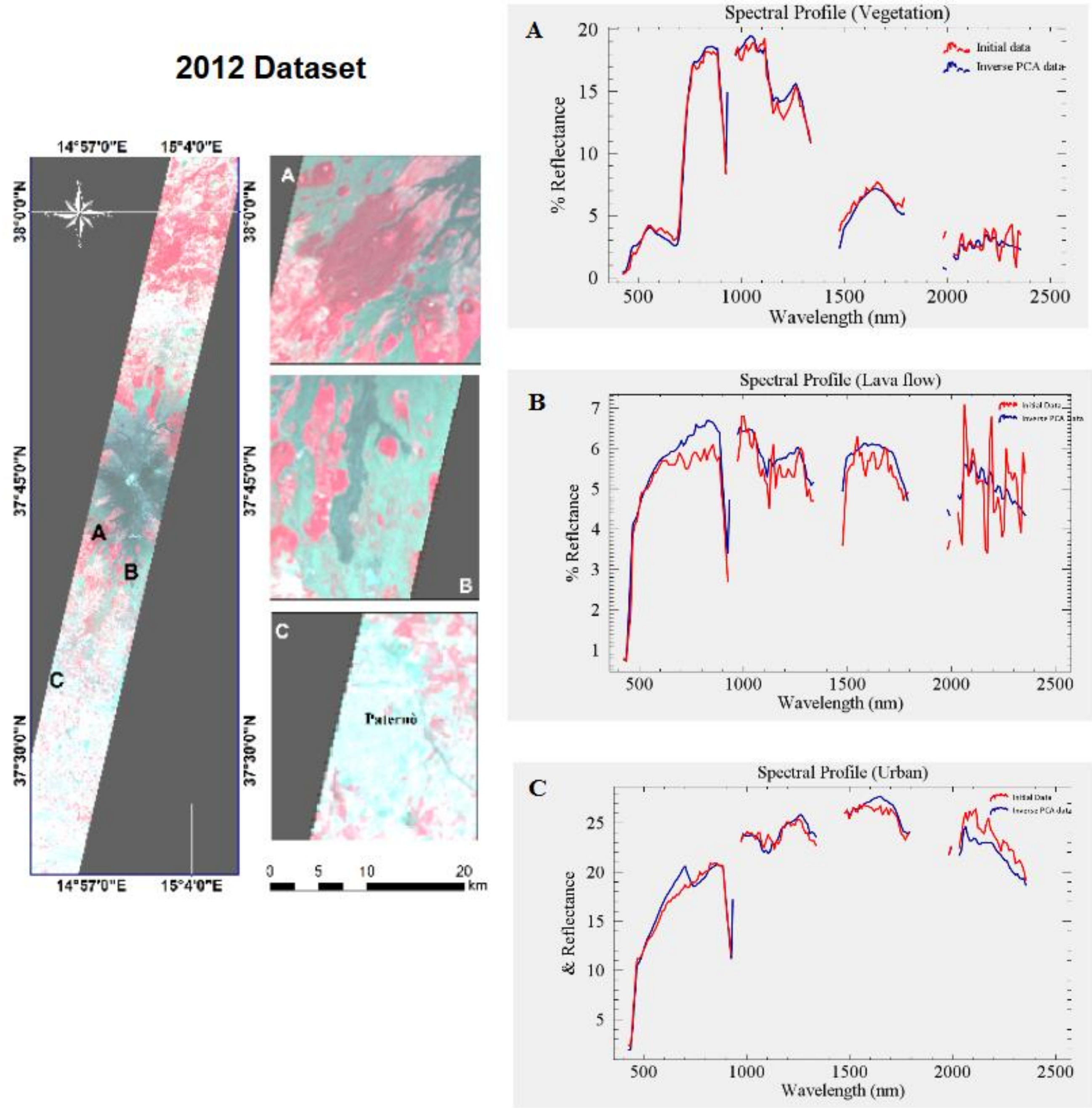


***Figure 5.2.1.1.8: Differences in spectral profiles between initial data (red) and after inverse PCA (blue).***

### 5.2.1.1.(E) Vegetation Mapping & Masking

The Normalized Difference Vegetation Index (NDVI) is used to map and mask the presence of chlorophyll vegetation areas. It can be implemented both as a broadband greenness index (uses spectrum ranges, usually applied in MSI and as a narrowband greenness index (using specific parts of the spectrum, according to the sensor's spectral response, usually applied in HSI).

NDVI is the most used vegetation index and it was created by Rouse et al (1973), although the idea was proposed by Krigler et al (1969). The vegetation's presence is calculated by the following equation 24.

$$\mathrm{NDVI} = \frac{\rho\mathrm{NIR}-\rho\mathrm{R}}{\rho\mathrm{NIR}+\rho\mathrm{R}} \qquad (24)$$

The practicality of the index is based on the theory, where the vegetation absorbs the solar radiation in visible red (R) and reflects in near-infrared (NIR). The index normalization gives a range of values from -1 (negative vegetation presence) to +1 (positive vegetation presence), where values close to 0 indicate no vegetation presence. The typical NDVI values of vegetation fluctuate from 0.2 to 1, while the NDVI for healthy vegetation is usually above 0.6. For the datasets of this study, the NDVI is transformed to the following equation (25)

$$\mathrm{NDVI} = \frac{\mathrm{R}_{874}-\mathrm{R}_{681}}{\mathrm{R}_{874}+\mathrm{R}_{681}} \qquad (25)$$

The produced results are depicted in Figure 5.2.1.1.9. Using the NDVI values threshold (Table 5.2.1.1.7) in each dataset, we can segregate the vegetated areas-unvegetated areas and mask the vegetation presence from the study area, (Figure 5.2.1.1.10).

***Table 5.2.1.1.7: The NDVI range of values used to separate vegetated to non-vegetated areas in 2007, 2009 and 2012 Hyperion L1T datasets***

| | Vegetated areas | Non-vegetated areas |
|---|---|---|
| 2007 | 0.41-0.90 | -0.52-0.40 |
| 2009 | 0.42-0.90 | -0.1-0.41 |
| 2012 | 0.42-0.90 | -0.1-0.41 |

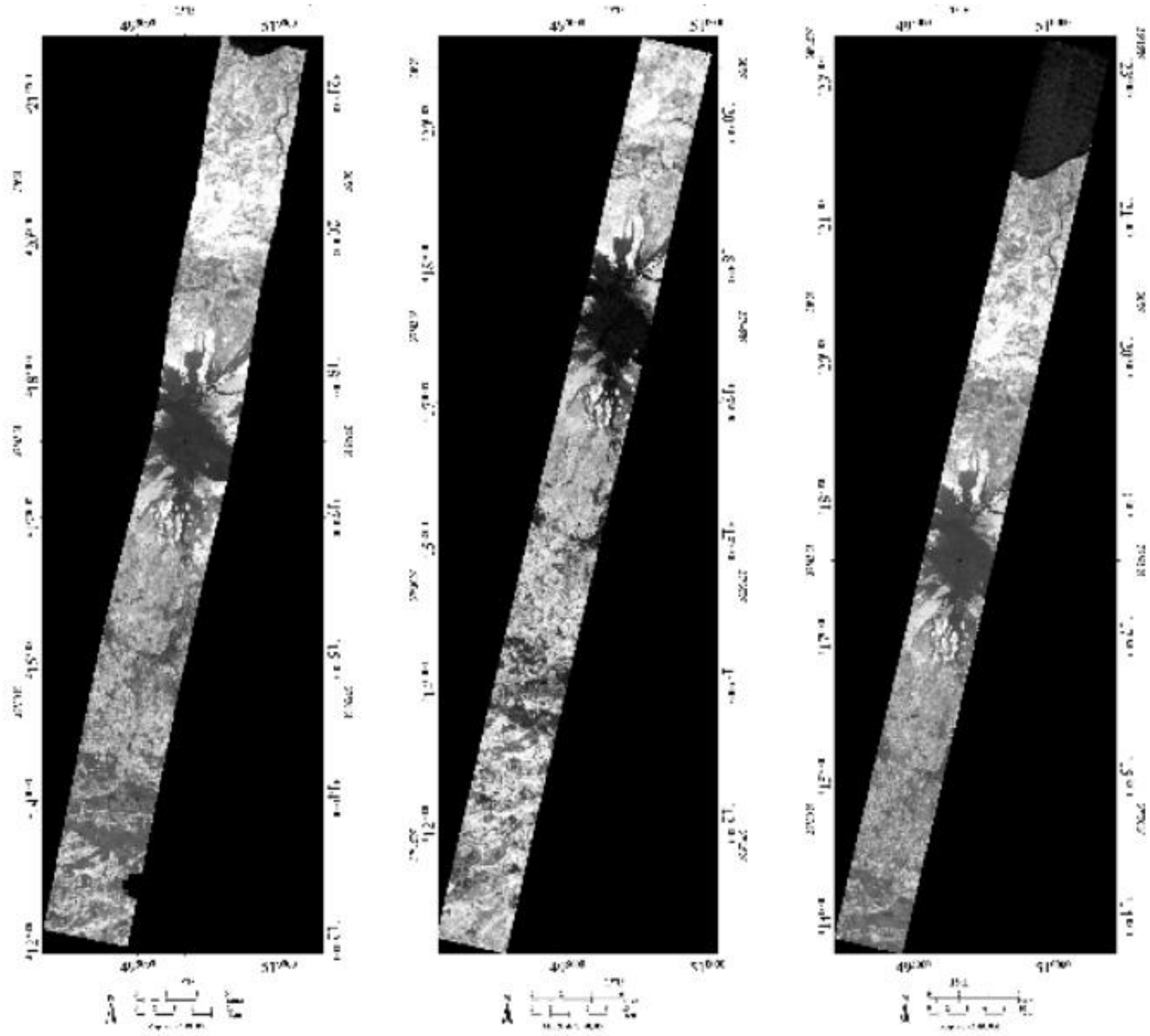

***Figure 5.2.1.1.9: The NDVI calculation for 2007 (left), 2009 (middle) and 2012 (right) datasets after the inverse PCA rotation.***

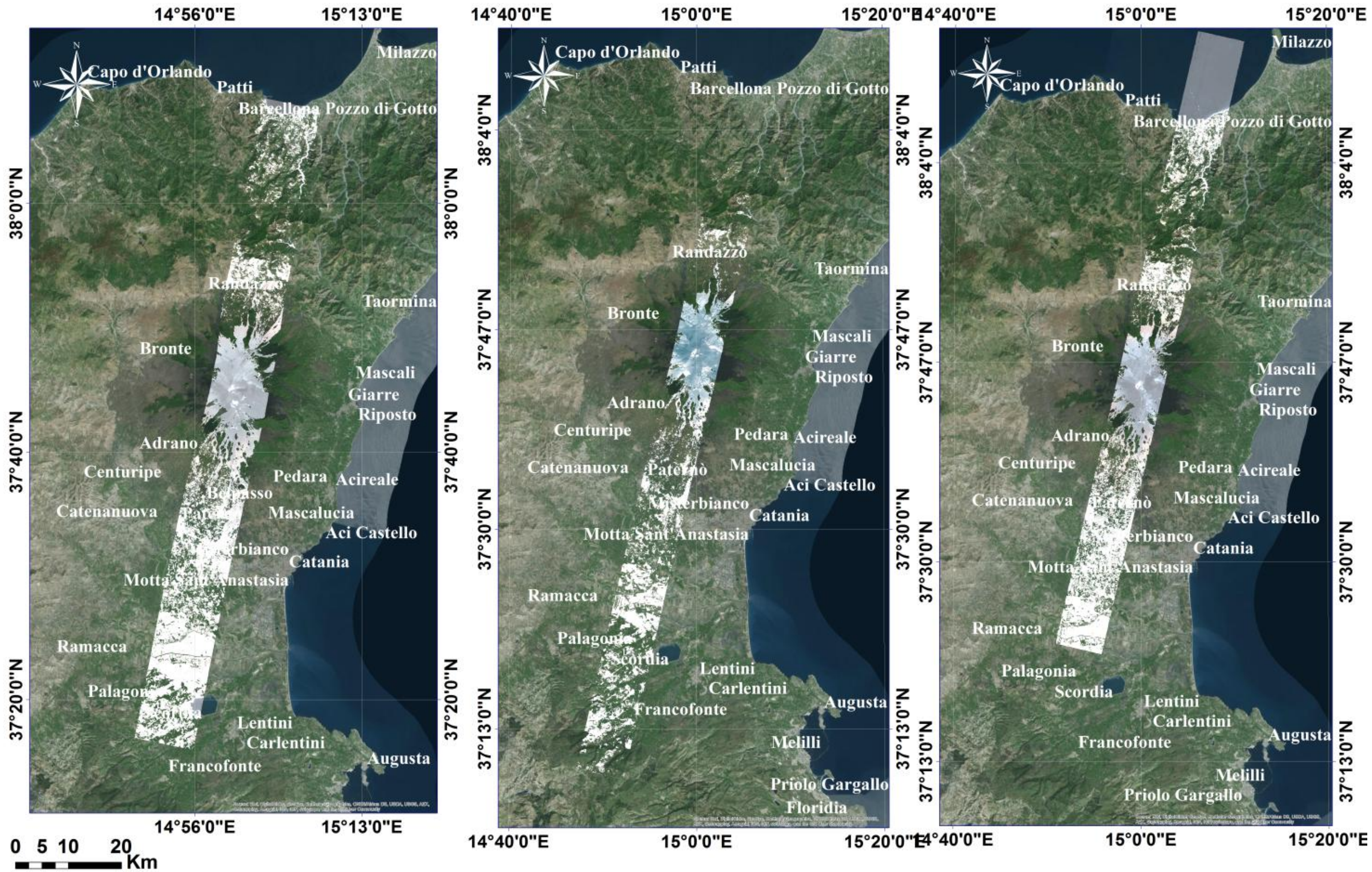


*Figure 5.2.1.1.10: The 2007 (left), 2009 (middle), 2012 (right) datasets, without the vegetation presence.*

#### 5.2.1.1. (F) High & Low Active Areas

As it was presented in Chapter 3 (Study Area), Mt Etna is characterized by tense volcanic eruptions with lava flow deposits, with change the LULC rapidly, continuously and rigorously. According to the volcanic eruptions between 2007 and 2012 (Figure 4.5), we observe that the most active region is Valle del Bove (VdB). In addition, our goal is to investigate the lava flow temporal changes that are noted in the low activity region of the Etna volcano. Stretch & Viles (2002); Spinetti et al (2009); Li et al (2015) etc. proved that lava flows are affected by alteration, weathering oxidation and herbaceous vegetation growing, especially lichens. Also, it has demonstrated that lichens growing rate is higher, especially in outdated lavas than in other similar land cover types.

For this purpose, VdB is excluded from the rest of the study area, from all the datasets, by generating a region of interest (ROI), producing a mask and isolating the area. It should be pointed out that this ROI is used for all datasets, because they are co-registered. Figure 5.2.1.1.11 depicts the produced result.

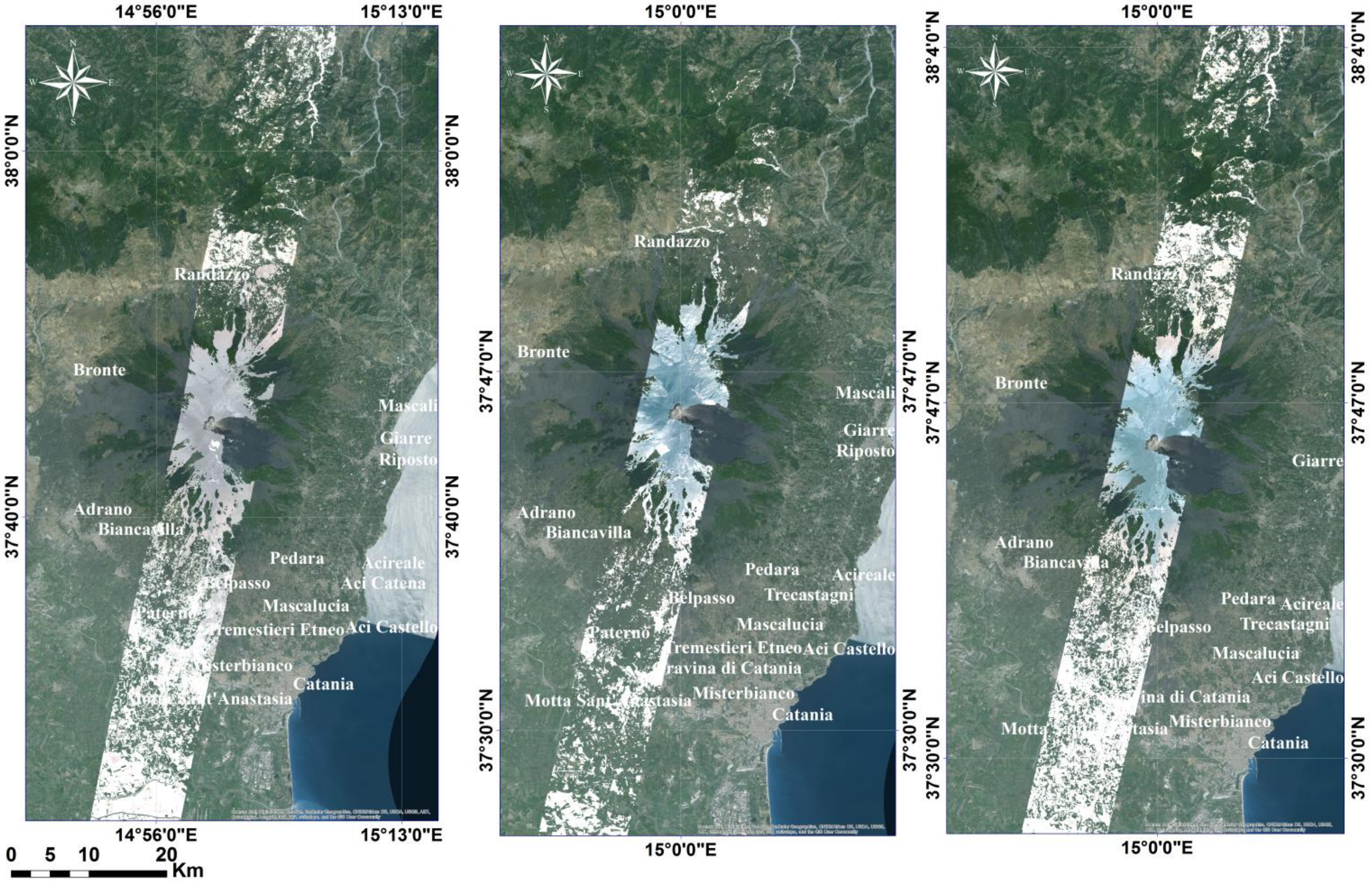


***Figure 5.2.1.1.11: The 2007 (left), 2009 (middle) and 2012 (right) datasets, without the high active section (VdB).***

### 5.2.1.2. SAR Pre-Processing Steps

Two S1-A GRD, IW datasets were used, dated on 16.07.2016 and 22.07.2016, on descending and ascending satellite geometry, respectively. Also, they transmit/receive single vertical (VV) and dual (VH) polarizations. S-1A swath width is 250km (5*20m pixel size), which covers almost the whole geographic area of Sicily. Figure 5.2.1.2.1 show the flow chart data procedure, which were performed using SNAP toolbox, designed by the European Space Agency (ESA).

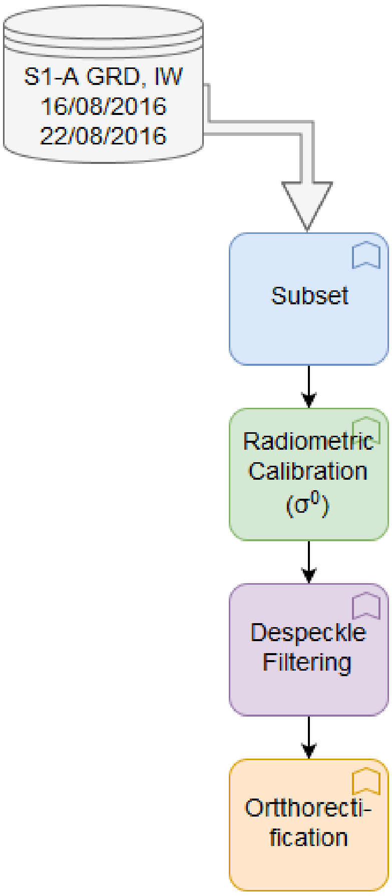


*Figure 5.2.1.2.1.: The descending & ascending Pre-processing flow chart.*

### (A) Image Subsetting

As it was mentioned above S-1A products covers an enormous spatial area and depending on this fact; the processing procedure consumes a lot of time and computational capabilities. Figure 5.2.1.2.2 the subsetted area performed in the Ascending imagery in radar geometry, compared with the initial dataset. It should be pointed out that firstly, both ascending and descending datasets were subsetted separately. After the geometric correction; imagery subset is applied again using the same coordinates, in order to cover pixel-by-pixel the same area.

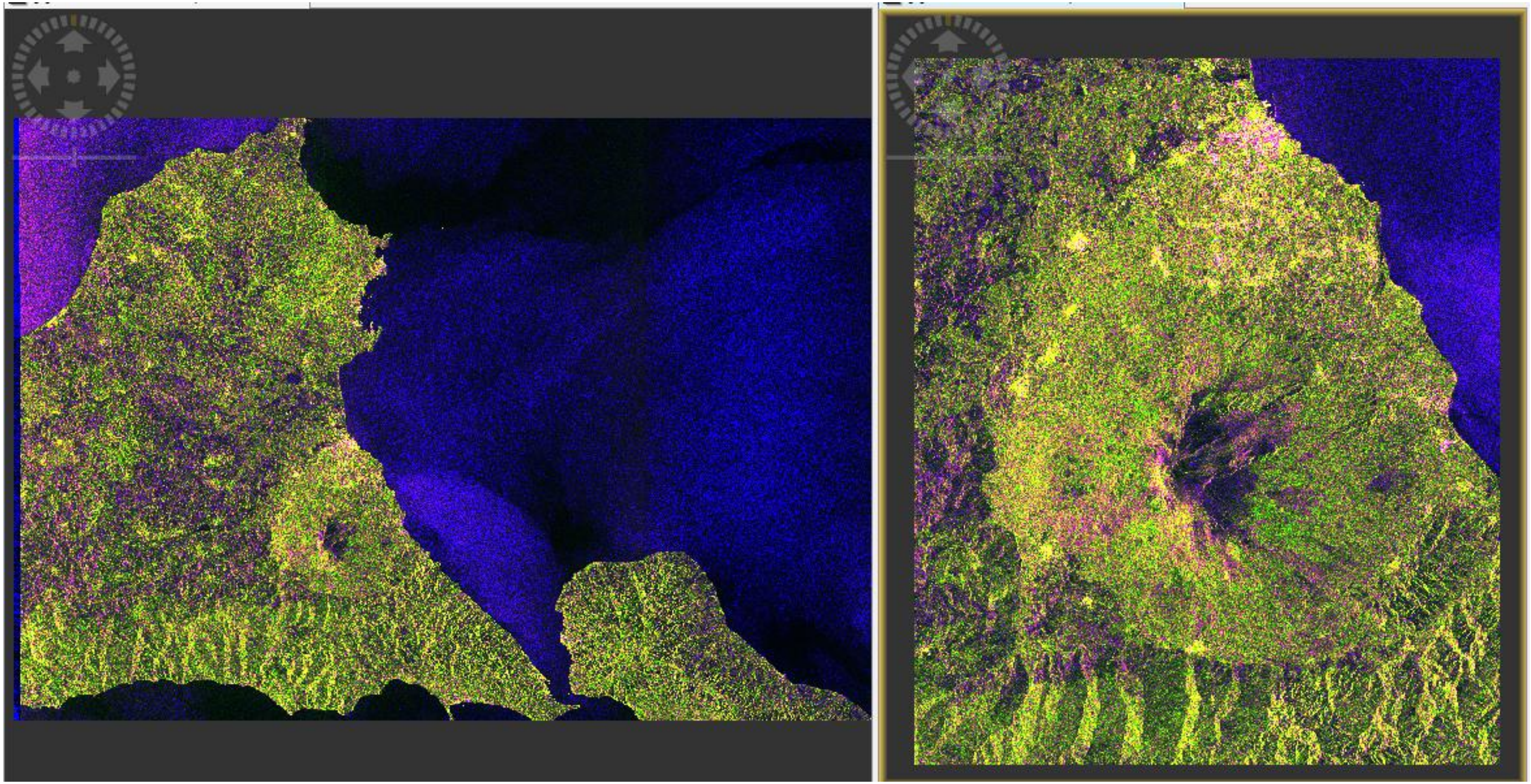

***Figure 5.2.1.2.2: Ascending imagery subset.***

### 5.2.1.2. (B) Radiometric Calibration

For the conversion of the pixel values to radiometrically calibrated backscatter coefficient, intensity values are required and provided from each S1 product. A calibration vector is included as an annotation in the product allowing simple conversion into sigma, beta or gamma nought values.

The objective of SAR calibration is to provide imagery in which the pixel values can be directly related to the radar backscatter of the scene. To do this, the application output scaling applied by the processor must be undone and the desired scaling must be applied. For GRD products, a constant offset is also applied. The radiometric calibration is applied by the Equation (4)

$$\mathrm{value(i)} = \frac{|\mathrm{DN_i^2}|}{\mathrm{A_i^2}}, \qquad (4)$$

Where:

- Value(i) = one of $\beta_i^0$, $\sigma_i^0$ or $\gamma_i^0$ or original $DN_i$
- $A_i$ = one of beta nought (i), sigma nought (i), gamma nought (i) or DN(i)

The ascending, descending datasets intensity values are radiometrically corrected in sigma nought values, for VV and VH polarizations, *(SNAP help Desktop)*.

### 5.2.1.3. (C) Despeckle Filtering

Initial processing and speckle reduction was performed in ascending ($\sigma_{VV}$, $\sigma_{VH}$) and descending ($\sigma_{VV}$, $\sigma_{VH}$) datasets using Refine Lee and Gamma Map despeckle algorithms. The best speckle reduction effect was achieved by Gamma MAP. However, we also test the effect of the 3*3 and 5*5 kernels, in order to avoid the excessive speckle removal. Figures 5.2.1.2.3 and 5.2.1.2.4 display the despeckle filtering, applying in ascending imagery for VH and VV polarizations, correspondingly.

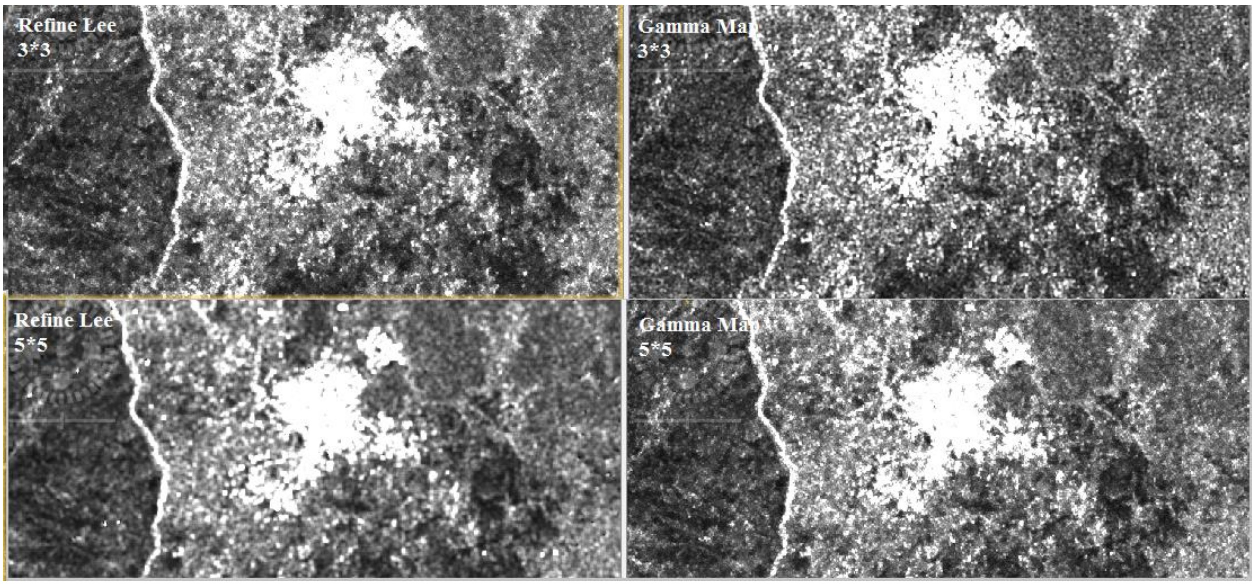


*Figure 5.2.1.2.3: Refine Lee (3*3 & 5*5) and Gamma Map (3*3 & 5*5) despeckle filtering in VH polarization.*

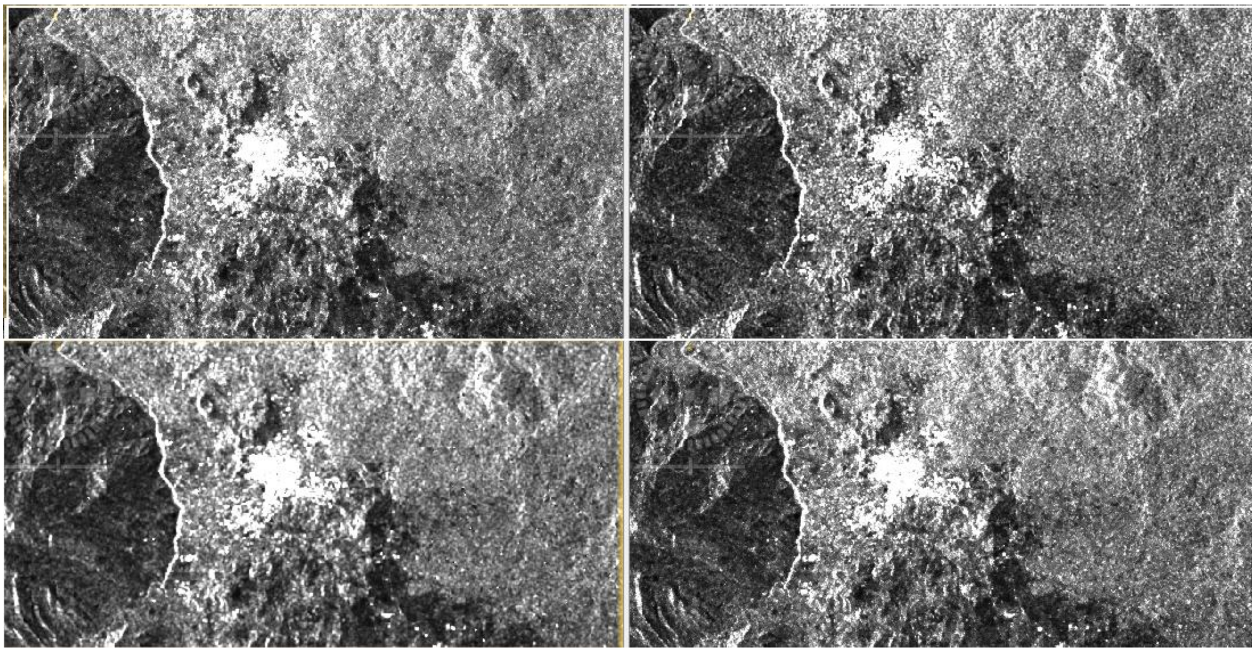

*Figure 5.2.1.2.4: Refine Lee (3*3 & 5*5) and Gamma Map (3*3 & 5*5) despeckle filtering in VV polarization.*

## 5.2.1.4.(D) Orthorectification

In order to compensate the topographical and sensor's distortions and to projected S-1A datasets to a Cartesian coordinate system (WGS '84, UTM 33N) from radar geometry; Range Doppler Terrain Correction operator was applied. To perform this procedure the DEM that was analyzed in chapter 5.1 is also used, in order to simulate the topography of the study area. The geometry of topographic distortions in SAR imagery is shown in Figure 5.5.1.2.5. Here we can see that point

B with elevation h above the ellipsoid is imaged at position B’ in SAR image, though its real is B”. The offset Δr between B’ and B” exhibits the effect of topographic distortions, *(SNAP help Desktop)*.

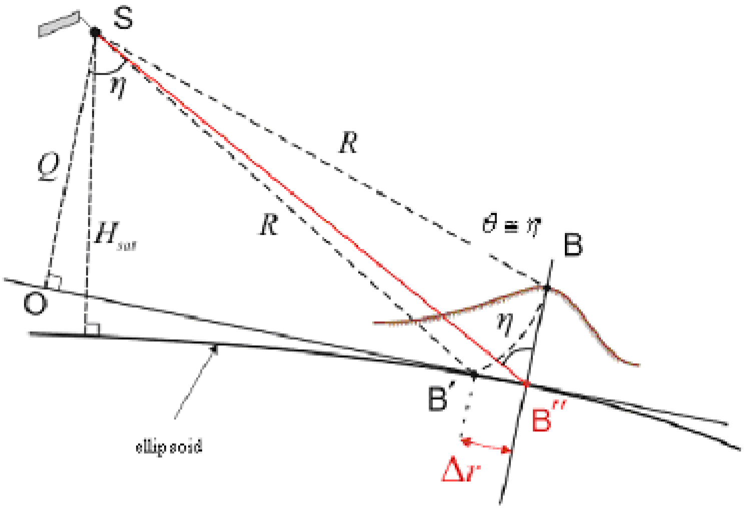


***Figure 5.5.1.2.5: The topographic distortions on SAR imagery, (adapted from SNAP help Desktop*).**

## 5.2.2 Main Processing

The main processing describes the steps were followed in order to investigate the temporal LULC changes on Etna volcano, using Hyperion L1T and S-1A GRD, IW datasets. With a view to quantify and qualify this change, statistical data analysis procedures were applied. In order to materialize the aforementioned operation, the following steps are implemented. (i) Training sets collection for the four volcanic categories according to the different volcanic products in the Geological Map, *(Branca et al, 2011)* and (ii) creation of the topographic variables (aspect and slope), which may affect the backscatter signal, (Figure 5.2.2.1).

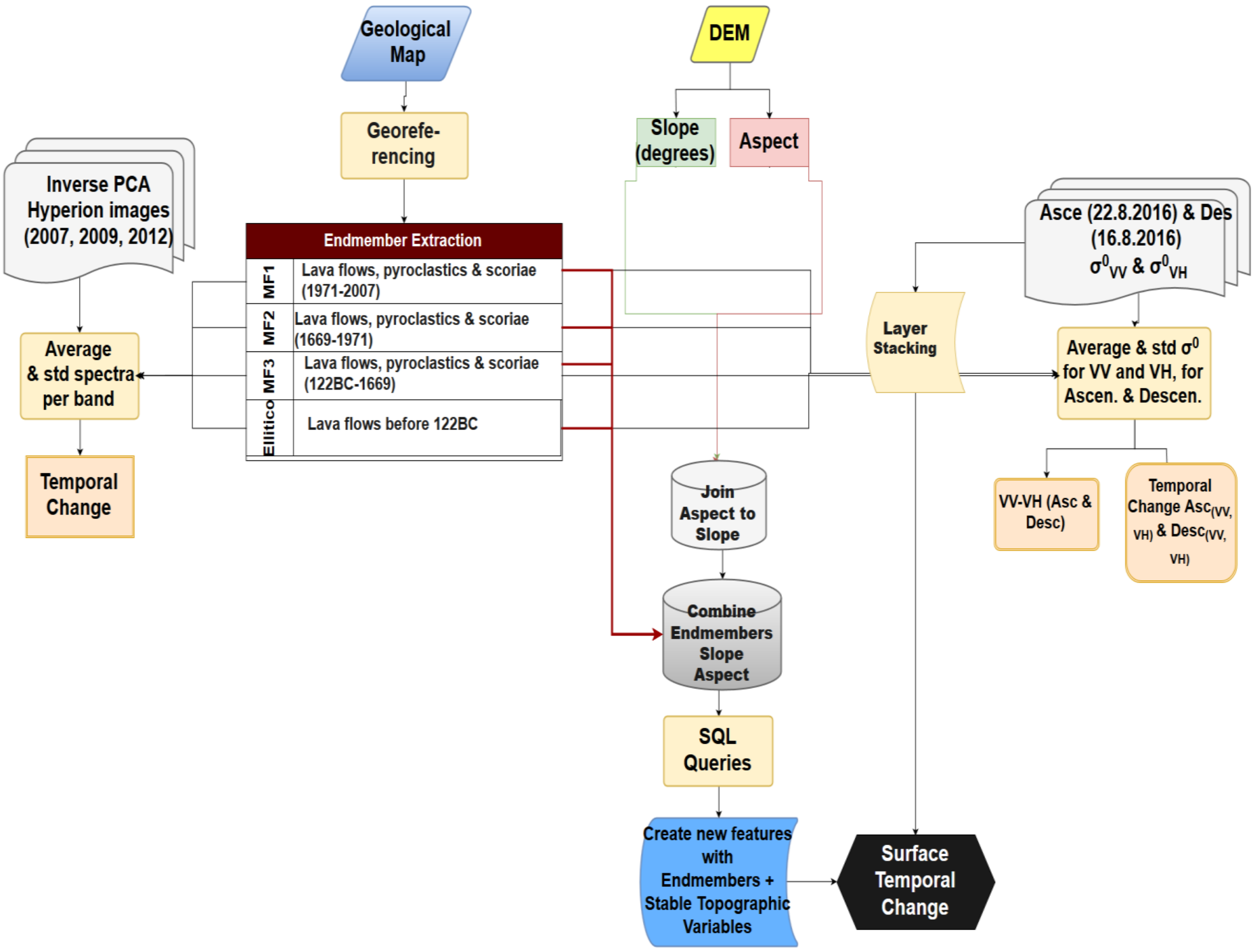


*Figure 5.2.2.1: Main processing flow chart.*

### 5.2.2.1 Geological Map Georeferencing

In Chapter 5.1.3 we presented the Geological Map in 1:50.000 scale, created by Branca et al (2011) and acquired from INGV, which segregates the volcanic products due to Il Piano

Synthem (Mongibello Volcano) and in Concazze Synthem (Ellitico volcano) and their subdivisions. Due to the initial Portable Document Format (PDF) of the geological map, the scanner coordinates were transformed into the WGS ’84, UTM 33N Cartesian coordinate system in order to be used as a reference for the endmembers extraction.

For the georeferencing, the road network of the area, in vector format, derived from Openstreet Map was utilized. 17 GSP’s were detected and the total RMS error, using a second polynomial equation was 15.5494, which is acceptable because it is lower than the 1/3 of map’s scale. The ArcGIS 10.3 software was used for the georeferencing procedure.

### 5.2.2.2 Endmember Extraction

In general, an endmember usually defines a surface reflectance spectrum or a group of spectra, which are characterized by one pure reference material. Various algorithms have been designed, such as Pixel Purity Index (PPI), N-FINDR and Automated Morphological Endmember Extraction (AMEE) etc, *(Martinez et al, 2006)* for a more accurate or automatic endmember extraction.

Procedures, which can be used for the detection of different compositions of lava flows and examine their temporal change, are the laboratory spectrometry, with decimeter-size samples *(Abrams et al, 1991)*, field spectrometry producing in situ data *(Spinetti et al, 2009)* and a hybrid method which utilizes a map (e.g. Geological Map) which can be used as a reference, in order to extract the spectral reflectance of different lava flows.

In this study, the endmember extraction was implemented according to the Geological Map and its volcanic products segregation. In particular, four main categories were defined (MF1, MF2, MF3 and Ellitico) and each category includes samples from each lava flow that has been recorded. It also should be pointed out that the three first categories also embody scoria and pyroclastic products of specific lava flows; named $MF_{(1, 2, 3)}$ *sc* and $MF_{(1, 2, 3)}$ *py*, respectively. Table 5.2.2.2.1 describes and Figure 5.2.2.1.1 visualizes the MF1, MF2, MF3 and Ellitico volcanic categories and theirs subdivisions.

***Table 5.2.2.2.1: The Endmembers categories and theirs subdivisions according to the date of lava flow as shown in the Geological map of Etna. The symbololism is the same as in the map.***

| **MF1** | **MF2** | **MF3** | **Ellitico** |
|---|---|---|---|
| **1971** | 1727-28/32-33 | 1536 | EC_24ci |

| | | | |
|---|---|---|---|
| **1975-77** | 1735-36/58-59 | 1566 | EC_24cs |
| **1977-78** | 1760-64 | 1610 | EC_24mn |
| **1980-81** | 1763 | 1614-24 | EC_24pn |
| **1981** | 1764-65 | 1634-36 | EP_22dc |
| **1983** | 1766 | 1646-47 | EP_22el |
| **1985** | 1780 | 1669 | EP_22fu |
| **1986-87** | 1787 | sc1610 | EP_22gc |
| **1998** | 1792 | sc1646-47 | EP_22pa |
| **1999** | 1809 | 1536 | EP_22ta |
| **2001** | 1865 | | EP_22vr |
| **2002-03** | 1879 | | EPD_21a |
| **2006** | 1886 | | EPD_21b |
| **2007** | 1892 | | EPG_25a |
| **py1981** | 1910 | | EPG_25b |
| **py1999-01** | 1911 | | ESC_20 |
| **py2002-03** | 1923 | | |
| **sc2001** | 1942 | | |
| **sc2002** | 1947 | | |
| | 1949 | | |
| | 1957/60-64/66-71 | | |
| | 1960-64 | | |
| | 1964 | | |
| | py1879 | | |
| | sc1763 | | |
| | sc1766 | | |
| | sc1832 | | |
| | sc1843 | | |
| | sc1879 | | |
| | sc1892 | | |

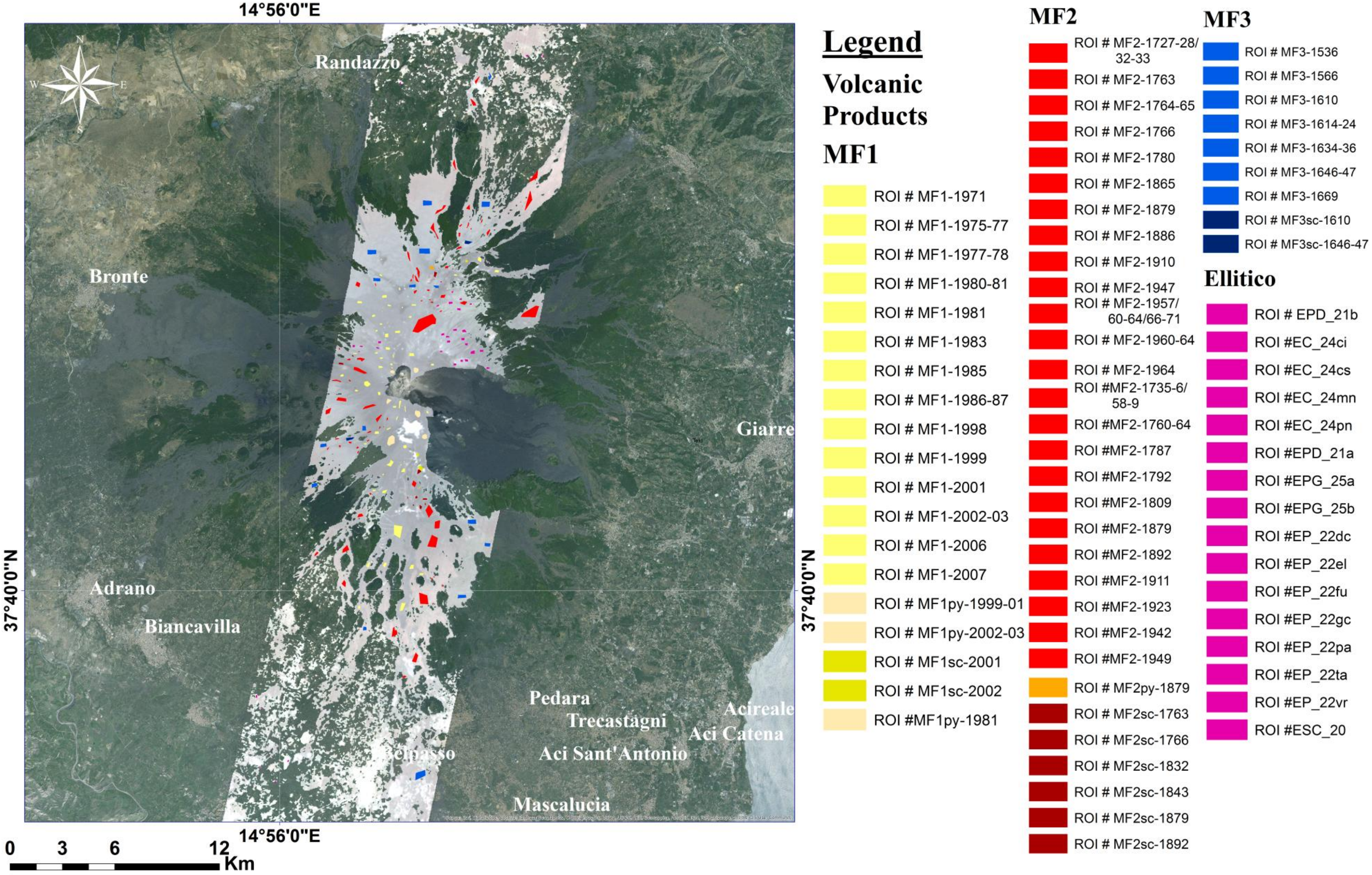


***Figure 5.2.2.2.1: ROIs used for the endmembers extraction on the Hyperion image. The main volcanic products and their differentiation, due to lava flow deposits along with their corresponding colors are shown on the right.***

### 5.2.2.3 Topography Variables

LULC depends on environmental variables. Among the environmental variables, topography is of significant importance. Topographic variables comprise altitude, slope and aspect. This information brings out the patterns, the heterogeneity and the complexity of a surface, *(Wondie et al, 2012)*. To analyze the contribution of topographic effects to lava flows change, we calculate the slope in degrees and aspect, (Figure 5.2.2.3.1), utilizing the digital elevation model (DEM). Moreover, using the endmembers, which are described below, we examined the temporal change of both layers. Before further processing the Fill tool was used (in ArcGIS), in order to discard any small sinks' imperfections present in the DEM.

### (A) Slope

The topographic Slope is calculated as the maximum rate of change between each pixel and its neighbors; for example, the steepest downhill descent for the pixel (the maximum change in elevation over the distance between the cell and its eight neighbors). Every pixel in the output raster has a slope value. ArcGIS software is able to calculate the topographic slope for each pixel, either in degrees or in percentage values. The lower the slope value, the flatter the terrain; the higher the slope value, the steeper the terrain. Figure 5.2.2.3.1 presents an example of the slope calculation according to three different angles. If in a right triangle the slope angle (θ) is 45 degrees the two vertical sides; named rise and run, will be equal. If we transform the degree slope into the percentage value, then the slope angle will be 100%. As the slope approaches vertical (90 degrees), the percentage slope approaches infinity.

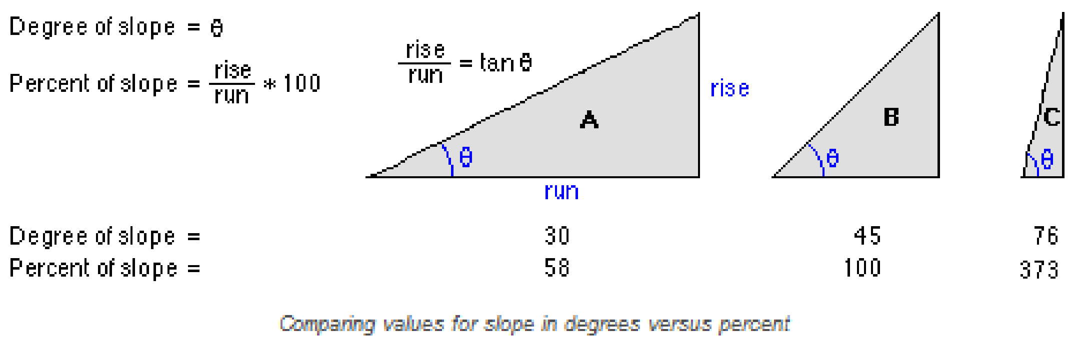


***Figure 5.2.2.3.1: Slope calculation, (source: ArcGIS Desktop 9.3 Help)***

## (B) Aspect

The Aspect identifies the downslope direction of the maximum rate of change in value from each cell to its neighbors. The Aspect can be considered as the slope direction. The values of the output raster are the compass direction of the aspect and they are calculated in degrees according to the ArcGIS “aspect tool”,. Each pixel values are transformed in degrees with the range of $0^o$ (north) until $360^o$ (again north). Flat surfaces have no direction and they are represented with the value -1, (Figure 5.2.2.3.2). In particular, the aspect tool uses a 3*3 kernel with its neighbor values (z-values), (Figure 5.2.2.3.3), which are used for aspect calculation in each central pixel. When the kernel moves, it repeats the aspect calculation for the whole area. The kernel’s direction depicts the processing orientation of each pixel.

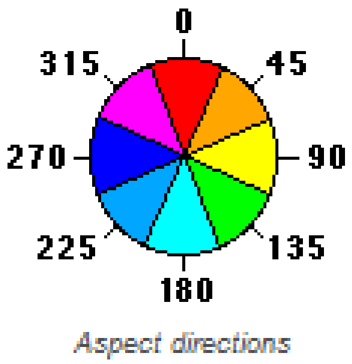


*Figure 5.2.2.3.2: The representation of aspect directions. The direction of the aspect changes clockwise, (source: ArcGIS Desktop 9.3 Help).*

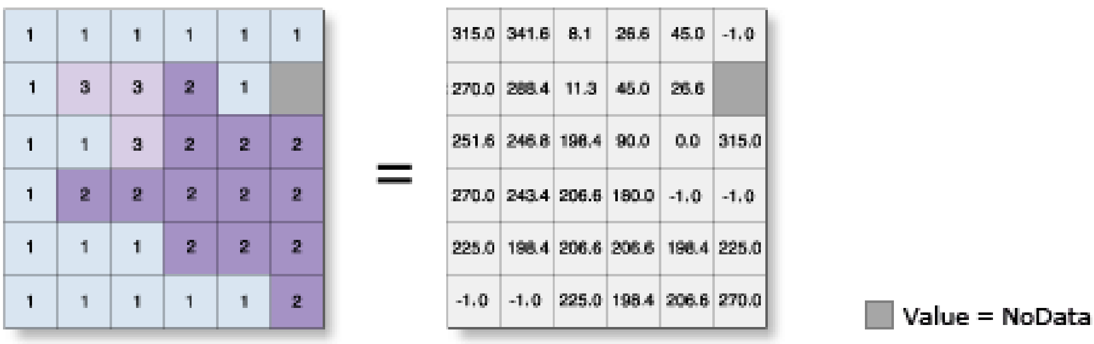


*Figure 5.2.2.3.3: Aspect 3*3 kernel, (source: ArcGIS Desktop 9.3 Help).*

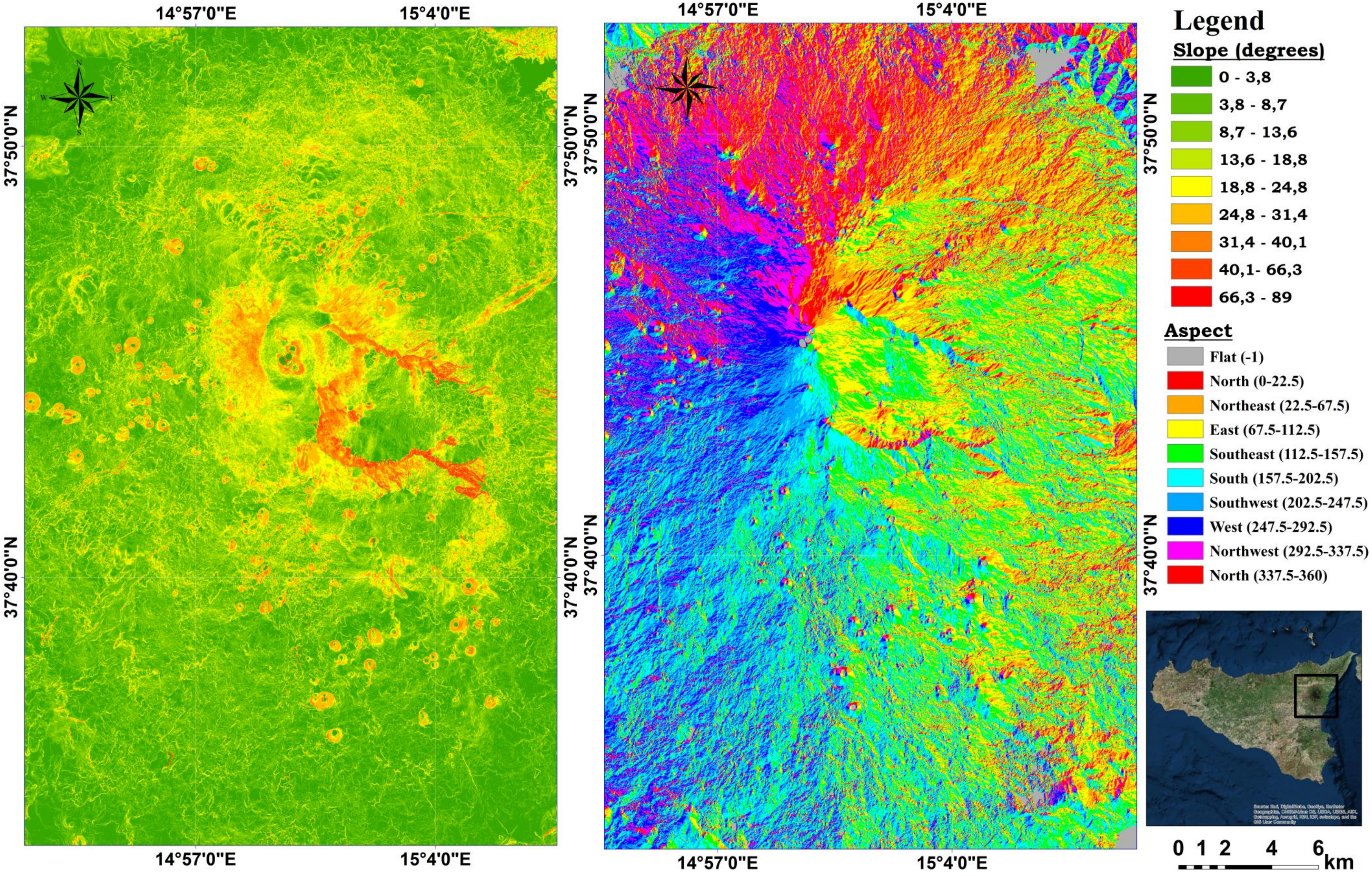


*Figure 5.2.2.3.4: Images of the calculated topographic Slope (left) and Aspect (right) of the Etna volcano.*

### 5.2.2.4. Statistical Data Analysis

In HSI the spectral signature of a target group can significantly vary as the result of differences in illumination conditions, viewing geometry, material composition and spatial shape. In addition to this inherent variability of targets is the variability caused by the presence of atmospheric effects and sensor noise, *(Manolakis et al, 2001)*. Whereas, MSI can be acquired at very high spatial resolution (e.g. Pleiades, 0.5-2m), spatial resolution of HSI remains low (e.g. Hyperion, 30m) and spectral mixing is thus a major problem. Ensuring that the illumination conditions are similar, except for 2009 dataset due different seasonality (Table 5.2.2.4.1) and eliminating the noise and the atmospheric effects, we investigate the remaining variables, according to their spectral behavior.

***Table 5.2.2.4.1: The illumination conditions of HSI, (acquired from metadata files).***

| | **Sun Azimuth ($^o$)** | **Sun Elevation (km)** |
|---|---|---|
| **9/7/2007** | 114.178 | 61.393 |
| **8/10/2009** | 150.68 | 42.123 |
| **14/7/2012** | 116.72 | 61.449 |

Respectively, backscatter coefficient target groups vary due to the topography, surface rugosity, dielectric constant (moisture) and sensor and geometry distortions. Furthermore, minimizing the moisture presence by selecting datasets in august, correcting the geometric and sensors distortions we analyzed the topographic correlation with the backscatter coefficient ($\sigma^0$). Lastly, stabilizing the topographic variables, we investigated the texture temporal change, according to the backscatter coefficient variability.

For this purpose, we used the volcanic formations categorization and their subcategorization according to the lava flow records (see chapter 5.2.2.1 B), in order to investigate the temporal change on the low active section of Etna volcano, with the application of statistical methods in HSI, SAR data and topographic variables.

### 5.2.2.4. (A) Hyperspectral statistical data analysis

While lava surfaces are exposed to various environmental conditions, several factors could change their spectral behavior over time. Many studies have shown that biological weathering (vegetation colonization) and chemical weathering (*Rothery & Lefevre, 1985; Abbott et al, 2013; Benedetti, 2003; Figlia et al, 2007; Yamasaki et al, 2011*) have a significant impact on the spectra of aging lava flows by increasing the reflectance response in the NIR, *(Li et al, 2015; Head et al, 2013)*. In particular, the most common vegetation specie that covers the lava flows and increases the reflectance spectra are lichens (*Rothery & Lefevre, 1985; Abbott et al, 2013; Benedetti, 2003; Figlia et al, 2007; Yamasaki et al, 2011*; *Stretch & Viles, 2002; Rothery & Lefevre, 1985)*. In addition, lichen cover on lava flow can therefore alter the pattern of lava spectra (e.g. 24, 33). Concerning Mt Etna lichens' growth, the rate is higher than in other similar areas according to Spinetti et al. (2009). Exposure to the surface also promotes oxidation of lava. This process is produced by multiple factors such as climate conditions, relief, lithology, vegetation cover, and lava age as well as the surface roughness resulting from lava flow emplacement dynamics *(e.g. Benedetti, 2003*; *Yamasaki et al, 2011*). It has been reported that oxidation increases the reflectance curve in the visible part of the spectrum over time *(Abrams et al, 1991)*.

Based on the above, we hypothesized that in short term, surface alteration and sparse vegetation growth will increase the surface reflectance. Older lavas will be mostly characterized either by surface alteration or by growth of sparse vegetation, are expected to present higher reflectance in the NIR and absence of the Red Edge pattern according to the presence or absence of vegetation respectively. On the other hand, recent lava flows will present lower reflectances, especially when moisture and dust is present (lower that 4% in the NIR), *(Spinetti et al, 2009)*. According to that assumption, we expect that the surface reflectance will increase (i) from the MF1 formation to Ellitico formation, (ii) from 2007 dataset to 2012 dataset and that the MF3 and Ellitico formations will be influenced by a sparse vegetation presence. The vegetation presence is expected to be detected due to the mixed pixels where the applied NDVI mask failures to identify them as dense vegetation cover.

To examine the spectral behavior of lava flows, spectral average and standard deviation calculations were calculated for each volcanic formation. In particular, as it was mentioned, the volcanic formations were categorized into four groups: MF1, MF2, MF3 and Ellitico. Each volcanic target group also contains the spectral information about different lava flows, until the May of 2007. So, using the 2007, 2009, and 2012 datasets, we calculated the average and standard deviation spectral information for each subcategory. It should also be pointed out that for each volcanic formation the pyroclastic and scoria averaged spectra were calculated separately, because their material composition and surface texture are different, even if they were produced from the same eruptive episode.

The visualization of (i) the averaged spectral profiles for each volcanic formation, (ii) the standard deviation (error bars) of each volcanic subcategory and (iii) the temporal change of the latest categories, is conducted on MATLAB.

### 5.2.2.4. (B) SAR statistical data analysis

As aforementioned, the radar backscatter coefficient is affected by four factors, local slope, roughness, orientation of the slopes and dielectric constant of surface material, *(Saepuloh & Koike, 2010).*

It has been proved that polarimetric SAR data and technology play a significant role in rapid identification and mapping of lava and pyroclastic flows after eruptive episodes. SAR can also be a useful means to distinguish the recent lava deposits from the outdated along with the contributing environmental factors. Such discrimination depends on the SAR parameters, which are frequency polarization, incidence angle and spatial distribution *(Gaddis, 1992).*

Dierking & Haack (1998) have proved that the younger and rougher lava flows can be identified easily in SAR images because of their comparatively high backscatter intensity, in particular at cross-polarization. The rather higher backscatter coefficients at cross-polarization indicate that the contribution of multiple scattering to the received signal is significant. On the other hand, rougher lava flows can be discriminated clearly from the surrounding terrain, using the depolarization ratio $[2\sigma^0_{HV} / (\sigma^0_{VV} + \sigma^0_{HH})]$. In addition, the very rough a'a lava reveals high backscatter coefficient values, whereas for the smooth pahoehoe lava, they are very low.

The common type of volcanic surfaces at Mt. Etna is a'a. However, there is a remaining less than 10% of the surface covered by pahoehoe lava type (i.e. 1614-1624 lava flow deposits), (*Chester et al, 1985; Spinetti et al, 2009).* According to the above, we expect the backscatter coefficient values of the MF1 and MF2 volcanic formations to be higher, in comparison with the MF3 and Ellitico formation, especially in cross-polarization.

To investigate the backscatter intensity, according to the different volcanic formations, for each formation category and their subdivisions, the average and standard deviation backscatter coefficient were calculated. Following, we examine how the satellite geometry and different polarization contribute to the recognition of different volcanic formations. For this purpose, we calculated the average and standard deviation of $\sigma^0_{VV}$ and $\sigma^0_{VH,}$ for each endmember, for both ascending and descending acquisition modes. Continuing, we subtract the $\sigma^0_{VV}$ and $\sigma^0_{VH}$ that derived from ascending and descending acquisition mode, for each endmember, in order to investigate which mode is more suitable for the detection of the different volcanic formations.

In order to locate some significant backscatter intensity patterns, due to temporal change, the backscatter coefficient temporal change is also analyzed, for each polarization, in ascending and descending mode and according to the lava flow deposits chronology. Finally, since the backscatter signal is affected by the topography we extract the slope and aspect values for each endmember and we examine the correlation (r) with the backscatter coefficient values, for the same endmembers. We assume that the correlation coefficient will reveal high values (>0.60).

### 5.2.2.4. (C) Temporal Surface Change Analysis

Temporal change analysis is based on the aforementioned fact that the backscatter retrieved signal depends on various factors, like topography, surface rugosity, dielectric constant (moisture) and sensor and geometry distortions. The effects from the dielectric constant, sensor and geometry distortions were minimized as it was described in the previous paragraph.

Then, we assumed that we could estimate the surface roughness contribution in the backscatter signal, if we examine the backscatter coefficient values, when the slope and aspect values are immutable.

For this purpose, we classified the topographic aspect and slope into four main categories, so as to combine the topographic variables with the MF1, MF2, MF2 and Ellitico formations (excluding the pyroclastic and scoria formations). We examined each topographic combination of slope and aspect and the geologic formations in order to detect potential variations of the $\sigma^0_{VV}$ and $\sigma^0_{VH}$ in both ascending and descending acquisition modes. The processing steps are further analyzed and visualized in Figure 5.2.2.4.1. This procedure was implemented in ArcMap 10.3 software, utilizing the model builder operation, which gives the ability to create a Database Management System (DBMS), using the relational model and to restore it any time, by including it in your own toolbox. The statistical analysis was performed using ENVI 5.3 software and the production of the resulting diagrams was performed in excel.

The processing steps of this approach are:

- **Slope and Aspect reclassification** into four categories ($15^o$, $30^o$, $45^o$ and $90^o$) and ($90^o$, $180^o$, $270^o$ and $360^o$), for the generalization and better manipulation of their various values.
- **Raster to Vector transformation** of the reclassified slope and aspect layers, in order to create an attribute table with entities of the aforementioned categories. The initial spatial layers could not provide this information.
- **Resizing slope and aspect** spatial dimensions according to the MF1, MF2, MF3 and Ellitico dimensions.
- **Joining** slope and aspect attribute tables, using as connecting attribute, their primary key (OBJECTID), applying the "one to one (1:1)" relationship type.
- **Spatial Joining** the new attribute tables, which include the records of the aspect and slope entities, with the attribute tables of MF1, MF2, MF3 and Ellitico volcanic formations. It should be pointed out that for this relation, we didn't use the "simple join" because the topographic variables and the volcanic formations were related only based on their relative spatial location. In order to implement this operation we used the "one to one (1:1)" join operator, which joins the features that have the same spatial relationship with a single target feature and the attribute tables are aggregated using the a field map merge rule. In addition, all the target features were kept and intersect was defined as the match option, because the features in the join features will be matched if they intersect a target feature.
- **SQL Queries:** In this part we wanted to create spatial features, which include entries for each slope class and for each aspect class, for each volcanic formation. For example, for the MF1 formation, the slope category $30^o$ was combined with each of the aspect categories ($90^o$, $180^o$, $270^o$ and $360^o$). This procedure was also applied for the $30^o$, $45^o$ and $90^o$ slope categories and for MF2, MF3 and Ellitico formations.
- **New Spatial features:** For each SQL query, an amount of records were selected. So, we created new spatial features, isolating only the selected tuples.
- **Layer Stacking:** Combining the Descending VV, Descending VH, Ascending VV, Ascending VH layers into a single dataset, in order to calculate the average from all layers at the same time.
- Average backscatter coefficient calculation, for each new spatial feature, which was created from the SQL queries.
- Visualization of the backscatter variation.

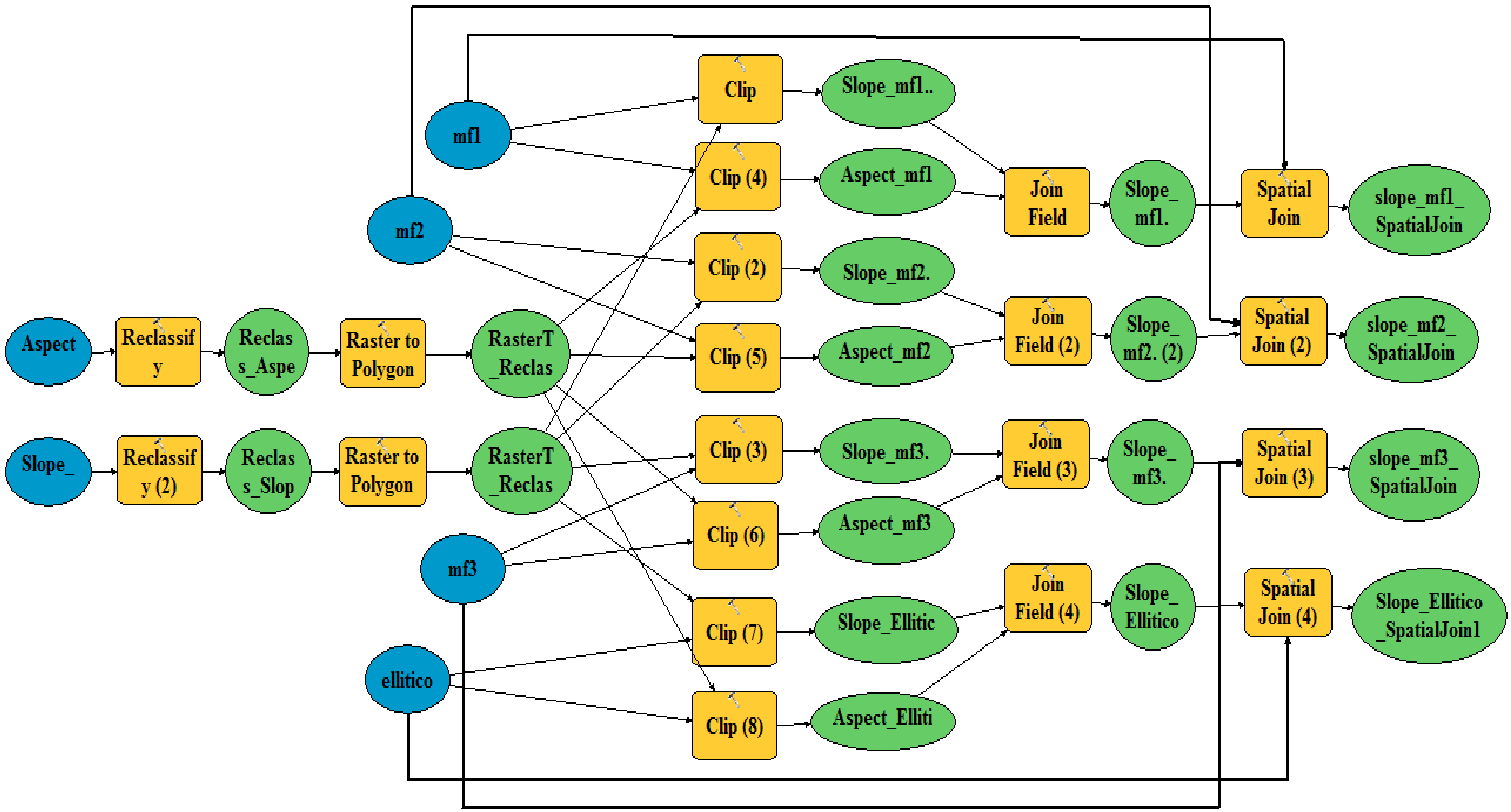


*Figure 5.2.2.4.1: The processing flow chart, for the calculation of the backscatter coefficient temporal variation, which defines the temporal surface change*

# Chapter 6: Results

## Background

This chapter presents the results of the hyperspectral and SAR statistical approaches, investigating the temporal surface change, including only the lava flows land cover type and especially the low activity section of Mt. Etna. Hyperspectral statistical data approach depicts the spectral curve behavior in four main volcanic formations, during five years (2007-2012). Surface alteration, oxidation and vegetation growth (mostly lichen colonization) in lava flows composition are also tested. The aforementioned ascertainments were based on Spinetti et al (2009) and Sgavetti et al (2006) studies. On the other hand, the backscatter coefficient ($\sigma^0$) variation, according to several variables, such as polarization, satellite orbit for each volcanic formation, is examined. Finally, we investigate the contribution of topographic features such as slope and aspect in microwave backscatter signal.

## 6.1. Hyperspectral Statistical Data Approach

Four major problems arose from the analysis of the three datasets. The first was the noise level in the Hyperion datasets, which required several spectral bands to be removed, mostly in the SWIR region. As a consequence, the observation of some of the absorption bands (e.g. 1 μm iron absorption) critical for main alteration analyses was precluded. Secondly, mixed pixels, due to medium spatial resolution disinclined the identification of several minerals, which might occur on Etna. Thirdly, an absorption in 1.114 μm was revealed, especially to the 2009 image due to water vapor presence. This potentially occurred, due to the atmospheric correction failure to reduce the contribution of the water vapor in this spectral region. Figure 6.1.1 depicts the water vapor (atm*cm) values in 2007, 2009 and 2012 datasets, derived from four selected regions, which are located in the low activity section of the volcano. Almost in every region of interest (ROI), 2009 dataset revealed higher water vapor values.

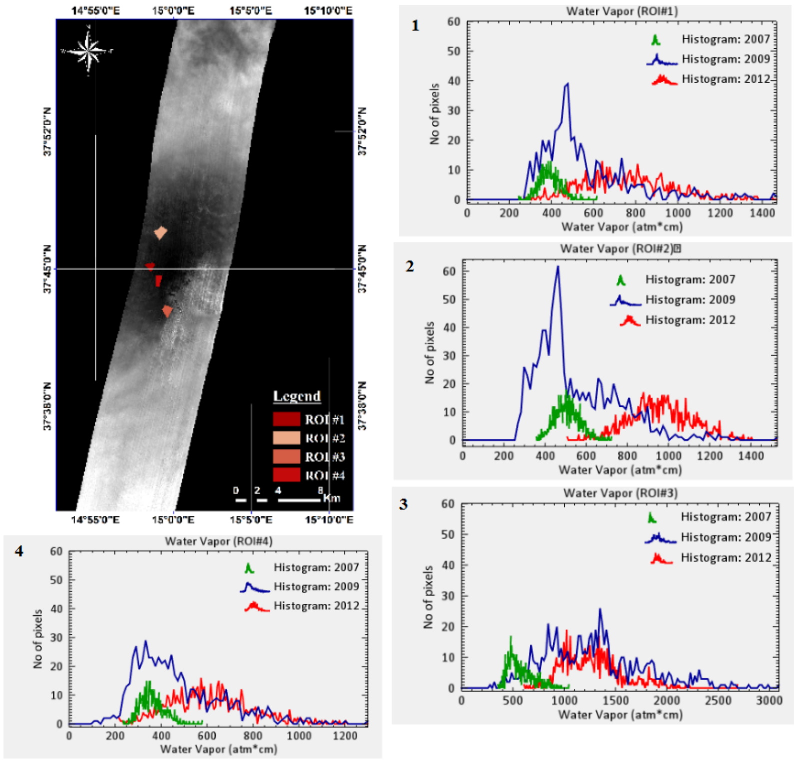


***Figure 6.1.1: The water vapor values for each ROI, calculated for each pixel. This product is available after the atmospheric correction.***

Spinetti et al (2009) proved that old lava deposits present higher spectral responses, while the opposite occur in recent lava flows. So, we assume that during the time period 2007-2012, the reflectance will increase from 2007 to 2012. This indeed happened in the case between 2009 and 2012 surface reflectances. However, reflectance percentages were higher in 2007 image. We hypothesized that this is probably due to one of the three following factors (or a combination of them); different aerosol concentrations, presence of high altitude clouds and/or sensor's artifacts.

For this purpose, we examined the Aerosol Optical Depth (AOD) and the Cloud cover values over Etna volcano, for the three Hyperion acquisition dates using Moderate-resolution imaging spectroradiometer (MODIS) sensor measurements, (Figure 6.1.2). We observed that the 2007 date presented high AOD values, in the southwestern of the summit crater, which shows that probably this is not the main cause.

On the contrary, the 2009 and 2012 AOD values were similar. Likewise, the cloud cover values, derived after the atmospheric correction, were almost the same in 2007 and 2012 dates, and higher in 2009. The above show that we cannot be conclusive as to the atmospheric contribution, so, it is also possible that this is due to the sensor or both. Further investigation is required as this was out of the scope of this work.

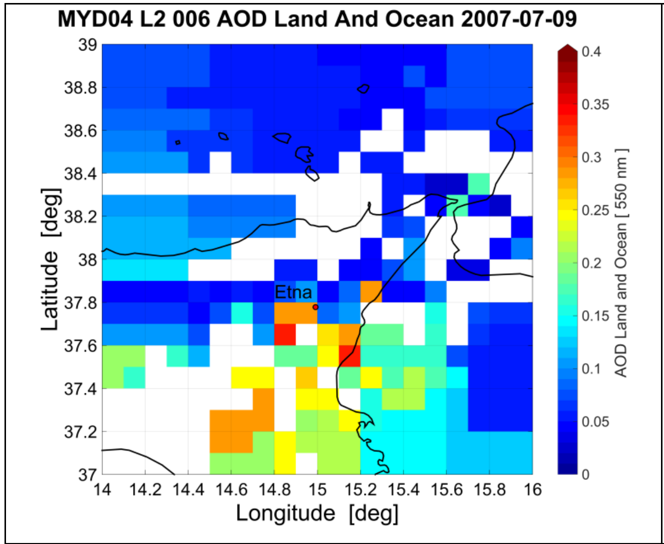

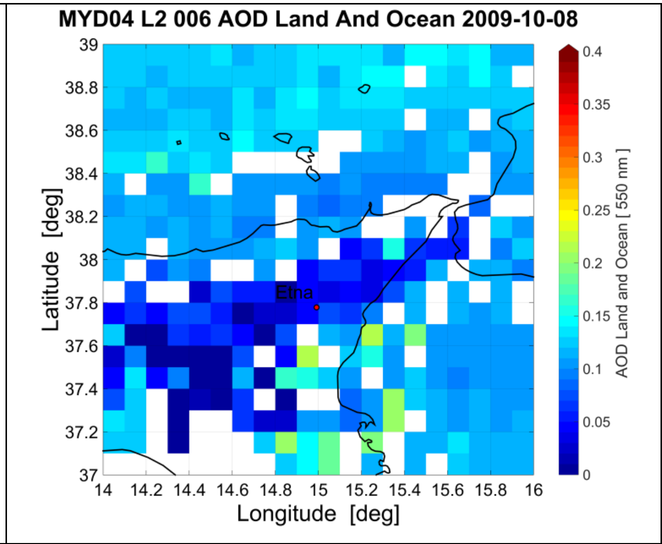

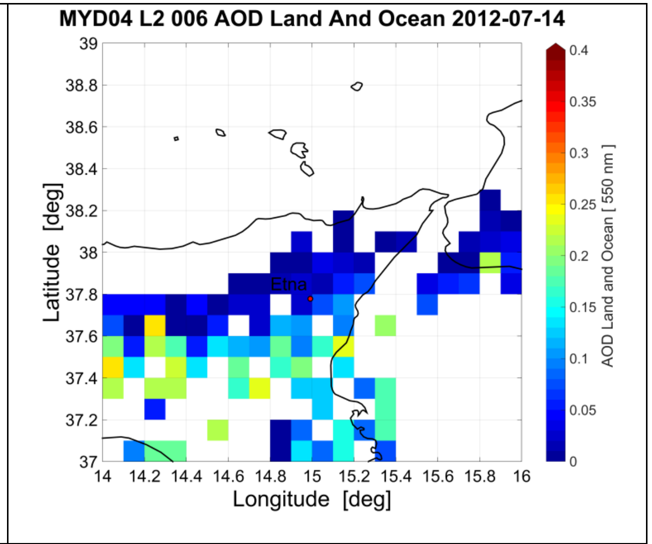


***2007 - AOD at 550nm*** ***2009 - AOD at 550nm*** ***2012 – AOD at 550nm***

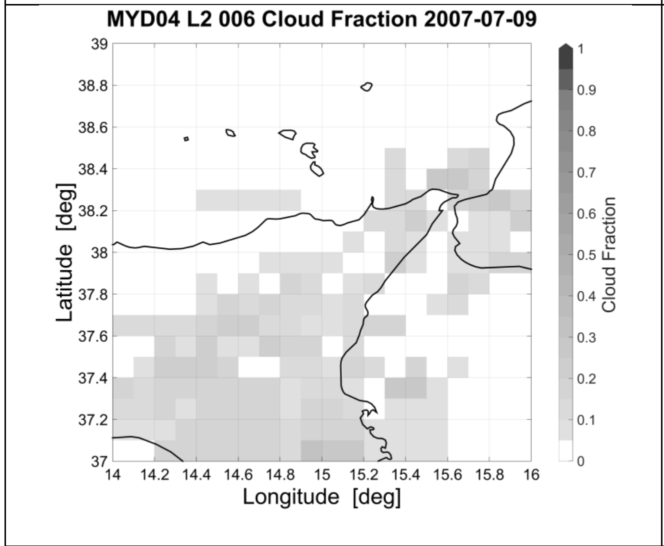

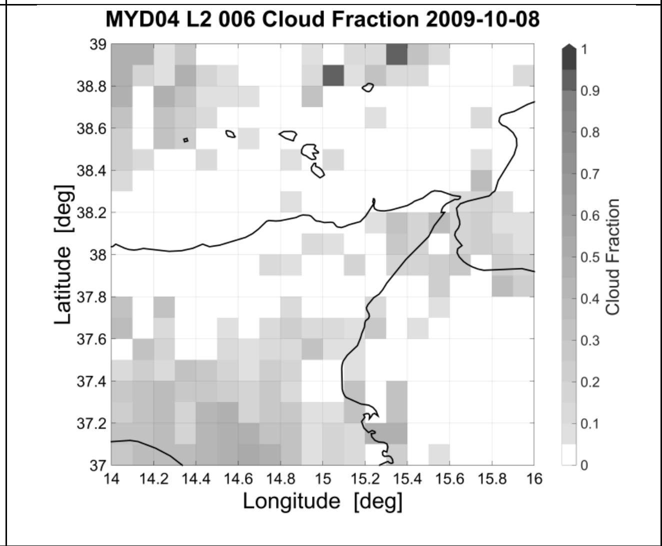

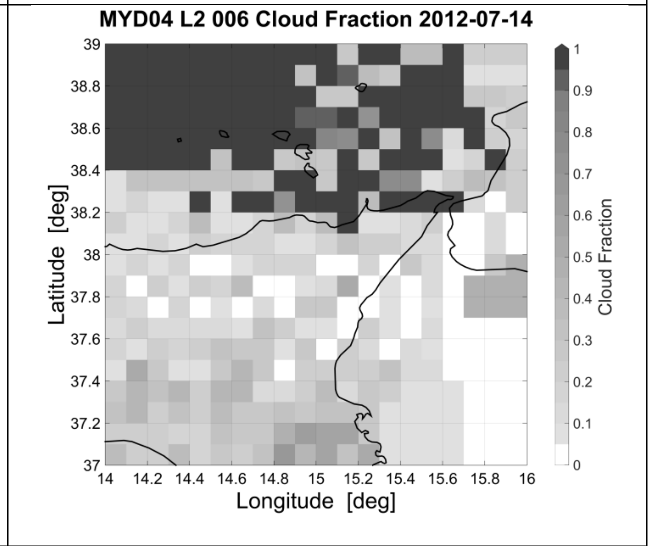


***2007 – cloud fraction*** ***2009 – cloud fraction*** ***2012 – cloud fraction***

***Figure 6.1.2: AOD at 550nm and cloud fraction values acquired from MODIS data, for 9/7/2007 (left), 8/10/2009 (middle) and 14/7/2012 (right), on eastern Sicily with Mt. Etna as the central location***

- **Mongibello Torre del Filosofo 1 Formation (1971-2007) – MF1**

Figures 6.1.4 and 6.1.5 present the average reflectance curves derived from 2007, 2009 and 2012 Hyperion datasets, from each lava flow deposit, which are included to the MF1 (1971-2007) category. The first figure includes the mean lava flow surface reflectances and the second the pyroclastic and scoriae volcanic products. The average and variation of the aforementioned is also depicted, in order to examine in detail the spectral curve of each sample and the purity of the endmembers (Figures 6.1.10-17). Graphic representations for each endmember; presenting the spectral variation between 2007, 2009 and 2012 images were also applied, (Figures 6.1.43-45).

Endmembers' spectral curves derived from 2007, 2009 and 2012 revealed continuous increases and decreases in the reflectance values, in the SWIR region, due to the low signal-to-noise ratio (SNR) values. Most of the endmembers derived from 2009 image had strong absorption in 0.7 μm, due to the chlorophyll absorption and a decrease of the spectral response in 1.16-1.2μm, probably due to the water absorption, *(Li et al, 2015)*. This indicates the potential existence of sparse vegetation (e.g. lichen cover).

Recent lavas depict an absorption in 0.4-0.5 μm. The surface reflectances extracted from 2007 and 2009 images present more homogenous spectral patterns than the 2012. According to the heterogeneity in 2012 endmembers' spectral curves, we grouped the 2012 lava flows spectral curves into five categories: (i) 1998, (ii) 2002-03, 1985, 1999, (iii) 2001, 1983, (iv) 1975-77, 1977-78, 1980-81, 1981, 1986-87 and (v) 1971, 2006 and 2007, due to their pattern similarity and we compared them with 2007 and 2009 corresponding samples.

**(i) 1998 Lava flow:** In 2012 image, the highest reflectances are observed, in 0.4-0.8 μm, while in 0.7 μm absorption occurred (~1%). In 1.1-1.2 μm a steep slope revealed, decreasing ~2% the reflectance response. According to Spinetti et al (2009) and Sgavetti et al (2006) reflectance measurements, this spectral curve did not have any resemblance with recent, old, altered, oxidized or pyroclastic volcanic products (Figure 6.1.3), while it might be a combination of different materials (mixed pixels). On the other hand, the same lava flow, in 2007 and 2009 images, was more homogeneous with all other MF1 spectral curves, while a small absorption in 1.1-1.2 μm is the only common with the 2007 endmember. In contrast to the 2007 and 2012 spectra, the 2009 reflectance curve decreases in the SWIR. The 2007 spectral curve increases significantly from 1.5 μm and to longer wavelengths.

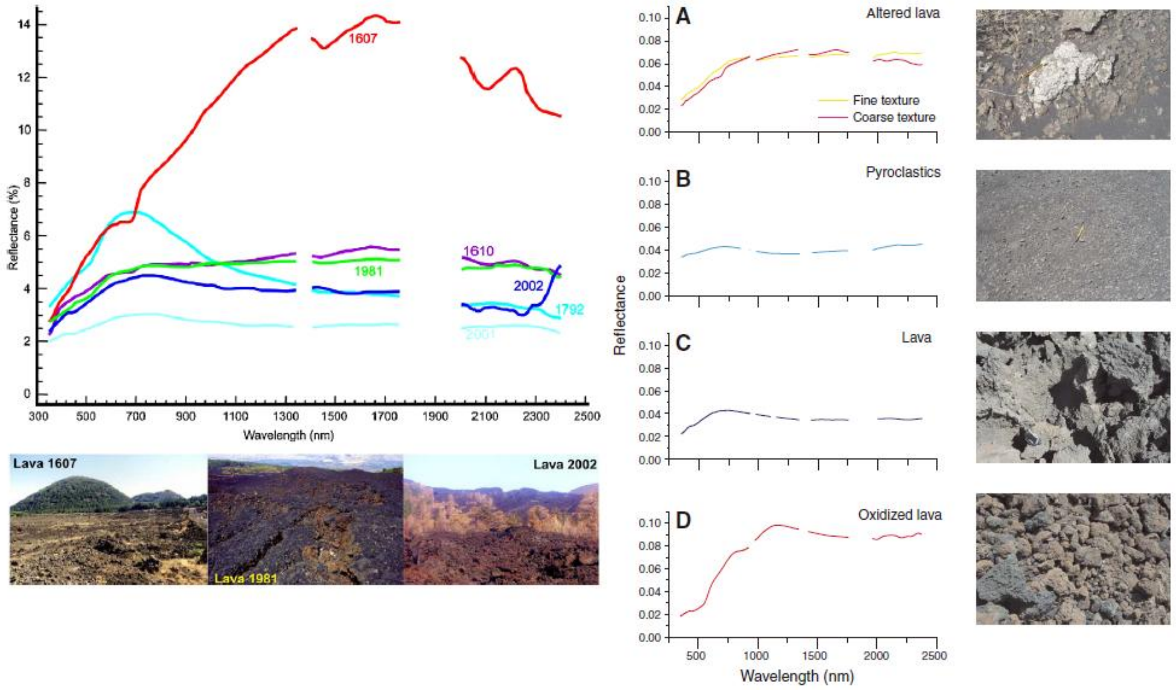


*Figure 6.1.3: Spinetti et al (2009), (left) and Sgavetti et al (2006), (right) field measurements.*

**(ii) 2002-03, 1985, 1999 Lava flows:** For this category, the 2007 reflectances fluctuate from 7% to 8%. An absorption is observed within 1.1-1.2 μm and 1.6-1.7 μm, while in SWIR, the reflectance values increase up to 0.1-0.2%. The reflectance in 2009 and 2012 images is ~4%, with a strong absorption (1%) in 1.14 μm and in 1.1-1.2 μm, due to iron presence. From 1.4-2.4 μm reflectance values remain stable, (4%). The 2012 reflectances range between 4-5%, with a 0.1% increase, in 1.14 μm, compared with 2009 image, although 0.1% absorption is observed in 1.1-1.2 μm. Between 1.4-2.4 μm, reflectances do not change, but the overall area shows an increase of 0.1%, compared with 2009.

**(iii) 2001 & 1983 Lava flows:** These particular lava flows present the highest reflectance values in all datasets. In 2007, the mean reflectance is 10%, with an absorption (0.2-0.3%) in 1.14 μm. In contrast, the endmembers from 2009 and 2012 images display a decrease in reflectance at 2.3 μm. The reflectance range in the 2009 dataset is 5.8-6.2%. The only observable change, comparing with the other dates, is the reflectance increase (0.2-0.3%) in 1.55-1.65 μm. In the 2012 image, the reflectances of 2001 and 1983 lava flows remain the same from 0.4 μm to 0.9 μm, in contrast to the corresponding 2007 and 2009 endmembers, which present a 0.2-0.3% difference. Differentiations of 0.1% are observed between the spectral areas 1-1.3 μm, 1.45-1.8 μm and 2.1-2.4 μm.

**(iv) 1975-77, 1977-78, 1980-81, 1981, 1986-87 Lava flows:** The endmembers from this category show an average 6-8% reflectance range in the 2007 image. In 1.14 and 2.1-2.4 μm reflectance increased (~1%), comparing with the 1.1-1.2 & 1.55-1.65 μm spectrum ranges, where the reflectance percentage was ~8%. Correspondingly, the 2009 reflectances range from 3-4.5%, with strong absorption in 1.14 μm and overall spectral variation of 3%. The 2012 reflectances range between 6-4.5% and seem to be affected by sparse vegetation (red absorption in 0.7 μm and red edge). The 1.14 μm reflectance is increased, in contrast to the corresponding one of the 2009 dataset while between 1.55-1.65 μm reflectances seem to be decreased.

**(v) 1971, 2006 and 2007 Lava flows:** Endmembers derived from 2007 image had the same spectral behavior, as the endmembers from the previous category had, whereas their reflectance values are decreased by 2%. A strong absorption, located in 1.14μm, is depicted in the 2009 endmembers. The overall spectrum continues to decrease between 1.15-1.65 μm. However, the 2012 endmembers have a completely different spectral behavior compared with either the two other datasets or the other spectral curves from the same image. In particular, reflectance values are decreased up to 2% in 0.7-0.9 μm, unlike the corresponding ones in 2007 and 2009 datasets. Reflectance values are also increased by 0.1% between 1.55-1.7 μm and by 0.2% in all SWIR.

**Pyroclastic & Scoriae:** The most characteristic difference between the three datasets are observed in 2001 scoria. More specifically, the 2007 reflectance values vary between 12-16%, in 2009 between 4-6% and in 2012, between 4.5-6.5%. This is probably due to the presence of mixed pixels. Furthermore, in 1.14 μm, the reflectance is decreased in 2009 endmember, unlike with the 2007 and 2012 ones. Between 1-1.3 μm, the 2007 spectrum presents an absorption in contrast to the 2009 and 2012 corresponding ones.

The reflectance values of pyroclastic endmembers (py1989, py1999-01, and py2002-03) present an absorption in 0.7μm. The overall reflectances decrease with the following order: py1989> py2002-03> py1999-01 in 2007/2009 datasets and py2002-03> py1999-01> py1989 in 2012. The reflectance values of scoriae endmembers (sc2001 and sc2002) decrease by the following sequence: sc2001> sc2002 for all datasets. In particular, the difference between sc2001 and sc2002 in 2007 was 12%, while both present an absorption in 0.65μm. In the 2009 image, the spectral profile of the sc2002 coincides with py1999, in 0.4-0.9 μm; they differ however by 0.1% in the rest of the spectrum range. This is also observed in the 2012 image, between the sc2001 and py1999 endmembers. The 2001 scoriae in the 2009 and 2012 images, present higher reflectances between 1.4-1.65 μm. The opposite occurs in the 2007 image for the same formations. Finally, the sc2001 reflectance response increases between 1.6-1.8μm and conversely the sc2002 reflectance decreases in 0.7μm.

- **Mongibello Torre del Filosofo 2 Formation (1669-1971) – MF2**

Figures 6.1.6 and 6.1.7 present the average reflectance curves derived from 2007, 2009 and 2012 Hyperion datasets, from each lava flow deposit, included to the second volcanic category. Figure 6.1.6 shows surface reflectances of lava deposits, recorded from 1669 to 1971 and Figure 6.1.7 show the pyroclastic and scoriae volcanic products, for the same time period. In addition, average and standard deviation reflectance plots are also presented in Figures 6.1.18-32. Graphic representations for each endmember; presenting the spectral variation between 2007, 2009 and 2012 images were also applied, (Figures 6.1.46-50).

According to Li et al (2015), three main factors could change the chemical composition of lava flow: alteration, oxidation and vegetation growth (biological weathering). Sgavetti et al (2006) segregated the alteration into two types, coarse and fine, based on surface texture. For example, the vegetation presence in a lava flow spectral curve can be recognized by the absorption in 0.7 μm, the red edge, the absorption in 1720-1730nm (cellulose presence) and the absorption in 2300-2315nm (lichen species cover), *(Li et al, 2015)*. According to the Figure 6.1.3, which depicts the field measurements from various volcanic products around the Etna; we could examine the potential presence of vegetation presence and coarse alteration to MF2 spectral curves.

The altered lava flows are identified by the reflectance increase in 0.4-0.9 μm, a small absorption effect (~1%) in 0.7μm and an increase again in 1.5-1.6 μm with a curved shape. Surface texture alteration is categorized in coarse and fine. In coarse the reflectance response decreases in SWIR, while in fine texture remain stable.

Comparing Sgavetti et al (2006) field measurements with the MF2 endmembers and investigating the above characteristics, we could claim that various lava flows and scoriae reflectances were affected by coarse alteration and biological weathering. Although, we also assumed that this is not observed in pyroclastic products. Table 6.1.1 presents the endmembers that influenced by the aforementioned factors, for 2007, 2009 and 2012 datasets.

***Table 6.1.1: List of endmembers affected by coarse alteration (A) and vegetation growth (V) in Hyperion datasets.***

| Volcanic Products | 2007 | 2009 | 2012 |
|---|---|---|---|

| Lava flows | | | |
|---|---|---|---|
| **1727-28/32-33** | V | V | |
| **1763** | | V | V |
| **1766** | V | V | V |
| **1780** | A | A+V | A |
| **1809** | V | V | V |
| **1879** | V | V | V |
| **1886** | A | A | A |
| **1892** | A | A | A |
| **1910** | A | A + V | A |
| **1911** | A | A + V | A |
| **1923** | A | A + V | A |
| **1947** | A | A + V | A |
| **1960-64** | V | V | V |
| **Scoriae** | | | |
| **sc1766** | V | V | |
| **sc1892** | V | V | V |

Except from the above factors which affect the surface reflectance, there are some endmembers (the same in 2007, 2009 and 2012 images), which reveal the same reflectance behavior in some spectral regions. This behavior is categorized into two classes. The first includes the lava flow endmembers, which have an absorption in 1-1.3 μm and an increase in 1.6-1.7 μm. The second contains the lava flow endmembers, which are characterized by an absorption in 1.2-1.3 μm absorption and reflectance stability in 1.6-1.7 μm. Table 6.1.2 depicts which lava flow is characterized by these categories.

***Table 6.1.2: Categorization of the MF2 lava flows, which reflect and absorbs in the same spectral regions. The first category corresponds lavas presenting common absorption feature in 1-1.13μm. The second category corresponds to lava flows presenting an absorption feature between 1.2-1.3μm***

| | MF2 lava flows |
|---|---|
| **1st category** | 1910, 1911, 1886, 1780, 1892 1923 |
| **2nd category** | 1727-28/32-33, 1735-36/58-59, 1760-64, 1763, 1947, 1949, 1957/60-64/66-71, 1960-64, 1964 |

Specifically for the second category, lava flow belonging to the same class but different subdivision behaves differently. In particular, in 1.35-1.36 μm, the endmembers which are extracted from the 2007 and 2012 datasets show an absorption. However, this absorption is not present in the corresponding spectra of 2009. In particular, in 1.37μm the reflectance response increases by 0.03%. Moreover in 2009 and 2012 images we observed an absorption in 1.75-1.78 μm, which was not revealed in 2007 image. Specifically, the reflectance response, in 2007 image, increased 0.03% in 1.78μm.

Reflectances between 1.15-1.17μm of the 2007 and 2012 images are increased by 0.02% compared to the corresponding 2009 one which, on the contrary, shows a slight decrease by 0.02-0.05%. Finally, in the 2009 dataset, the 1780 lava flow shows higher reflectances compared with 1886 and 1911 lava flows. The opposite occurs for the same endmember in 2007 and 2012 images.

Figure 6.1.5 shows the spectral profiles from pyroclastic and scoriae endmembers. The pyroclastic spectral patterns are in good agreement with the field measurement spectra presented by Sgavetti et al (2006) (Figure 6.1.2). The lowest reflectance is revealed in 1843 scoriae. The 1879 pyroclastics and 1879 and 1832 scoriae endmembers are characterized by lower reflectance values (~3%) in 2009, and ~7% and ~5%, in 2007 and 2012 images, respectively. Finally, scoriae recorded in 1763, 1766 and 1892 show an increase in their overall reflectance values from 2007 to 2012.

- **Mongibello Torre del Filosofo 3 Formation (122BC – 1669AD) – MF3**

Figures 6.1.8 and 6.1.9 present the average reflectance spectra derived from 2007, 2009 and 2012 Hyperion datasets, from each lava flow deposit, included in the third volcanic category. Figure 6.1.8 presents the surface reflectance of lava deposits, recorded from 122BC to 1669AD and Figure 6.1.9 the corresponding average spectra of the scoriae volcanic products, for the same time period. In addition, spectral plots of the average (and standard deviation) of the aforementioned formations are shown in Figures 6.1.33-36. Graphic representations for each endmember; presenting the spectral response change between 2007, 2009 and 2012 images were also applied, (Figure 6.1.51).

MF3 endmembers (lava flows and scoriae) are long exposed to the various environmental procedures. In MF2 formation, we mentioned some indicators in field reflectance measurements, which show the possibility of a lava flow to be affected by sparse vegetation and alteration. Vegetation presence alters the pattern of lava spectra by increasing the spectral response in the NIR spectral region *(Li et al, 2015; Head et al, 2013)*, whereas alteration enlarges the slope of the reflectance curve in the visible part of the spectrum over time, *(Abrams et al, 1991)*.

We examine the potential presence of the sparse vegetation according to the absorption effect in 0.7μm and the red edge. The alteration effect was investigated, according to the reflectance increase in 0.4-0.6 μm, a small absorption effect (~1%) in 0.7μm and an increase again in 1.5-1.6 μm with a curved shape. Also, Sgavetti et al (2006) proved the discrimination of the fine and coarse alteration according to the field measurements, because fine texture presents stable reflectance response in SWIR region, while coarse texture decrease the reflectance response in the same region of the EMS.

Examine the presence of the above characteristics to the mean and the variation of the spectral curves of the MF3 endmembers (lava flow and scoriae deposits) we hypothesized that various lava flows and scoriae reflectances are affected by coarse alteration and biological weathering. Also, it seems that vegetation affects more the endmembers extracted from the 2009 image. Table 6.1.2 presents which of these factors contributed to the MF3 endmembers extracted from 2007, 2009 and 2012 datasets, according to the aforementioned hypotheses.

***Table 6.1.2: List of endmembers affected by coarse Alteration (A) and Vegetation growth (V) in Hyperion datasets.***

| **Volcanic Products** | **2007** | **2009** | **2012** |
|---|---|---|---|
| | | **Lava flows** | |
| **1536** | A | V | A |
| **1566** | A + V | V | A + V |
| **1610** | V | V | |
| **1614-24** | V | V | |
| **1646-47** | V | V | |
| **1669** | A | A | A |
| | | **Scoriae** | |
| **1610** | V | V | |
| **1646-47** | V | V | V |

Table 6.1.2 shows that lava flow endmembers extracted from 2007 image seems to be affected more by sparse vegetation and alteration, in comparison with the 2009 and 2012 endmembers. The indication of vegetation existence is based on the absorption on the 0.7μm and on the steep increase of the reflectance response in 0.8-1 μm. The visual assessment of the alteration presence can correlate with the reflectance increase and the curved shape of the spectral profile, in 1.6-1.7μm and reflectance decrease in 2.1-2.3μm. On the contrary, lava flow spectral signature in 1.6-1.7μm and in 2.1-2.3μm is more “straight”. Furthermore, vegetation effect is also revealed in scoriae deposits.

The most characteristic changes in spectral curves were depicted in 1536, 1566 and 1669 lava flows. In the first, the maximum reflectance value in 2007 is 27%, 16% for 2009 and 25% for 2012.

In particular, in 0.4-0.9 μm spectral region (visible), the endmembers are different in the three datasets. There is a 10% reflectance increase in 2007 and an absorption in 0.7 μm probably due to sparse vegetation installed. In 2009 and 2012, we observe an absorption of ~3% in 0.78-0.9 μm. The 1566 lava flows extracted from the 2007 reveal a reflectance increase in 0.7 μm and an absorption in 2012 image, on the same spectral region. The same absorption is observed in the 2009 corresponding spectrum, with lower reflectance enlargement.

The spectral response of the 1669 lava flow endmember extracted from 2007 and 2012 presents more similarities in the spectral pattern, in comparison with the 2009 endmember. Although, 2007 and 2012 endmembers reveal a slight variation in 0.7 μm, because 2007 reflectance decreases by ~1% and ~3-4% in 2012. Continuing, if we examine the mean reflectances of 1610, 1614-24 and 1646-47, we will see that their reflectance response is differentiated a lot between the three datasets. For example, in 2007 and 2009 the reflectance response of these endmembers is similar, while it changes in 2012 endmembers. 2012 endmember of 1646-47 lava flow reveal higher reflectance (i.e. in NIR and SWIR region) percentages. Finally, investigating the spectral responses of scoriae endmembers, we could say that they behave with the same way as the above lava flows, because the difference in reflectance response between the scoria 1610 and 1646-47 becoming higher from 2007 to 2012.

- **Ellitico Formation**

Figure 6.1.10 presents the average reflectance spectra derived from 2007, 2009 and 2012 Hyperion datasets, from each lava flow deposit, for the oldest volcanic formation in Etna, named Ellitico. Scoriae and pyroclastic volcanic products weren’t found in this category. Each lava deposit is characterized by a different acronym, according to their spatial location in the volcano (see Chapter 5.1.3). In addition, the averaged spectra (including standard deviation) are also presented in Figures 6.1.37-42. Graphic representations for each endmember; presenting the spectral variation between 2007, 2009 and 2012 images were also applied, (Figures 6.1.52-53).

All endmembers were divided into two categories, based on their spectral pattern. The first category includes the EC24cs, EC24mn, EC24pn, EP22el, EP22fu and EP22ta endmembers (see Table 5.1.3.1), which had the highest reflectance values (e.g. 2007-37%, 2009-27% and 2012-35%), due to vegetation (0.7 μm absorption) and alteration (0.4-0.9μm absorption and 1.5-1.75 μm reflectance increase) presence. Although, the EP22fu reflectance responses differently in 2007, 2009 and 2012 images. In particular, the 2007 and 2012 EP22fu endmembers reveal an absorption in 0.7μm, while this absorption is lesser in the 2009 endmember.

The second includes the EP22pa, EP22gc, EPD21a,b, EPG25a,b, which are characterized by lower reflectance values and affected by vegetation. An exception of these endmembers is the ESC20 volcanic product. This endmember isn’t affect by alteration and vegetation and its spectral pattern is very similar with the lava flow spectral curve of the Sgavetti et al (2006) field measurements. Also, this spectral pattern doesn’t change in none of the three datasets. Finally, investigating the reflectance increase, which is located in 1.5-1.75μm, in the endmembers of the second category, we see that it become minor. However, this alignment is revealed in different order in the three datasets. For example, in 2007 image the curvature of the spectral profile is aligned by the following order: EP22pa> EP22gc> EPG25a,b> EPD21a,b> ESC20.. In 2009 image the order is: ESC20 >EPG25b > EP22gc> EPG25a< EPD21a,b <EP22pa and in 2012 image is: EP22gc> EP22pa> >EPG25b > EPG25a< EPD21a,b < ESC20.

## Averaged Surface Reflectance

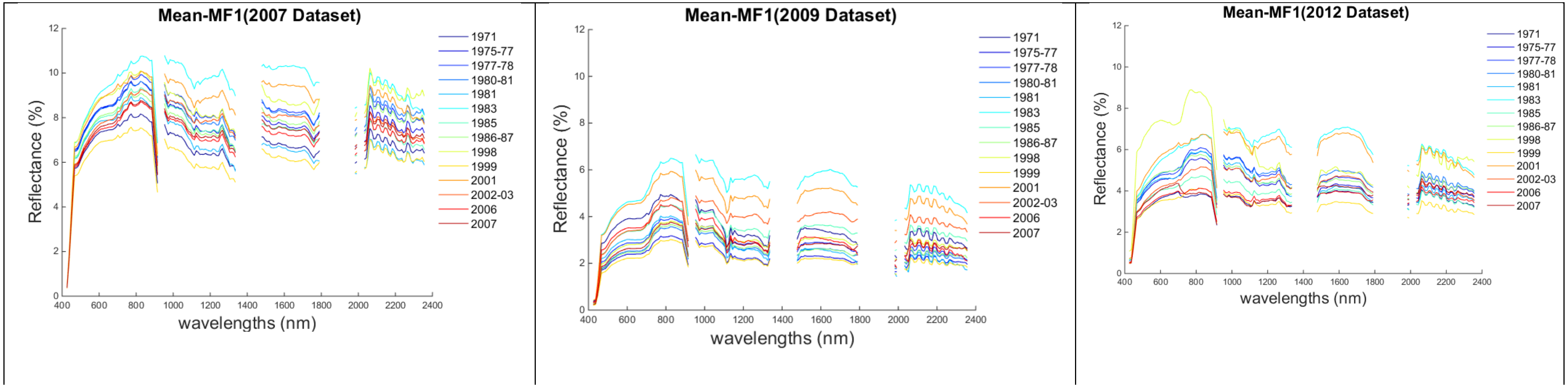


*Figure 6.1.4: Mean reflectance values of each lava flow deposit endmember of the MF1 formation (1971-5/2007), extracted from 2007 (left), 2009 (middle) and 2012 (right) datasets*

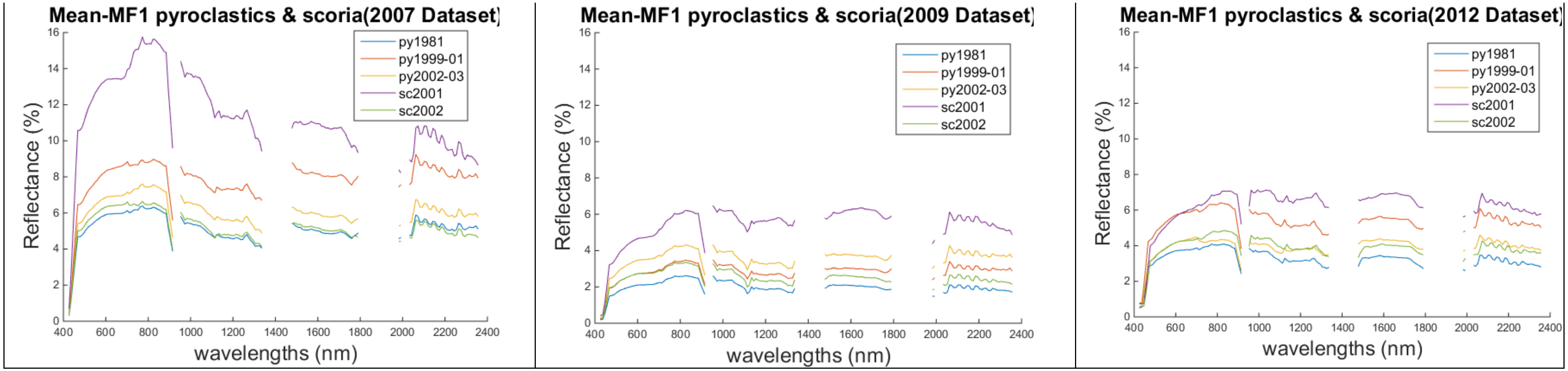


*Figure 6.1.5: Mean reflectance spectra of each pyroclastic and scoriae deposit endmember of the MF1 formation (1971-5/2007), extracted from 2007 (left), 2009 (middle) and 2012 (right) datasets*

## MF2 Volcanic Formation (1669-1971) – Lava Flows

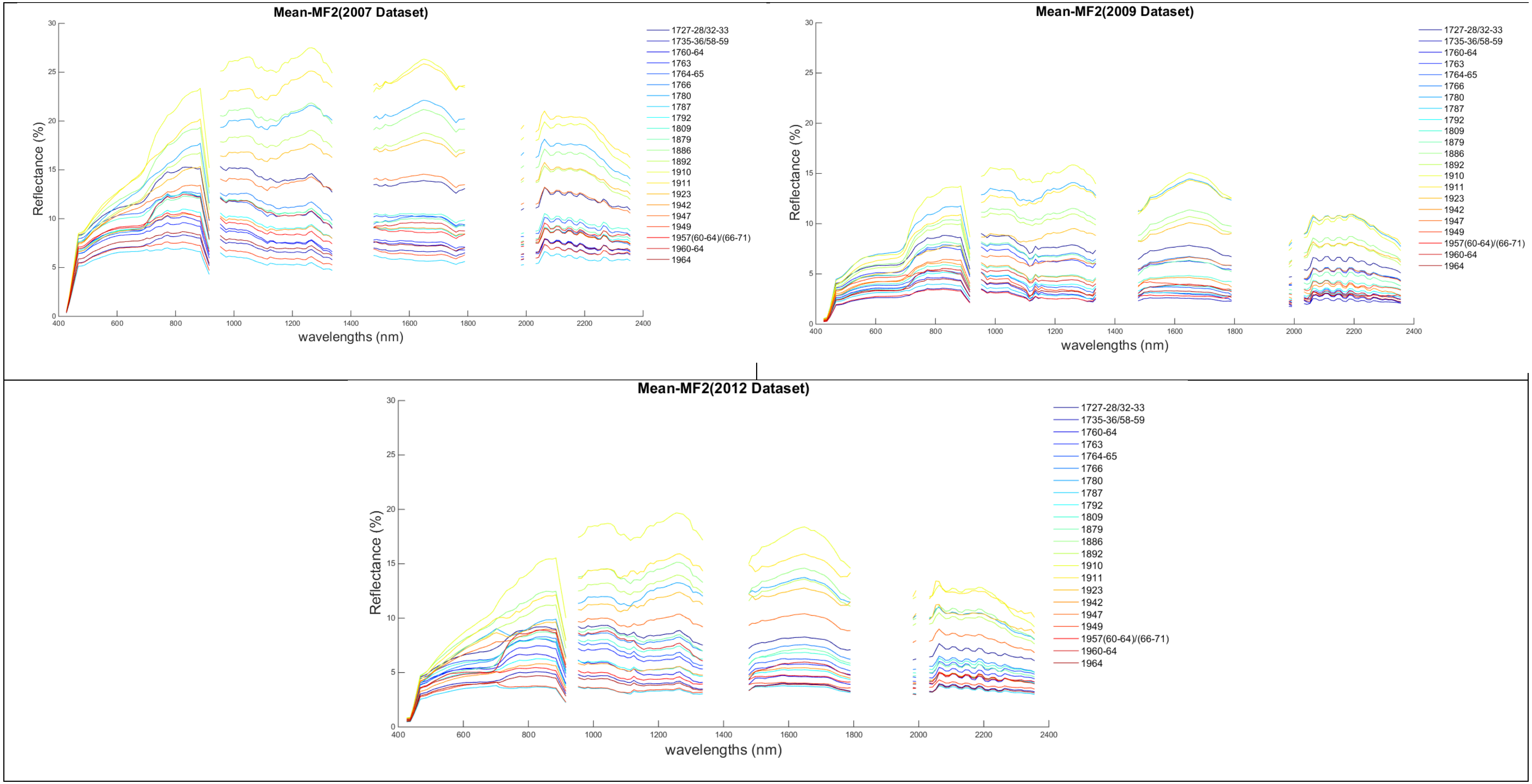


*Figure 6.1.6: Mean reflectance spectra of each lava flow deposit endmember of the MF2 Volcanic Formation (1669-1971) extracted from 2007 (left), 2009 (right) and 2012 (bottom) datasets.*

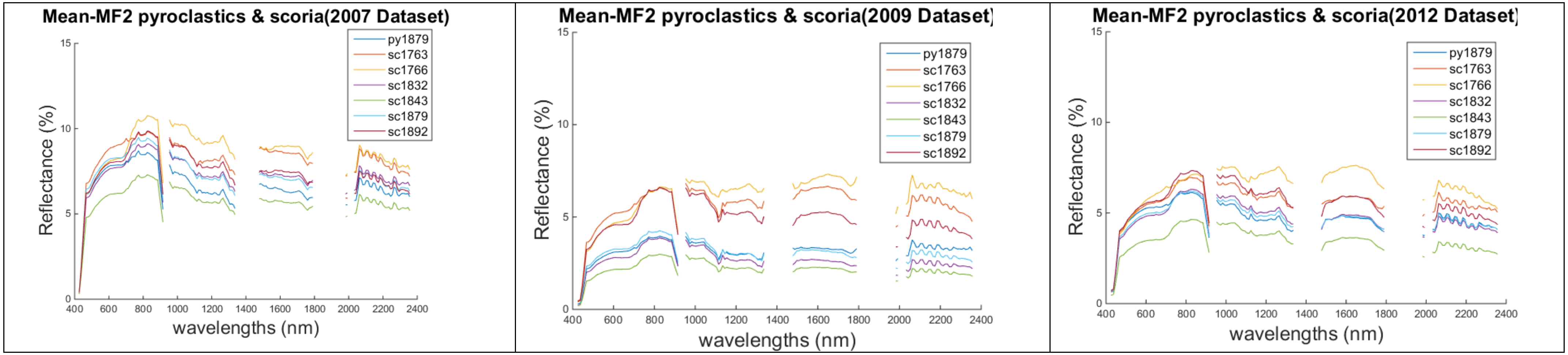


*Figure 6.1.7: Mean reflectance values of each pyroclastic and scoriae deposit endmember categorized in MF2 Volcanic Formation (1669-1971) extracted from 2007 (left), 2009 (middle) and 2012 (right) datasets.*

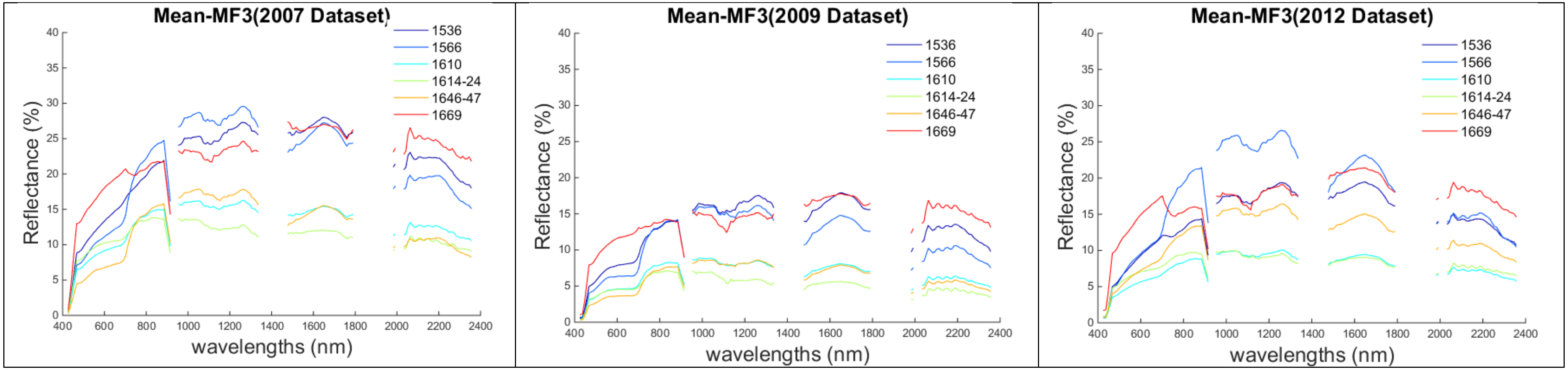


*Figure 6.1.8: Mean reflectance specta of each lava flow deposit endmember of the MF3 Volcanic Formation (122BC-1669AD) extracted from 2007 (left), 2009 (middle) and 2012 (right) datasets.*

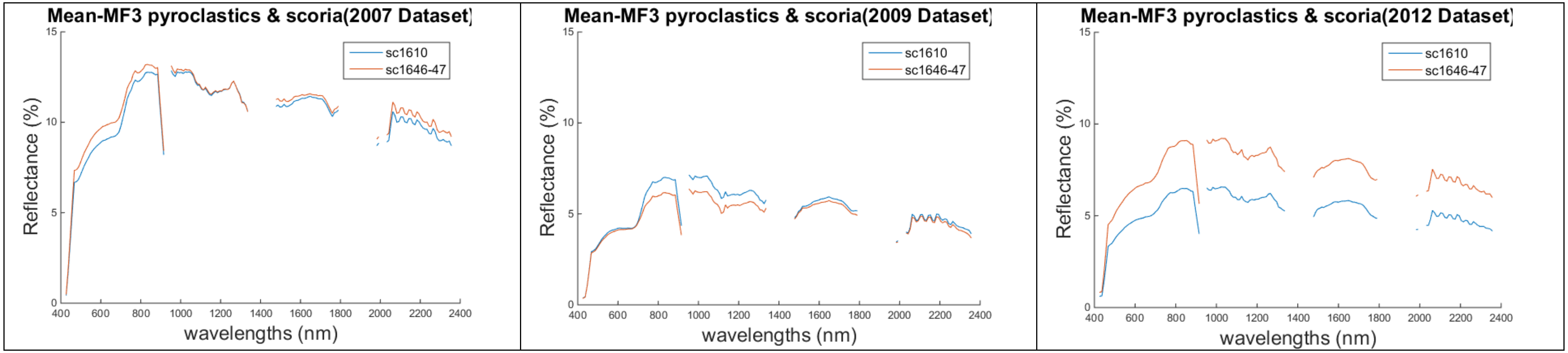


*Figure 6.1.9: Mean reflectance values of each pyroclastic and scoriae deposit endmember of the MF3 Volcanic Formation (122BC-1669AC) extracted from 2007 (left), 2009 (middle) and 2012 (right) datasets.*

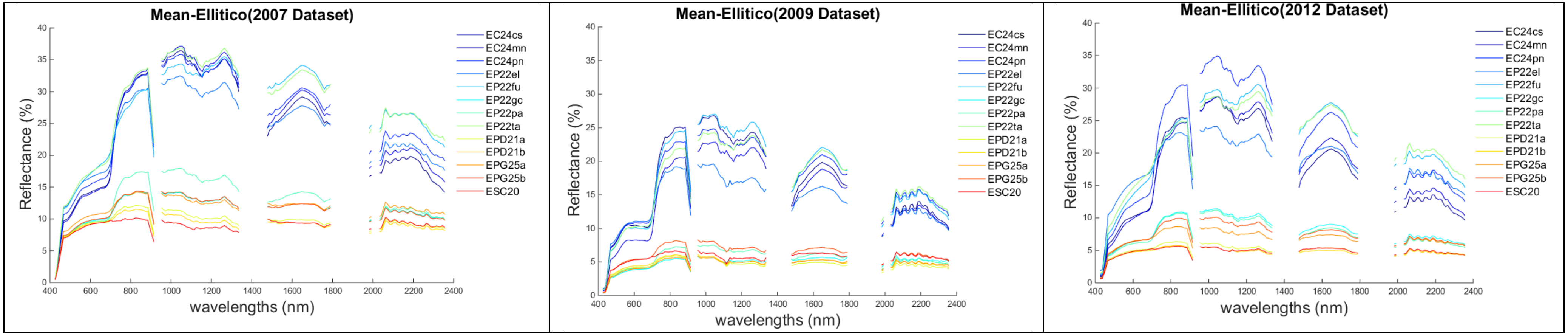


*Figure 6.1.10: Mean reflectance spectra of each lava flow deposit endmember of the Ellitico Volcanic Formation (Before 122BC) extracted from 2007 (left), 2009 (middle) and 2012 (right) datasets.*

## Mean spectrum and spectral variation of lava flow endmembers

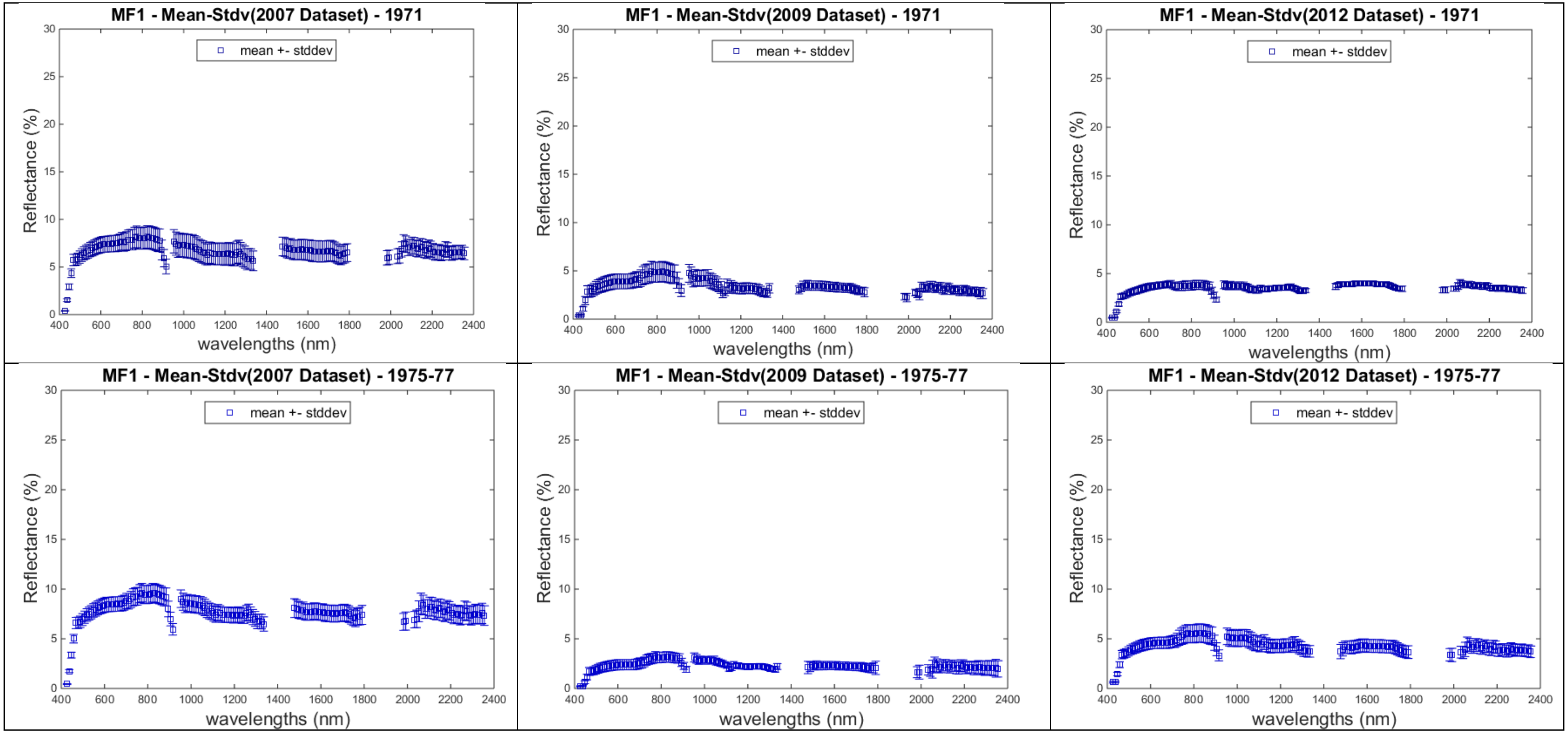


*Figure 6.1.10: Mean spectra and spectral variations of 1971 and 1975 lava flow endmembers of the MF1 formation (1971-5/2007) extracted from 2007 (left), 2009 (middle) and 2012 (right) datasets*

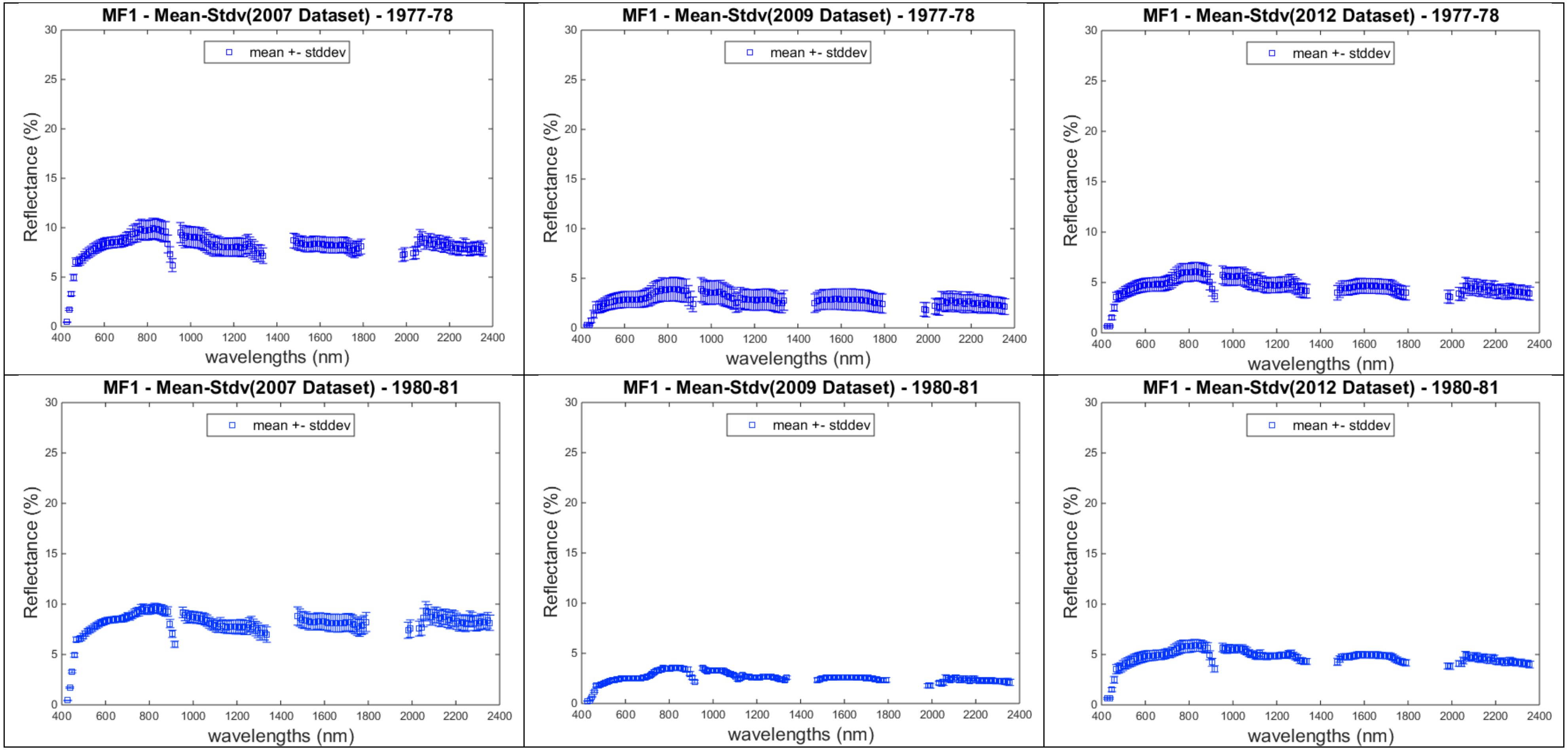


*Figure 6.1.10: Mean spectra and spectral variations of 1977-78 and 1980-81 lava flow endmembers of the MF1 formation (1971-5/2007) extracted from 2007 (left), 2009 (middle) and 2012 (right) datasets*

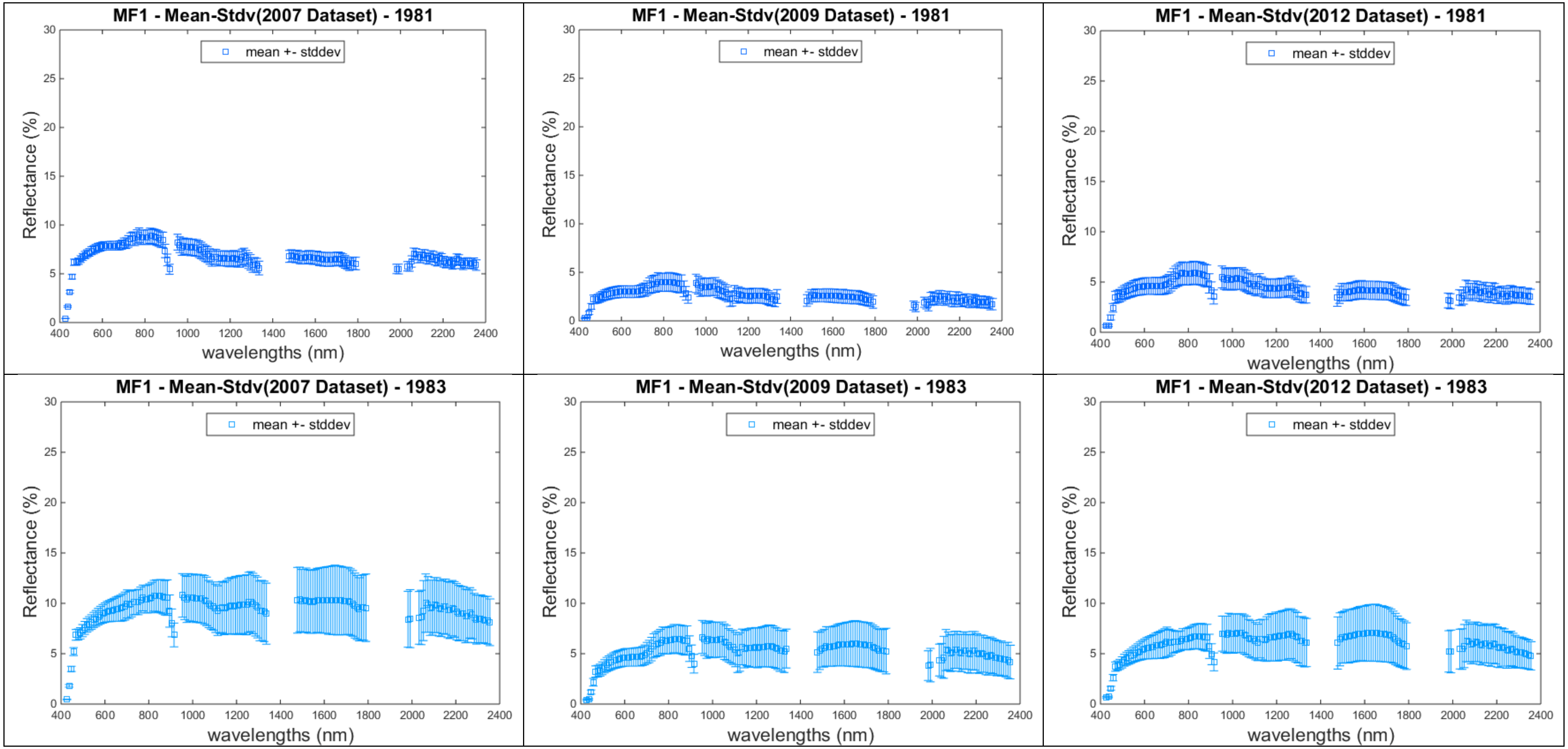


*Figure 6.1.11: Mean spectra and spectral variations of the 1981 and 1983 lava flow endmembers of the MF1 formation (1971-5/2007) extracted from 2007 (left), 2009 (middle) and 2012 (right) datasets*

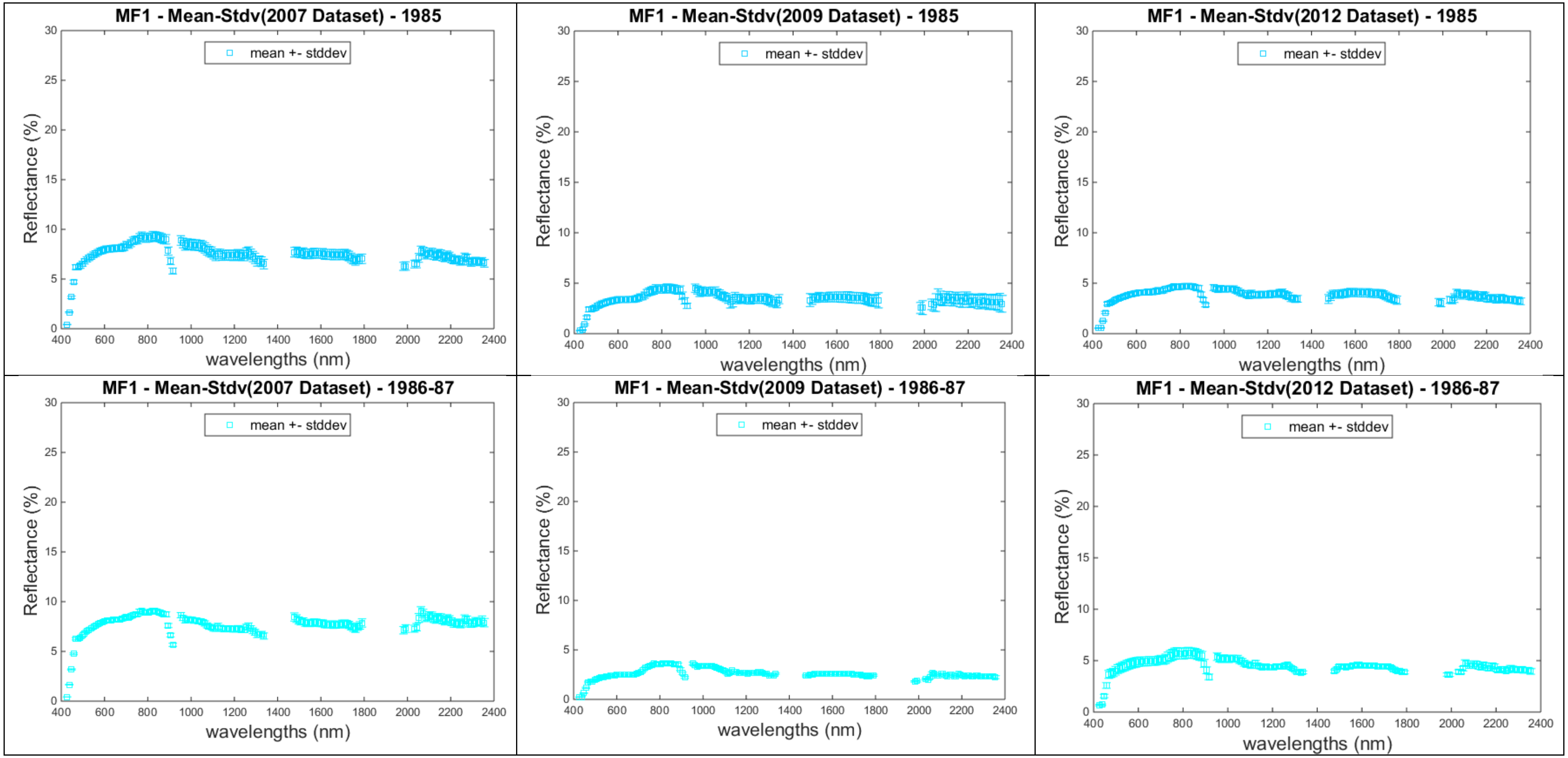


***Figure 6.1.12: Mean spectra and spectral variations of the 1985 and 1986-87 lava flow endmembers of the MF1 formation (1971-5/2007) extracted from 2007 (left), 2009 (middle) and 2012 (right) datasets***

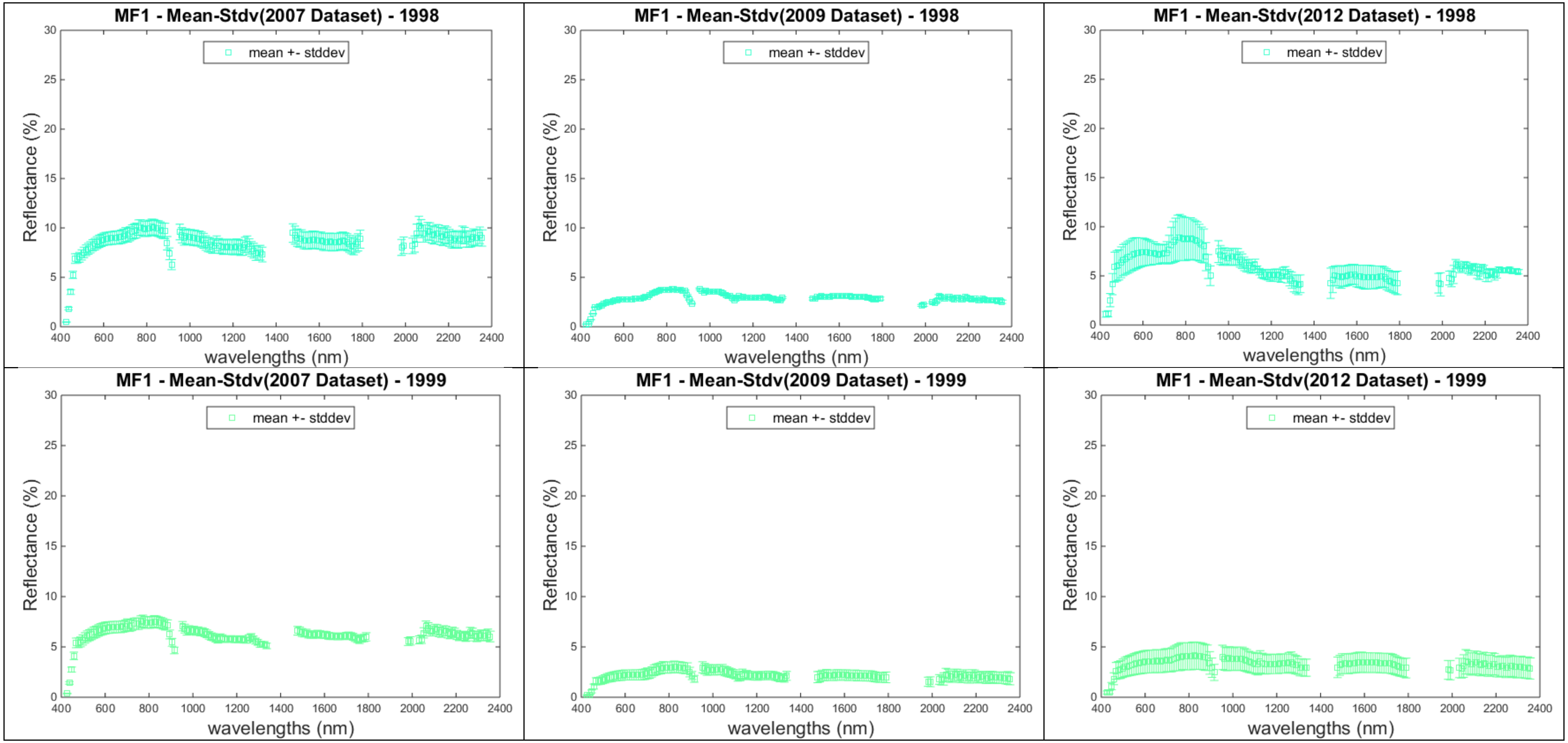


***Figure 6.1.13: Mean spectra and spectral variations of the 1998 & 1999 lava flow endmembers of the MF1 formation (1971-5/2007) extracted from 2007 (left), 2009 (middle) and 2012 (right) datasets***

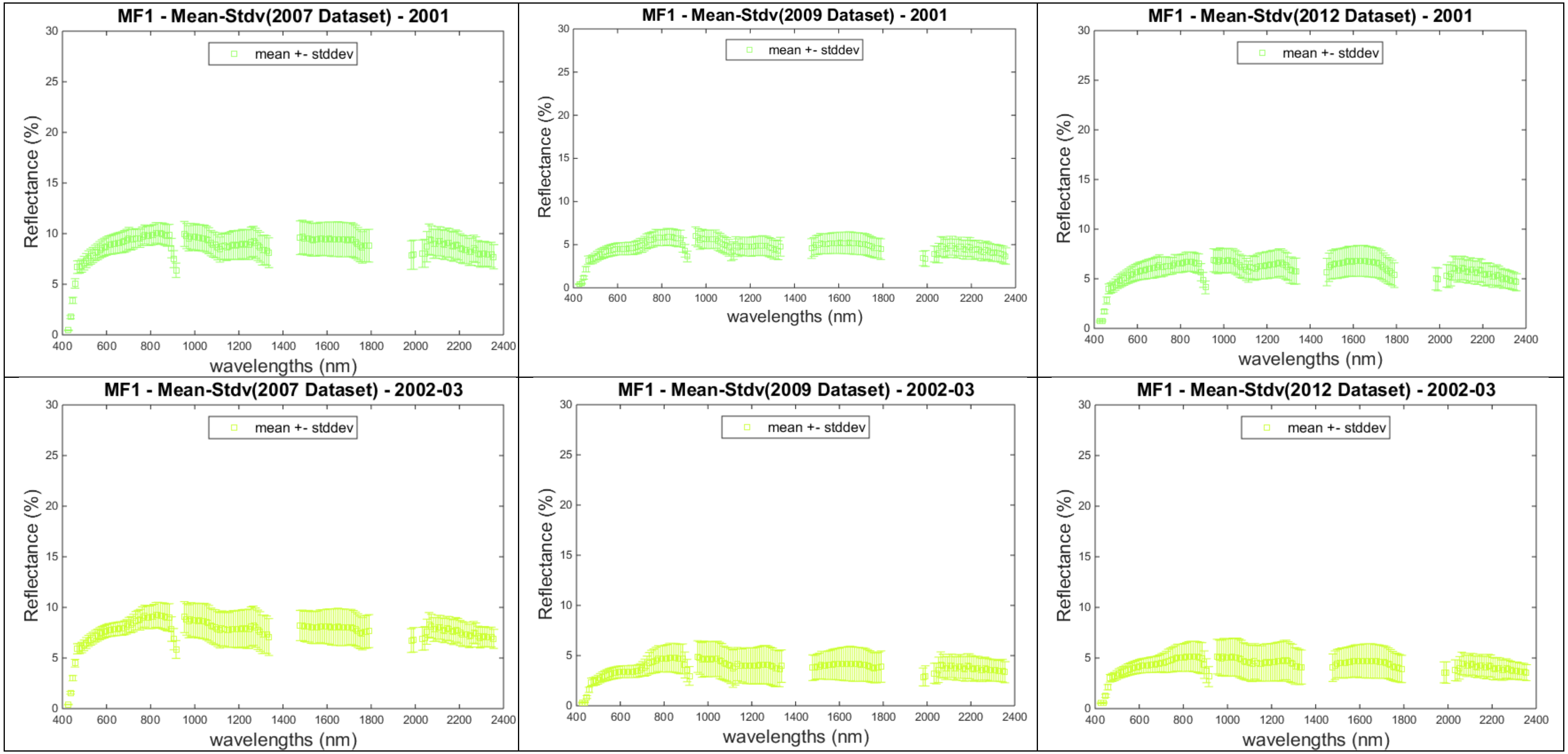


*Figure 6.1.14: Mean spectra and spectral variations of the 2001 and 2002-03 lava flow endmembers of the MF1 formation (1971-5/2007) extracted from 2007 (left), 2009 (middle) and 2012 (right) datasets*

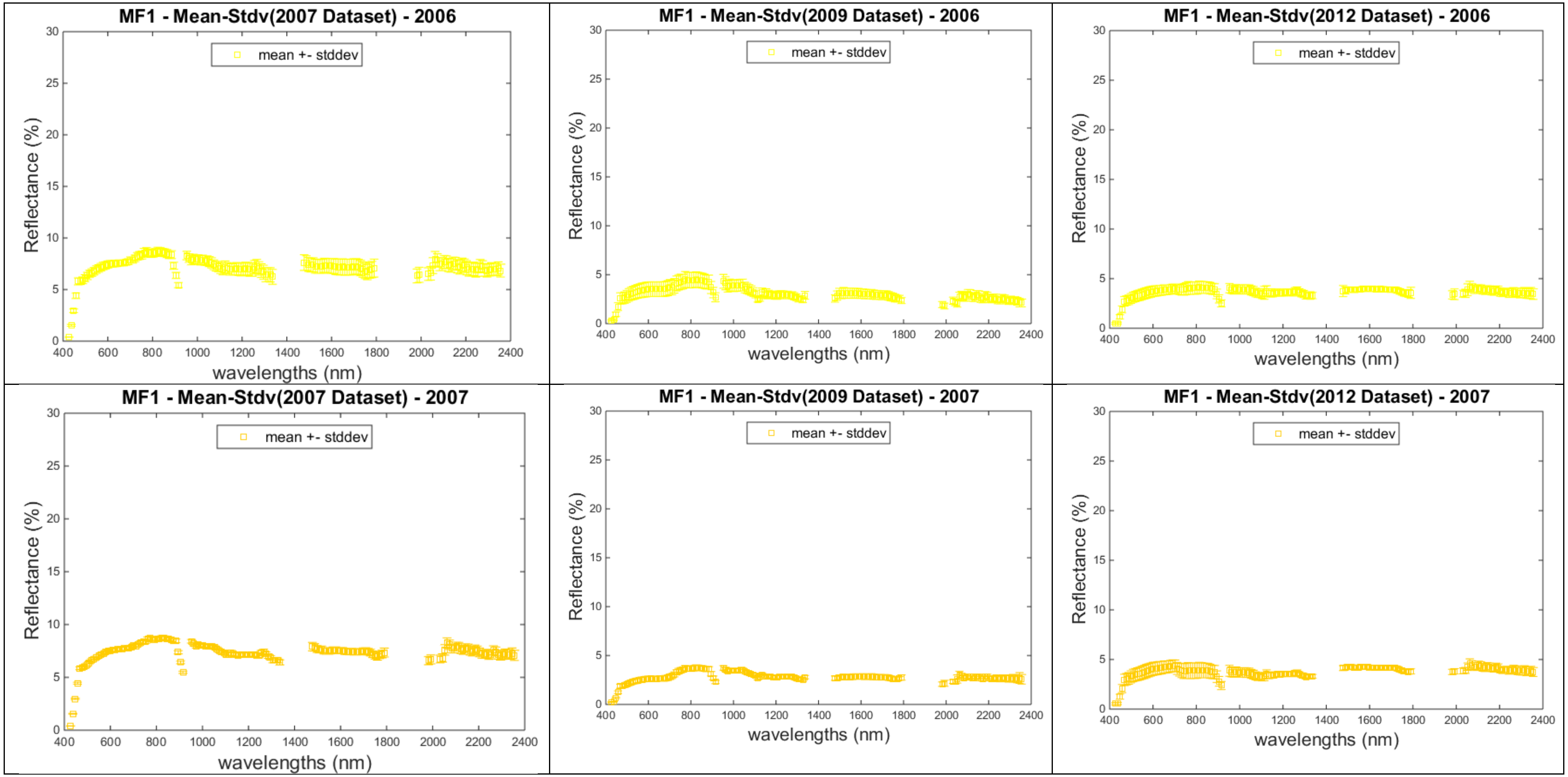


***Figure 6.1.15: Mean spectra and spectral variations of the 2006 and 2007 lava flow endmembers of the MF1 formation (1971-5/2007) extracted from 2007 (left), 2009 (middle) and 2012 (right) datasets***

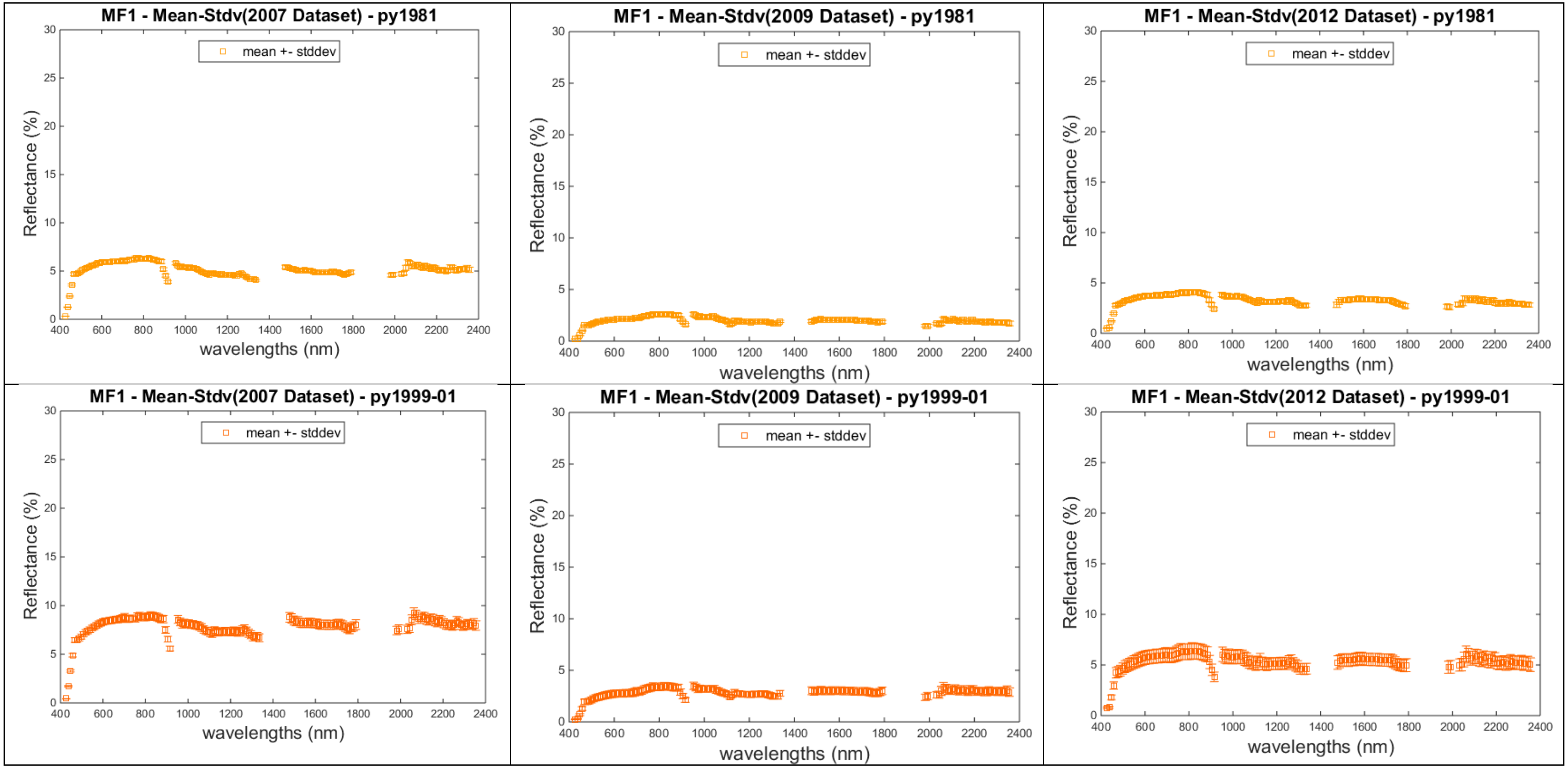


***Figure 6.1.16: Mean spectra and spectral variations of the 1981 & 1999-01 pyroclastic endmembers of the MF1 formation (1971-5/2007) extracted from 2007 (left), 2009 (middle) and 2012 (right) datasets***

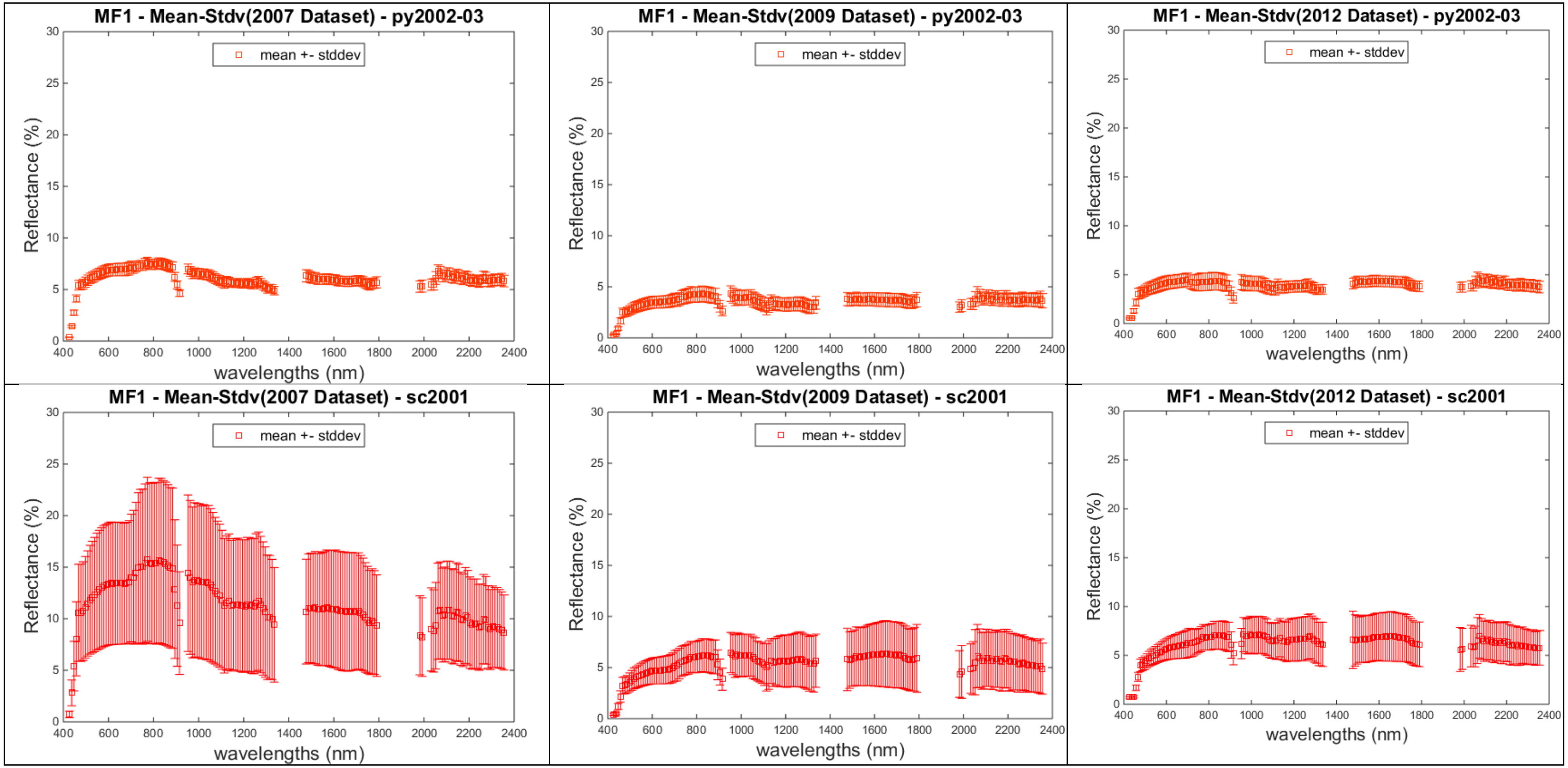


*Figure 6.1.17: Mean spectra and spectral variations of the 2002-03 pyroclastic & 2001 scoriae endmembers of the MF1 formation (1971-5/2007) extracted from 2007 (left), 2009 (middle) and 2012 (right) datasets*

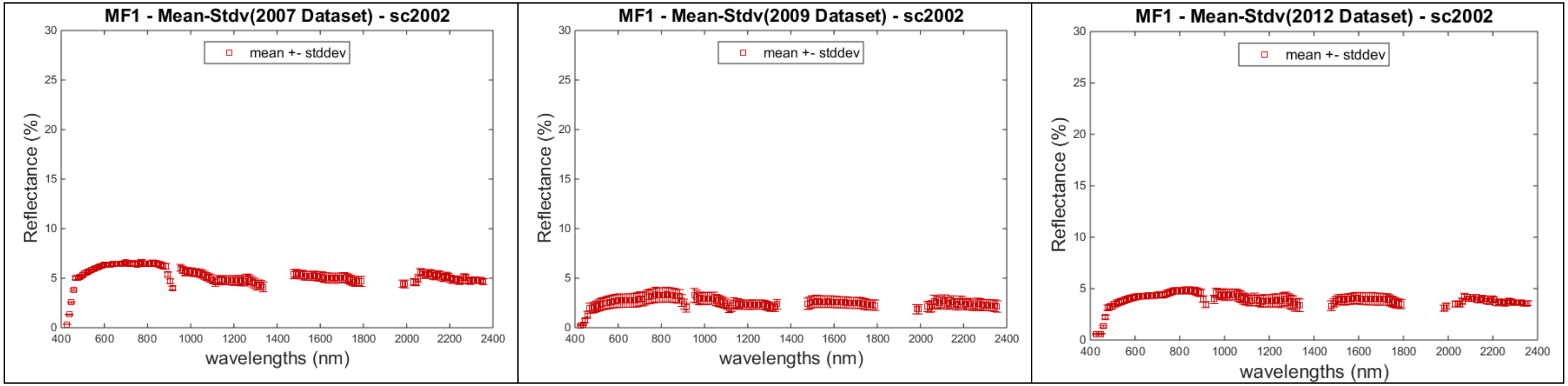


*Figure 6.1.17: spectra and spectral variations of the 2002 scoriae endmember of the MF1 formation (1971-5/2007) extracted from 2007 (left), 2009 (middle) and 2012 (right) datasets*

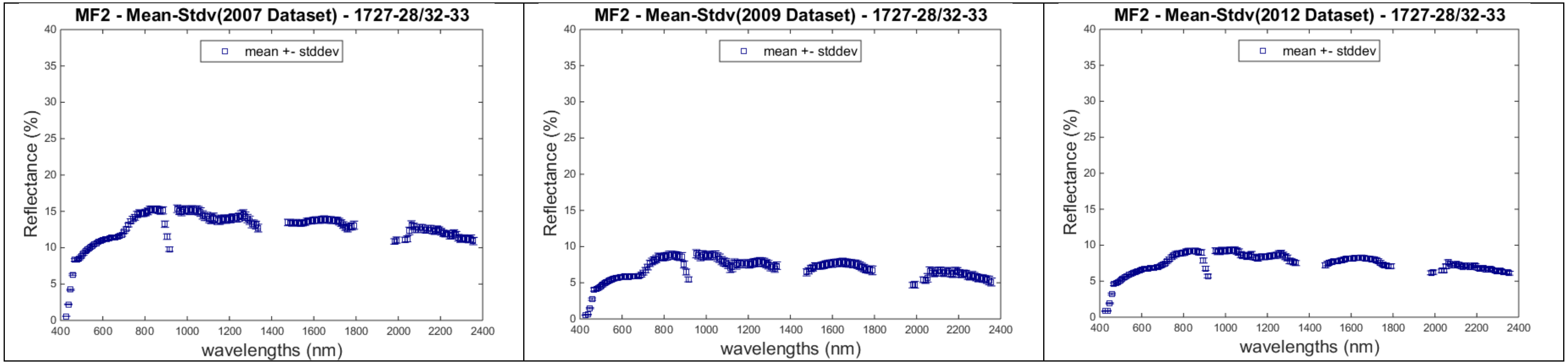


*Figure 6.1.18: Mean spectra and spectral variations of the 1727-28/32-33 lava flows endmembers of the MF2 formation (1669-1971) extracted from 2007 (left), 2009 (middle) and 2012 (right) datasets*

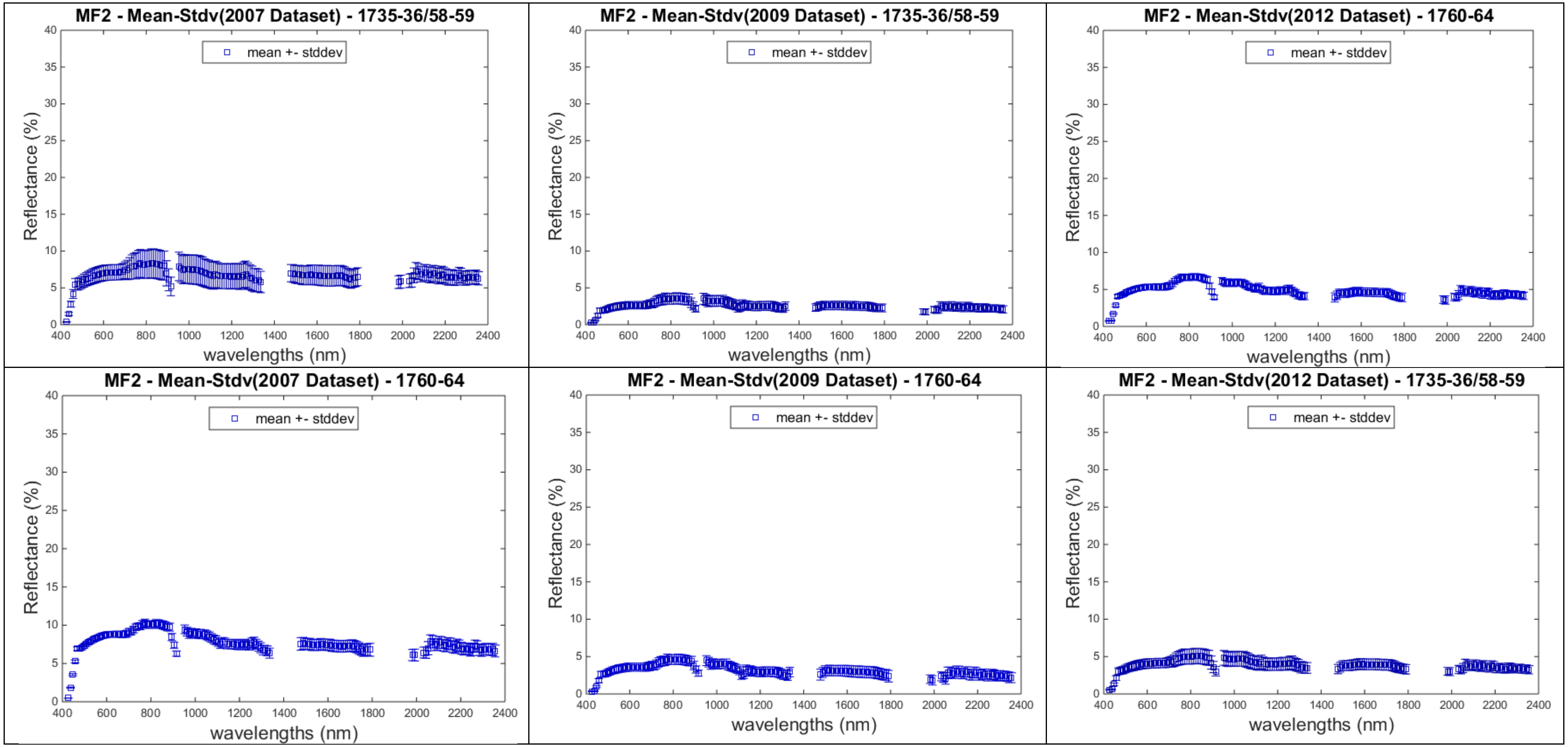


*Figure 6.1.19: Mean spectra and spectral variations of the 1735-36/58-59 & 1760-64 Lava flows endmembers of the MF2 formation (1669-1971) extracted from 2007 (left), 2009 (middle) and 2012 (right) datasets*

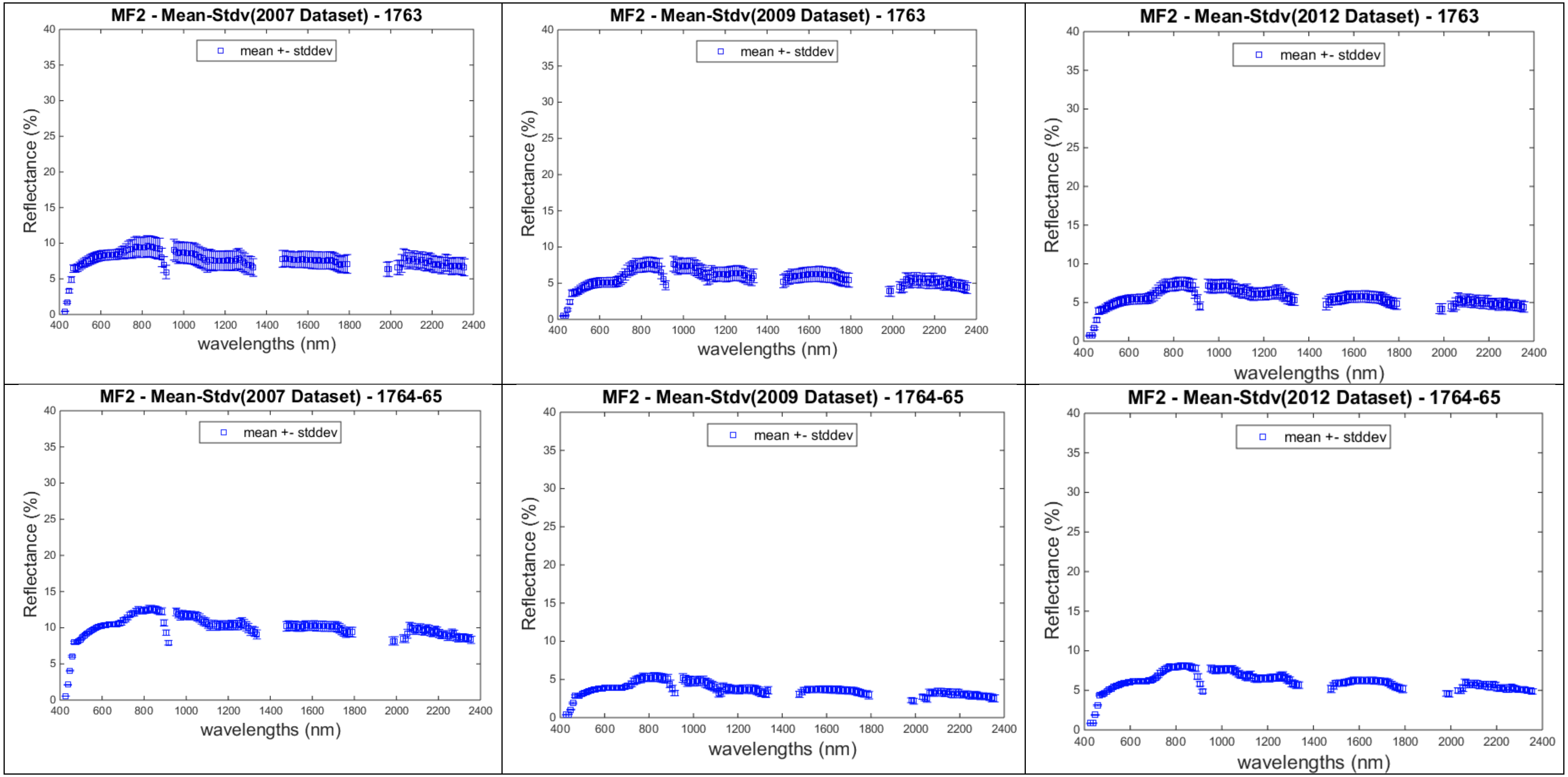


*Figure 6.1.20: Mean spectra and spectral variations of the 1763 & 1764-65 Lava flows endmembers of the MF2 formation (1669-1971) extracted from 2007 (left), 2009 (middle) and 2012 (right) datasets*

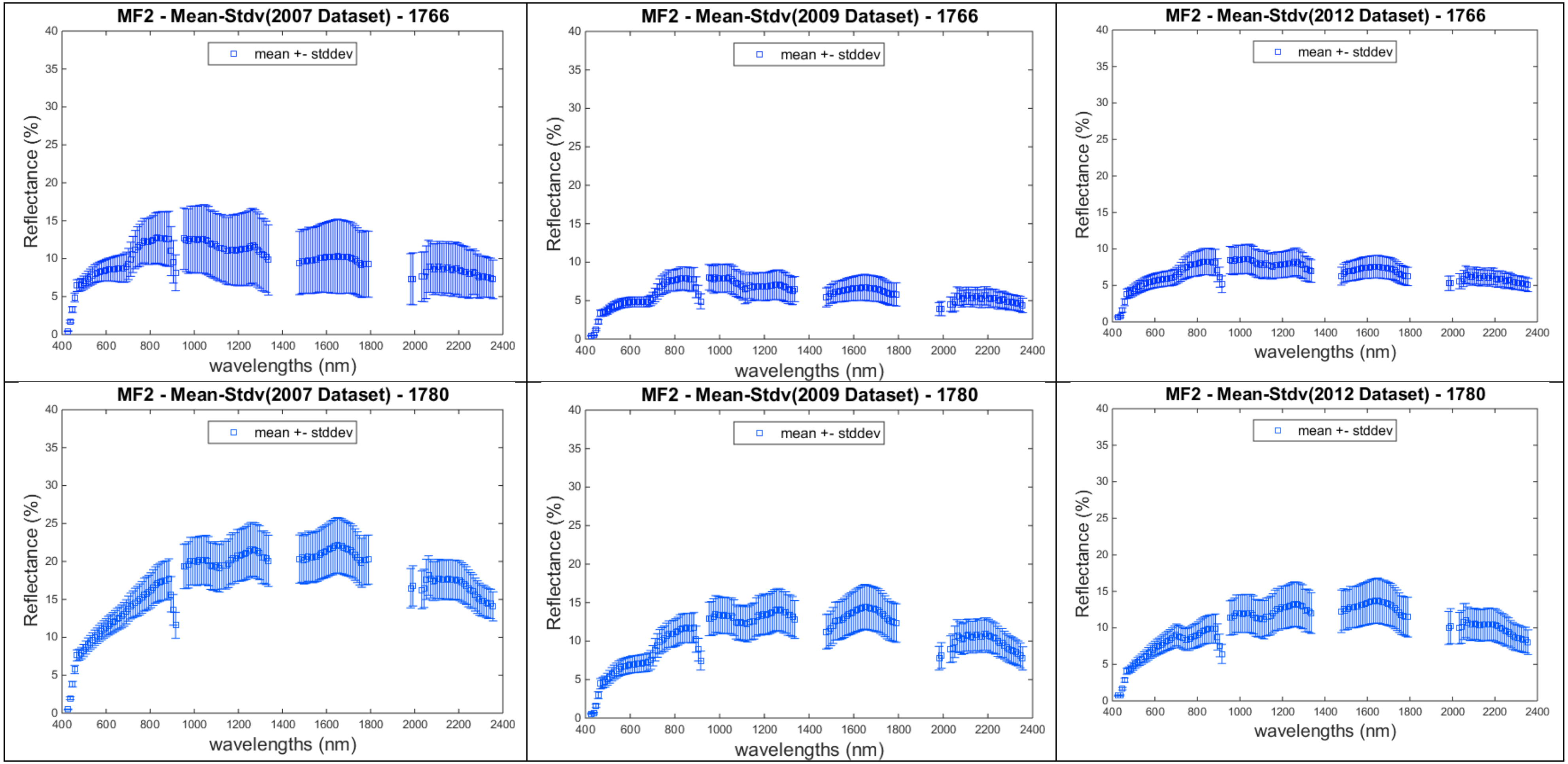


*Figure 6.1.21: Mean spectra and spectral variations of the 1766 & 1780 Lava flows endmembers of the MF2 formation (1669-1971) extracted from 2007 (left), 2009 (middle) and 2012 (right) datasets*

## MF2- Volcanic Formation - Lava flows 1787 & 1792

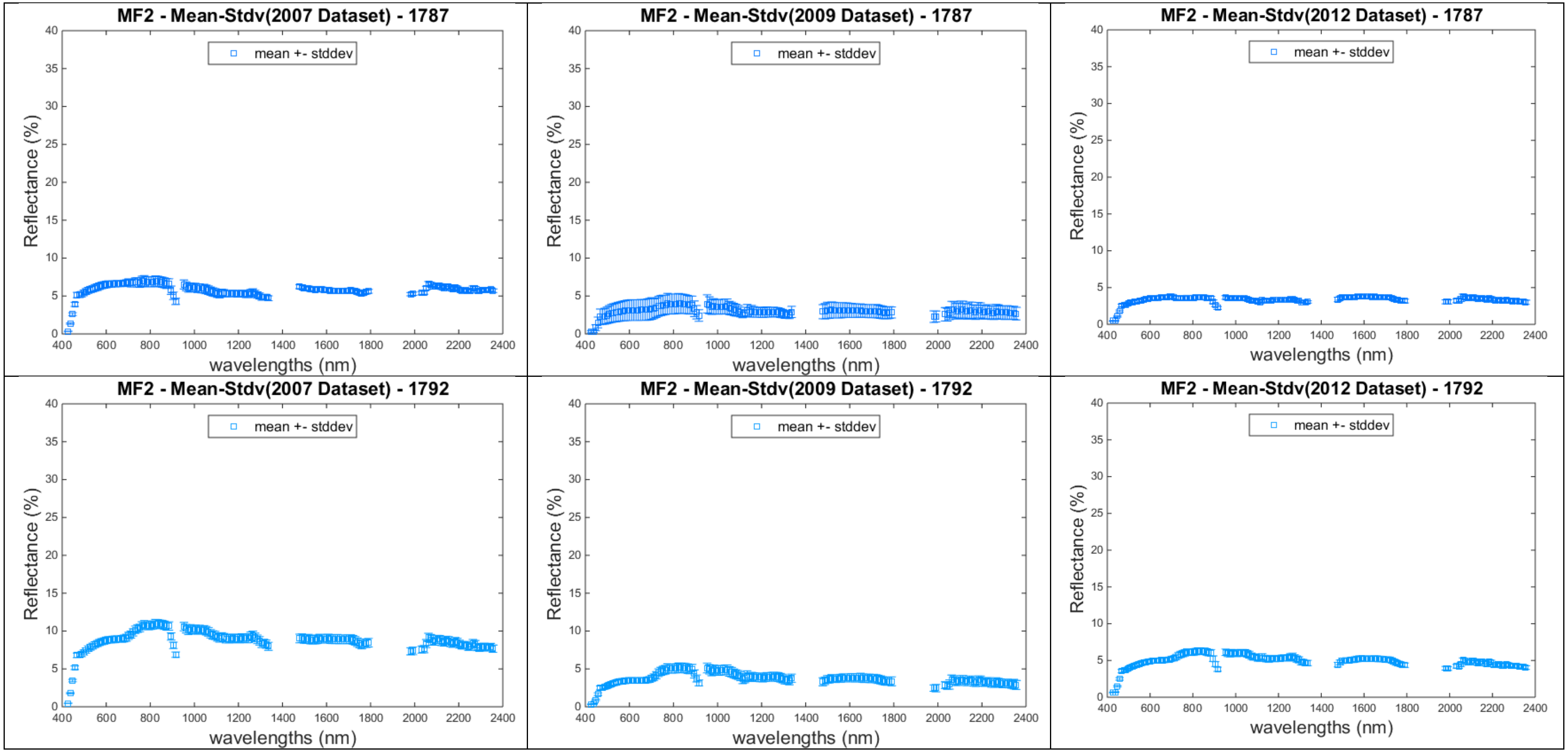


*Figure 6.1.22: Mean spectra and spectral variations of the 1787 & 1792 Lava flows endmembers of the MF2 formation (1669-1971) extracted from 2007 (left), 2009 (middle) and 2012 (right) datasets*

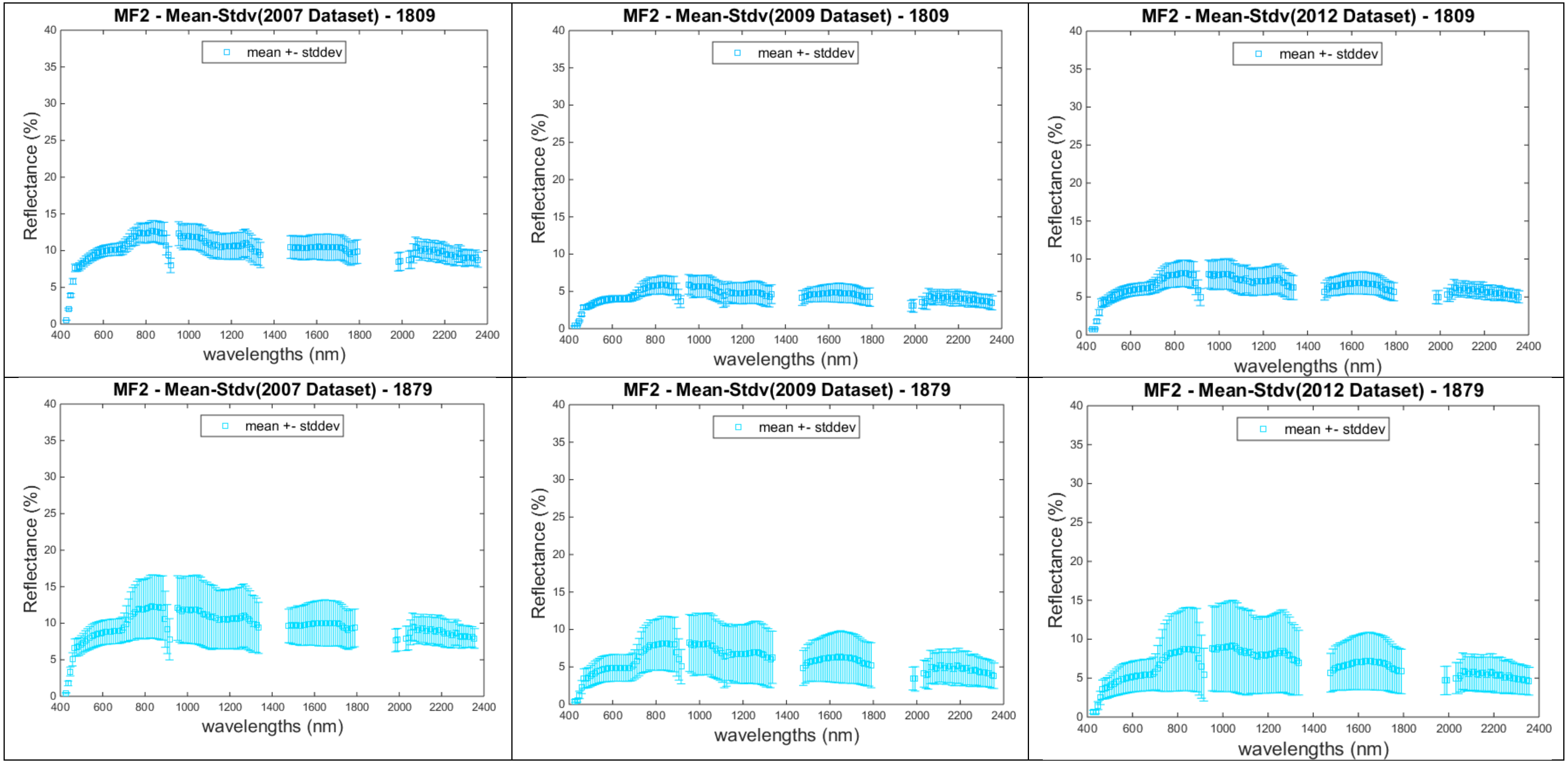


*Figure 6.1.23: Mean spectra and spectral variations of the 1809 & 1879 Lava flows endmembers of the MF2 formation (1669-1971) extracted from 2007 (left), 2009 (middle) and 2012 (right) datasets*

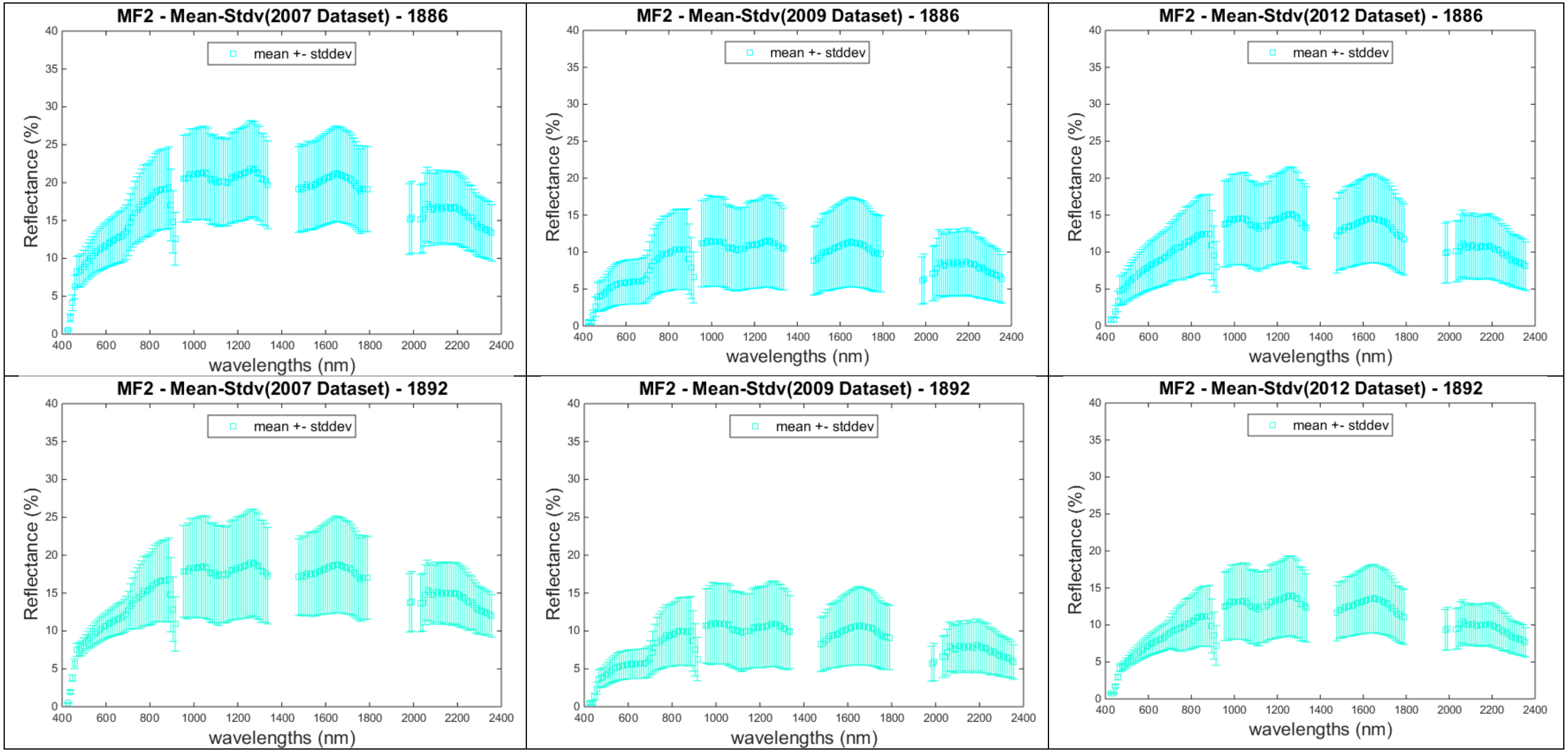


***Figure 6.1.24: Mean spectra and spectral variations of the 1886 & 1892 Lava flows endmembers of the MF2 formation (1669-1971) extracted from 2007 (left), 2009 (middle) and 2012 (right) datasets***

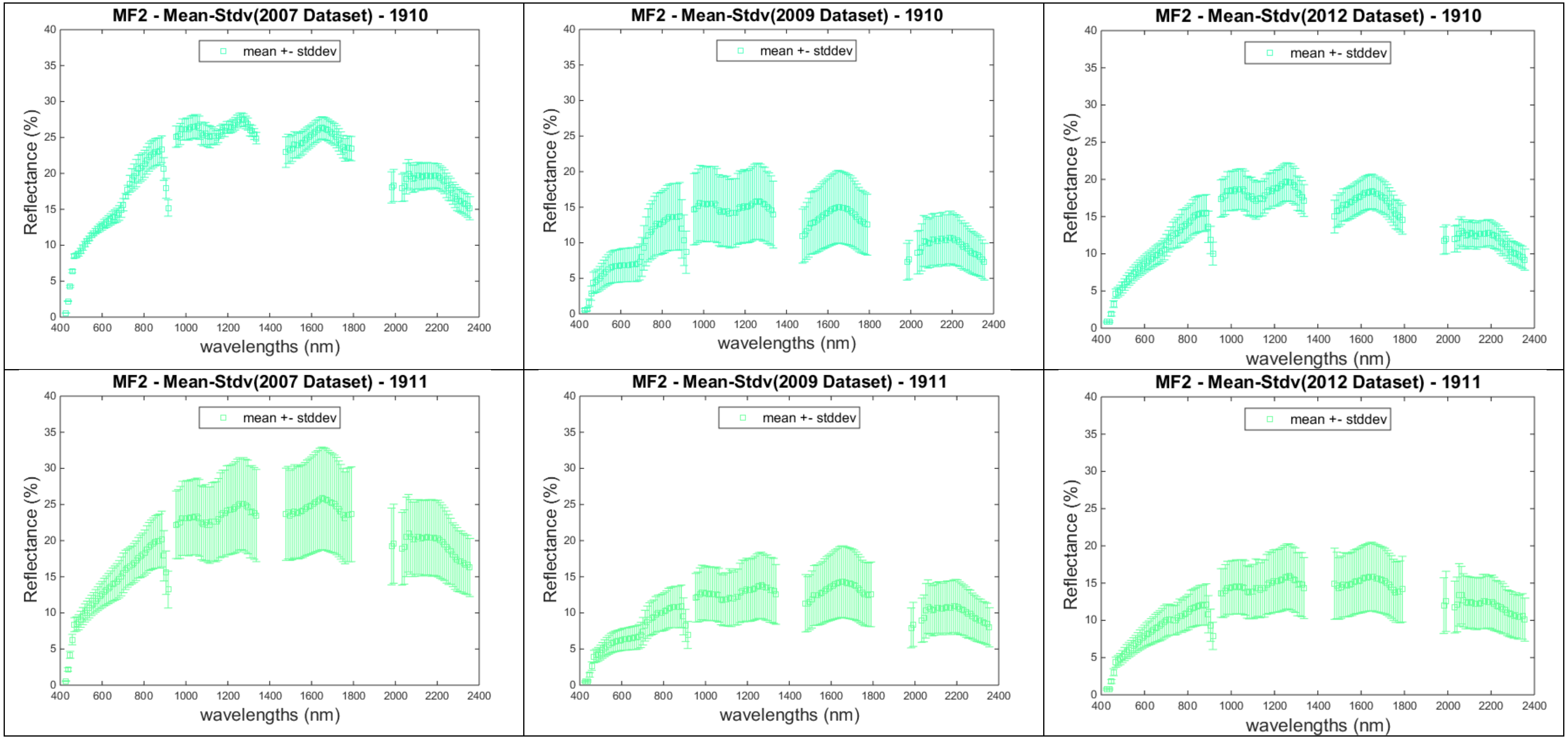


***Figure 6.1.25: Mean spectra and spectral variations of the 1910 & 1911 Lava flows endmembers of the MF2 formation (1669-1971) extracted from 2007 (left), 2009 (middle) and 2012 (right) datasets***

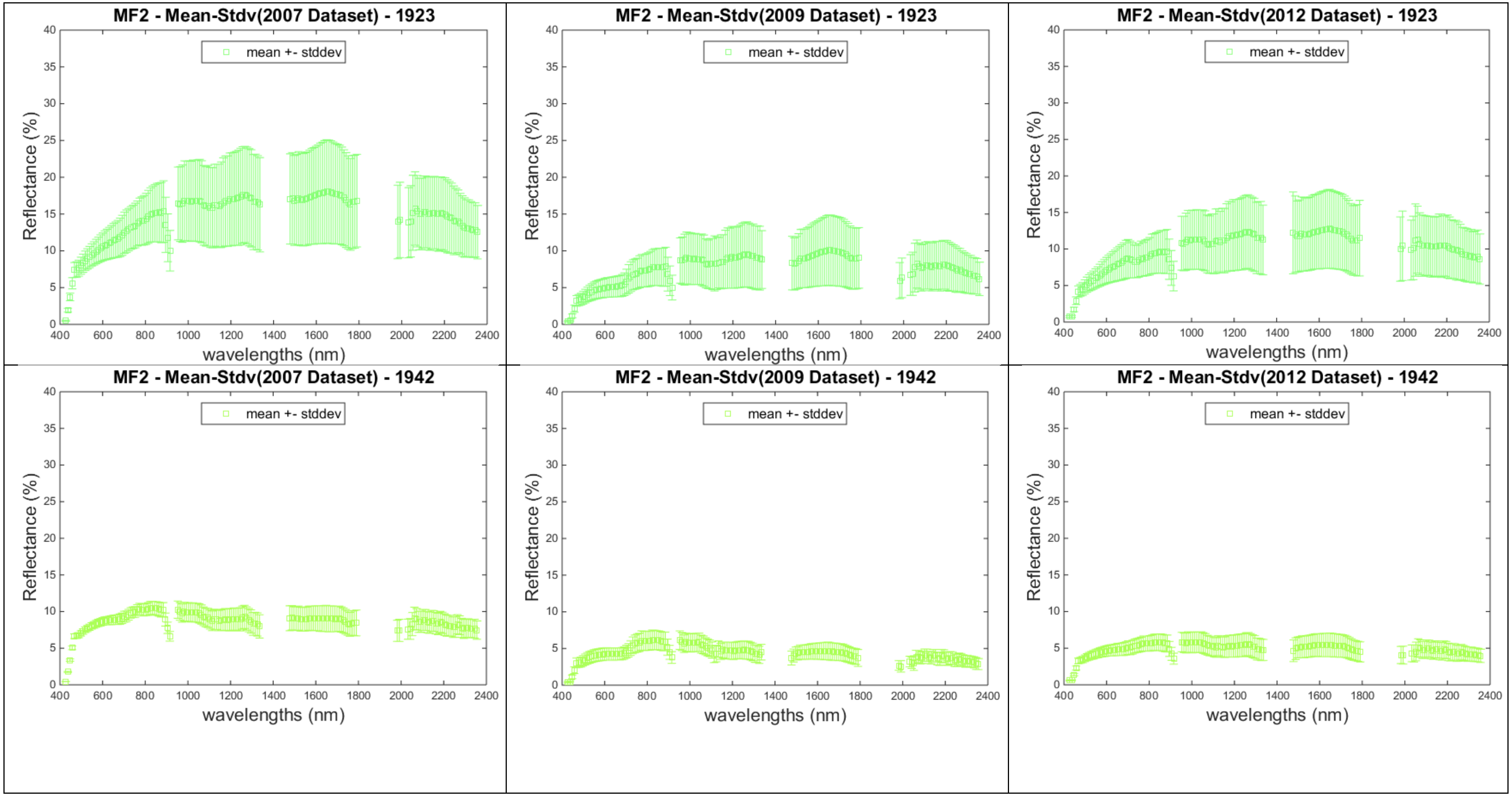


*Figure 6.1.26: Mean spectra and spectral variation of the Lava flows 1923 & 1942 endmembers categorized in MF2 formation (1669-1971) extracted from 2007 (left), 2009 (middle) and 2012 (right) datasets*

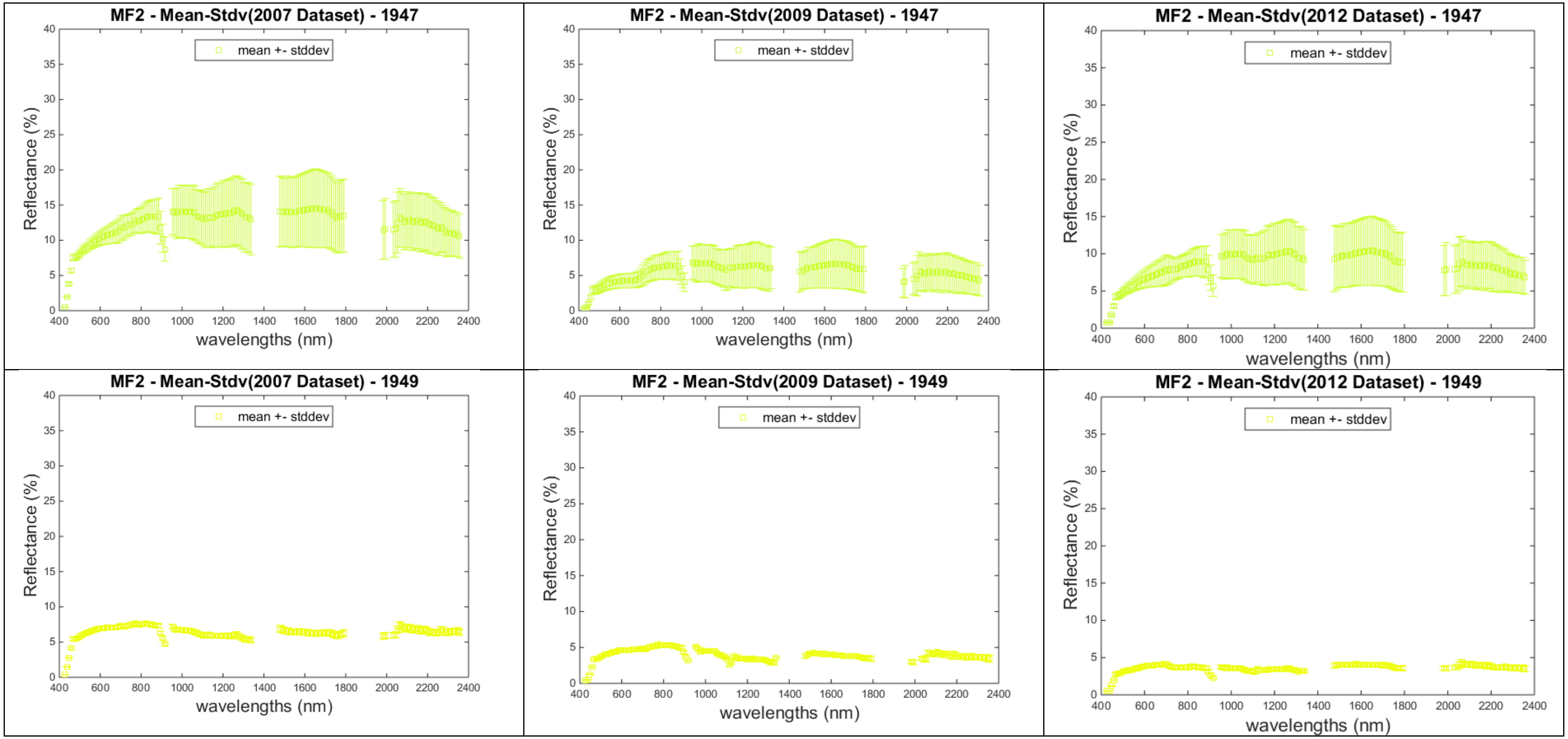


***Figure 6.1.27: Mean spectra and spectral variation of the Lava flows 1947 & 1949 endmembers categorized in MF2 formation (1669-1971) extracted from 2007 (left), 2009 (middle) and 2012 (right) datasets***

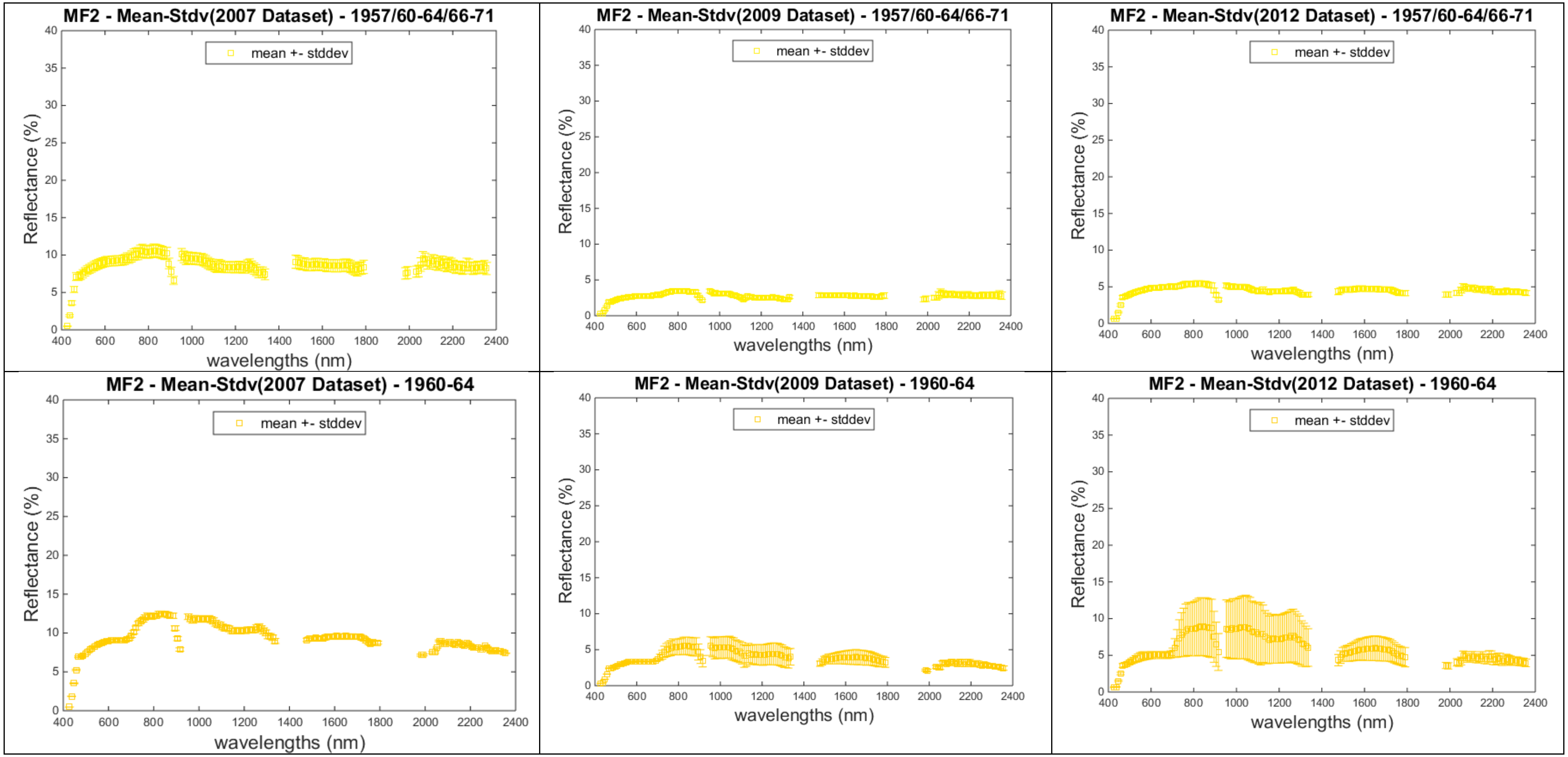


*Figure 6.1.28: Mean spectra and spectral variation of the Lava flows 1957/60-64/66-71 & 1960-64 endmembers categorized in MF2 formation (1669-1971) extracted from 2007 (left), 2009 (middle) and 2012 (right) datasets*

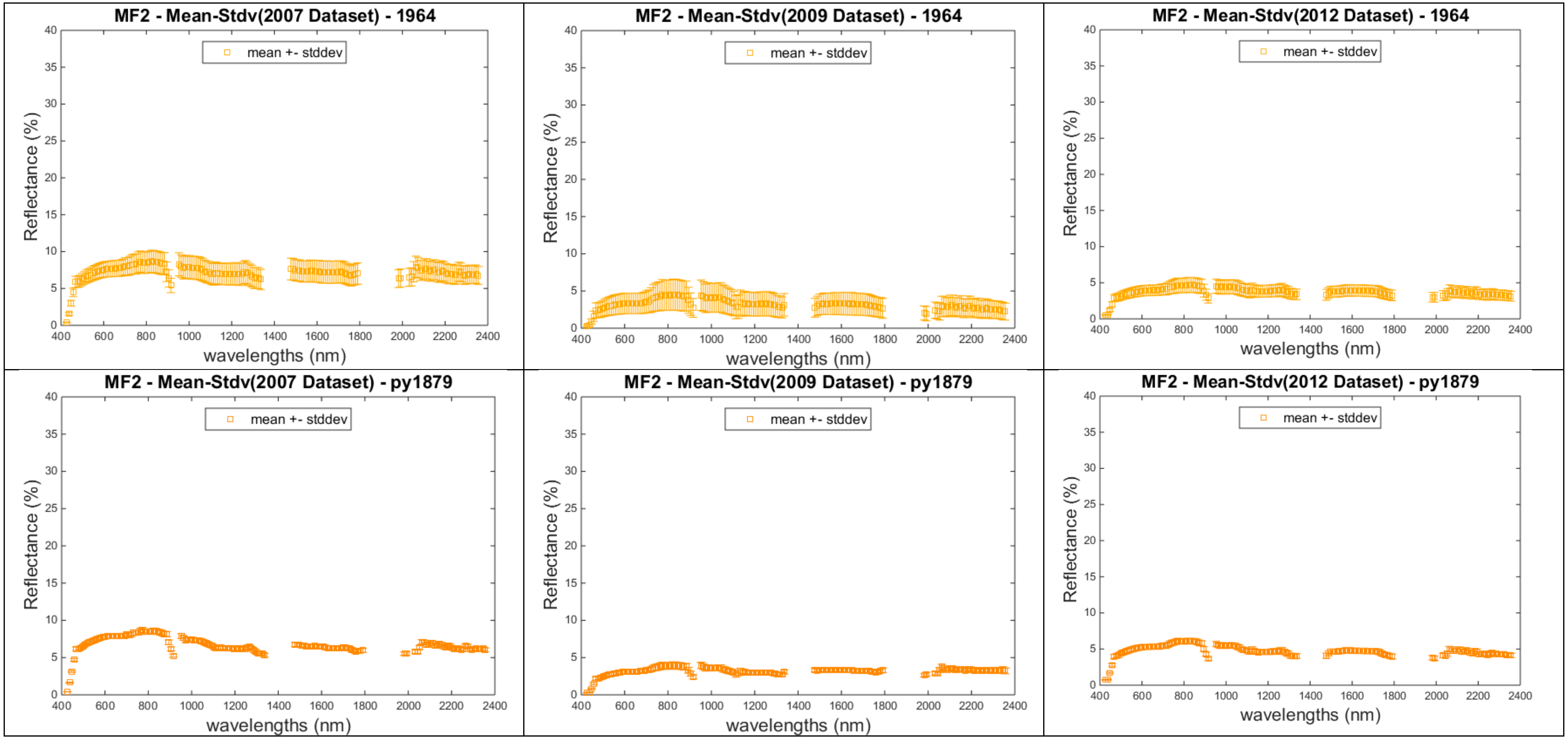


***Figure 6.1.29: Mean spectra and spectral variation of the Lava flows 1964 & Pyroclastic1879 endmembers categorized in MF2 formation (1669-1971) extracted from 2007 (left), 2009 (middle) and 2012 (right) datasets***

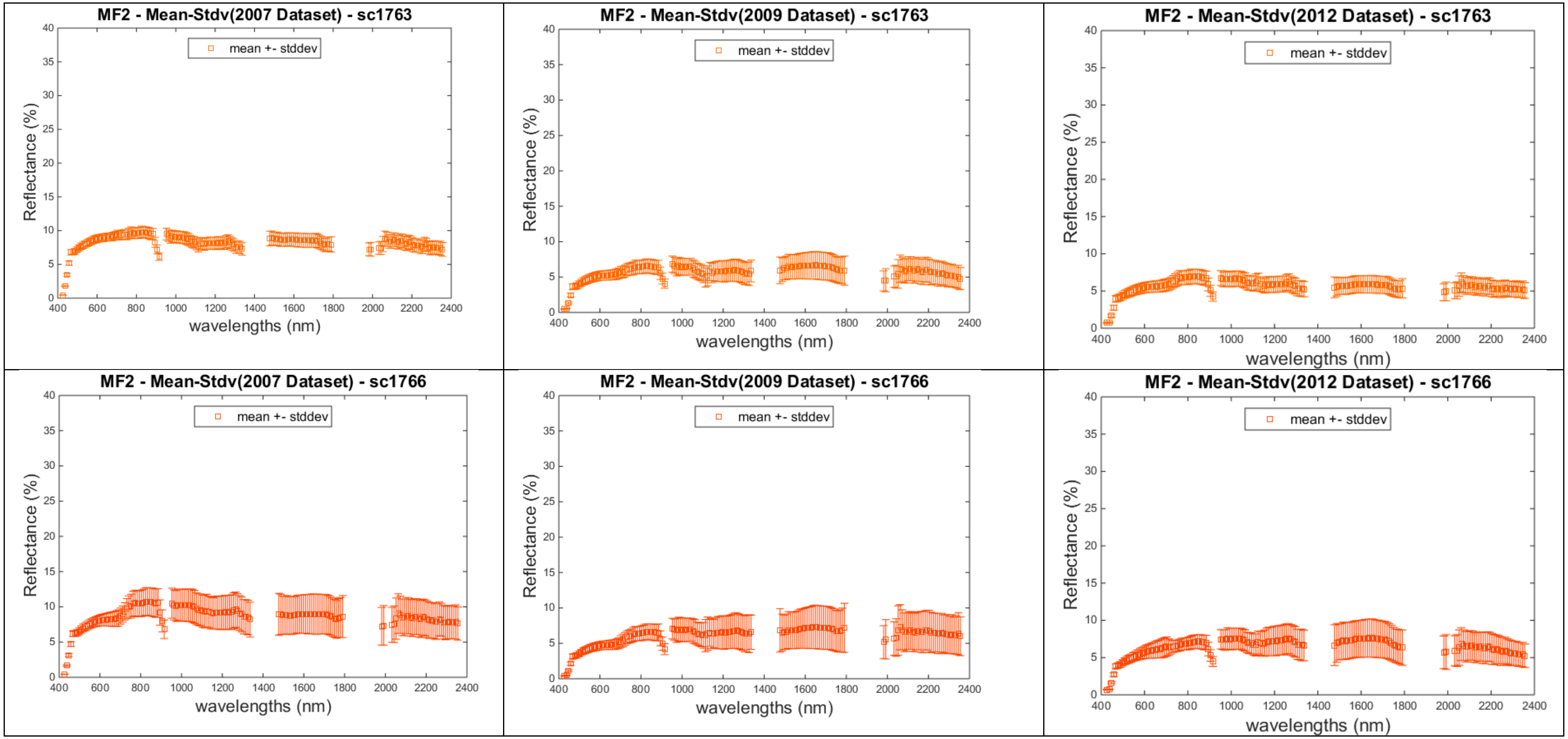


***Figure 6.1.30: Mean spectra and spectral variation of the Scoriae 1763 & 1766 endmembers categorized in MF2 formation (1669-1971) extracted from 2007 (left), 2009 (middle) and 2012 (right) datasets***

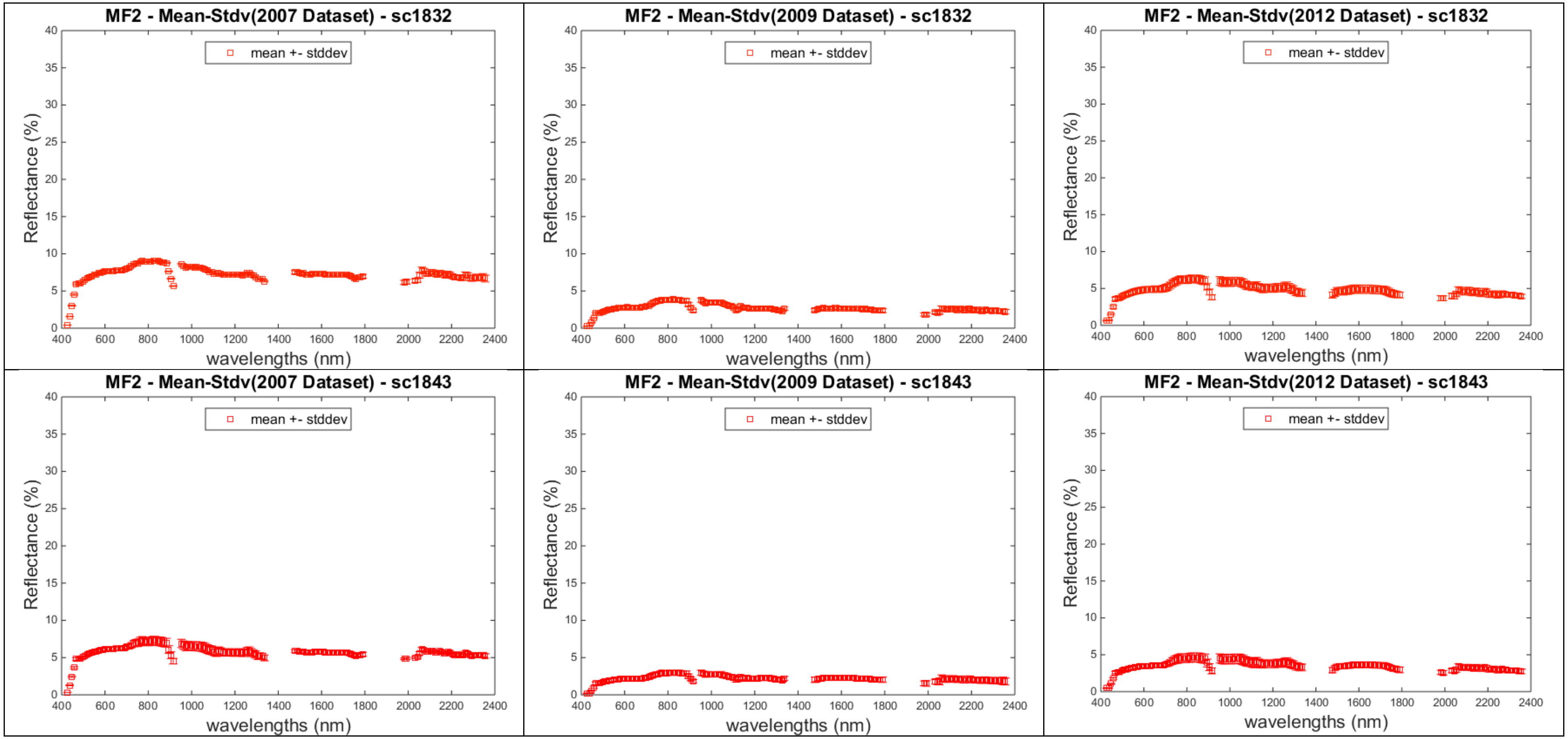


***Figure 6.1.31: Mean spectra and spectral variation of the Scoriae 1832 & 1843 endmembers categorized in MF2 formation (1669-1971) extracted from 2007 (left), 2009 (middle) and 2012 (right) datasets***

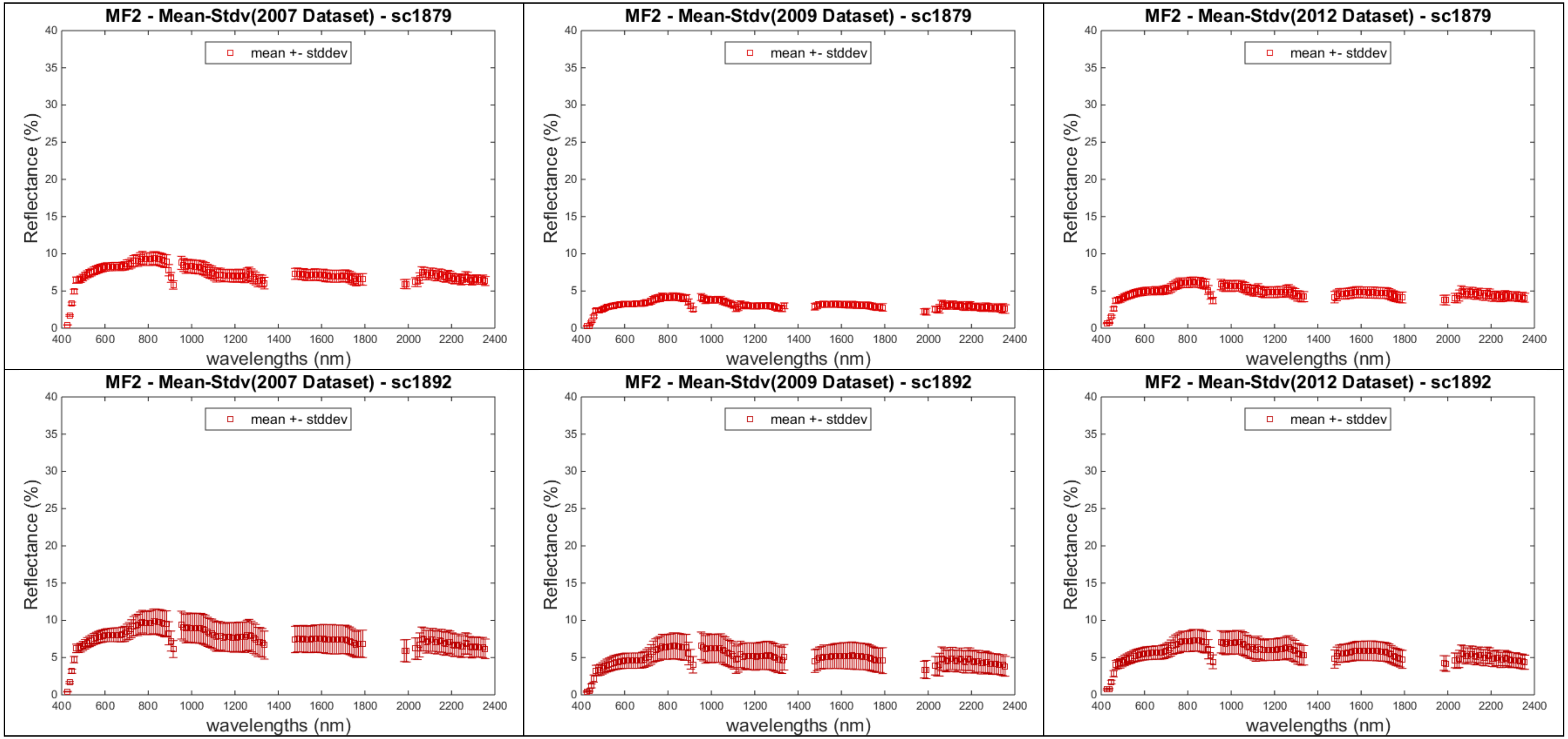


***Figure 6.1.32: Mean spectra and spectral variation of the Scoriae 1879 & 1892 endmembers categorized in MF2 formation (1669-1971) extracted from 2007 (left), 2009 (middle) and 2012 (right) datasets***

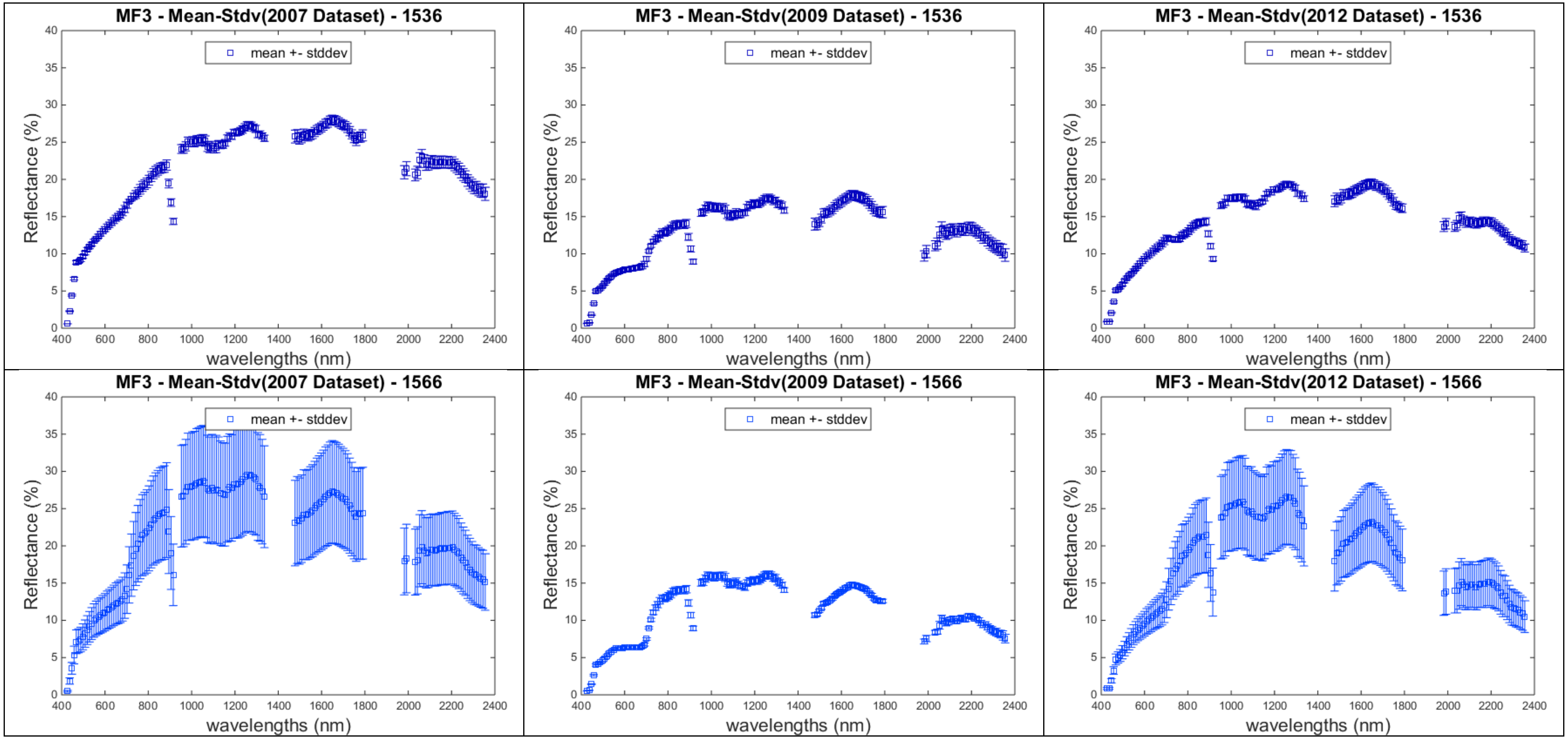


***Figure 6.1.33: Mean spectra and spectral variation of the Lava flows 1536 & 1566 endmembers categorized in MF3 formation (122 BC-1669AD) extracted from 2007 (left), 2009 (middle) and 2012 (right) datasets***

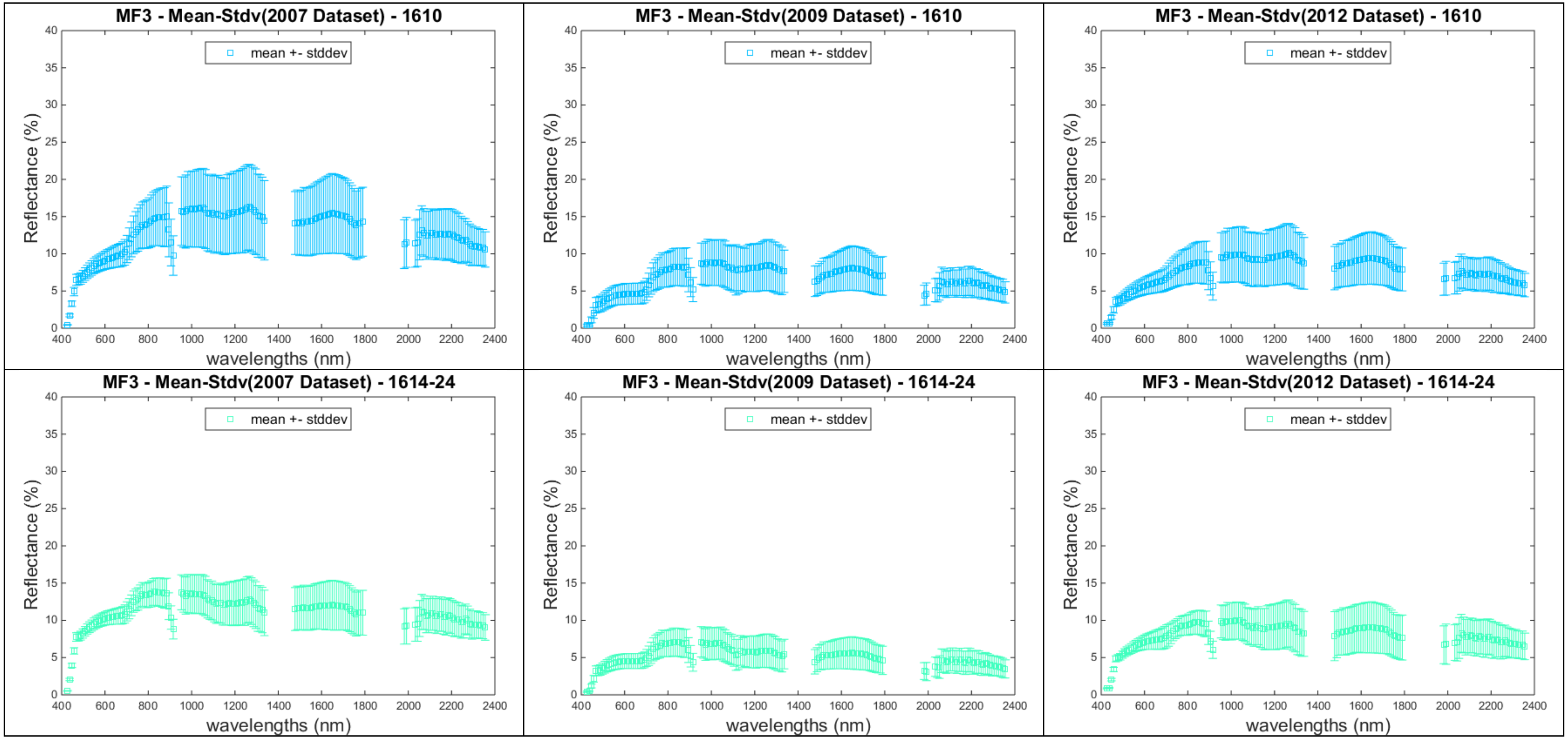


***Figure 6.1.34: Mean spectra and spectral variation of the Lava flows 1610 & 1614-24 endmembers categorized in MF3 formation (122 BC-1669AD) extracted from 2007 (left), 2009 (middle) and 2012 (right) datasets***

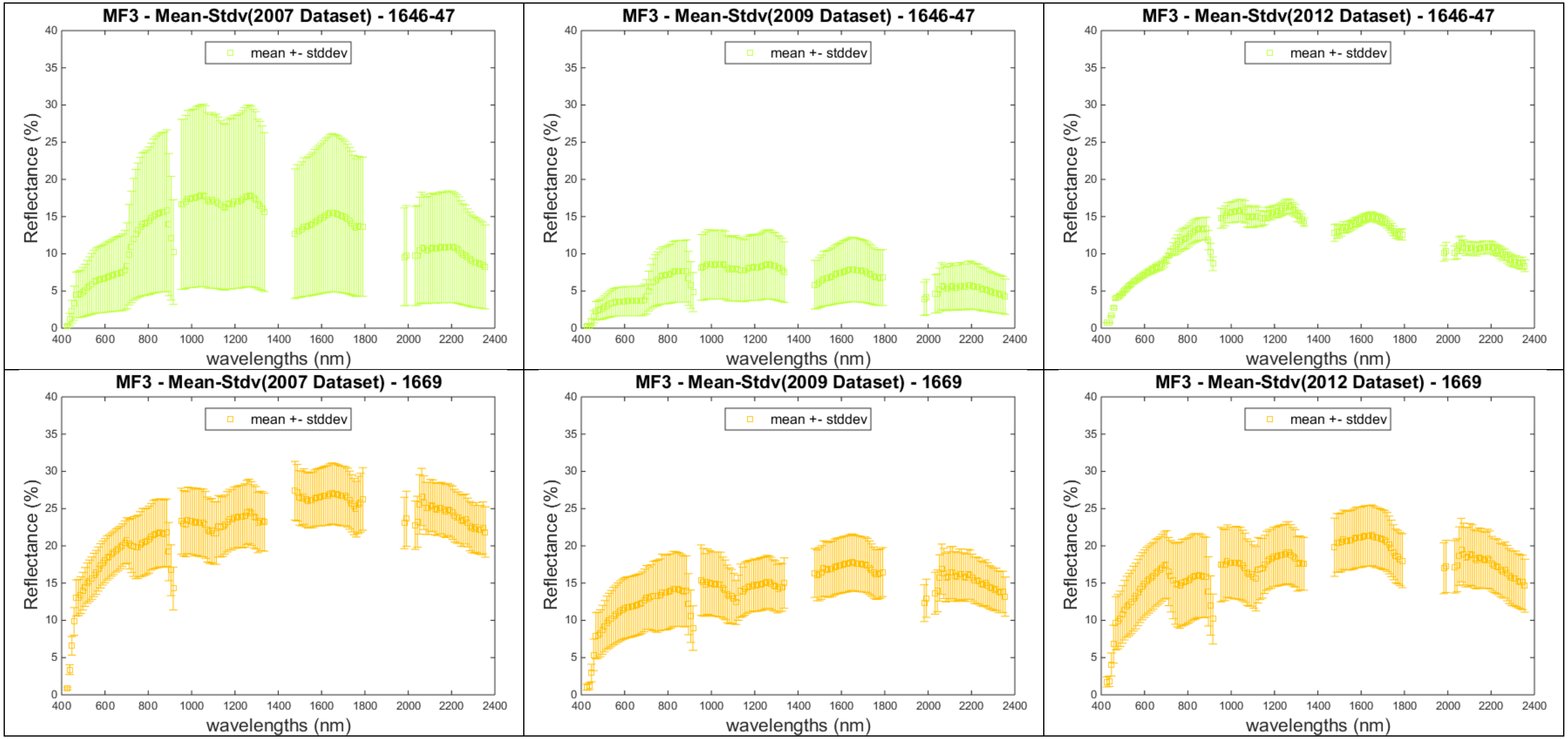


***Figure 6.1.35: Mean spectra and spectral variation of the Lava flows 1646-47 & 1669 endmembers categorized in MF3 formation (122 BC-1669AD) extracted from 2007 (left), 2009 (middle) and 2012 (right) datasets***

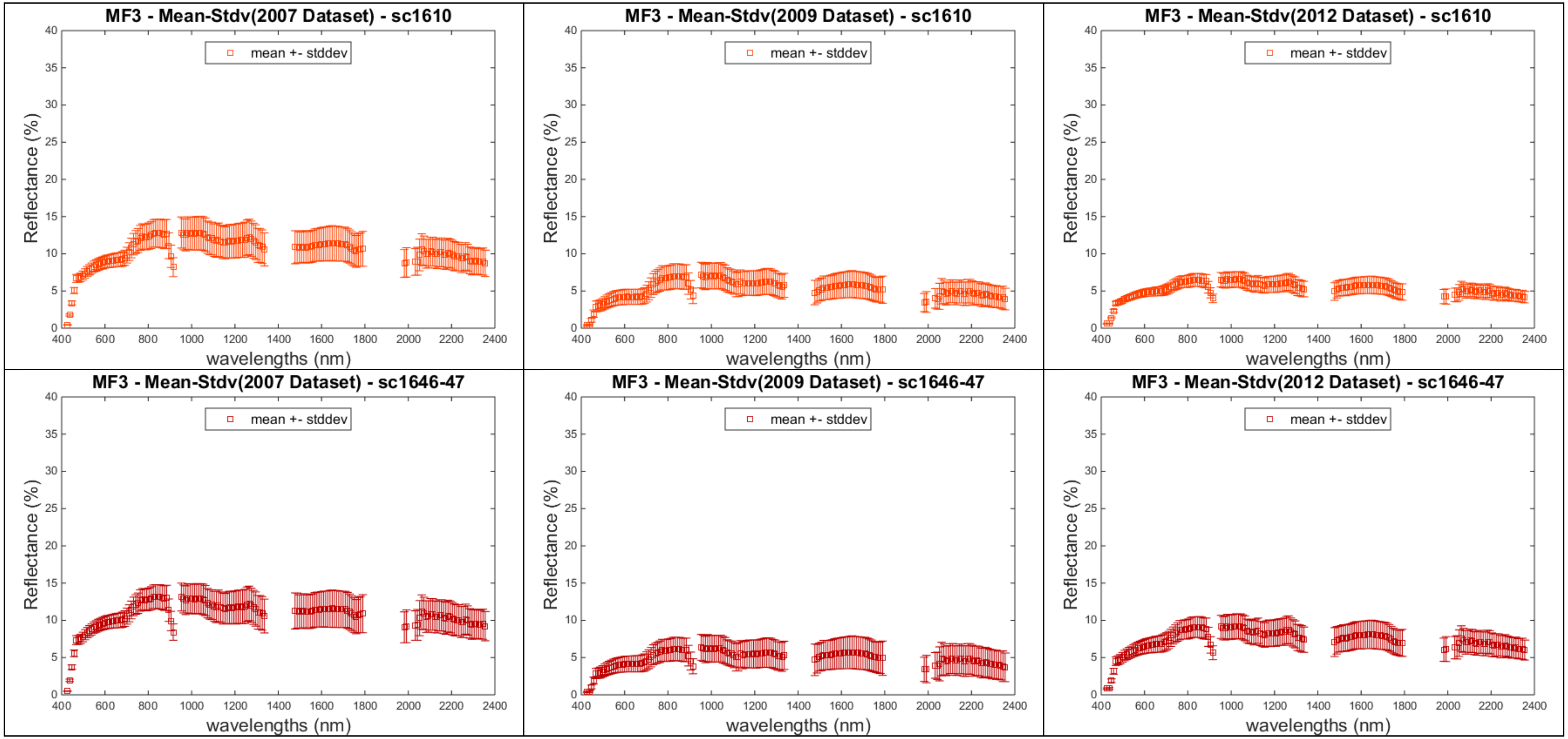


***Figure 6.1.36: Mean spectra and spectral variation of the Scoriae 1610 & 1646-47 endmembers categorized in MF3 formation (122 BC-1669AD) extracted from 2007 (left), 2009 (middle) and 2012 (right) datasets***

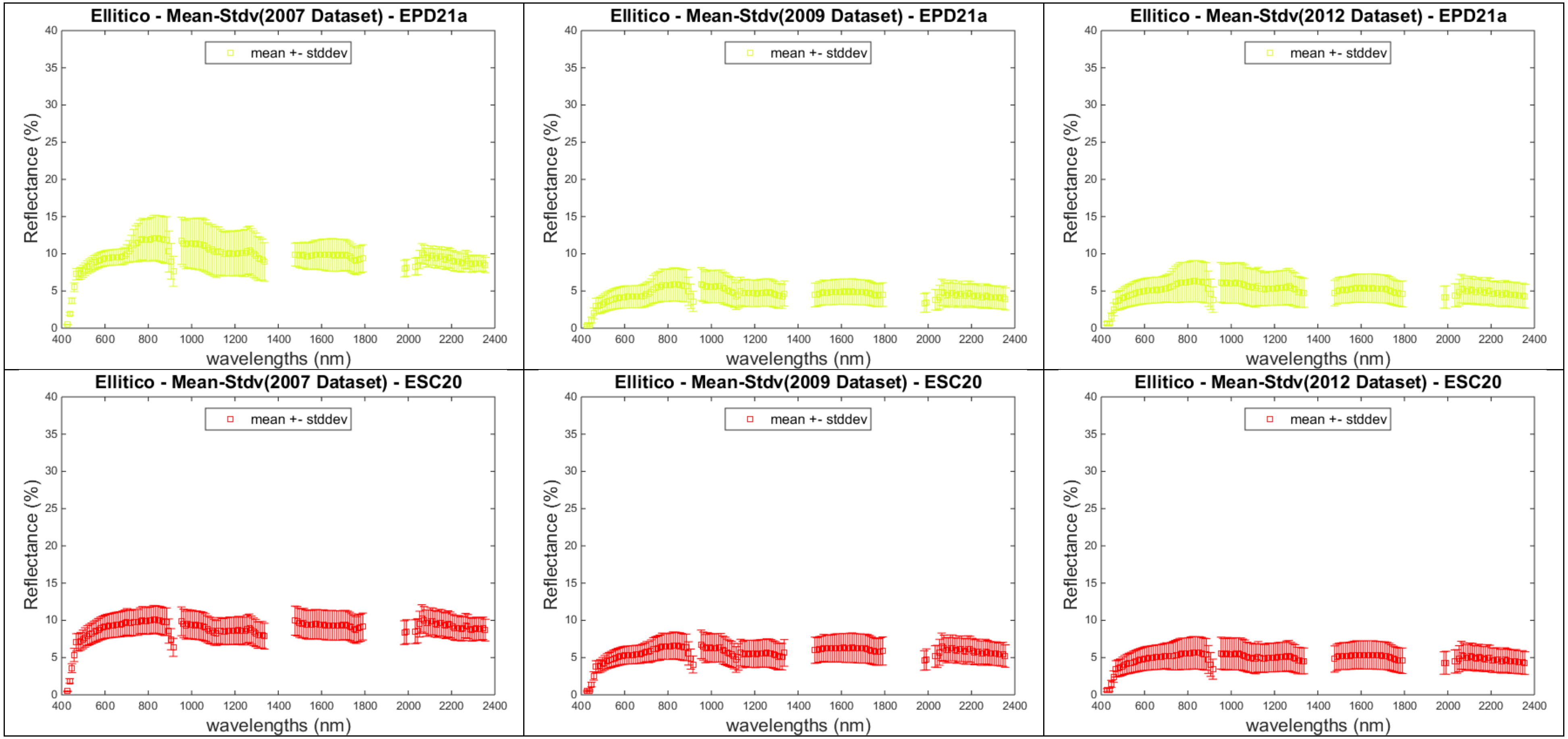


*Figure 6.1.37: Mean spectra and spectral variation of theESC20 & EPD21a endmembers categorized in Ellitico formation (Before 122 BC) extracted from 2007 (left), 2009 (middle) and 2012 (right) datasets*

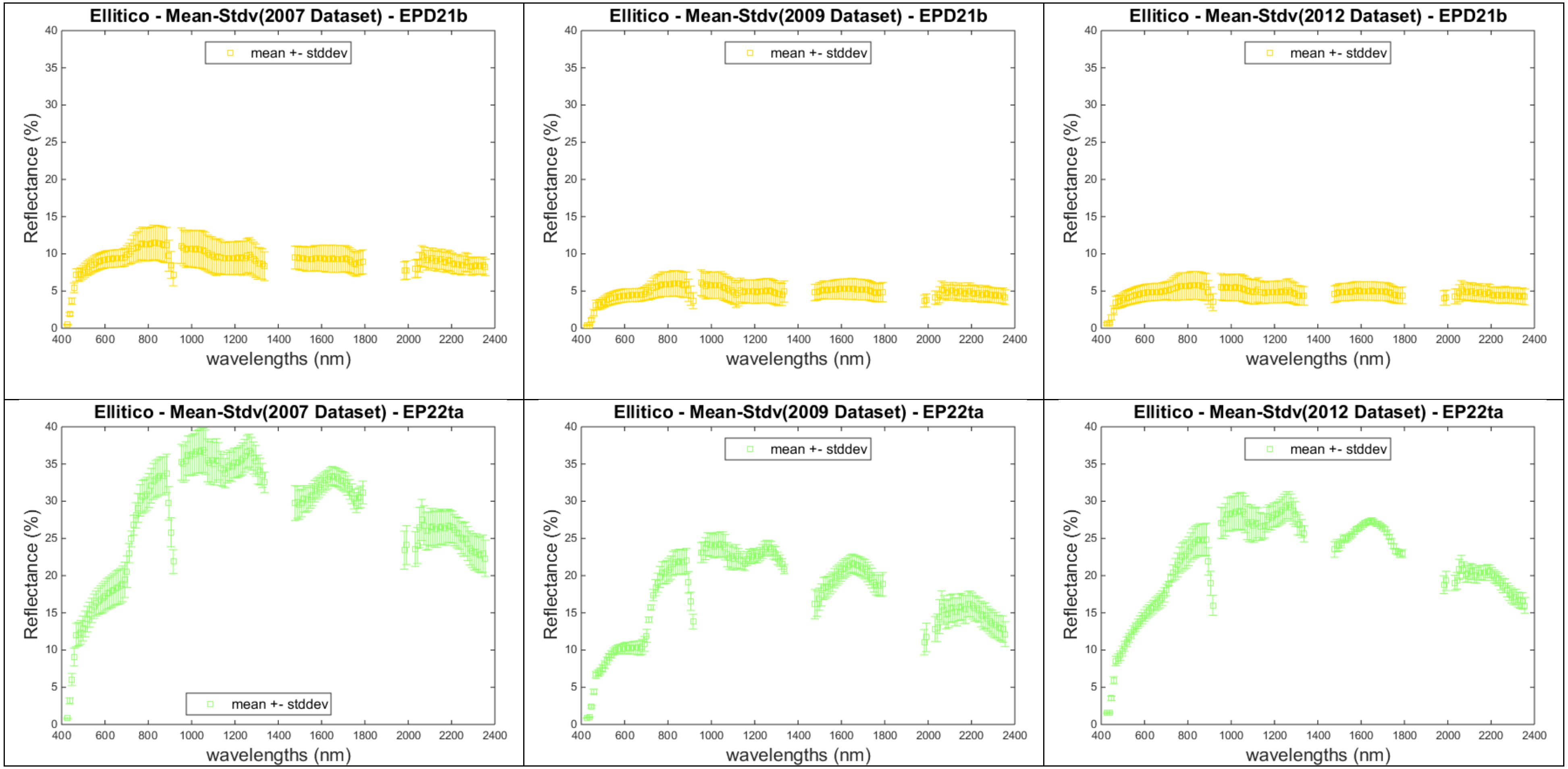


*Figure 6.1.38: Mean spectra and spectral variation of theEPD21b & EP22ta endmembers categorized in Ellitico formation (Before 122 BC) extracted from 2007 (left), 2009 (middle) and 2012 (right) datasets*

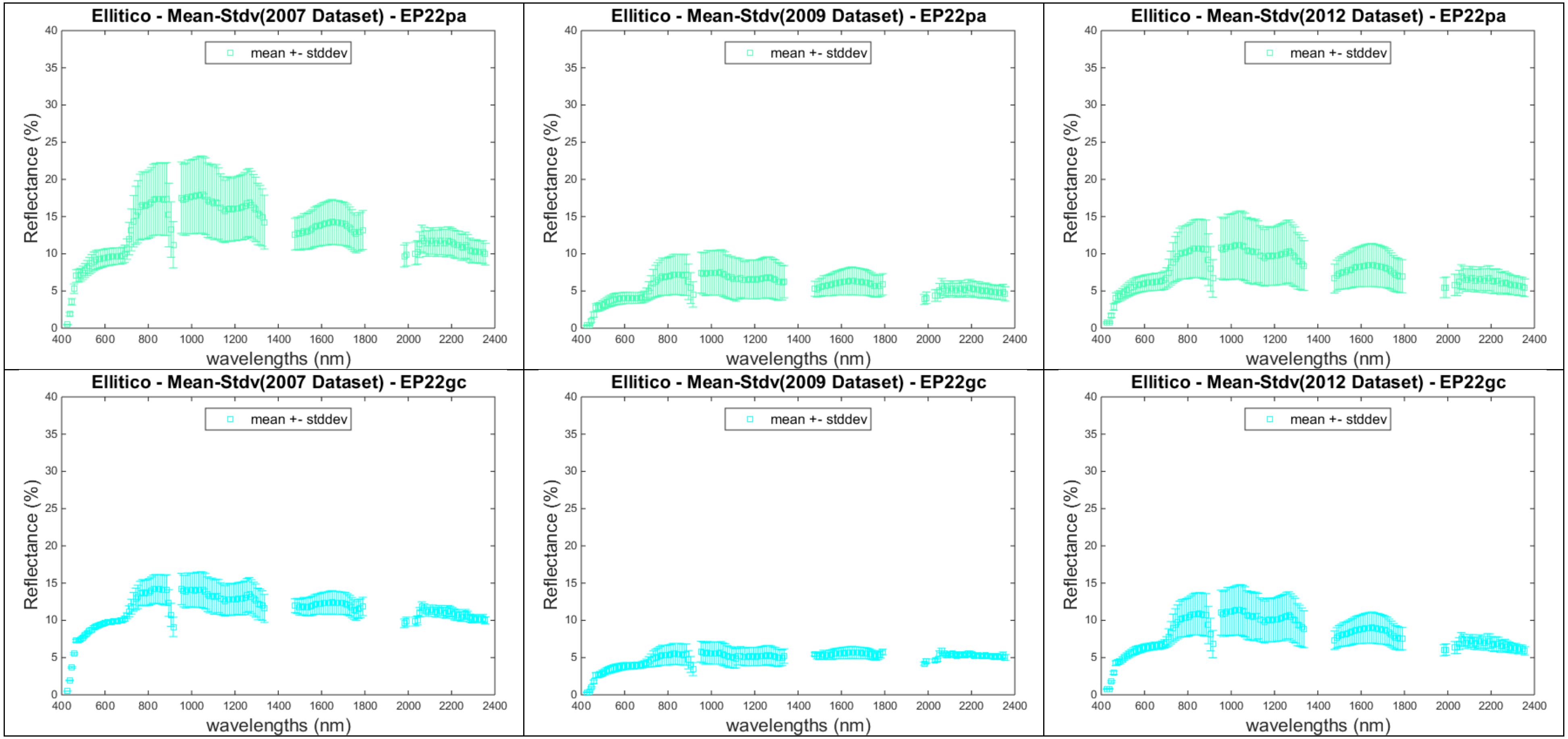


***Figure 6.1.39: Mean spectra and spectral variation of theEP22pa & EP22gc endmembers categorized in Ellitico formation (Before 122 BC) extracted from 2007 (left), 2009 (middle) and 2012 (right) datasets***

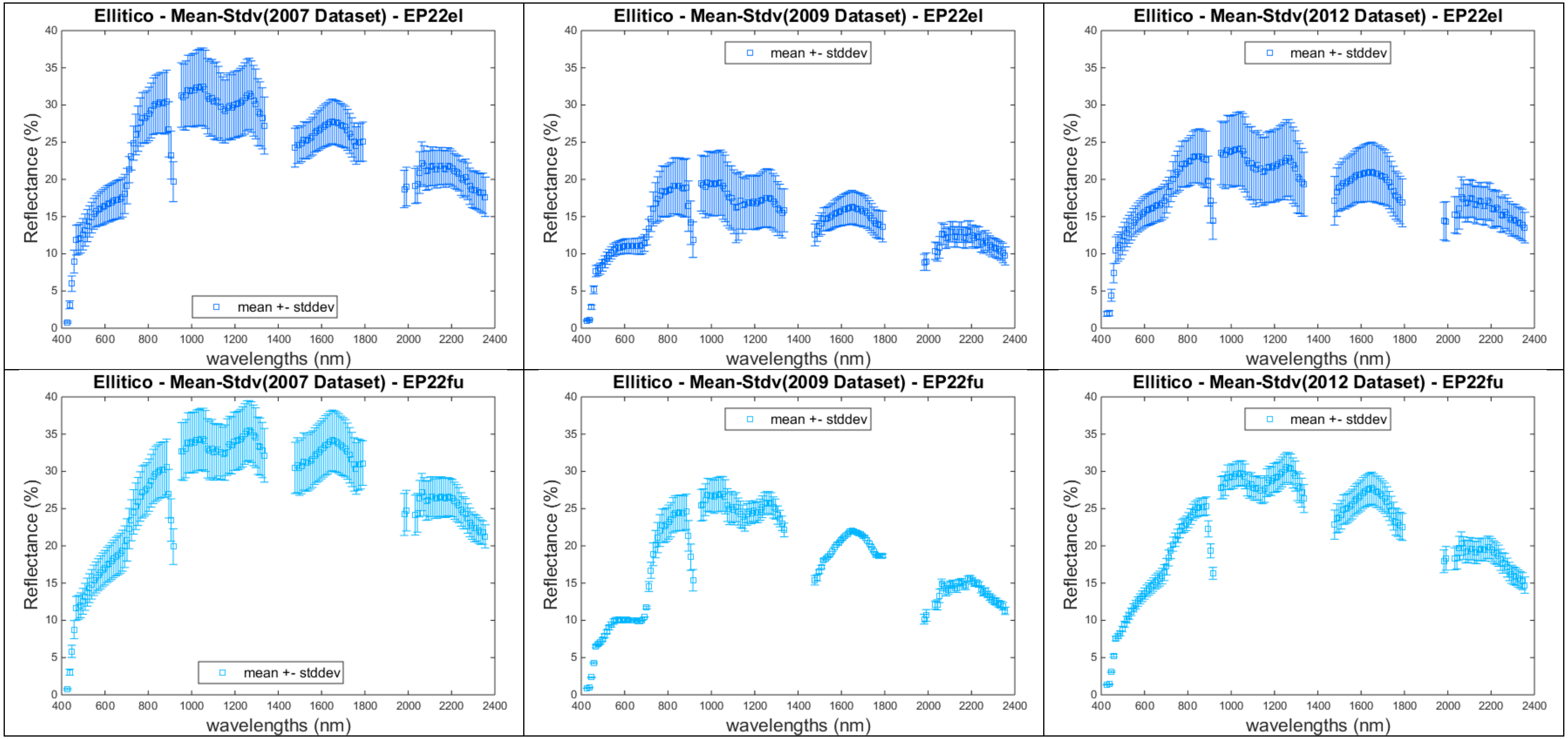


***Figure 6.1.40: Mean spectra and spectral variation of theEP22el & EP22fu endmembers categorized in Ellitico formation (Before 122 BC) extracted from 2007 (left), 2009 (middle) and 2012 (right) datasets***

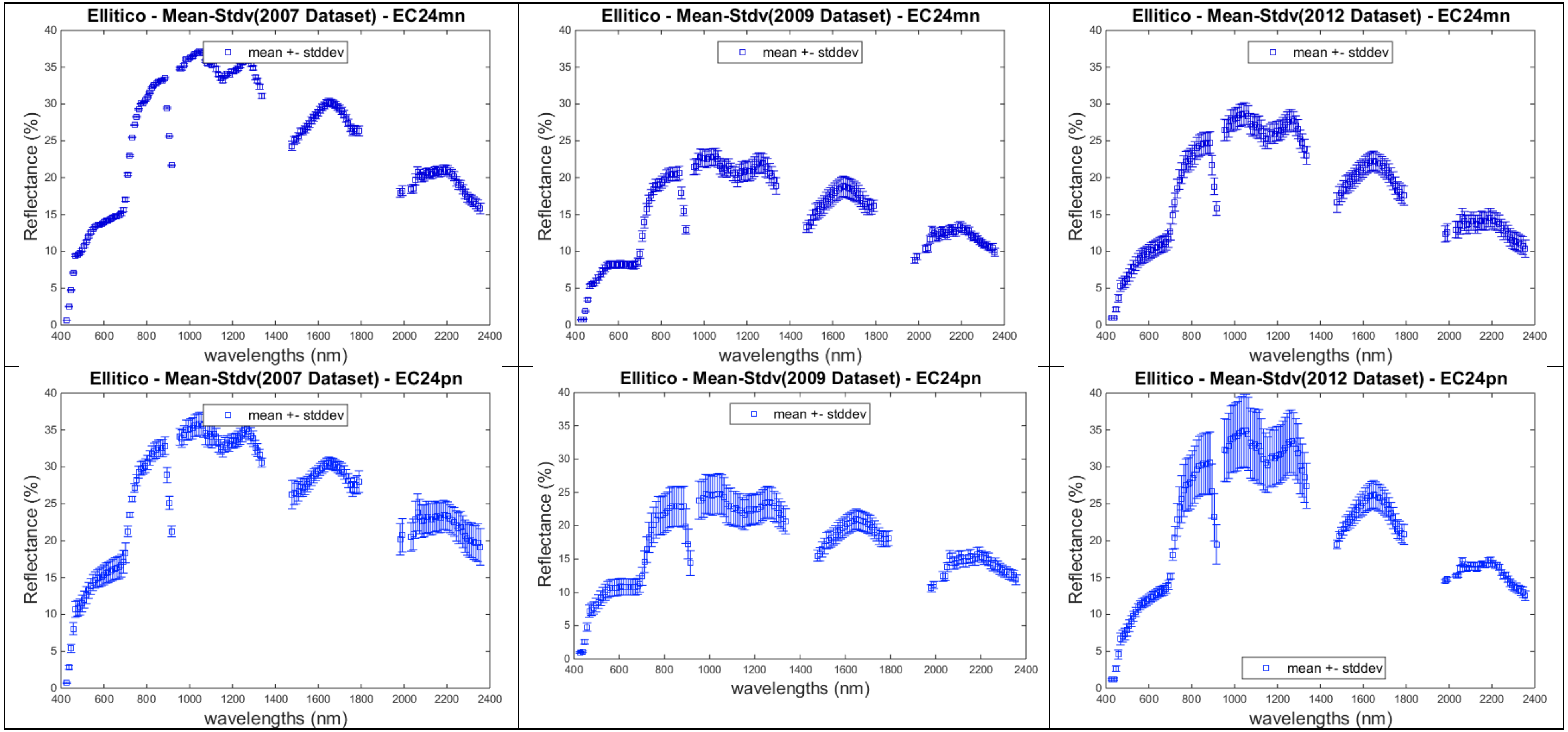


***Figure 6.1.41: Mean spectra and spectral variation of the EC24mn & EC24pn endmembers categorized in Ellitico formation (Before 122 BC) extracted from 2007 (left), 2009 (middle) and 2012 (right) datasets***

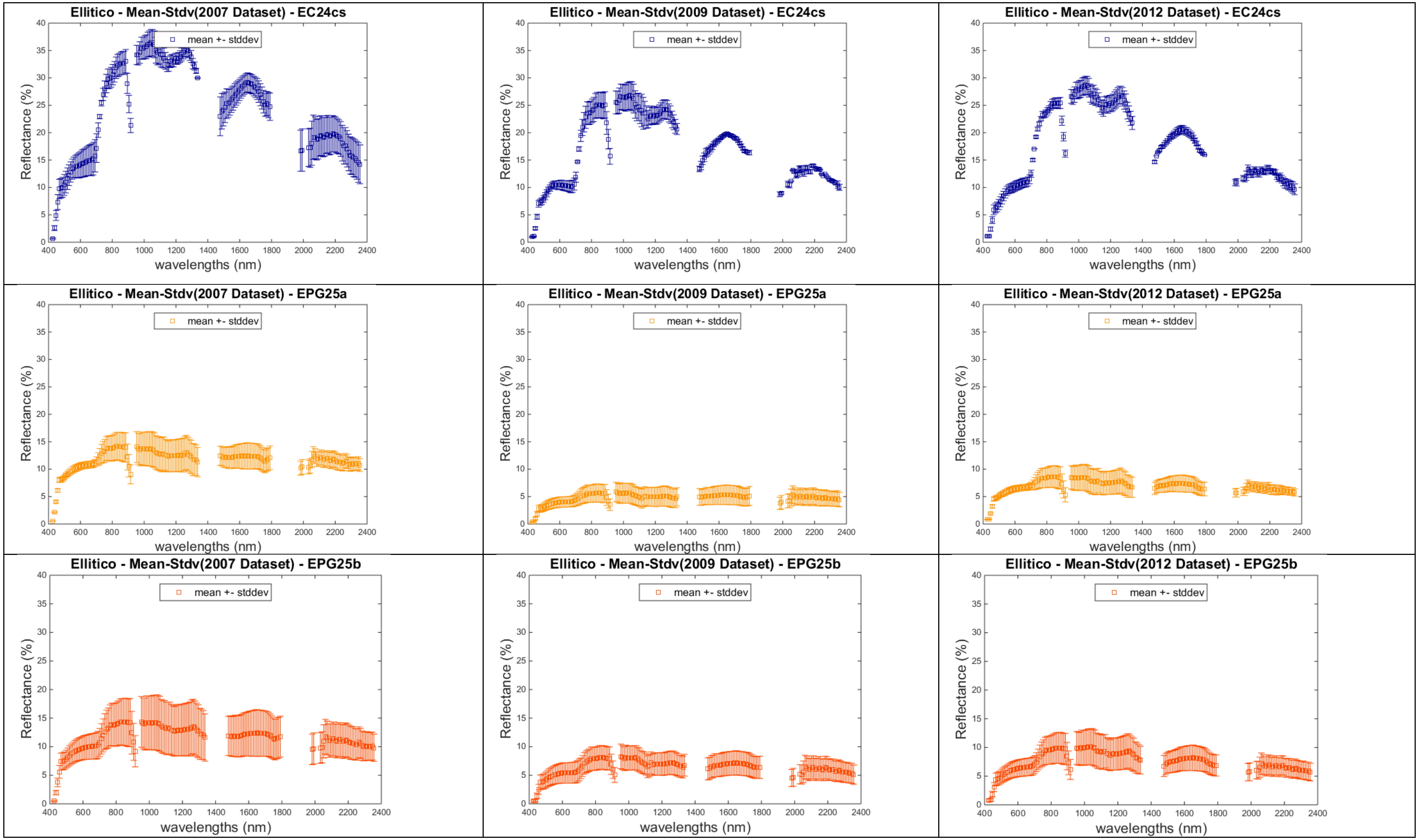


***Figure 6.1.42: Mean spectra and spectral variation of theEC24cs & EPG25a/b endmembers categorized in Ellitico formation (Before 122 BC) extracted from 2007 (left), 2009 (middle) and 2012 (right) datasets***

## Temporal change in reflectance response

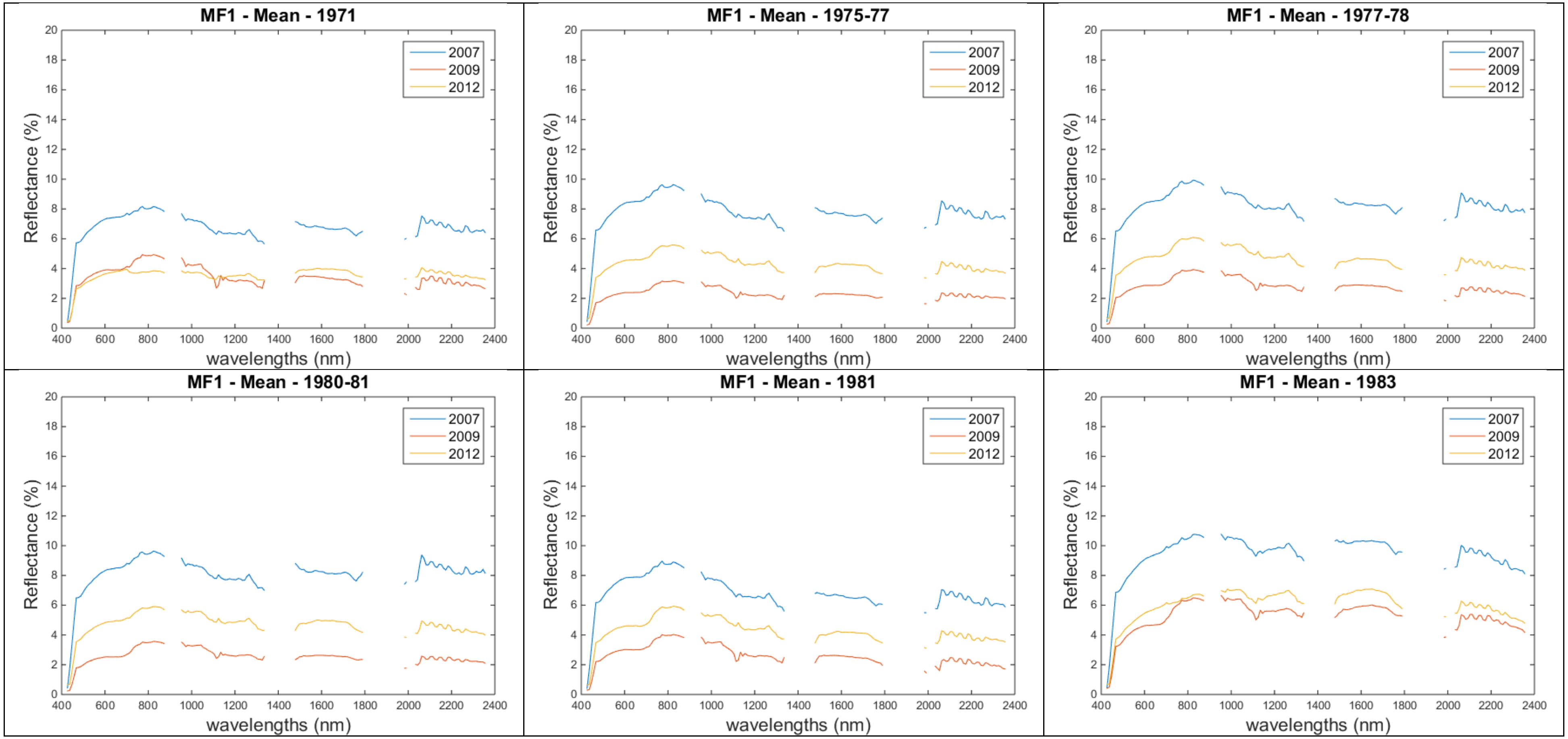


*Figure 6.1.43: Mean spectra of Lava flows from 1971 to 1983 endmembers categorized in MF1 Volcanic Formation (1971-5/2007) extracted from 2007, 2009 and 2012 datasets*

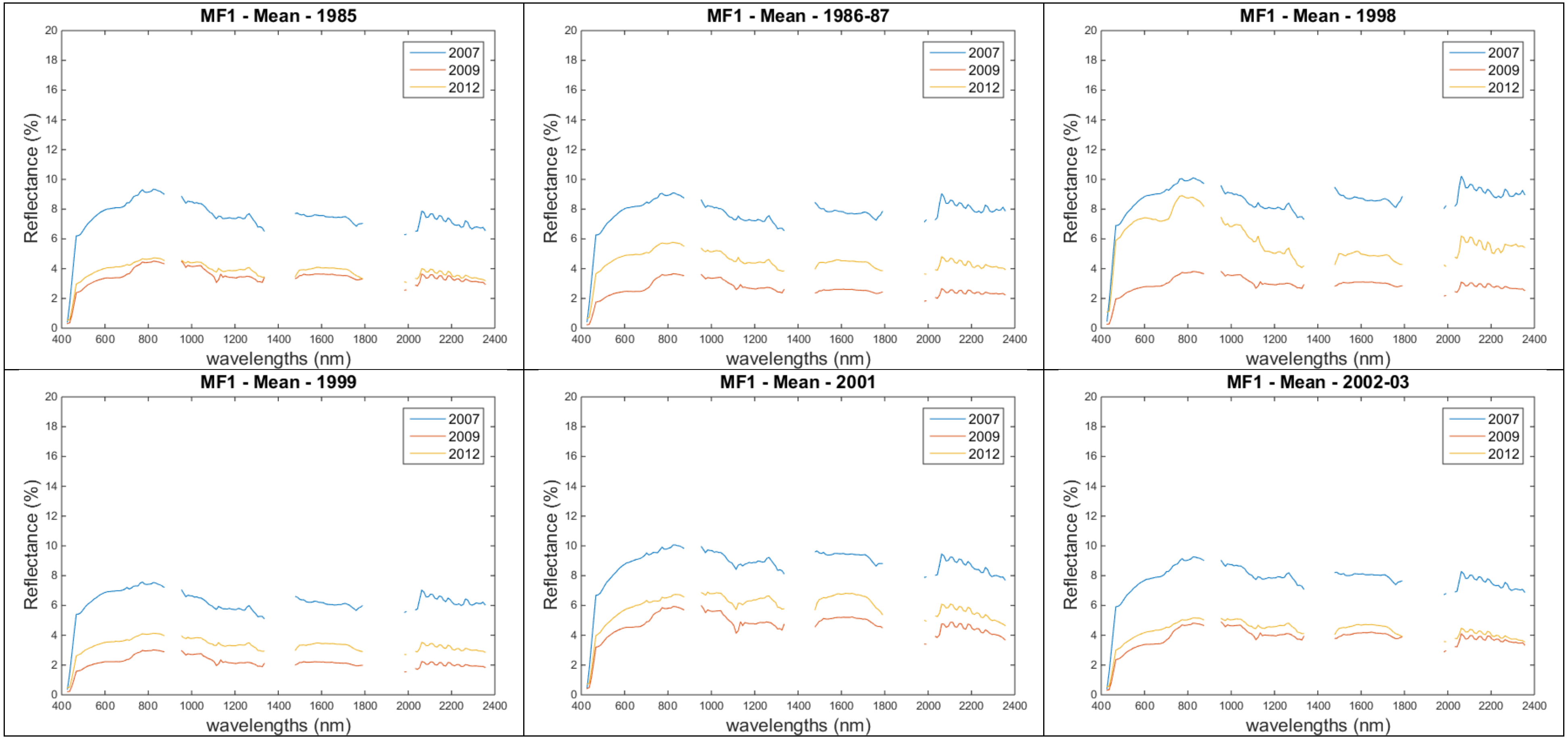


***Figure 6.1.44: Mean spectra of Lava flows from 1985 to 2003 endmembers categorized in MF1 Volcanic Formation (1971-5/2007) extracted from 2007, 2009 and 2012 datasets***

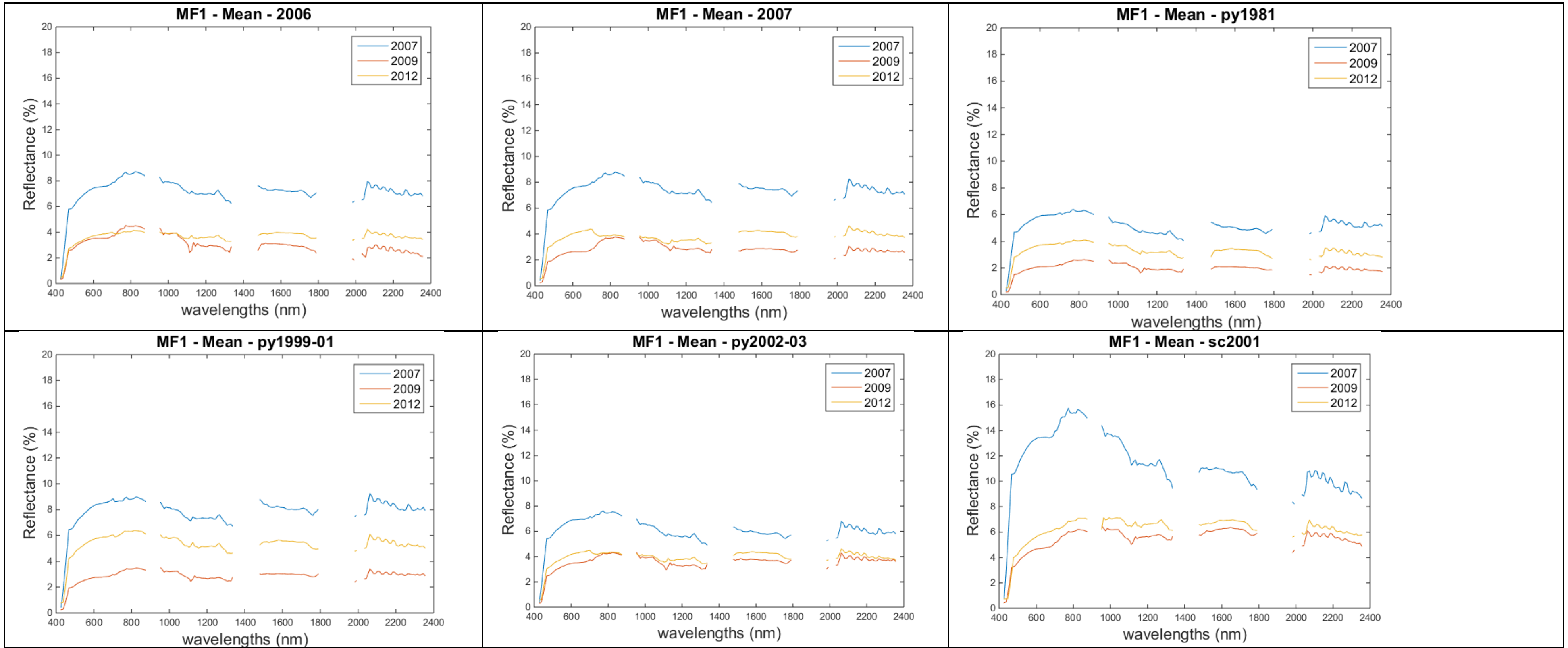


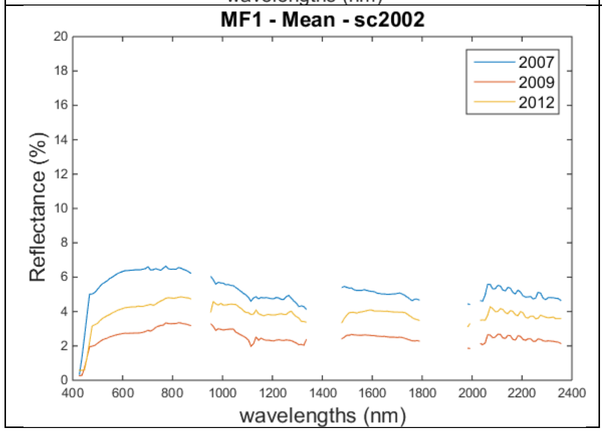


***Figure 6.1.45: Mean spectra of Lava flows from 2006 to 2007 & Pyroclastic from 1981 to 2003 & Scoriae from 2001 to 2002 endmembers categorized in MF1 Volcanic Formation (1971-5/2007) extracted from 2007, 2009and 2012 datasets***

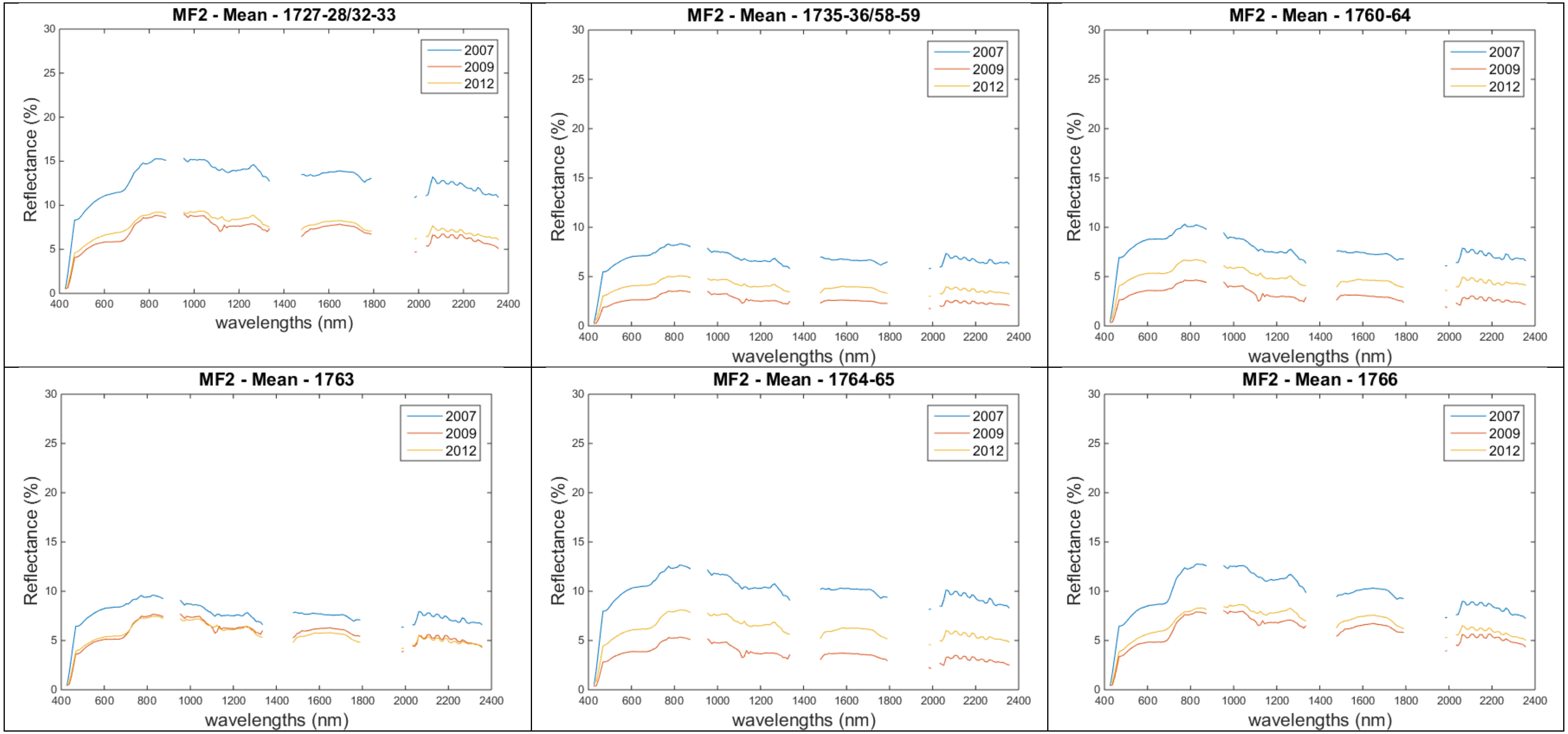


***Figure 6.1.46: Mean spectra of Lava flows from 1727 to 1766 endmembers categorized in MF2 Volcanic Formation (1669-1971) extracted from 2007, 2009 and 2012 datasets***

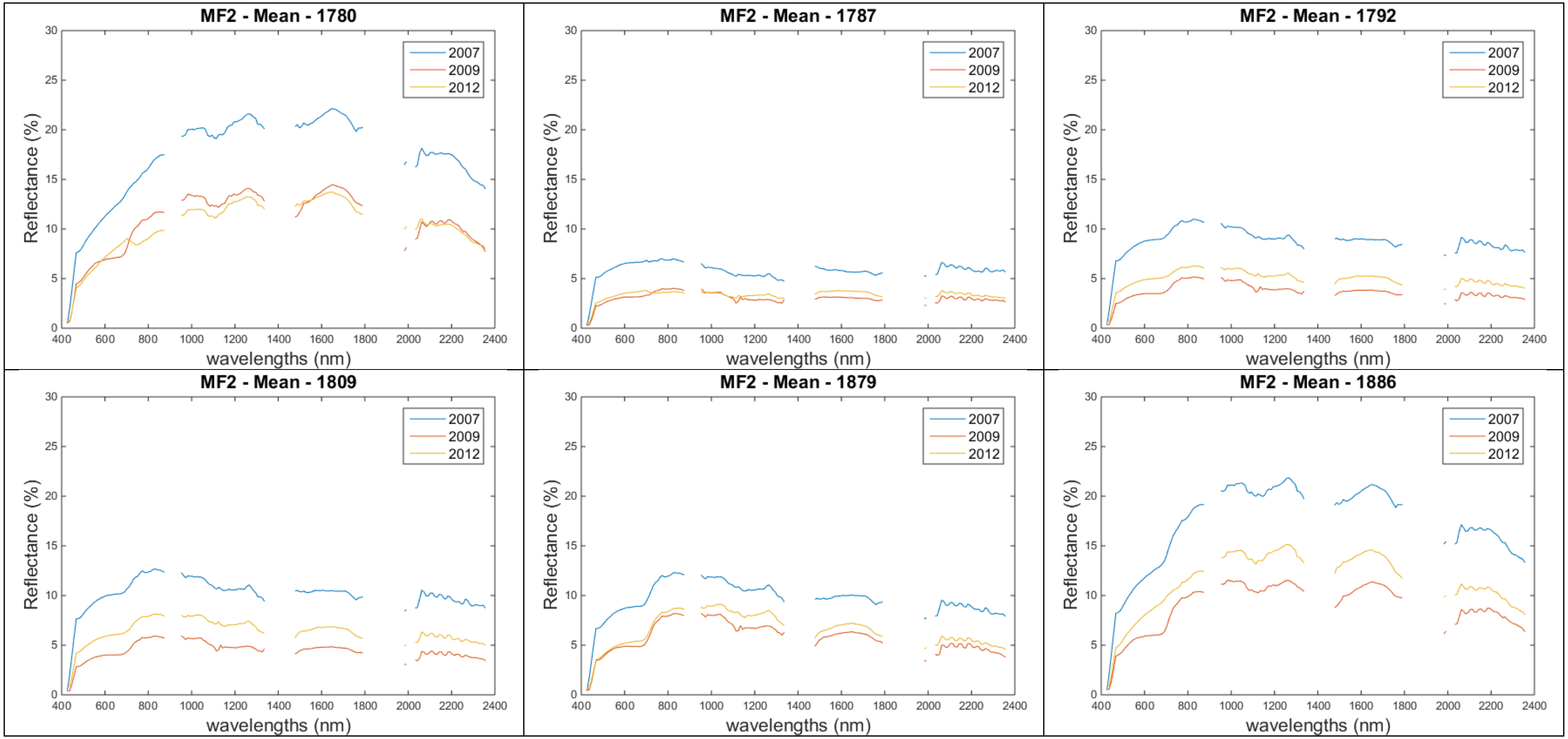


*Figure 6.1.47: Mean spectra of Lava flows 1780 to 1886 endmembers categorized in MF2 Volcanic Formation (1669-1971) extracted from 2007, 2009 and 2012 datasets*

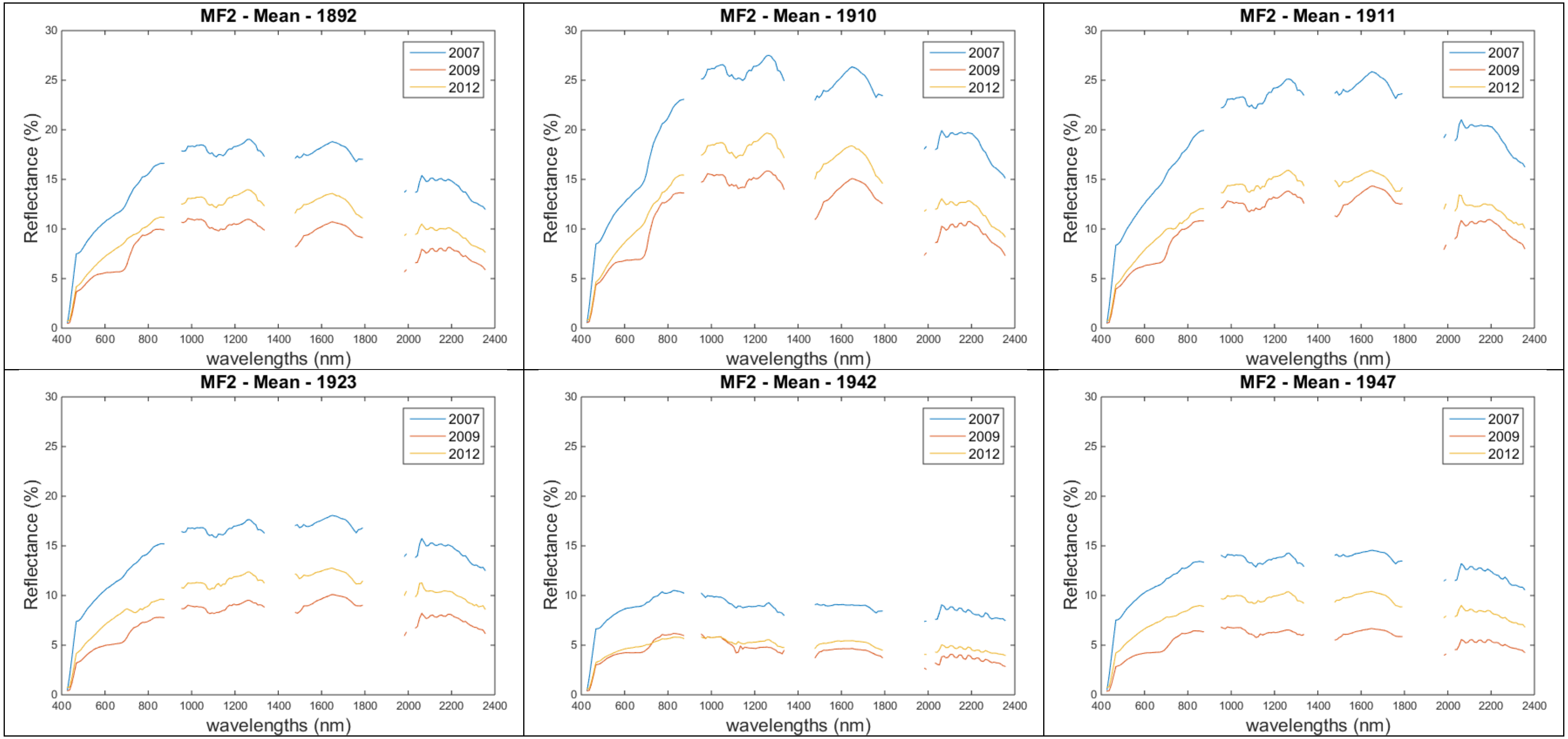


***Figure 6.1.48: Mean spectra of Lava flows 1892 to endmembers categorized in MF2 Volcanic Formation (1669-1971) extracted from 2007, 2009 and 2012 datasets***

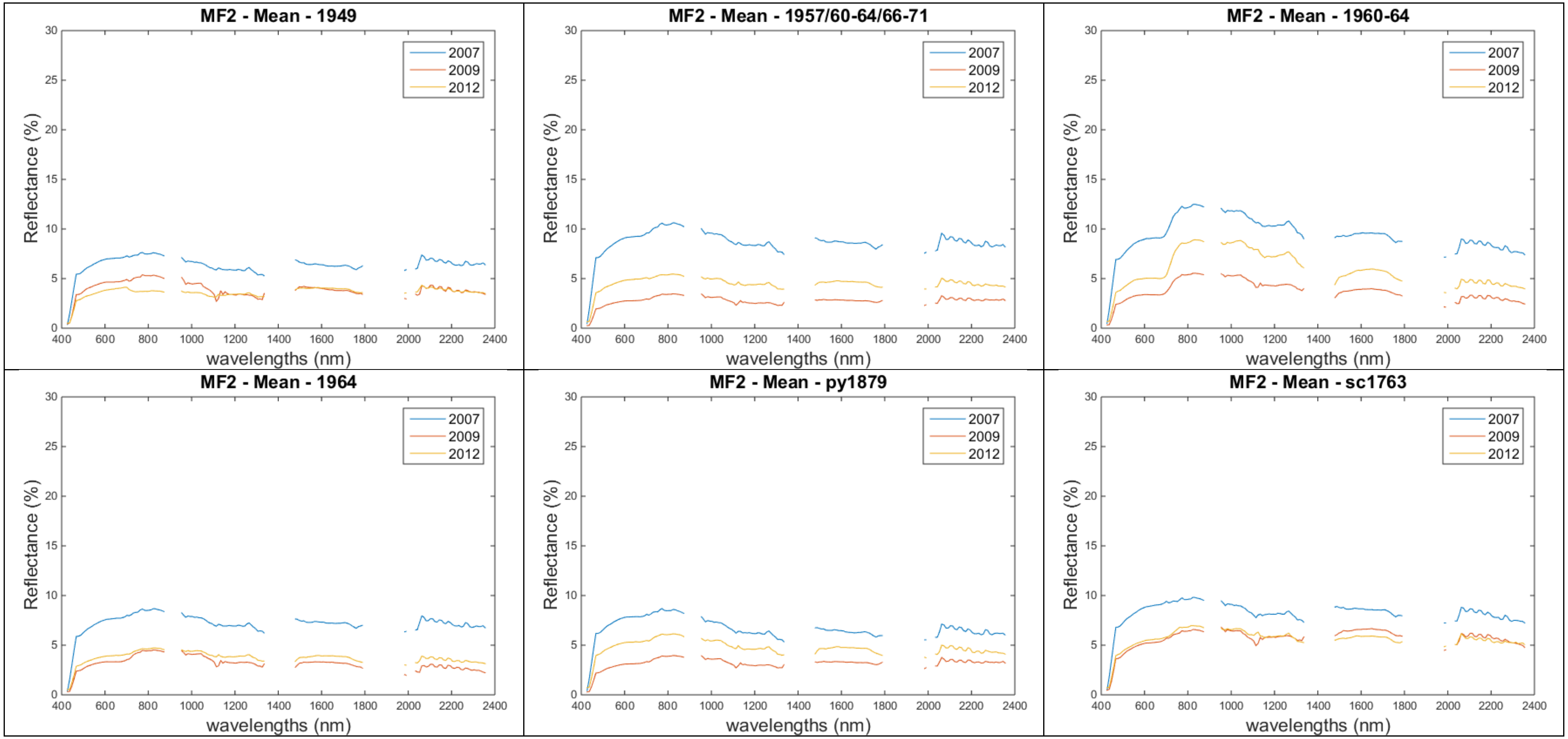


***Figure 6.1.49: Mean spectra of Lava flows 1949 to 1964, pyroclastic 1879 and scoriae 1763 endmembers categorized in MF2 Volcanic Formation (1669-1971) extracted from 2007, 2009 and 2012 datasets***

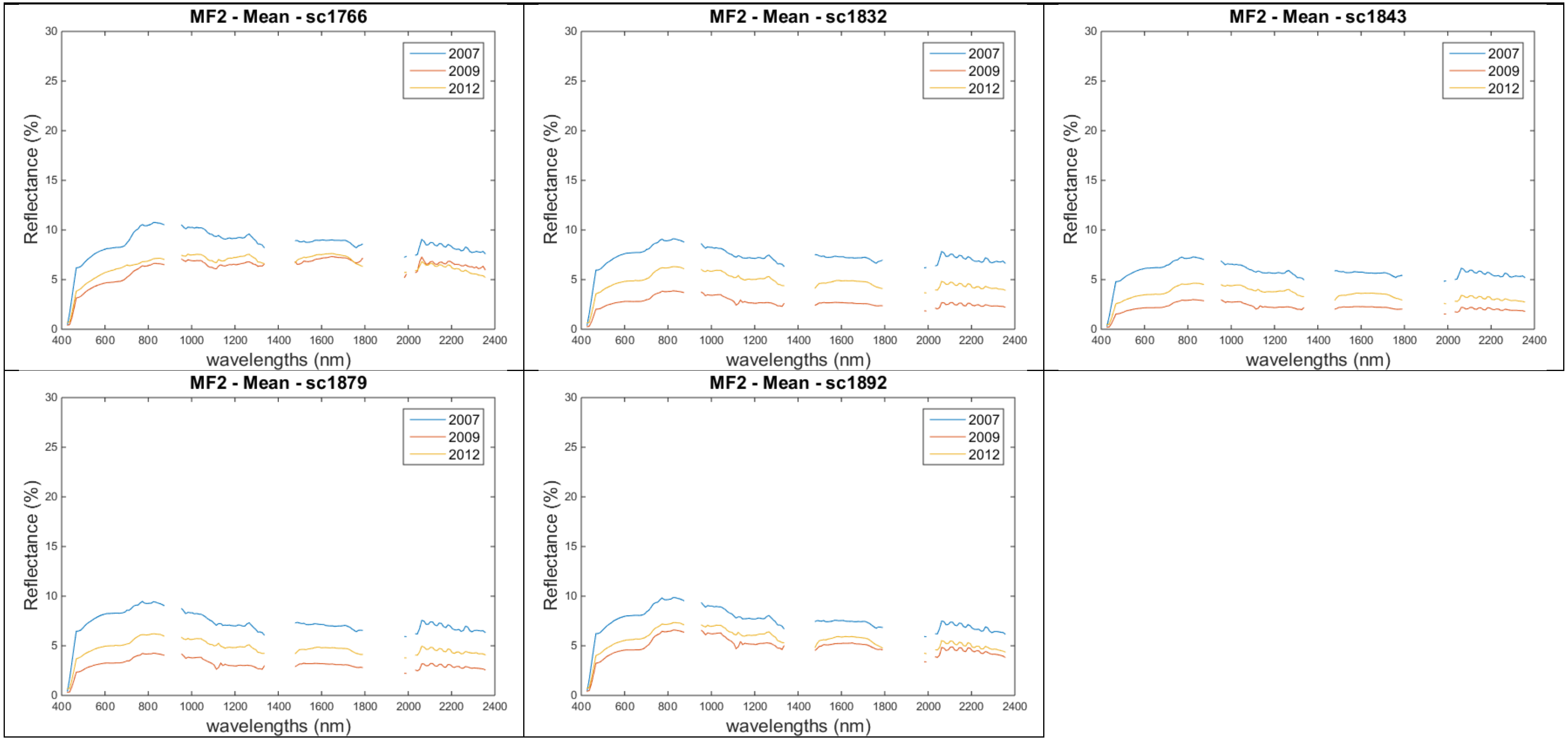


*Figure 6.1.50: Mean spectra of scoriae from 1766 to 1892 endmembers categorized in MF2 Volcanic Formation (1669-1971) extracted from 2007, 2009 and 2012 datasets*

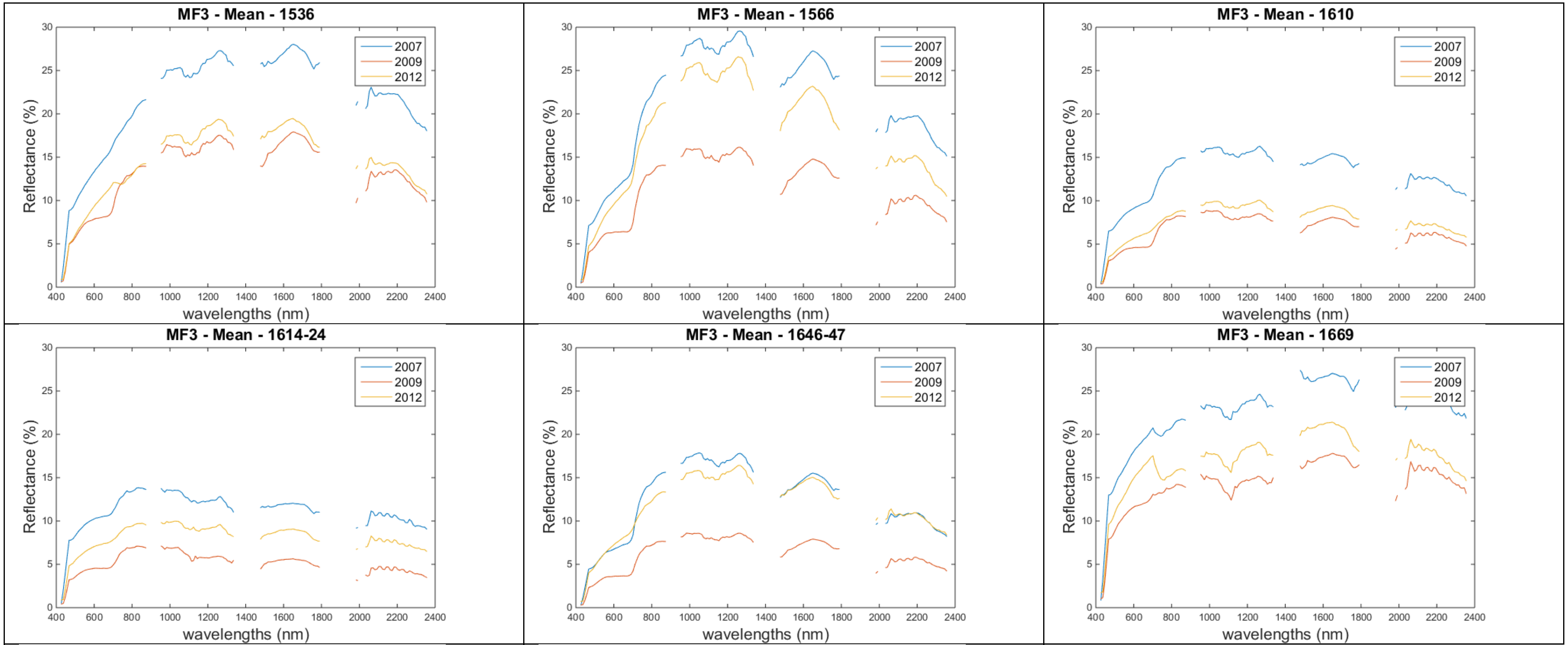


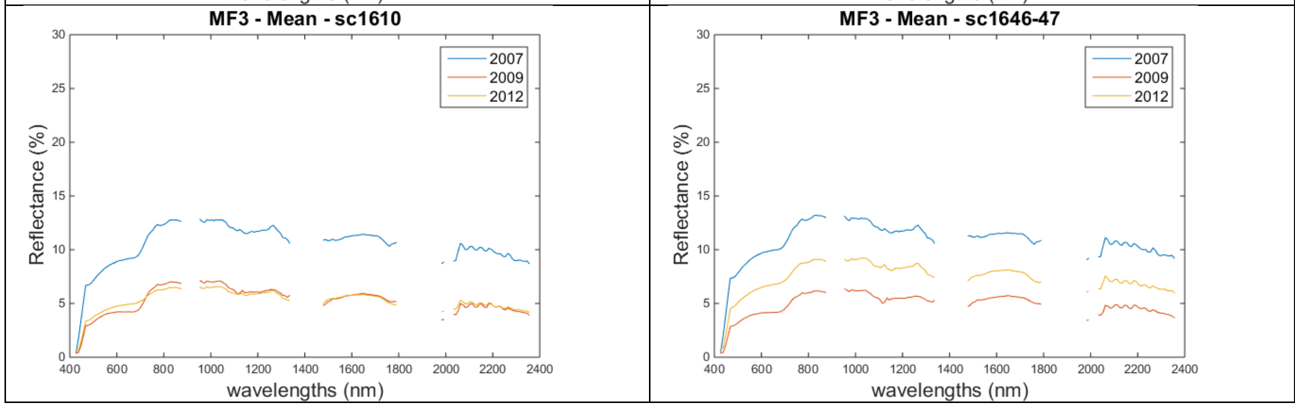


***Figure 6.1.51: Mean spectra of Lava flows from 1536 to 1669 and scoriae from 1610 to 1647 endmembers categorized in MF3 Volcanic Formation (122 BC-1669AC) extracted from 2007, 2009 and 2012 datasets***

## Ellitico Volcanic Formation (Before 122 BC)

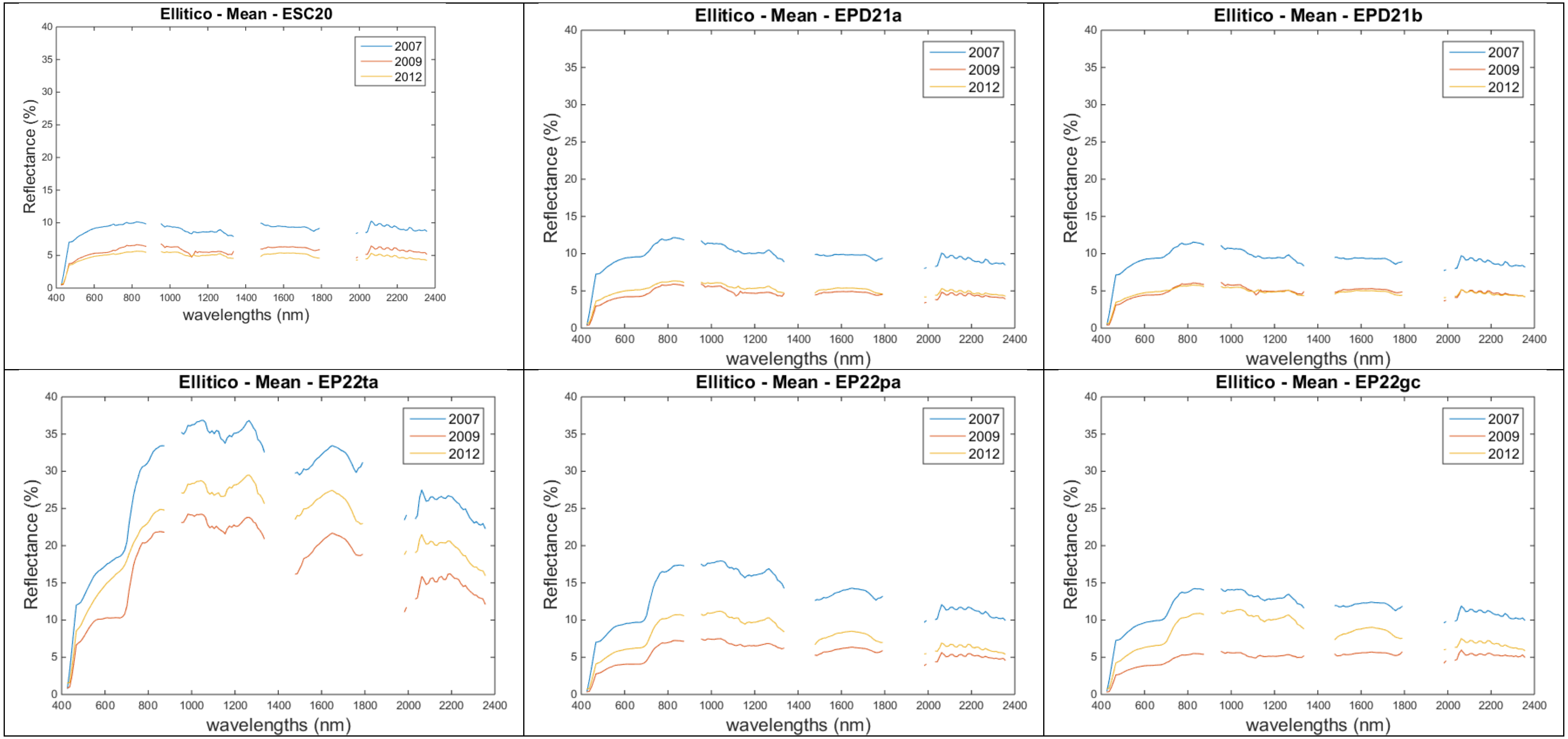


*Figure 6.1.52: Mean spectra of Lava flows ESC20, EPD21a,b, EP22ta,pa,gc endmembers categorized in Ellitico Volcanic Formation (Before 122 BC) extracted from 2007, 2009 and 2012 datasets*

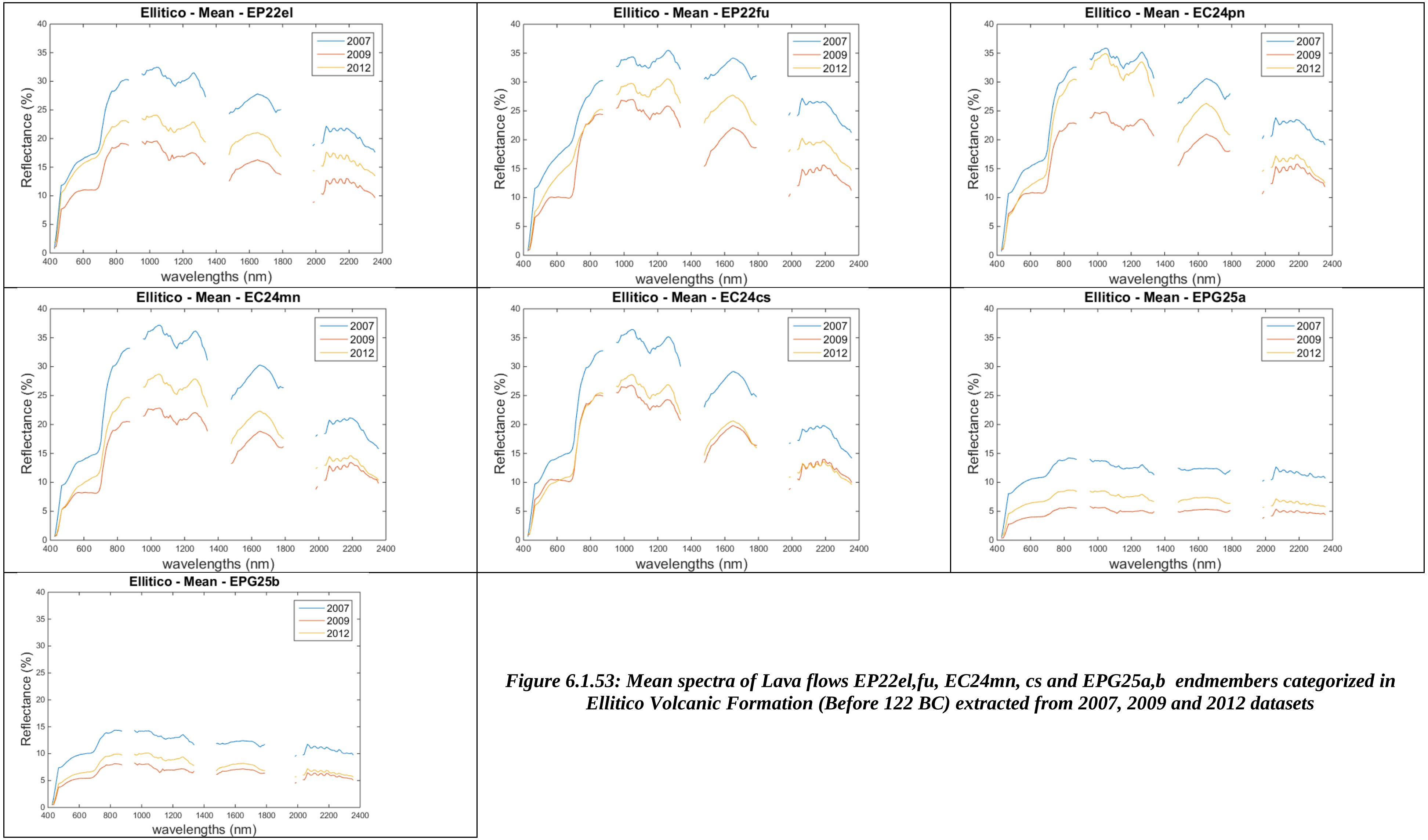


***Figure 6.1.53: Mean spectra of Lava flows EP22el,fu, EC24mn, cs and EPG25a,b endmembers categorized in Ellitico Volcanic Formation (Before 122 BC) extracted from 2007, 2009 and 2012 datasets***

## 6.2. SAR Statistical Data Analysis

In this chapter we investigate the mean backscatter coefficient values of each volcanic formation, which were extracted from the ascending (VV & VH polarization) and descending (VV & VH polarization) SAR images. Our primary results are as follows:

- The VV polarization reveals the highest backscatter coefficient values in every volcanic formation.
- Backscatter coefficient decreases from the MF1 formation to the MF3
- Ellitico dB values are higher in comparison with the younger volcanic formations (MF1, MF2 and MF3).
- The backscatter coefficient values of each volcanic product don't decrease or increase according to their age categorization.
- The backscatter coefficient values of the volcanic products are affected from the shadowing and foreshortening distortions, due to the local topography and the acquisition geometry. A potential approach would be the estimation of the regions which are affected by these distortions and exclude them from our study. Although such study fall beyond the scope of our current study.

- **MF1 Formation - Mean Backscatter Coefficient values**

Figures 6.2.1 and 6.2.2 show the mean backscatter coefficient values of each MF1 volcanic product (lava flows, pyroclastic and scoriae) in single and cross polarizations, in ascending and descending satellite orbits. The difference between the mean $\sigma^0$ values in descending and ascending acquisition pass is also depicted, for VV and VH polarization, of each volcanic product, (Figure 6.2.3).

Lava flows are characterized by higher $\sigma^0$ values in ascending orbit and in VV polarization. Furthermore, it seems (Figures 6.2.1-2) that when in ascending pass, the sigma0 value of a lava flow decreases, compared with the sigma0 values of the other lavas, the respective value in descending pass increases and vice versa. However, the descending pass always reveals lower backscatter values in each formation compared with the ascending pass.

A characteristic example of the above description is the 1999 lava flow. The 1999 lava flow is described by the highest sigma0 values in the ascending mode for both VV (0.8 dB) and VH (0.1 dB) polarizations. In the descending orbit the same formations show 0.06 dB for VV and 0.01 dB for VH corresponding values. According to these findings, we investigate the spatial location, where the 1999 lava flow was recorded and thus we assume that one potential reason that may affect the 1999 lava flow $\sigma^0$ in ascending pass, is the combination of the local topography (high slope more than $30^o$) and the geometry of the acquisition (foreshortening distortion), (Figure 6.2.4).

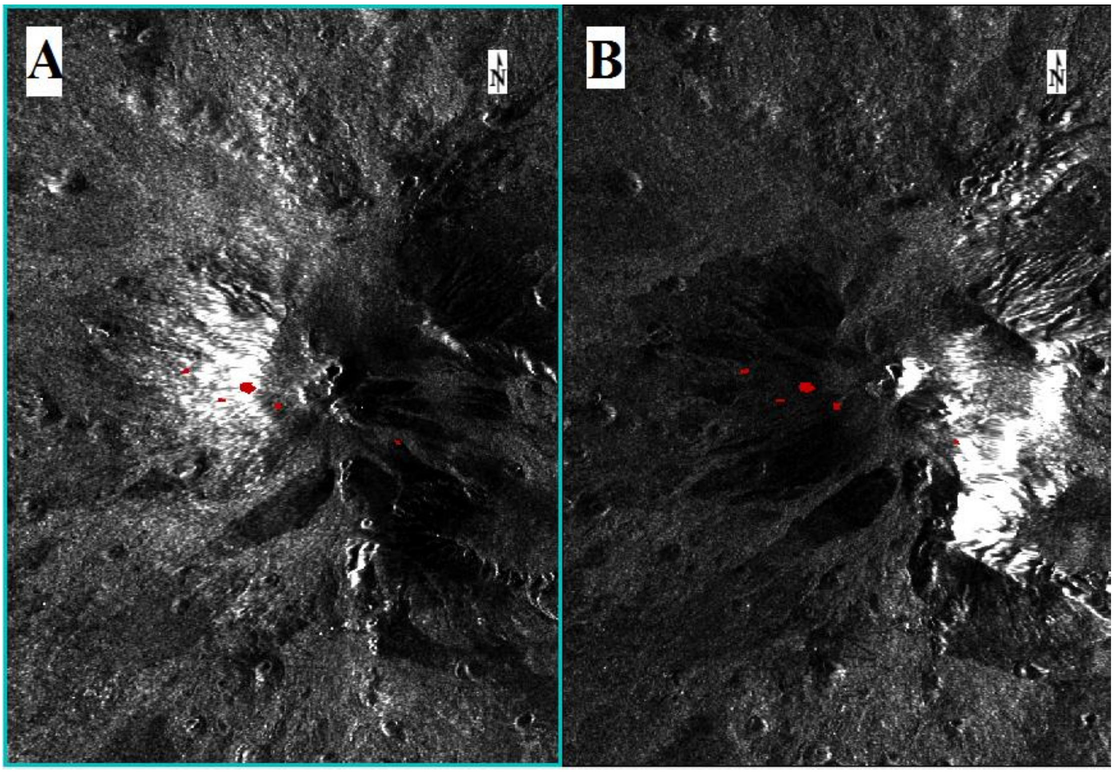


***Figure 6.2.4: The spatial location of the the 1999 lava flow samples in the ascending (A) the descending (B) acquisition geometry in VV polarization.***

Ascending $\sigma_{VV}{}^0$ and $\sigma_{VH}{}^0$ values decrease from 0.3 dB to 0.1 dB and 0.03dB to 0.01dB, but not with a significant and continuous trend, according to the recorded age of the lava flows. For example, in VV polarization, the 1971 and 1975-77 lava flows are characterized by the 0.2dB and 0.18dB sigma0 values. Continuing, the backscatter coefficient value is increased by 0.12dB in the 1977-78 lava flow and again decreased by 0.17dB in the 1980-81 lava flow. This finding isn't observed in descending pass, because the highest backscatter coefficient values are observed in the 1981, 1983, 1985 lava flows, which are located in the middle of the MF1 time period. This fact is contradictory since according to Dierking and Haack (1998) study, recent lava flows are characterized by higher $\sigma^0$ values.

According to the above observations we assume that recent lava flows have lower backscatter coefficient values due to topography (the slopes and their orientation), acquisition geometry and surface roughness.

Although, it is not significant, the surface changes over time and how this fact affects the backscatter coefficient. Thus, we cannot be conclusive about the ability of the backscatter coefficient to discriminate the volcanic products, recorded in different dates, according to the surface change. Our ongoing study is to investigate, the variation degree of the backscatter coefficient due to the topography and the acquisition geometry.

Pyroclastic and scoriae volcanic products have in general lower $\sigma^0$ values in comparison with lava flows, either in both polarizations or in both two satellite orbits. The pyroclastic products, except from the 1999-01 product, reveal the almost the same backscatter coefficient values in VH polarization in both acquisition geometries. The 1999-01 pyroclastic product is attributed with the highest $\sigma^0$ values in descending pass (0.7dB), while in ascending pass the sigma0 value is (0.4dB). Continuing, the scoriae volcanic products present a decrease in the backscatter coefficient values from the oldest (2001) to the most recent (2002), in both polarizations and acquisition geometries.  The above description is more noticeable in the ascending pass.

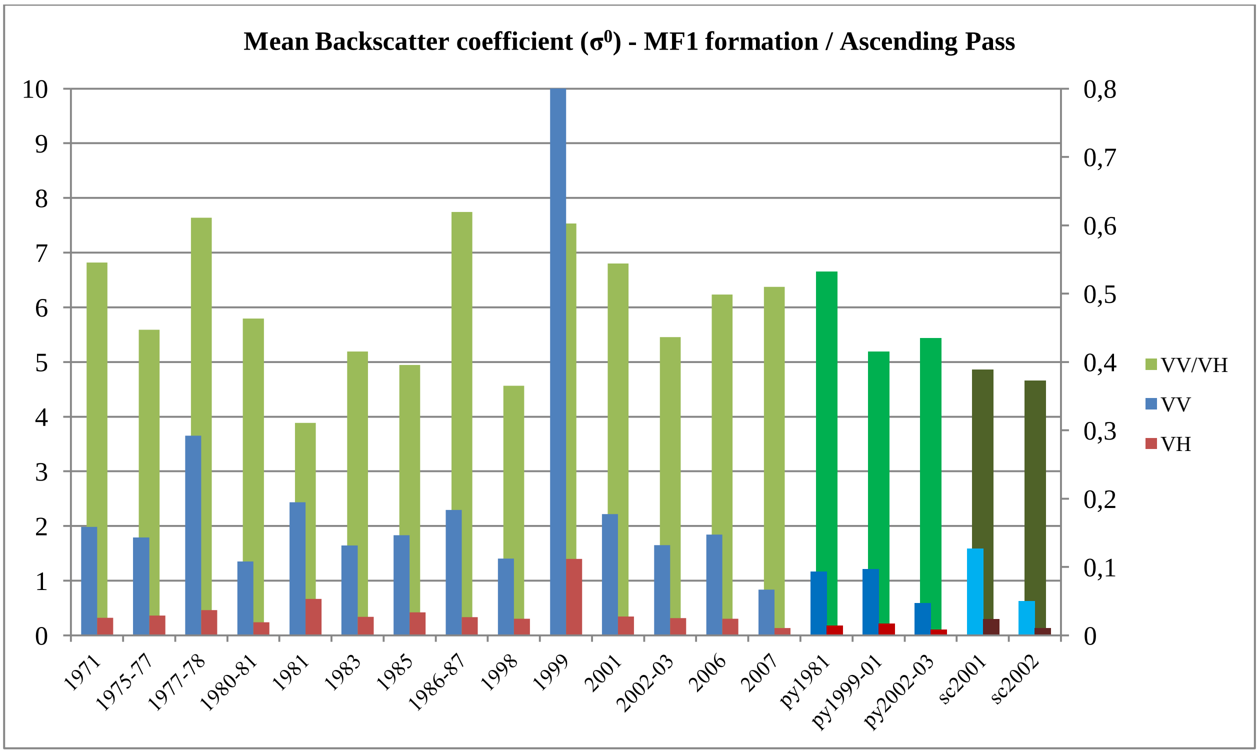


***Figure 6.2.1: Mean $\sigma_{VV}{}^0$, $\sigma_{VH}{}^0$ and $\sigma_{VV/VH}{}^0$ values, extracted for ascending image, of each MF1 volcanic product.***

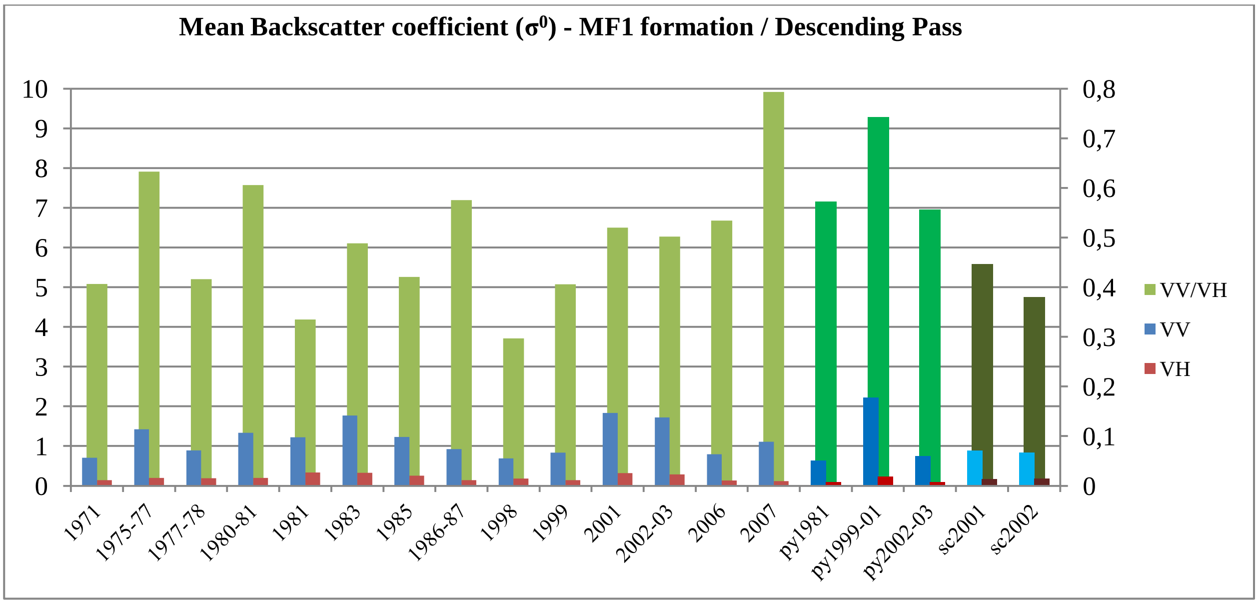


*Figure 6.2.2: Mean $\sigma_{VV}{}^{0}$, $\sigma_{VH}{}^{0}$ and $\sigma_{VV/VH}{}^{0}$ values, extracted for descending image, of each MF1 volcanic product.*

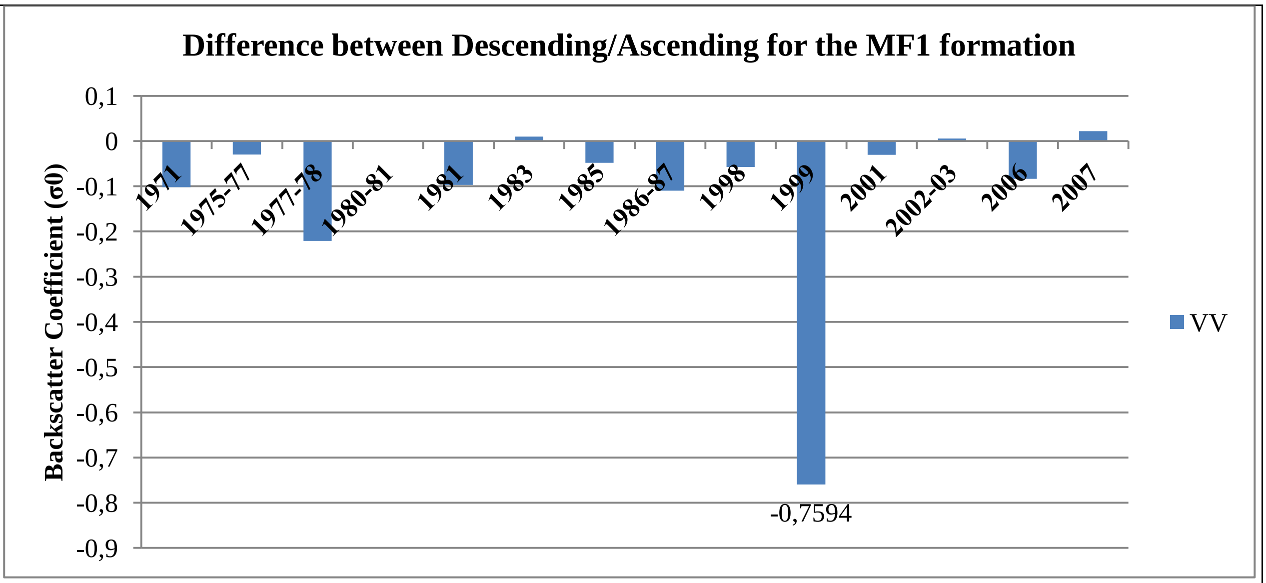


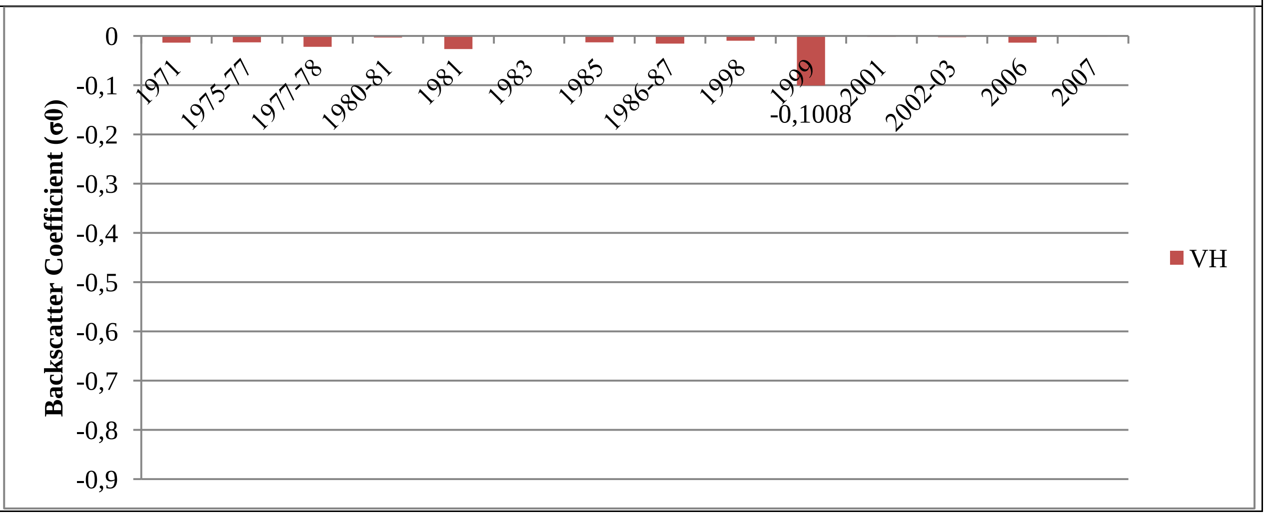

***Figure 6.2.3: Difference between descending and ascending mean $\sigma_{VV}^0$ & $\sigma_{VH}^0$ values, of each MF1 volcanic product.***

- **MF2 Formation - Mean Backscatter Coefficient values**

Figures 6.2.5 and 6.2.6 visualize the mean backscatter coefficient values, of single and cross polarization, extracted from each MF2 volcanic product (lava flows, pyroclastic and scoriae), in ascending and descending pass. Differences between the ascending and descending mean $\sigma^0$ values of each volcanic product are depicted, for both polarizations, (Figure 6.2.7).

The single vertical polarization in ascending acquisition geometry reveals higher backscatter coefficient values in MF2 formation. The backscatter coefficient values decreases with the same trend in both polarizations, but it differs in ascending and descending pass. Also, the $\sigma^0$ decreases from the oldest to the most recent lava flows in both passes.

The 1735-36/58-59 lava flow is characterized by the highest sigma0 values in ascending pass for both VV (0.7 dB) and VH (0.05 dB) polarizations, while in descending pass the values are 0.05 dB for VV and 0.01 dB for VH. According to these findings, we examine the spatial location of the 1735-36/58-59 lava flow, in order to investigate the variables which potentially affect the backscatter coefficient values of the lava flow, in both satellite orbits. Thus, we assume that the combination of the local topography (high slope, more than $30^o$) and the acquisition geometry contribute in the backscatter coefficient values of this lava flow. In Figure 6.2.8, we can see the foreshortening distortions in ascending pass and the shadowing distortions in the descending pass.

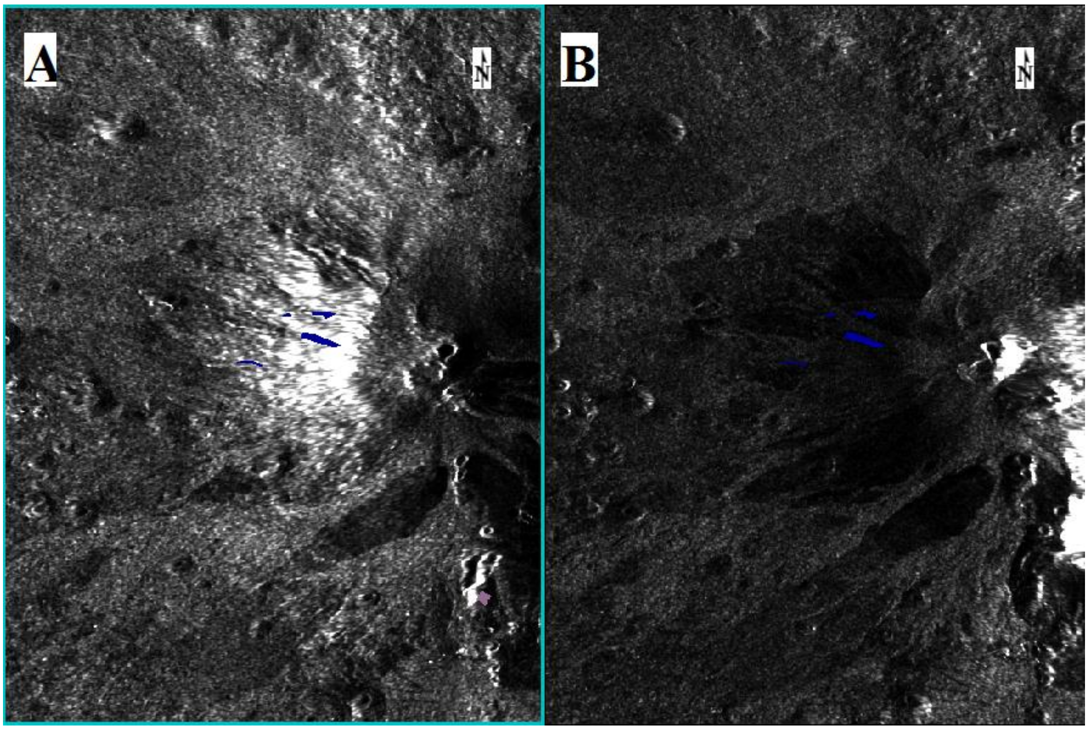


***Figure 6.2.8: The spatial location of the the 1735-36/58-59 lava flow samples in the ascending (A) the descending (B) acquisition geometry in VV polarization.***

The backscatter coefficient values in the 1766 lava flow are the lowest, compared with the other volcanic products, while in ascending pass the σ0 values (0.046 dB) are lower than in descending pass (0.088 dB) According to this result, we investigate the spatial location of the 1766 lava flow, in order to examine the potential effect of the shadowing distortion in the backscatter signal, (Figure 6.2.9).

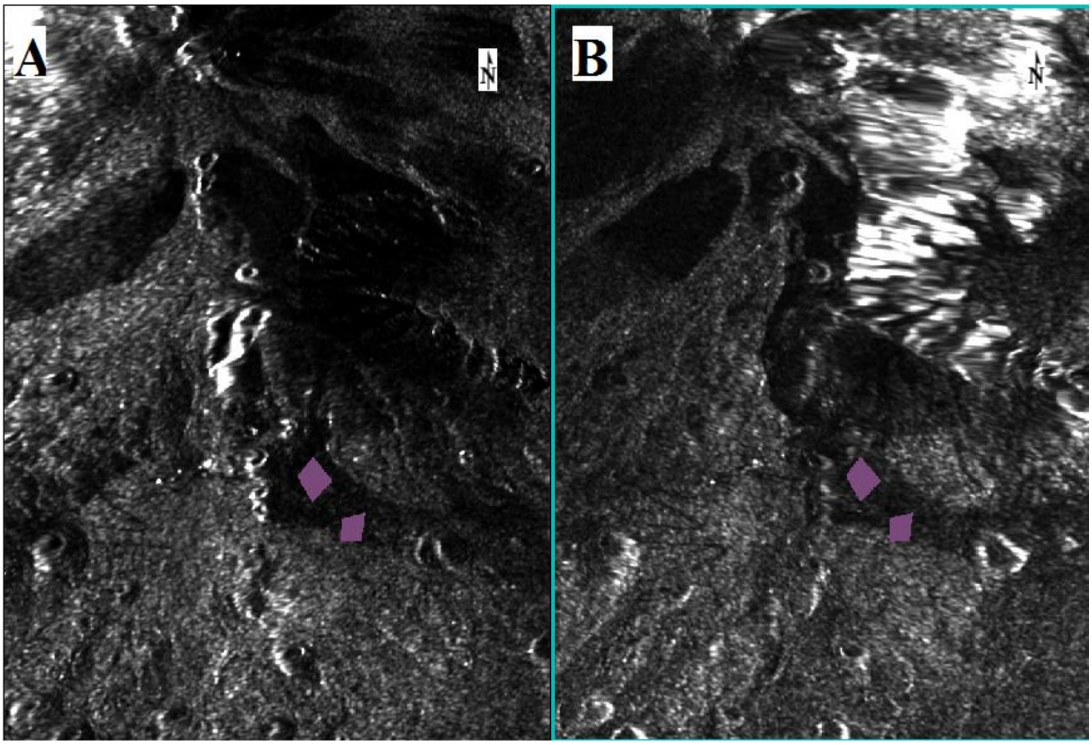


***Figure 6.2.9: The spatial location of the 1766 lava flow samples in the ascending (A) the descending (B) acquisition geometry in VV polarization.***

In Figure 6.2.9, we can see that the 1766 lava flow (1848m altitude) is located behind of two volcanic cones, whose altitude was 1948m. Thus, we hypothesize that in ascending acquisition geometry the backscatter signal in this location was potential affected by the shadowing distortion. In details, we observe that in ascending pass the terrain of the volcanic cones seems more intense than in descending pass and thus probably prevents more the transmition of the backscatter signal in the 1766 lava flow location. Lastly, lava deposits recorded in 1910, 1911 and 1923 are identified by higher $\sigma^0$, as a potential result of the coarser surface and the vegetation presence (mixed pixels).

Pyroclastic deposits are characterized by lower backscatter coefficient values in both acquisition geometries and polarizations. Moreover, it seems that their sigma0 values in ascending and descending pass are almost equal, (Figures 6.2.5-6). In scoriae deposits, the sigma0 values decrease from the older to the younger, with an exception in the 1892 volcanic product. Although, the ascending pass reveal higher $\sigma^0$ values, in comparison with the descending orbit.

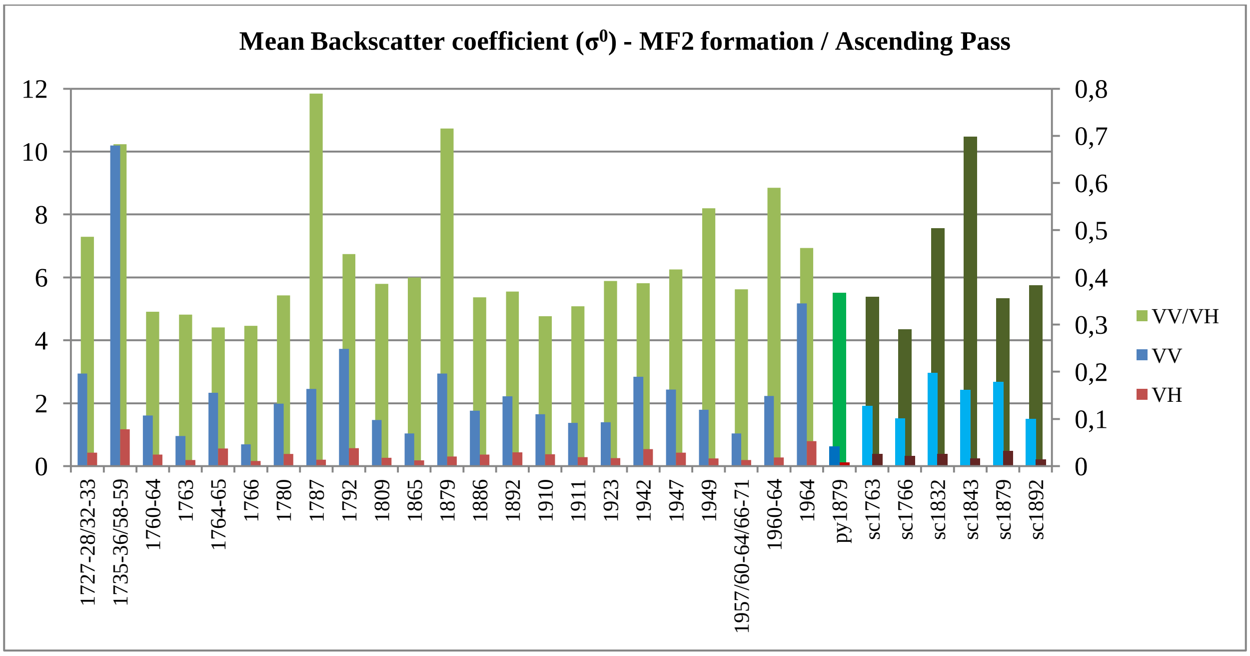


*Figure 6.2.5: Mean $\sigma_{VV}^0$, $\sigma_{VH}^0$ and $\sigma_{VV/VH}^0$ values, extracted for ascending image, of each MF2 volcanic product.*

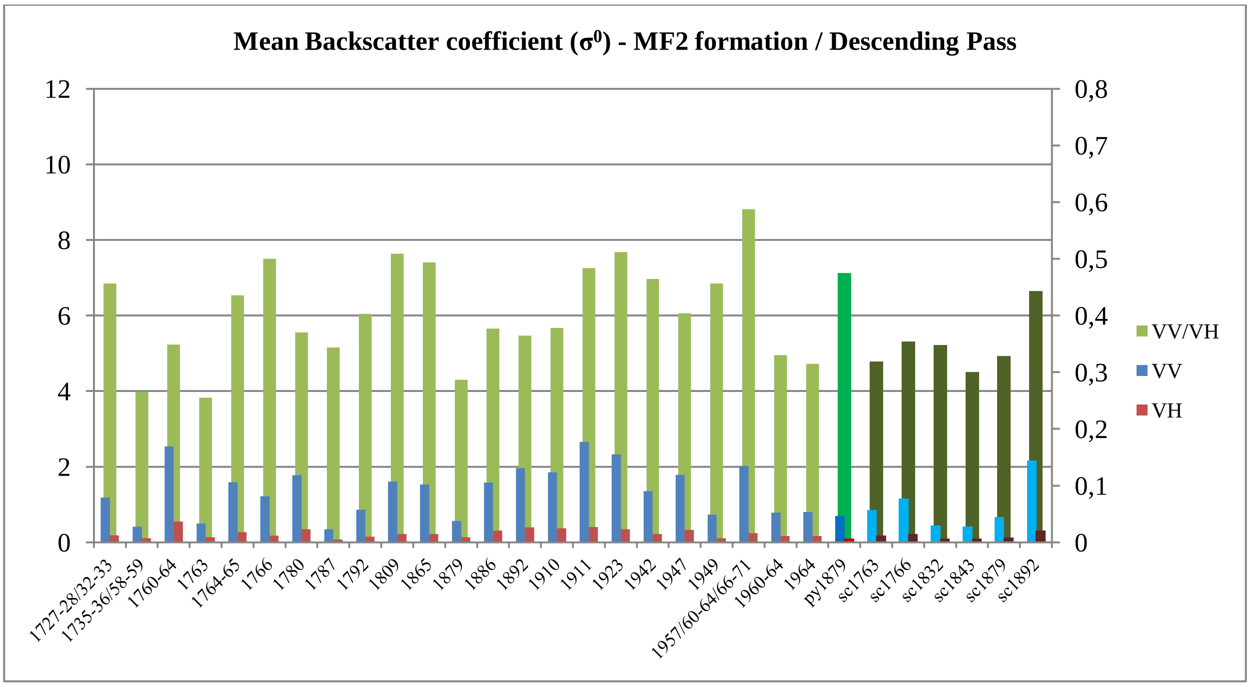


*Figure 6.2.6: Mean $\sigma_{VV}^0$, $\sigma_{VH}^0$ and $\sigma_{VV/VH}^0$ values, extracted for descending image, of each MF2 volcanic product.*

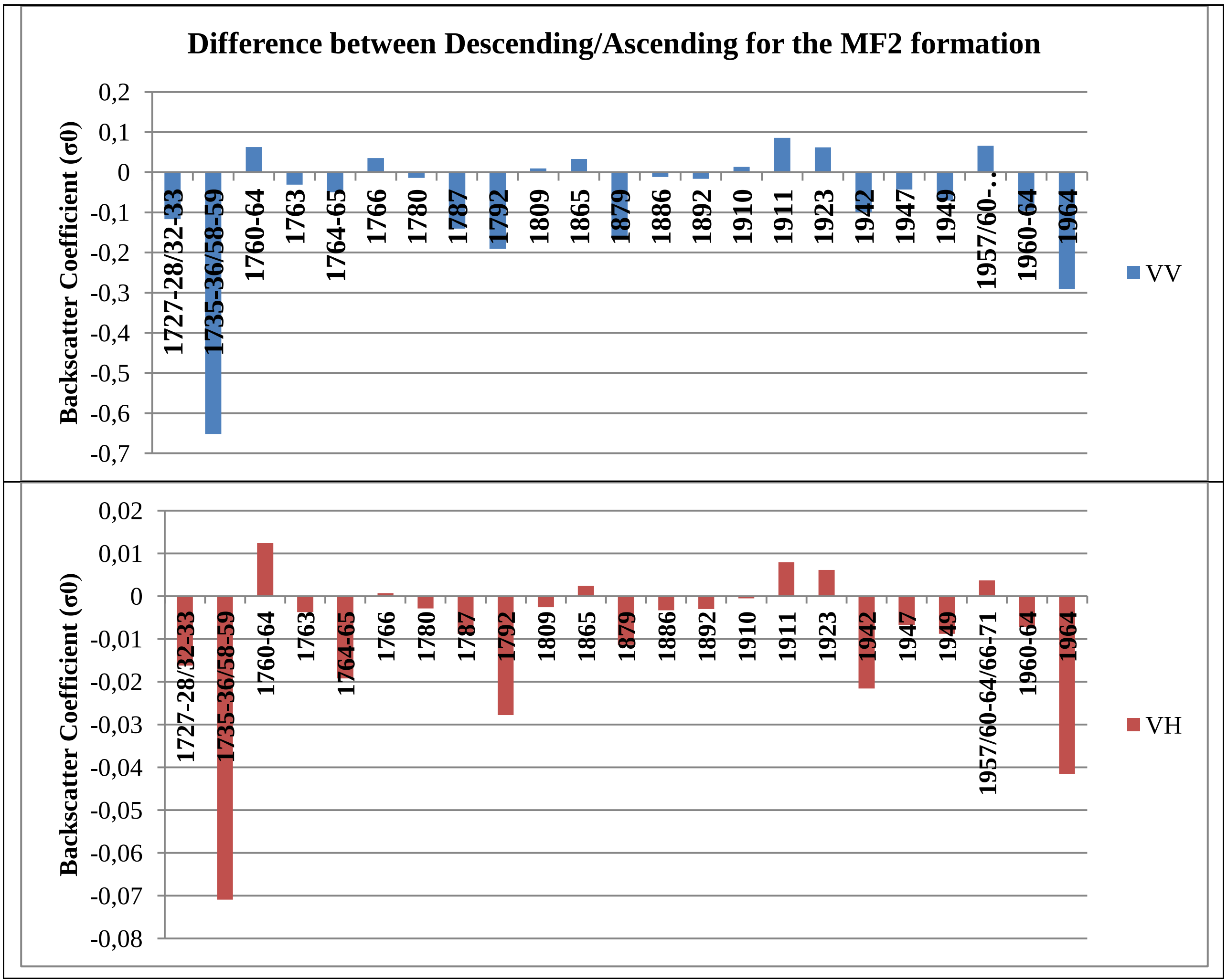


***Figure 6.2.7: Difference between descending and ascending mean $\sigma_{VV}{}^{0}$& $\sigma_{VH}{}^{0}$ values, of each MF2 volcanic product.***

- **MF3 Formation - Mean Backscatter Coefficient values**

Figures 6.2.10 and 6.2.11 visualize the mean backscatter coefficient values of each MF3 volcanic formation (lava flows, pyroclastic and scoriae) derived from the ascending and descending acquisition geometry and from the two polarizations. Differences between the mean $\sigma^0$ values in descending and ascending pass, in single and cross polarization are also depicted (Figure 6.2.12).

The VV polarization reveal higher backscatter coefficient values in all the MF3 volcanic products. However, the MF3 formation is the first formation, where the sigma0 values in ascending pass are not always higher, in comparison with the sigma0 values in descending pass. It seems that the most of the volcanic products are located in lower slopes (15$^{o}$-30$^{o}$) and thus we assume that the topographic effects are diminished, (Figure 6.2.13). Also, the ascending acquisition geometry, which reveals higher sigma0 values, maybe is able to discriminate in a more effective way the different volcanic products.

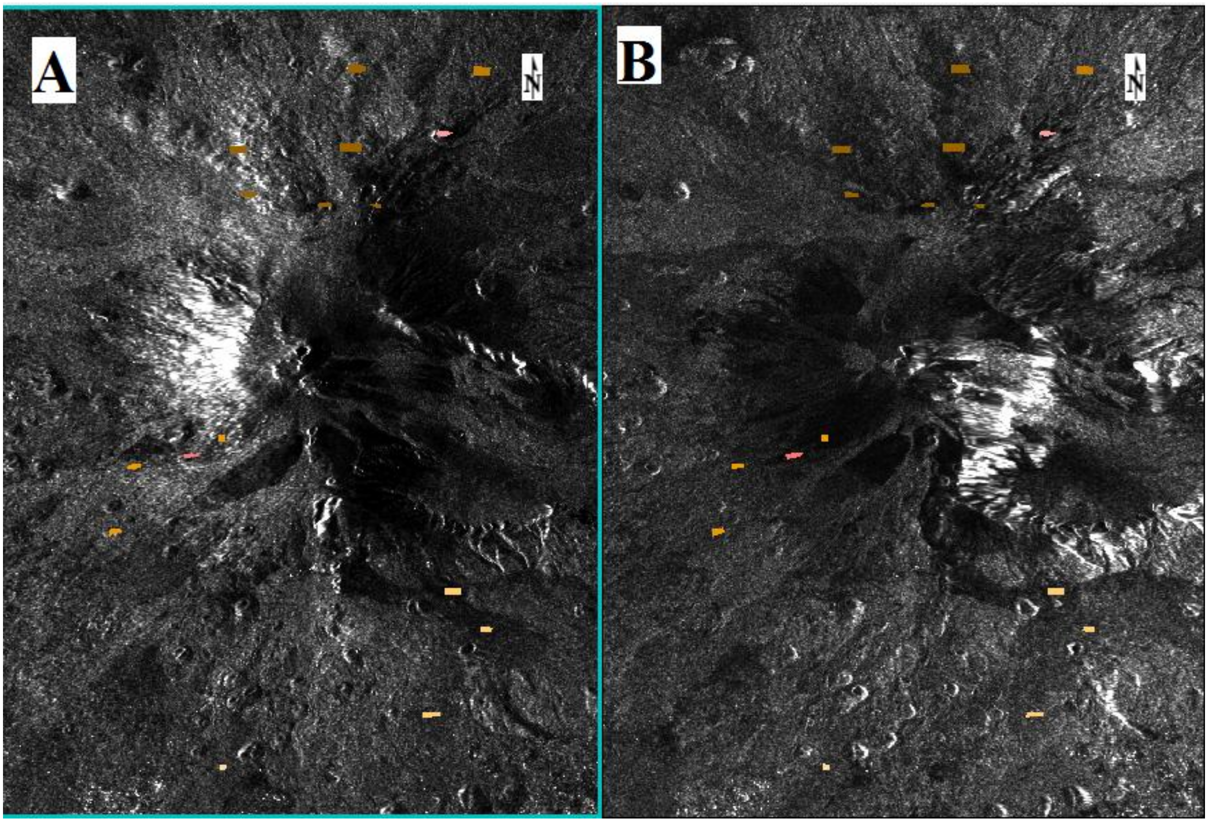


***Figure 6.2.13: The spatial location of the MF3 volcanic products in ascending (A) and descending (B) pass in VV polarization.***

The mean backscatter coefficient values in descending pass and VV polarization increase from the oldest volcanic product to the most recent, while the opposite occurs to the ascending vv, vh and descending vh. According to Spinetti et al (2009) and Dierking and Haack (1998) studies, pahoehoe lava flows (e.g. the 1614-24 lava flows) are described with lower $\sigma^0$ values. This fact is not proved in our study. In particular, the 1614-24 lava flow reveals the highest sigma0 values in ascending pass.

The 1646-47 and 1669 lava flows are identified by a characteristic difference in their backscatter coefficient values in the ascending and descending pass. In particular, in ascending pass the sigma0 values are 0.1 dB and 0.14 dB in VV polarization and 0.02 dB and 0.02 dB in VH. In descending pass the corresponding values are 0.12 dB and 0.13 dB in VV polarization and 0.02 dB and 0.02 dB in VH. Thus, it is indicated that the 1646-47 and 1669 lava flows can be discriminated better in ascending pass and in VV polarization.

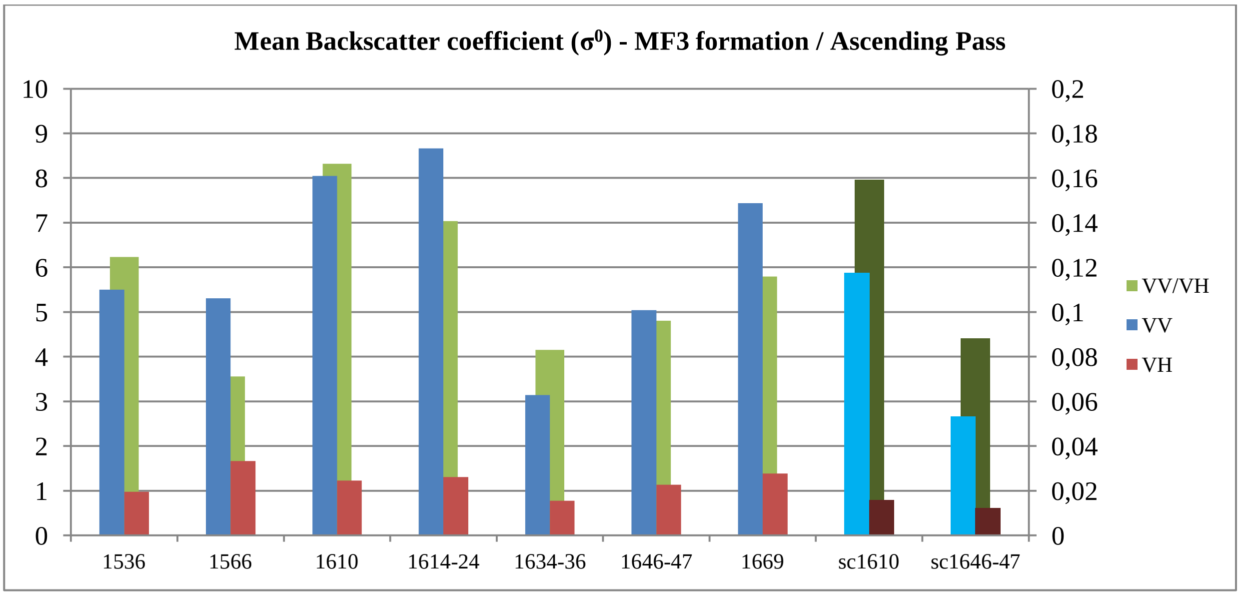


*Figure 6.2.10: Mean $\sigma_{VV}^{0}$ & $\sigma_{VH}^{0}$ values, extracted for ascending image, of each MF3 volcanic product.*

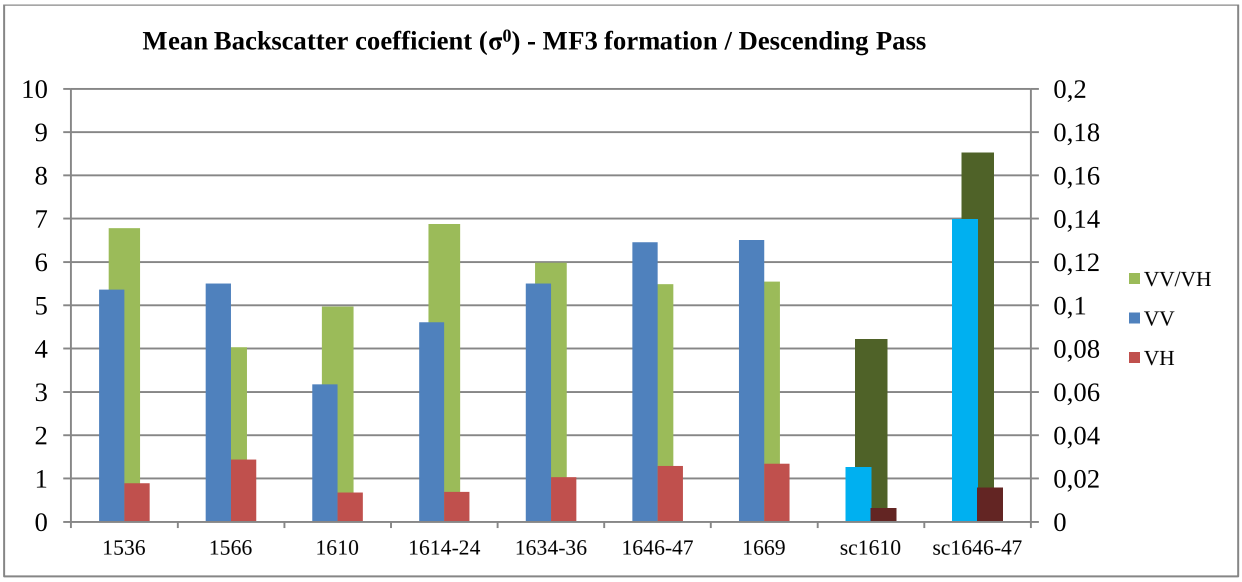


*Figure 6.2.11: Mean $\sigma_{VV}^{0}$ & $\sigma_{VH}^{0}$ values, extracted for descending image, of each MF3 volcanic product.*

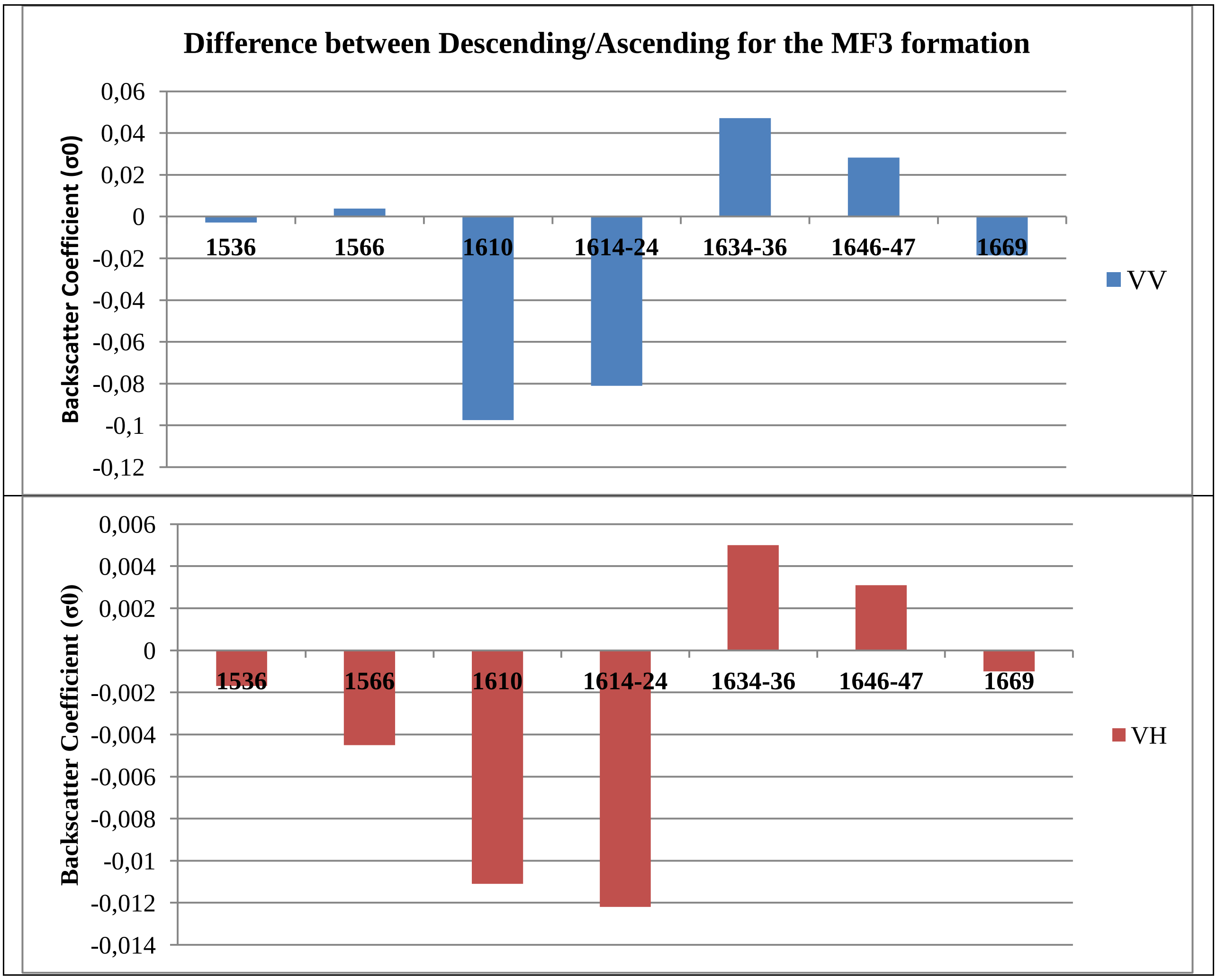


*Figure 6.2.12: Difference between descending and ascending mean $\sigma_{VV}^0$ & $\sigma_{VH}^0$ values, of each MF3 volcanic product.*

- **Ellitico Formation - Mean Backscatter Coefficient values**

Figures 6.2.13 and 6.2.14 visualize the mean backscatter coefficient values from ascending and descending acquisition mode, in single and cross polarization; of each Ellitico volcanic formation (lava flows). Differences between the ascending and descending mean $\sigma^0$ values are, in both polarizations of each lava flow are also depicted, (Figure 6.2.15).

Ellitico volcanic products are identified in a more effective way in single vertical polarization and lesser in cross polarization (VH). On the contrary with the MF1,2,3 volcanic formations, the highest backscatter coefficient values in Ellitico formation are revealed in the descending pass. Figure 6.2.16 depicts the spatial location, where the Ellitico volcanic products are depicted. It seems that the most of the volcanic products are located behind the NW, W ridges of the Valle del Dove. Thus, we hypothesize that the backscatter values in ascending pass are in general low, because the backscatter signal is affected by the local topography and the satellite acquisition geometry (shadowing distortion). This effect reveals lesser in descending pass.

The EPD_21a,b and EPG_25a,b deposits, which are located behind of the N, NW ridges of the Valle del Bove reveal lower backscatter coefficient values in ascending pass than in descending pass. The EP_22ta reveal high sigma0 values in VV polarization in both acquisition geometries. A potential cause of this phenomenon is the contribution of more than one land cover types in the backscatter coefficient, because the sample is located close to an urban area.

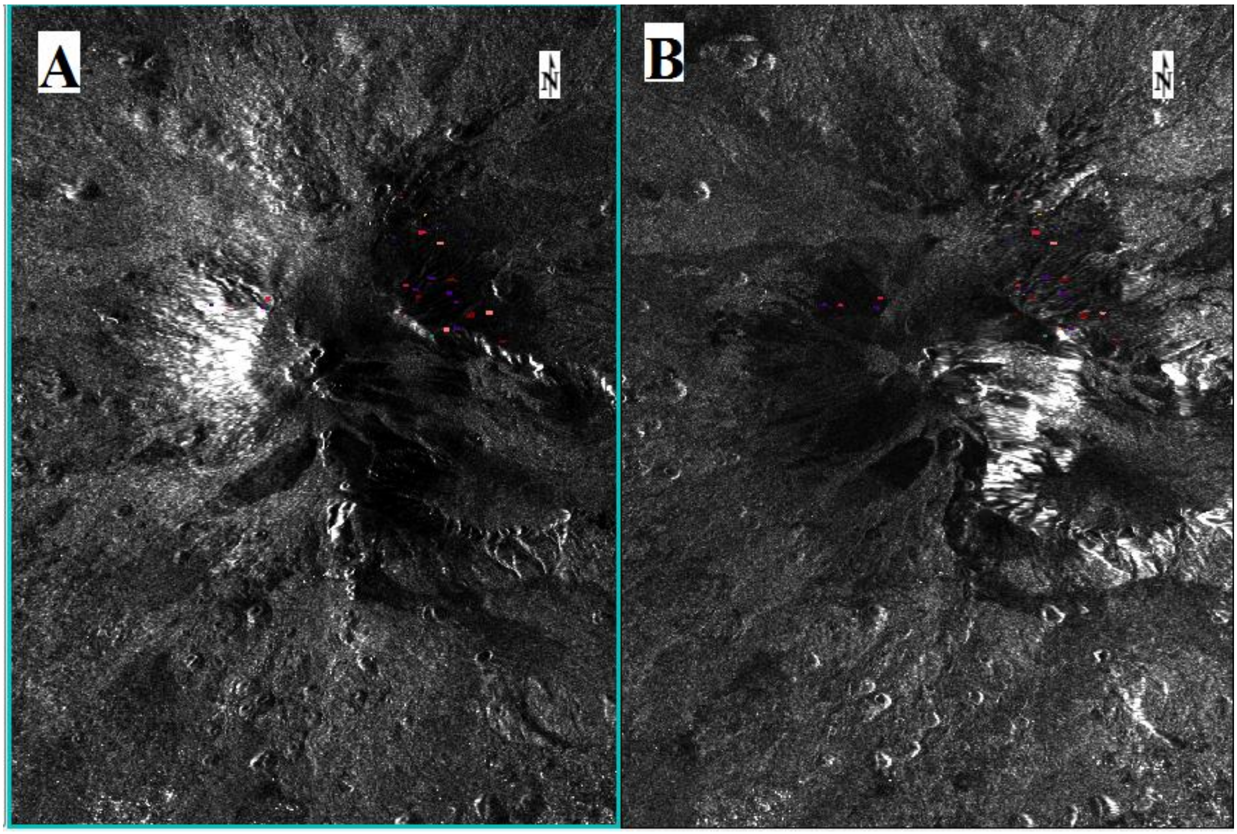


***Figure 6.2.16: The spatial location of the MF3 volcanic products in ascending (A) and descending (B) pass in VV polarization***

Continuing, in descending pass, the highest $\sigma^0$ values are depicted in EC_24cs,pn and EP_22gc lava flows, while in these particular formations, ascending sigma0 values are high as well. Excluding the above volcanic products, we could see that the backscatter coefficient values increase with a linear trend from the EC24 to ESC20 in descending pass, while in ascending pass the trend remain almost stable, with minor variations. Examinating both $\sigma_{VV}^0$ and $\sigma_{VH}^0$ values of each volcanic product in ascending and descending (Figure 6.2.13 & 6.2.14); we could see that when in ascending pass, the sigma0 values of a lava flow decrease, the backscatter coefficient values of the same lava also decrease in descending pass, compared with the other volcanic products and vice versa.

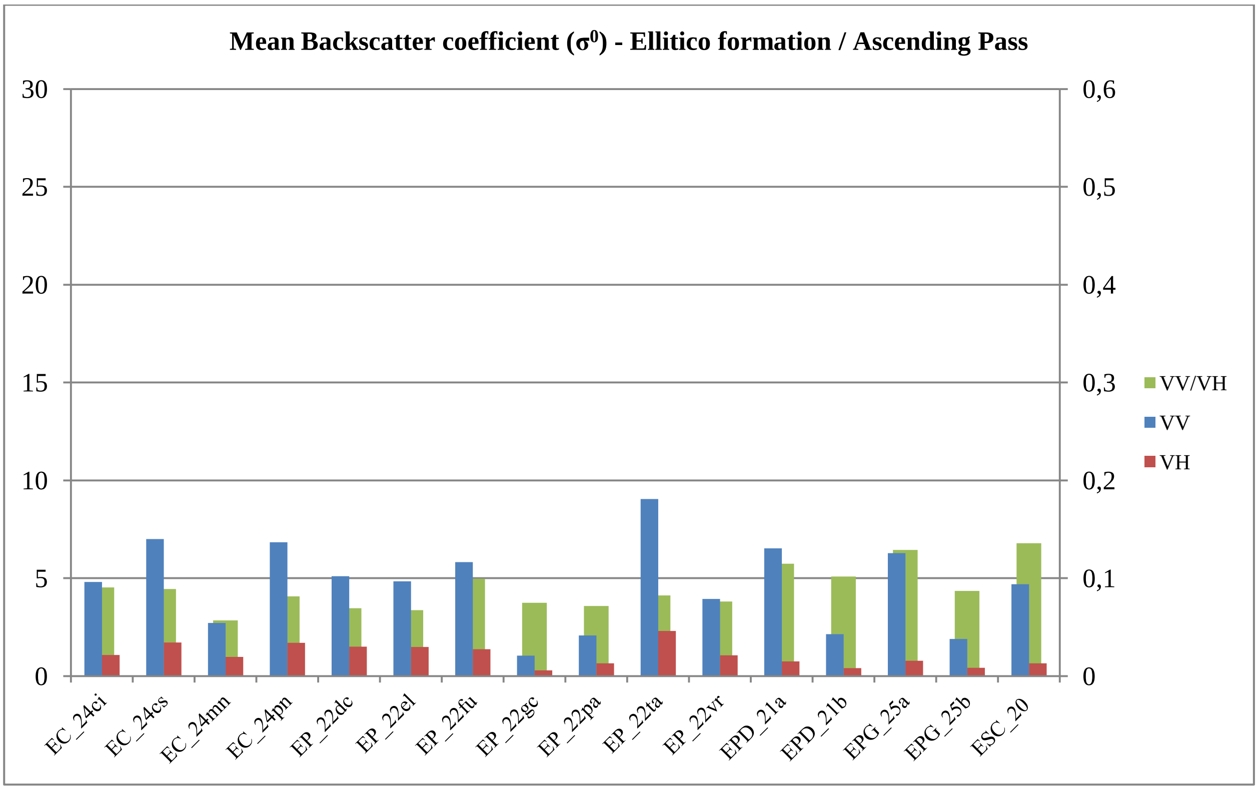


***Figure 6.2.13: Mean $\sigma_{VV}^{0}$, $\sigma_{VH}^{0}$ and $\sigma_{VV/VH}^{0}$ values, extracted of ascending image, for each Ellitico volcanic product.***

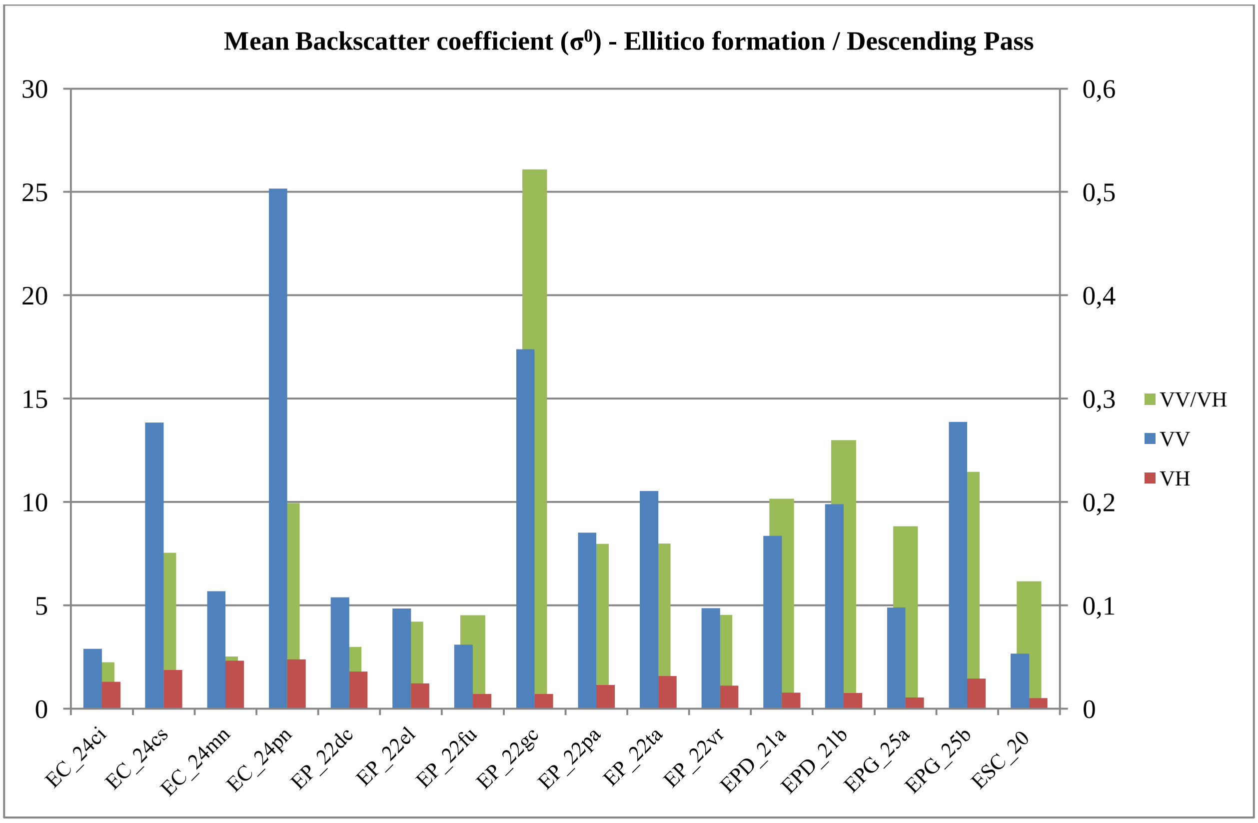


*Figure 6.2.14: Mean $\sigma_{VV}^0$, $\sigma_{VH}^0$ and $\sigma_{VV/VH}^0$ values, extracted of ascending image, for each Ellitico volcanic product.*

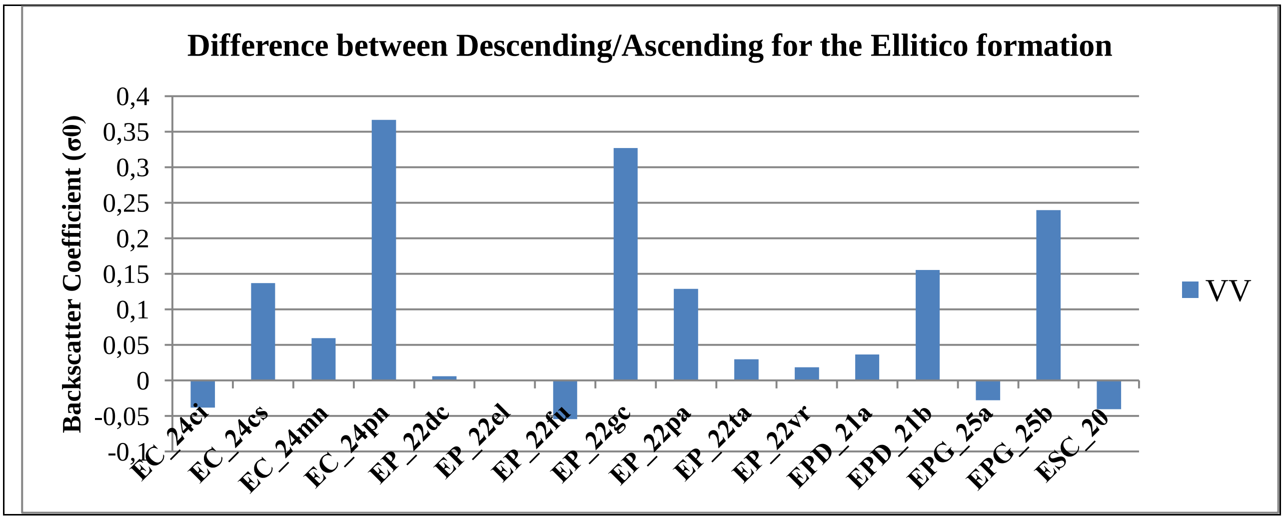

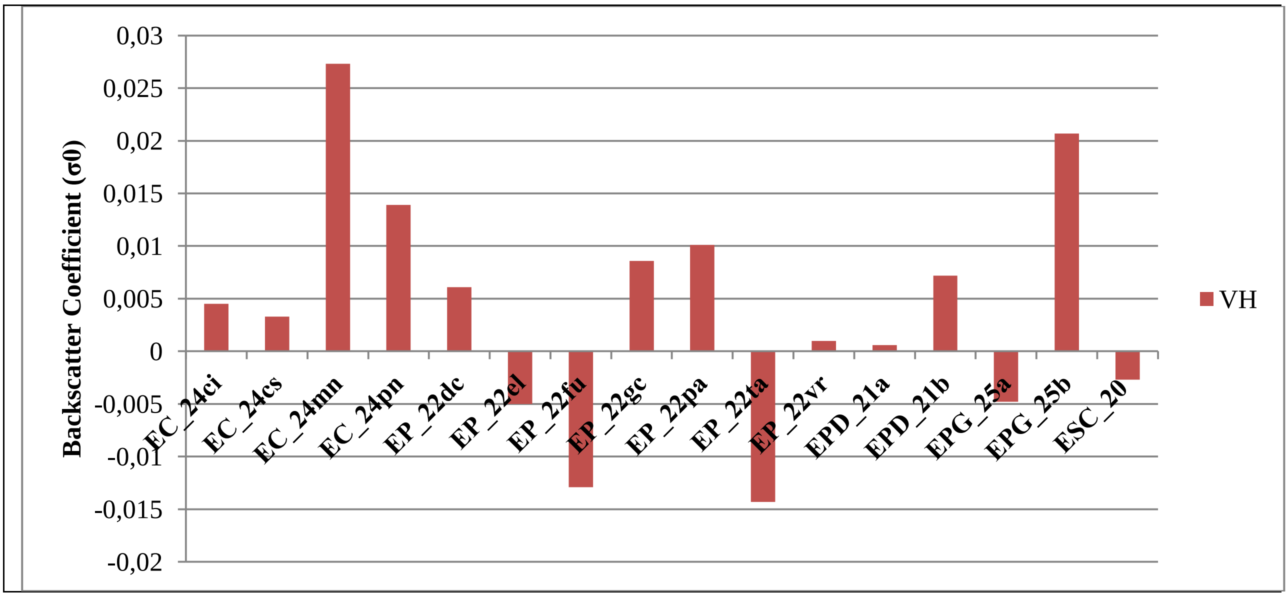


***Figure 6.2.15: Difference between descending and ascending mean $\sigma_{VV}^0$& $\sigma_{VH}^0$ values, of each Ellitico volcanic product.***

- **Temporal Change in Backscatter Coefficient**

According to the temporal plots (Figure 6.2.17), we ascertain that ascending $\sigma_{VV}^0$ and $\sigma_{VH}^0$ values increase from the oldest lava flow (Ellitico formation) to the most recent (MF1 formation), while the opposite occurs in descending $\sigma_{VV}^0$ and $\sigma_{VH}^0$ values. Furthermore, VH $\sigma^0$ values are more spreading, whereas in VV polarization $\sigma^0$ values are more homogeneous, with some exceptions, such as the 1735-36/58-59 and 1999 lava flow deposits.

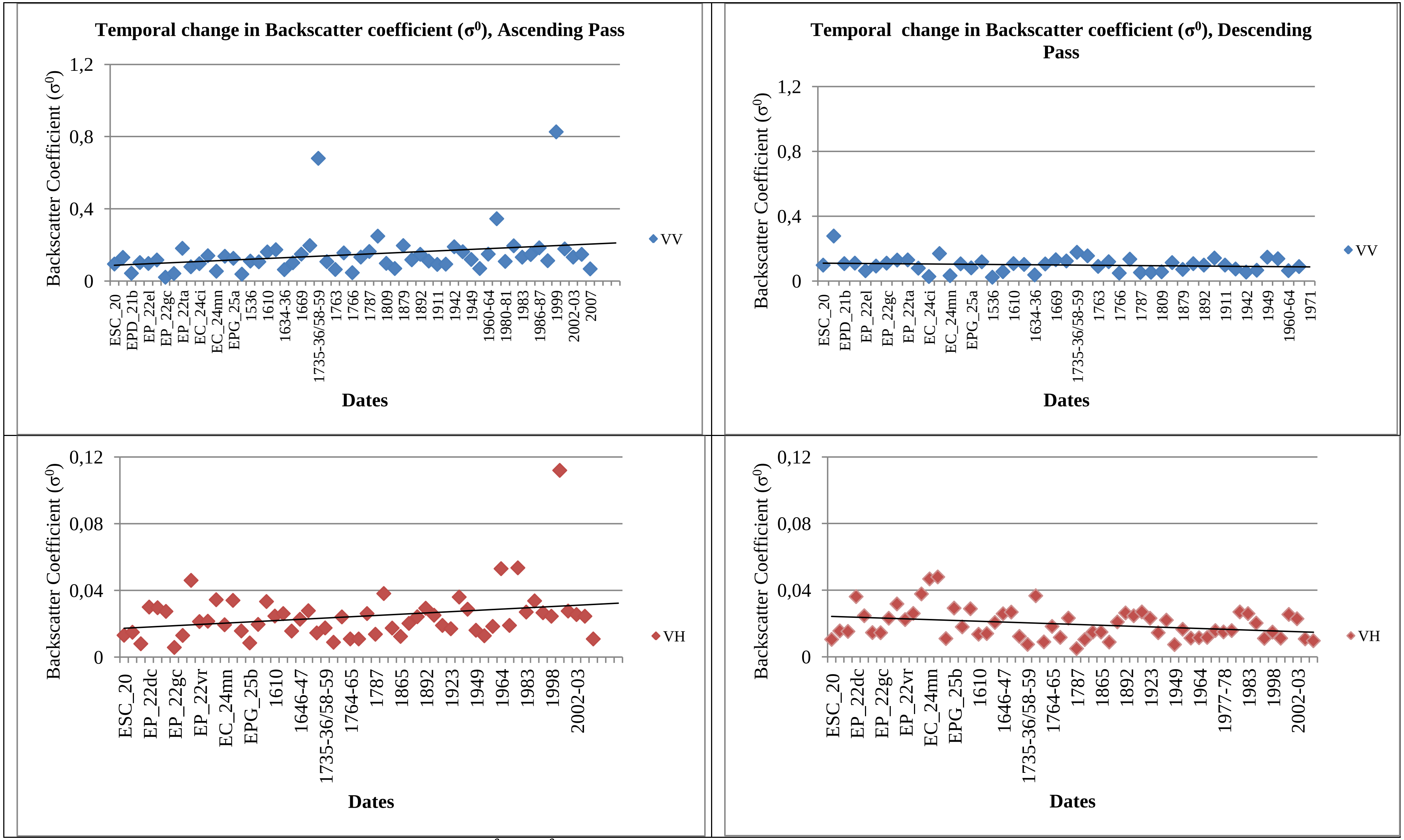


***Figure 6.2.17: Temporal change in mean $\sigma_{VV}{}^{0}$& $\sigma_{VH}{}^{0}$ values of each volcanic formation, extracted from the ascending and descending SAR images.***

- **Correlation between the Backscatter Coefficient ($\sigma^0$) and the Topographic Variables**

For the estimation of the linear correlation between the backscatter coefficient and the topographic variables, we applied the correlation coefficient (r) between the backscatter coefficient values (both polarizations and satellite orbits) and the topographic variables values (slope and aspect) of each volcanic formation (MF1, MF2, MF3 and Ellitico). Table 6.2.1 and 6.2.2 represent the correlation coefficient values between the backscatter coefficient and the aspect and slope, respectively. Also, Figure 6.2.18 visualizes the above results.

Correlation coefficient values are ranging from -1 (negative correlation) to +1 (negative correlation), while 0 depicts none correlation. Thus, we classified the aforesaid values into four categories; (i) r> ±0.60: strong correlation, (ii) ±0.59<r<±0.40: moderate or weak correlation, (iii) ±0.20<r<±0.39: weak correlation and (iv) r> ±0.1: none correlation.

Our primary assumption is that the topography and the backscatter coefficient are not correlated, because the most correlations are moderate or weak and some of them reveal no correlation. An exception to that conclusion are the r values from the $\sigma_{VV}^0$ in (i) ascending (0.69) and descending (-0.85) in the MF3 formation, which are correlated with the aspect, (ii) the descending $\sigma_{VV}^0$ (-0.61) and MF3 $\sigma_{VH}^0$ (-0.64) in the MF2 formation with the slope and (iii) ascending $\sigma_{VV}^0$ (0.60) and MF3 $\sigma_{VH}^0$ (-0.64) in the MF1 formation, with the slope.  Also, we ascertain that almost all the descending r values are negative, while in ascending pass the r values are positive. Finally, correlation coefficient values between the backscatter coefficient in ascending and descending pass and slope are equal in both polarizations, in MF3 and Ellitico volcanic formations.

***Table 6.2.1: Correlation Statistics between Polarizations in Descending, Ascending pass and Aspect of each volcanic formation.***

| | MF1 Formation | | MF2 Formation | | MF3 Formation | | Ellitico Formation | |
|---|---|---|---|---|---|---|---|---|
| | **VV** | **VH** | **VV** | **VH** | **VV** | **VH** | **VV** | **VH** |
| **Descending** | **-0,43** | **-0,24** | **-0,57** | **-0,46** | **-0,85** | **-0,60** | **-0,24** | **-0,08** |
| **Ascending** | **0,27** | **0,30** | **0,52** | **-0,01** | **0,69** | **0,22** | **0,42** | **0,22** |

***Table 6.2.2: Correlation Statistics between Polarizations in Descending, Ascending pass and Slope of each volcanic formation.***

| | MF1 Formation | | MF2 Formation | | MF3 Formation | | Ellitico Formation | |
|---|---|---|---|---|---|---|---|---|
| | **VV** | **VH** | **VV** | **VH** | **VV** | **VH** | **VV** | **VH** |

| | | | | | | | | |
|---|---|---|---|---|---|---|---|---|
| **Descending** | -0,24 | -0,40 | -0,61 | -0,58 | -0,25 | -0,64 | 0,04 | -0,48 |
| **Ascending** | 0,60 | 0,49 | 0,39 | 0,21 | -0,25 | -0,64 | 0,04 | -0,48 |

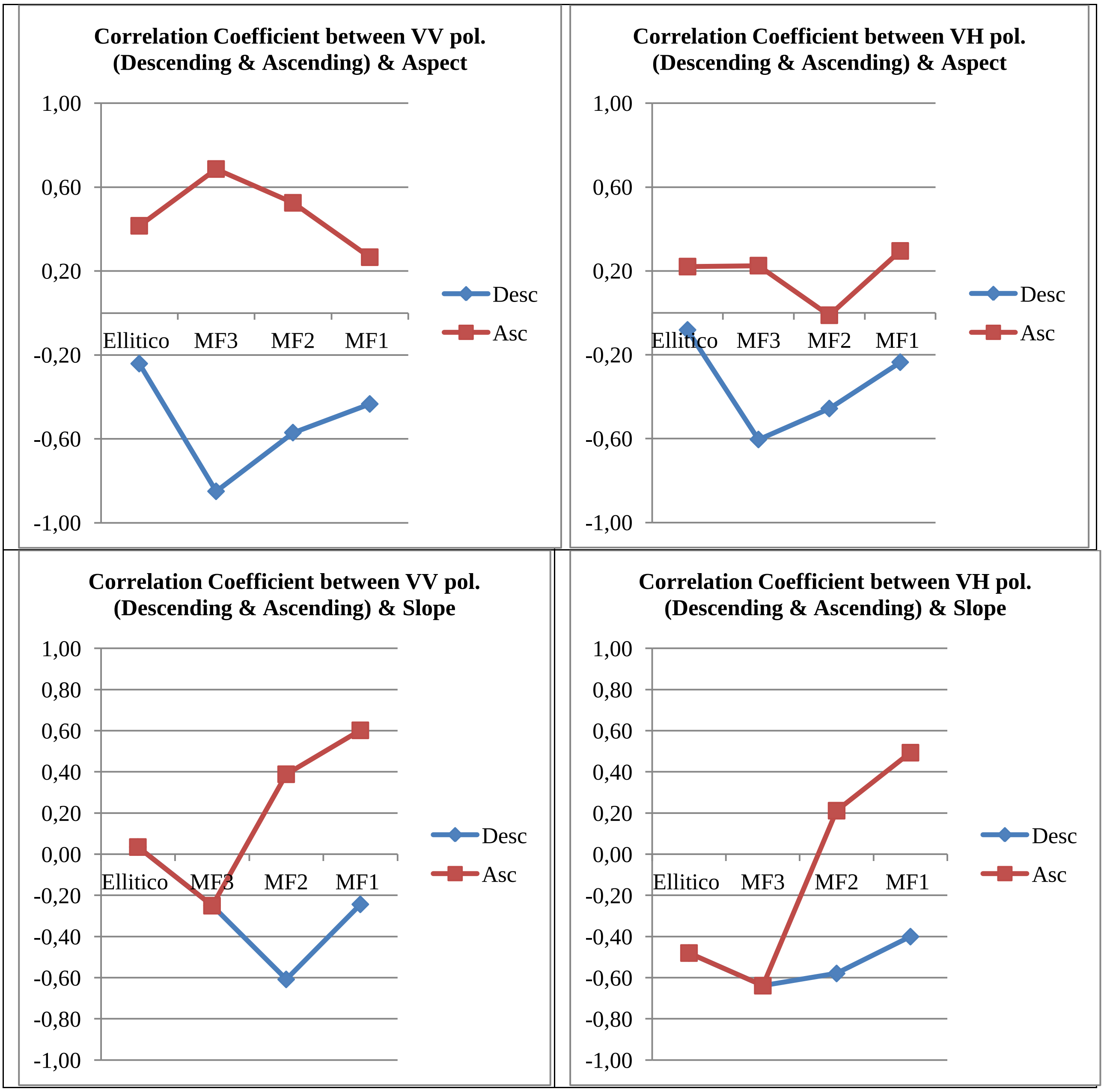


*Figure 6.2.18: Correlation coefficient calculation of each volcanic formation, between VV and VH Polarizations in Descending, Ascending pass and Topographic variables (aspect & slope).*

## 6.3. Temporal Surface Change Analysis

Analyzing the backscatter coefficient mean and the standard deviation values, (Figure 6.3.1), we assume that regardless the local topography (aspect and slope) and acquition mode (ascending and descending); VV polarization give higher mean values in every lava flow, compared with VH polarization. Also, mean backscatter coefficient presents higher variance in VV, in every formation, unlike with the VH which displays lower $\sigma^0$, especially in the descending satellite orbit.

It is not able to discriminate the volcanic formation in the VH polarization, in ascending pass, because the mean and standard deviation slightly change. In ascending pass the VV polarization reveals higher values, with the maximum variance, especially in MF1 formation. However, it seems that the $\sigma_{VH}^0$ values maybe are able to discriminate the volcanic formations in a more effective way. For example, we investigate the backscatter coefficient values in VH polarization, in both satellite orbits and we observe a linear decreasing trend from the most recent formation to the oldest (MF1→MF21→MF3→Ellitico).

Consequently, the ascending pass is probably able to discriminate better the volcanic formations; more in VV polarization and lesser in VH polarization. Likewise, a decreasing trend is detected from the younger to the oldest volcanic formation, regardless the satellite orbit.

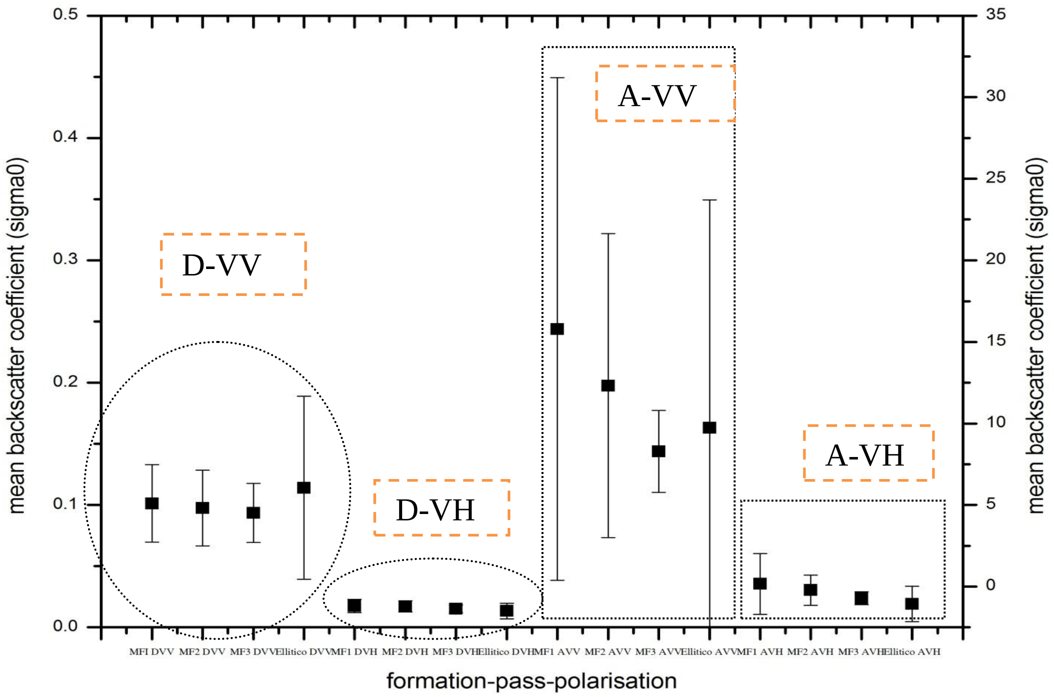


***Figure 6.3.1: Mean backscatter coefficient of the four formations under study (from left to right: MF1, MF2, MF3 and Ellitico), for VV and VH polarization in ascending (A) & descending pass (D).***

*D corresponds to Descending pass, A corresponds to Ascending pass.*

Continuing, Figure 6.3.2 depicts the mean backscatter coefficient values variations in both polarizations and acquisition modes according to the topography categories. From these graphical representations Table 6.3.1 is extracted.

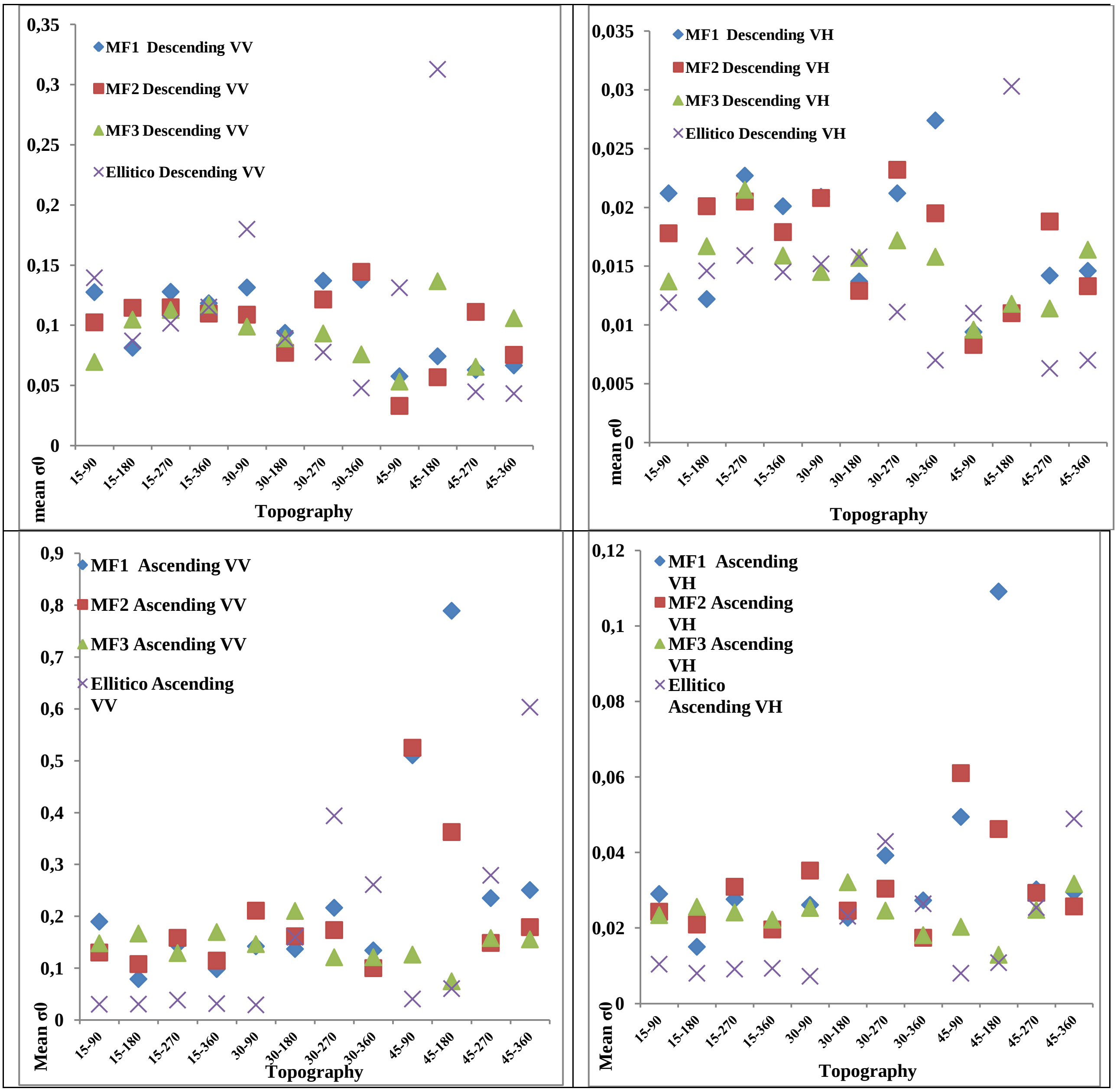


*Figure 6.3.2: Mean backscatter coefficient variation to topography characteristics.*

*Table 6.2.1: The topographic characteristics, where minimum and maximum values were observed, in each volcanic formation.*

| | Ellitico | MF3 | MF2 | MF1 |
|---|---|---|---|---|

| | DESCENDING | | | | | | | |
|---|---|---|---|---|---|---|---|---|
| | **VV** | **VH** | **VV** | **VH** | **VV** | **VH** | **VV** | **VH** |
| **$\sigma^0$ ↑** | 15-90 | 45-180 | 45-180 | 45-360 | 15-180 | 15-180 | 15-270 | 15-90 |
| | 30-90 | | | | 30-360 | 30-90 | 15-360 | 15-270 |
| | 45-90 | | | | 45-270 | 30-270 | 30-90 | 15-360 |
| | | | | | | 45-270 | 30-180 | 30-90 |
| | | | | | | | 30-270 | 30-360 |
| | | | | | | | | |
| **$\sigma^0$ ↓** | 15-270 | 15-90 | 15-90 | ---- | 30-180 | 30-180 | 15-180 | 15-180 |
| | 30-270 | 15-270 | | | 45-90 | 45-90 | | |
| | 30-360 | 15-360 | | | 45-180 | 45-360 | | |
| | 45-270 | 30-270 | | | | | | |
| | 45-360 | 30-360 | | | | | | |
| | | 45-270 | | | | | | |
| | | 45-360 | | | | | | |
| | **ASCENDING** | | | | | | | |
| | **VV** | **VH** | **VV** | **VH** | **VV** | **VH** | **VV** | **VH** |
| **$\sigma^0$ ↑** | 15-90 | 15-90 | 15-180 | 15-180 | 15-270 | 15-270 | 15-90 | 15-270 |
| | 15-180 | 30-90 | 15-360 | 15-360 | 30-90 | 30-90 | 45-180 | 15-360 |
| | 15-270 | 45-90 | 30-180 | 30-180 | 45-90 | 45-90 | | 30-180 |
| | 15-360 | | | | | 45-270 | | 30-270 |
| | 30-90 | | | | | | | |
| | 45-90 | | | | | | | |
| | 45-180 | | | | | | | |
| | | | | | | | | |
| **$\sigma^0$ ↓** | 30-270 | 15-270 | 30-270 | 30-270 | 30-360 | 45-360 | ---- | 15-180 |
| | 30-360 | 30-270 | 45-270 | 45-270 | 45-270 | | | |
| | 45-270 | 30-360 | 45-360 | | | | | |
| | 45-360 | 45-270 | | | | | | |
| | | 45-360 | | | | | | |

In descending pass, MF1 volcanic formation in both single and cross polarizations reveal the maximum topographic categories, while the categories existence decrease by the following order MF1> MF2> Ellitico> MF3. Ellitico formation presents the most topographic categories, when the σ0 values decrease, whereas its presence decreased according to the below order: Ellitico> MF2> MF1> MF3. In general MF2 and MF3 formations are characterized by the moderate backscatter coefficient values, comparing with MF1 and Ellitico formations.

On the other hand, the ascending mode depicts the opposite results in comparison with the descending mode, id est. more maximum sigma0 values in Ellitico, especially in VV polarization, while they decrease like below: Ellitico> MF2> MF1> MF3. Also, it should be pointed it out that when the frequency of the maximum values in VV polarization decreased, in VH polarization increased. Lastly, Ellitico formation had the most categories of minimum $\sigma^0$ values, while their appearance decreased from the oldest to the most recent (Ellitico> MF3> MF2> MF1).

Furthermore, observing the previous table, we could extract the topography categories, in which maximum values are represented, regardless the ascending and descending satellite orbits, (Table 6.3.2).

***Table 6.3.2: Topographic categories (slope, aspect), which were identified by maximum σ0 values, regardless the satellite orbits.***

| | **Ellitico** | | **MF3** | | **MF2** | | **MF1** | |
|---|---|---|---|---|---|---|---|---|
| | **Regardless Ascending/Descending pass** | | | | | | | |
| | **VV** | **VH** | **VV** | **VH** | **VV** | **VH** | **VV** | **VH** |
| | 15-90 | 45-180 | ---- | ---- | ---- | 30-90 | ---- | 15-270 |
| | 30-90 | 45-180 | | | | 45-270 | | 15-360 |
| **$\sigma^0$ ↑** | 45-90 | | | | | | | 30-90 |
| | | | | | | | | 30 (180-360) |
| | | | | | | | | 30-270 |
| | | | | | | | | |
| | 30-270 | 15-270 | ----- | ----- | ----- | 45-360 | ---- | 15-180 |
| | 30-360 | 30-270 | | | | | | |
| **$\sigma^0$ ↓** | 45-270 | 30-360 | | | | | | |
| | 45-360 | 45-270 | | | | | | |
| | | 45-360 | | | | | | |

According to the above table, we could probably claim that:

- For the categories that present the highest sigma0 values, in both polarizations and satellite orbits; potentially the backscatter signal is more affected by the roughness and less by the topography/viewing angle relation.
- The Ellitico formation, in VV and VH polarization, is predominated by greater slopes (30-45).
- The highest and lowest sigma0 values are depicted in East ($90^o$) and South ($180^o$) aspect orientations.
- In MF3 both polarizations and in MF1-MF2 single vertical polarizations, the backscatter signal is differentiated very much and it is proved by the no existence of one common topographic category.
- The VH polarization minimum and maximum values, in MF2 formation are observed in the highest slopes ($30^o$-$45^o$) and in North, East and West orientations.
- In MF1 formation, in VH polarization, we detect that maximum and minimum values are revealed in lower slopes ($15^o$-$30^o$), in North-South aspect.

Concluding, we could potentially claim that mean backscatter values are discriminated better in ascending pass. The VH polarization maybe is more suitable in differentiation of the volcanic formations because $\sigma_{VV}^0$ values present high variance. Regardless the ascending-descending acquisition modes; a linear decreasing trend is observed in VH polarization values, from the most recent volcanic formation (MF1) to the oldest (Ellitico). Additionally, we could probably infer that lava flows recorded in different dates are differentiated in a more effective way in VH polarization and in descending pass, due to the lower variance in their values. Also, the backscatter signal is increased from the oldest to the youngest formations almost linearly.

According to the topography; backscatter values are more affected by the roughness in Ellitico, in higher slopes ($30^o$-$45^o$) and East aspect. On the other hand, sigma0 values influenced more by the topography than by the rugosity in MF3, MF2 and MF1 formations. Maybe, roughness affects more the North and South slopes orientations.

# Chapter 7: Discussion

## 7.1. Hyperspectral Data Analysis

Limitations:

- Larger reflectance gaps in the SWIR region than in the VIS part of the EMS, confirm the much higher atmospheric contributions in the Hyperion SWIR range *(Li et al, 2015; Amici et al, 2014).*
- Due to Hyperion's low signal to SNRs (VNIR<200 & SWIR<100), it is difficult to retrieve spectral information of low reflectance materials *(Li et al, 2015; Amici et al, 2014; Stretch & Viles, 2002),* such us lava in volcanic terrains.
- Hyperion's medium spatial resolution (30m) generally induces mixtures in the overall pixel's reflectance and therefore the spectral signatures of the retrieved endmembers have a high probability of corresponding to a combination of different surface materials.
- There is a constant presence of water vapor absorption centered in 1.14μm, especially in 2009 image and another one in 1.78μm, mostly in 2007 image.
- Constant high reflectance responses in the whole 2007 image. The examination of AOD values and cloud fraction in the three acquisition dates indicates this is probably not due to atmospheric phenomena such aerosol load or low altitude cloud presence.

**Mongibello Torre del Filosofo 1 Formation (1971-2007) – MF1**

The spectral signatures of the endmembers extracted from the 2007 and 2009 images present with low variation. Recent lava flows reveal a weak absorption in 0.4-0.5μm. According to Table 7.1.1, lava deposits reflectance range is 8-10% for 2007, 1.5-5% for 2009 and 2.5-6% for 2012. The difference in reflectance response, between the 2009 and 2012 images is ~1%. Pyroclastic and scoriae endmembers have mainly lower reflectance in the three datasets, compared with lava flows. Moreover, reflectance doesn't increase from the recent to the old lava flows and even some of them present the same spectral pattern and reflectance magnitude.

All the 2007 endmembers spectra, except from 2001 scoria volcanic product, show an absorption in 1.78μm. Chlorophyll absorption in 0.7μm is observed in the older lava flows. Absorptions in 2.1μm and 2.3μm, are located in 1971, 1985, 1986-87, 1998, 2006 lava flows and 2001 scoriae.

Potential iron presence, in the 1-1.3μm area, is observed in almost every volcanic product (lava flows, pyroclastic and scoriae). A strong water absorption (1.14μm) is observed only in the 2001 lava flow.

The endmembers spectra extracted from 2009 dataset are characterized by a water (1.14μm) absorption. The chlorophyll absorption (0.7μm) is present in every lava flow and in the 2001 scoriae deposit. Absorptions in 2.1μm and 2.3μm continue to exist in the same lava flows, as in 2007 image. Pyroclastic and scoriae deposits don't reveal any of the above absorptions..Iron presence (1-1.3μm absorption) is depicted in 1975-77, 1977-78, 1980-81, 1981, 1983, 1985, 2002-03, 2007 lava flows and in 2002-03 pyroclastic deposit.

In the 2012 dataset, the oldest lava flows are characterized by the chlorophyll absorption. Potential iron presence in the 0.78-1μm spectral area is also present in the same endmembers, for the three dates. Water absorptions are not present in most endmembers with the exception on 1986-87 and 2001 lava flows. On the contrary, the reflectance is increased at 1.14μm. A continuous reflectance increase is also observed between 1.45-1.78μm. This particular spectral region always discriminates the 2009 from the 2012 endmembers.

Specific endmembers reveal higher or the same reflectance response in 2009 than in 2012. For example, the reflectance of the 1971 lava flow is higher in 0.78-1.15μm. The 2001 lava flow reflectance response is higher by 2% within 1.45-1.78μm. The 2006 lava flow reflectance is higher by 0.1% within 0.7-0.9μm. The 2007 lava flow reveals the same reflectance in both images within 0.7-1.15μm. The 2012 endmembers that have lower reflectance responses are usually characterized by an absorption in 0.7-0.9μm. The 2007 and 2012 endmembers present similar spectral patterns, although the 2002-03 pyroclastic and 2001 and 2002 scoriae deposits do not present the aforementioned similarities. Also, the 2001 and 2002 scoriae deposits present some similarities in the spectral pattern between the 2009 and 2012 images.

According to the above observations, Hyperion is able to identify the temporal changes in lava flows between the three datasets, according to their reflectance response or their spectral pattern. The endmember spectra are characterized by specific absorptions which depict the presence of vegetation (lichen cover), water vapor and iron. The spectral patterns are homogeneous in the three datasets, with some exceptions in 2012 image. The most characteristic temporal changes are depicted in the SWIR region, where the differences in reflectance response are more obvious. However, the most changes in spectral patterns between the volcanic products occur in the VNIR region.

***Table 7.1.1: The description of the spectral characteristics of each MF1 endmember of the 2007, 2009 and 2012 datasets. The description of the similarities and differences in the spectral pattern and reflectance response between dates is also provided.***

| | **2007** | **2009** | **2012** |
|---|---|---|---|
| **1971** | Refl. response: 9% (VNIR) & 8% (SWIR)<br>**1.78µm:** Absorption<br>**2.3µm:** Weak absorption<br>Differences:<br>2009: No absorption in 0.7µm<br>2012: Decrease by 0.5% in 1.1-1.3µm | Refl. response: 5% (VNIR) & 3.9% (SWIR)<br>**0.7µm:** Chlorophyll Absorption<br>**1.14µm:** Water absorption<br>**0.78-1.15µm:** Higher refl., comparing with 2012<br>**1.15-2.35µm:** Lower refl., comparing with 2012 | Refl. response 4%<br>**0.78-0.87µm:** slight decrease of the refl. response<br>Potential iron presence |
| **1975-77** | Refl. response: 9.5% (VNIR) 8% (SWIR)<br>**0.7µm:** Weak Chlor. Absorption (potential vegetation presence)<br>**1-1.3µm:** Decreased refl.<br>**1.45-1.75µm:** "Smooth" spectral pattern<br>**1.78µm:** Absorption<br>Spectral pattern is almost the same with 2009 and 2012 images | Refl. response: ~2%<br>**0.7µm:** Weak Chlor. Absorption (potential vegetation presence)<br>**1-1.3µm:** Decreased refl.<br>**1.14µm:** Weak water absorption<br>**1.45-1.78µm:** Reflectance stable<br>Difference by 2% in overall reflectance, comparing with 2012 | Refl. response: ~5%<br>**0.7µm:** Weak Chlor. Absorption (potential vegetation presence)<br>**1-1.3µm:** Decreased refl.<br>**1.45-1.78µm:** Reflectance increases by 0.3%. |
| **1977-78** | Spectral behavior is the same with 1975-77 lava flow.<br>Refl. response: 9-10% (2007), 2-3% (2009), 5-6% (2012) | | |
| **1980-81** | Spectral behavior is the same with 1975-77 lava flow.<br>Refl. response: 8-10% (2007), 3% (2009), 5% (2012)<br>Difference: 2.1µm: Refl. response increases, comparing with SWIR range (2007) | | |

| | | | |
|---|---|---|---|
| **1981** | Refl. response: 8-8.5% (VNIR), 6.5-7% (SWIR)<br>**0.7µm:** Weak Chlor. Absorption (potential vegetation presence)<br>**1-1.3µm:** Decreased refl.<br>**1.78µm:** Absorption<br>**2.1-2.35µm:** Refl. increase<br>The same spectral pattern with 2009 and 2012 | Refl. response 3.5%<br>**0.7µm:** Chlor. Absorption<br>**1.14µm:** Water absorption<br>**1-1.3µm:** Decreased refl.<br>**2.1µm:** Difference by 2% in overall reflectance | Refl. response 5.7%<br>**0.7µm:** Chlor. Absorption<br>**1.14µm:** Refl. increase |
| **1983** | Refl. response: 10.5%<br>**0.7µm:** No Absorption<br>**1-1.3µm:** Decreased refl.<br>Potential iron presence<br>**1.78µm:** Absorption<br>Similar spectral pattern with 2012 | Refl. response 5.5-6%<br>**0.7µm:** Chlor. Absorption<br>**1.14µm:** Water absorption<br>**1 -1.3µm:** decrease by 1%<br>Potential iron presence<br>**1.45-1.78µm:** Refl. increase (“curved” shape)<br>**0.8-0.9µm:** Difference by >0.1% in refl., comparing with 2012<br>Difference by 0.5% in the rest spectrum. | Refl. response 6%<br>**0.7µm:** No Absorption<br>**1.14µm:** Water absorption<br>**1.45-1.78µm:** Refl. increase (“curved” shape) |
| **1985** | Refl. response: 9% (VNIR), 7.5% (SWIR)<br>**0.7µm:** Weak Chlor. Absorption<br>**1-1.3µm:** Decreased refl.<br>(stronger, comparing with 2009 and 2012)<br>**1.78µm:** Absorption | Refl. response: 3%<br>**0.7µm:** Weak Chlor. Absorption<br>**1.14µm:** Water absorption<br>**1.78µm:** Weak absorption<br>**1-1.3µm:** Decreased refl. | Refl. response: 4%<br>**1-1.3µm:** Refl. decrease<br>**1.45-1.78µm**: Slight increase (more curved).<br>**2.3µm:** Weak absorption |

| | | | |
|---|---|---|---|
| | **2.3µm:** Weak absorption <u>Difference:</u> 1.45-1.75µm. "Smooth" spectral pattern<br><br>More similarities with 2009. | **2.3µm:** Weak absorption Reflectance difference with 2012 <1%. | |
| **1986-87** | Refl. response: 9%<br><br>**0.7µm:** Chlor. Absorption<br><br>**1.78µm:** Absorption<br><br>**2.3µm:** Weak absorption either *(Li et al, 2015)*<br><br>Refl. response decreases at 1.15µm and remains stable | Refl. response 3% (IR) 4% (VIS)%<br><br>**0.7µm:** Chlor. Absorption + red edge (vegetation presence)<br><br>**1.14µm:** Weak water absorption<br><br>**1.45-1.75µm:** "Smooth" spectral pattern<br><br>Difference by 2% in overall reflectance, comparing with 2012<br><br>Spectral pattern similar with 2012 | Refl. response 4% (IR), 5% (VIS)<br><br>**1.14µm:** Increased reflectance<br><br>**1.78µm:** Same reflectance value (3%) with 2009 |
| **1998** | Refl. response: 10%<br><br>**1.15-1.3µm:** Decreased reflectance<br><br>**1.5-2.35µm:** Increased refl. response<br><br>**1.78µm:** Absorption<br><br>**2.3µm**: Absorption | Refl. response: 2.5-3%<br><br>**0.7 & 1.14µm:** Slight absorption<br><br>**1.15-1.3µm:** Spectral pattern stable compared with the 2007 and 2012 | Refl. response: 8% (VIS), 4% (IR)<br><br>**0.7µm:** Chlor. Absorption<br><br>**1.15-1.3µm:** Steep slope decrease (from 7 to 4.5 %)<br><br>**2.3µm**: Absorption, |
| **1999** | Same spectra with 1975-77 lava flow<br><br>Refl. response: 7% (2007), 2.5% (2009), 3.5% (2012) | | |
| **2001** | Refl. response: 10%<br><br>**1.14µm:** Water absorption<br><br>**1.78µm:** Absorption<br><br>Similar spectral pattern with 2012 | Refl. response ~5%<br><br>**0.7µm:** Weak Chlor. absorption<br><br>**1.14µm:** Strong Water absorption<br><br>Highest difference by 2% in 1.45-1.78µm, | Refl. response 6%<br><br>**1.14µm:** Strong Water absorption<br><br>**1.45-1.78µm:** Increased reflectance increase presenting curvature |

| | | | |
|---|---|---|---|
| | | comparing with 2012 | |
| **2002-03** | Refl. response: 8.5-9%<br>Similar spectral pattern with 2012<br>**1.15-1.3µm:** Decreased reflectance<br>**1.78µm:** Absorption | Refl. response: 3-4 %<br>**0.7µm:** Chlor. absorption<br>**1.15-1.3µm:** Decreased reflectance<br>**1.78µm:** Weak absorption<br>Similar spectral pattern with 2012.<br>Difference by 0.3% in overall reflectance | Refl. response: 4.5 %<br>**1.15-1.3µm:** Decreased reflectance |
| **2006** | Refl. response: 8-8.5% (VIS), 7% (SWIR)<br>**1.15-1.3µm:** Refl. response decrease (1%)<br>**1.78µm:** Absorption<br>**2.3µm:** Weak absorption | Refl. response: 4.3% (VIS), 3% (SWIR)<br>**0.7µm:** Chlor. absorption + Weak red edge<br>**1.14µm:** Water absorption<br>**2.1µm:** Weak absorption<br>**0.7-0.9µm:** higher refl. by 0.1%, comparing with 2012<br>**1-1.12µm:** the same refl. response | Refl. response: 4%<br>"Smooth" spectral pattern in overall spectrum range |
| **2007** | Refl. response: 8%<br>Spectral pattern is similar with other lava flows spectral pattern in the same image, but differs from 2009 and 2012. Mostly in VIS and 1.45-1.78µm | Refl. response: 3%<br>**0.7µm:** Chlor. absorption<br>**1.14-1.45µm:** Refl. decrease (1%)<br>**0.7-1.15µm**: Same refl. with 2012 | Refl. response: 4%<br>**0.7-0.9µm:** Absorption (Potential presence $Fe^{+3}$)<br>**1.5-2.3µm:** Refl. increase up to 4%<br>**0.7-1.15µm:** Almost the same refl. response with 2009<br>Difference by 1.5% in reflectance in the rest spectrum |

| | | | |
|---|---|---|---|
| **py1981** | Refl. response: 5-6%<br>**1.78μm:** Absorption<br>**1-1.3μm:** Refl. decrease<br>**1.45-2.35μm:** Refl. increase<br>Lower reflectance comparing with the lava flow reflectances<br>Similar spectral pattern with 2009 and 2012 | 2009: Refl. response 1.5%<br>2012: Refl. response 2.5%<br>Almost the same spectral patterns<br>Difference by 1.5% in overall reflectance | |
| **py1999-01** | The same spectral pattern with py1981<br>Refl. response: 8% (2007), 2% (2009), 5% (2012) | | |
| **py2002-03** | Refl. response: 7% (VIS), 6% (IR)<br>Spectral pattern similar with 2012<br>**1.1-1.3μm:** Refl. response decreases by 2%<br>**1.78μm:** Absorption | Refl. response: 4% (VIS), 3% (IR)<br>**1.14μm:** Water absorption<br>**1.1-1.45μm:** Decreased reflectance by 1%<br>**0.7-1.15μm**: Same with 2012<br>Similarities with the 2007 lava flow endmembers | Refl. response: 4%<br>**0.78-0.9μm:** Refl. absorption (Potential presence of $Fe^{+3}$)<br>**1-1.3μm:** Refl. decrease<br>**1.5-2.3μm:** Refl. increases up to 4%<br>Similar with the 2007 lava flow endmembers |
| **sc2001** | Refl. response: 12% (IR), 16% (VIS)<br>**0.7μm:** Chlor. Absorption + red edge (potential presence of vegetation)<br>**1.15-1.3μm:** decrease by 5% | Refl. response: 5%<br>**0.7μm:** Weak Chlor. absorption<br>**1.14μm**: Water absorption<br>**1.3μm:** Absorption<br>**1.5-2.35μm:** Similar spectral pattern with 2012 endmember | Refl. response: 6%<br>VIS: Continuous increase in reflectance<br>**1-1.3μm:** Absorption (potential presence of $Fe^{+2}$) |
| **sc2002** | Refl. response: 6%<br>**1.15-1.3μm:** Decrease by 1%<br>**1.78μm:** Absorption | Refl. response: 3%<br>**1.14μm**: Water absorption<br>Similar spectral pattern | Refl. response: 4% |

| | | | |
|---|---|---|---|
| | **2.3µm:** absorption<br>Similar spectral pattern with 2012 endmember | with 2012 endmember | |

**Mongibello Torre del Filosofo 2 Formation (1669-1971) – MF2**

Some lava flows are categorized according to their similar spectral pattern in some particular spectral ranges. The 1910, 1911, 1886, 1780, 1892 and 1923 lava flows spectra present an absorption within 1-1.3 µm and a reflectance increase in 1.6-1.7 µm. The 1727-28/32-33, 1735-36/58-59, 1760-64, 1763, 1947, 1949, 1957/60-64/66-71, 1960-64 and 1964 lava flows spectra are characterized by an absorption in 1.2-1.3 µm and a "smooth" spectral pattern in 1.6-1.7 µm.

As shown in Table 7.1.2, lava deposits reflectances vary from 5.5% to 27% in 2007, from 3% to 15% in 2009 and from 4% to 18% in 2012. In the three datasets, the highest reflectance responses correspond to the middle ages of the MF2 lava flows and the lowest reflectances to both the oldest and most recent lavas. Thus, the reflectance response doesn't increase from the oldest to the most recent. However, the reflectance spectra of the MF2 endmembers are higher than those of the MF1 endmembers. The difference in reflectance response between 2009 and 2012 endmembers is ~2%. Pyroclastic and scoriae deposits have lower reflectance responses comparing with the lava flows of this formation.

In 2007 image, a 1.78µm absorption is observed as in MF1 endmembers. The presence of sparse vegetation is depicted in 1727-28/32-33, 1735-36/58-59, 1766, 1886, 1892, 1942 and 1960-64 lava flows and in the 1766 scoriae deposit. An absorption in 1-1.3µm (iron oxide presence) is observed in almost all the volcanic product endmembers. Only the 1792 lava flow is characterized probably by the presence of lichen (weak absorption in 2.3µm).

The 1780, 1886, 1892, 1910, 1911, 1923 and 1947 lava flows are described by a continuous reflectance increase in 0.4-0.9µm, 1.5-1.6µm and 2-2.35µm and a weak absorption in 0.7µm, which could be due to alteration. The endmembers, whose spectral signatures are described by chlorophyll absorption (e.g. lichen cover), present similar spectral patterns with the respective of 2009 and 2012 images. The spectral patterns of the endmembers, which are probably affected by the alteration, are differentiated mostly in VNIR of the EMS.

Most of the 2009 endmembers spectra indicate chlorophyll presence. The red edge slope becomes smoother./in the most recent volcanic products.. There is no vegetation indication in the 1735-36/58-59, 1760-64, 1764-65, 1947, 1949 and 1957/60-64/66-71 lava flow spectra, the 1763, 1832, 1843 and 1879 scoriae deposits spectra and all the pyroclastic endmembers. The water absorption feature in 1.14μm is weaker in lava deposits than in the MF1 endmembers. An absorption feature in 1-1.13μm is observed in almost all lavas and pyroclastic endmembers, but not in scoriae deposits. This feature is observed in the corresponding lava flows spectra in the 2007 image.

The 1727-28/32-33, 1766, 1792, 1879 and 1960-64 lava flows and the 1892 scoriae deposit of the 2012 image show chlorophyll absorption in 0.7μm. Absorption feature in 1-1.13μm is observed in the 1927-28/32-33, 1780, 1787, 1792, 1886, 1911, 1947 and 1960-64 lava flows and in the 1879 pyroclastic deposit. Water absorption features are not observed in any other endmember. Absorptions due to alteration are observed in the same lava flows spectra in the three data images.

The difference in reflectance response between the 2009 and 2012 endmembers varies from less than 0.1% to 3%. The highest differences in reflectance and in the spectral pattern between the endmembers are observed mostly in VNIR region. However, there are some lava flows whose reflectance response in 2009 is either higher or the same than in 2012.

According to the above observations, the spectral patterns are similar in the three images, except from the lava flows, which may be affected by alteration. These lava flows are differentiated due to the strong vegetation presence in the 2009 endmembers and to the absorption in 0.7-0.9μm (iron presence) in 2012 endmembers.

Potentially, two main factors alter the spectral curves of the MF2 endmembers. The sparse vegetation (e.g. vegetation), which is observed at 0.7μm (chlorophyll) and 1.72-1.73μm (cellulose) absorptions. The alteration, which is identified by the reflectance increase in 0.4-0.6 μm and in 1.5-1.6 μm (curved shape) and a small absorption effect (~1%) in 0.7μm Also, we assume that the surface texture is mostly coarse, because the reflectance response decreases in SWIR, *(Sgavetti et al, 2006).*

**Table 7.1.2:** ***The description of the characteristics of each MF2 endmember of the 2007, 2009 and 2012 datasets. The description of the similarities and the differences in spectral pattern and reflectance response between the images are also provided.***

| | **2007** | **2009** | **2012** |
|---|---|---|---|
| **1727-28/32-33** | Refl. response: 15%<br>**0.7-0.9µm:** refl. increase 5% (vegetation presence)<br>**1-1.3µm:** decrease by 1%<br>Potential iron presence<br>**1.78µm:** decrease by 0.5% | Refl. response: 7%<br>**0.7µm-0.9µm:** refl. increase 4% (vegetation presence)<br>**1.14µm:** Water absorption<br>**1-1.3µm:** decrease by 1%<br>Potential iron presence<br>**1.45-2.35µm:** same spectral patterns with 2012. Refl. response difference 1% | Refl. response: 9%<br>**0.7µm-0.9µm:** refl. increase 2% (vegetation presence)<br>**1-1.3µm:** decrease by 1%<br>Potential iron presence |
| **1735-36/58-59** | Refl. response: 8%<br>**1.27µm:** reflectance increase<br>**1.78µm:** decrease by 0.5%<br>Similar spectral pattern with 2009 and 2012 | Refl. response: 3%<br>**1.27µm:** Absorption | Refl. response: 4%<br>**1.14µm:** reflectance increase<br>**1.27µm:** reflectance increase |
| **1760-64** | Spectral pattern is the same with 1735-36/58-59 lava flow.<br>Refl. response: 2007 (9%), 2009 (4%), 2012 (5%)<br>Difference: 1.14µm water absorption is more “deep” in 2009 | | |
| **1763** | Refl. response: 9.5% (VIS), 7% (IR)<br>**1.15-1.3µm:** decrease by 2.5% | Spectral patter and reflectance response (7%) is the same in 2009 and 2012.<br>**0.7-0.9µm:** reflectance increase 2% (vegetation presence) | |
| **1764-65** | Spectral pattern is the same with 1735-36/58-59 and 1760-64 lava flows.<br>Refl. response: 2007 (13%), 2009 (5%), 2012 (7%) | | |

| | | | |
|---|---|---|---|
| | Reflectance response difference between the 1764-65 lava flow and the above: 2-3% | | |
| **1766** | Refl. response: 13% (VNIR) 10% (SWIR)<br>**0.7-0.9µm:** refl. increase 6% (vegetation presence)<br>**1.1-1.25µm:** refl. decrease 2%<br>Potential iron presence<br>**1.5-2.35µm:** refl. continuous to decrease (1%) | Refl. Response: 7% (VNIR), 5% (SWIR)<br>**0.7-0.9µm:** refl. increase 1.5% (vegetation presence)<br>**1.1-1.25µm:** refl. decrease 0.2%<br>**1.5-2.35µm:** refl. continuous to decrease (1%)<br>Refl. response difference with 2012 from >0.1% (VIS) to 0.5% (IR) | Refl. Response: 7% (VNIR), 6.5% (SWIR)<br>**0.7-0.9µm:** refl. increase 0.5% (vegetation presence)<br>Similar spectral pattern with 2007 and 2009 |
| **1780** | Refl. response: 15% (VIS & SWIR) 23% (NIR)<br>**0.4-0.9µm:** steep slope<br>**1.1-1.18µm:** absorption<br>**1.6-1.8µm:** refl. increase (curved spectral pattern) | Refl. response: 12%(VIS), 14%(IR)<br>**0.7-0.9µm:** refl. increase 5% (vegetation presence)<br>**1.1-1.18µm:** absorption<br>**1.6-1.8µm:** refl. increase (curved spectral pattern)<br>Refl. response higher than in 2012 | Refl. response: 10%(VIS) 13%(SWIR)<br>**0.7-0.8µm:** absorption<br>**1.1-1.18µm:** absorption<br>**1.6-1.8µm:** refl. increase (curved spectral pattern) |
| **1787** | Refl. response: 5.5%<br>**1.1-1.3µm:** refl. decrease (0.5%)<br>**1.78µm**: absorption<br>Similar spectral pattern with 2009 and 2012 | Refl. response: 3%<br>**0.7-0.9µm:** slightly refl. increase<br>**0.7-1.15µm:** refl. response higher than in 2012 | Refl. response: 3%<br>**0.7-0.9µm:** slightly refl. decrease (0.1%) |
| **1792** | Refl. response: 10%<br>**0.7µm:** Weak chlor. | Refl. response: 4-4.5%<br>**0.7µm:** Weak chlor. | Refl. response: 5-5.5%<br>**0.7µm:** Weak chlor. |

| | | | |
|---|---|---|---|
| | absorption<br>**1.1-1.3μm:** refl. decrease (1%)<br>Potential presence<br>**1.78μm**: absorption<br>**2.3μm:** Weak absorption either due to sparse lichen cover | absorption<br>**1.14μm:** Water absorption<br>**1.1-1.3μm:** refl. decrease (0.5%)<br>Similar spectral pattern with 2012 | absorption<br>**1.1-1.3μm:** refl. decrease (0.5%) |
| **1809** | Spectral pattern and Refl. response are the same with 1764-65 lava flow.<br>Refl. response: 2007 (13%), 2009 (5%), 2012 (7%) | | |
| **1879** | Spectral pattern and Refl. response are the same with 1766 lava flow.<br>Refl. response: 2007 (13%), 2009 (6.5-8%), 2012 (7-8%)<br>Difference: **0.7μm:** Absorption (vegetation presence)<br>**0.4-0.9μm:** 2009 has the same reflectance with 2012 | | |
| **1886** | Refl. response: 22%<br>**0.4-0.9μm:** refl. increase<br>**0.7μm:** absorption<br>**1.1-1.3μm:** refl. decrease (1%)<br>Potential iron presence<br>**1.5-1.6μm:** refl. increase with a curved shape<br>**2.2-2.35μm:** refl. decrease<br>Potentially alteration *(Sgavetti et al, 2006)*<br>Spectral pattern similar with 2009 | Refl. response: 11%<br>**0.4-0.9μm:** refl. increase<br>**0.7μm:** absorption (“more steep slope”)<br>**1.1-1.3μm:** refl. decrease (1%)<br>Potential iron presence<br>**1.5-1.6μm:** refl. increase with a curved shape<br>**2.2-2.35μm:** refl. decrease<br>Potentially alteration *(Sgavetti et al, 2006)* | Refl. response: 14-15%<br>**0.4-0.9μm:** refl. increase<br>**1.1-1.3μm:** refl. decrease (1%)<br>Potential iron presence<br>**1.5-1.6μm:** refl. increase with a curved shape<br>**2.2-2.35μm:** refl. decrease<br>Potentially alteration *(Sgavetti et al, 2006)* |
| **1892** | The same spectral pattern with 1886 lava flow. Different reflectance responses<br>Refl. response: 2007 (19%), 2009 (10%), 2012 (14%) | | |
| **1910** | The same spectral pattern with 1886 lava flow. Different reflectance responses<br>Refl. response: 2007 (27%), 2009 (15%), 2012 (18%) | | |
| **1911** | Refl. response: 25% | Refl. response: 13-15% | Refl. response: 14-15% |

| | | | |
|---|---|---|---|
| | **0.4-0.9µm:** refl. increase<br>**1.1-1.3µm:** refl. decrease (1%)<br>Potential iron presence<br>**1.5-1.6µm:** refl. increase with a curved shape<br>**1.78µm:** Absorption<br>**2.2-2.35µm:** refl. decrease<br>Potentially alteration *(Sgavetti et al, 2006)* | **0.4-0.9µm:** refl. increase<br>**0.7µm:** Chlor. absorption<br>**1.1-1.3µm:** refl. decrease (1%)<br>Potential iron presence<br>**1.5-1.6µm:** refl. increase with a curved shape<br>**2.2-2.35µm:** refl. decrease<br>Potentially alteration *(Sgavetti et al, 2006)*<br>Refl. response difference with the 2012: 1% (VIS) & 3% (IR) | **0.4-0.9µm:** refl. increase<br>**0.7µm:** slight absorption<br>**1.1-1.3µm:** refl. decrease (1%)<br>Potential iron presence<br>**1.5-1.6µm:** refl. increase with a curved shape<br>**2.1-2.18µm:** Absorption<br>**2.2-2.35µm:** refl. decrease<br>Potentially alteration *(Sgavetti et al, 2006)* |
| **1923** | The same spectral pattern with 1911 lava flow. Difference in spectral response<br>Refl. response: 2007 (16%), 2009 (7-8%), 2012 (8-10%)<br>Refl. response difference with the 2012: 1% (VIS) & 3% (IR) | | |
| **1942** | Refl. response: 10%<br>**0.7µm:** slight absorption<br>**1.1-1.3µm:** refl. decrease (1%)<br>Potential iron presence<br>**1.78µm:** Absorption | Refl. response: 4.7-5%<br>**0.7µm:** slight absorption<br>**0.75-0.9µm:** Refl. response higher than in 2012<br>**1-1.1µm:** the same refl. response with 2012<br>**1.14µm:** Water absorption<br>**1.45-2.35µm:** Difference by 1% | Refl. response: 5%<br>"Smooth" spectral pattern |
| **1947** | The same spectral pattern and reflectance response with 1923 lava flow.<br>Difference in 2007 endmember. **0.7 µm** reveal no absorption | | |
| **1949** | Refl. response: 7%<br>"Smooth" spectral pattern | Refl. response: 3%<br>"Smooth" spectral pattern | Refl. response: 2.5-3%<br>"Smooth" spectral pattern<br>**0.7-0.9µm:** refl. response |

| | | | |
|---|---|---|---|
| | **1.78µm:** Absorption | **1.14µm:** Water absorption<br>**VIS:** higher reflectance comparing with 2012<br>**IR**: the same reflectance | decrease (0.5%) |
| **1957/60-64/66-71** | Refl. response: 8-10%<br>**1-1.3µm:** refl. decrease (1%)<br>Potential iron presence<br>**1.78µm:** Absorption | The same spectral pattern.<br>Refl. response: 2009 (2%), 2012 (4.5%)<br>Difference in refl. response by 1.5% | |
| **1960-64** | Refl. response: 13%<br>**0.7µm:** Absorption (vegetation presence)<br>**1-1.3µm:** refl. response decrease (3%)<br>Potential iron presence<br>**1.78µm:** Absorption<br>Similar spectral pattern with 2009 and 2012 | Refl. response: 3-5%<br>**0.7µm:** Absorption (vegetation presence)<br>**1-1.3µm:** refl. response decrease (1%)<br>Potential iron presence | Refl. response: 5-7%<br>**0.7µm:** Absorption (vegetation presence)<br>**1-1.3µm:** refl. response decrease (3%)<br>Potential iron presence |
| **1964** | Refl. response: 6-7%<br>**1-1.3µm:** refl. response decrease (3%)<br>Potential iron presence<br>Similar spectral pattern with 2009 and 2012 | Refl. response: 2-3.5%<br>**0.7µm:** Slight absorption<br>**1.14µm:** Water absorption<br>**0.75-1.12µm:** same refl. response with 2012<br>**1.14µm-2.35µm:** difference in refl. response by 0.5% | Refl. response: 3-4%<br>“Smooth” spectral pattern |
| **py1879** | Refl. response: 6.5-8%<br>**1-1.3µm:** refl. response decrease (1.5%)<br>Potential iron presence<br>**1.78µm:** Absorption | Refl. response: 3%<br>**1-1.3µm:** refl. response decrease (1.5%)<br>Potential iron presence<br>**1.78µm:** Absorption | Refl. response: 5%<br>**1-1.3µm:** refl. response decrease (1.5%)<br>Potential iron presence<br>Refl. response difference |

| | | | |
|---|---|---|---|
| | The spectral pattern is the same with 2009 | | with 2009 is 2% |
| **sc1763** | The same spectral pattern and refl. response with the py1879 endmember, extracted from 2007 image | Refl. response 5%<br>**1.14μm:** Water absorption<br>**0.4-1.3μm & 2.1-2.35μm** the same spectral pattern and reflectance response with 2012<br>**1.45-1.78μm:** Higher refl. response by 0.2% comparing with 2012 | Refl. response 5%<br>Almost the same spectral pattern with 2009 |
| **sc1766** | Refl. response: 10.5%<br>**0.7μm:**Absorption (vegetation presence)<br>**1.78μm:** Absorption<br>The spectral pattern is similar with 2009 | Refl. response: 5.3%<br>**0.7μm:**Absorption (vegetation presence)<br>**1.78μm:** Absorption<br>**2.1-2.2μm:** The same refl. response with 2012<br>**2.2-2.35μm:** Higher refl. response, compared with 2012 | Refl. response: 5.5%<br>**1.45-1.78μm:** Slight refl. increase |
| **sc1832** | The same spectral pattern and reflectance response with the 1879 pyroclastic deposits. | | |
| **sc1843** | The same spectral pattern with the pyroclastic deposit in 1879 and 1832 scoria deposits. Refl. response difference by 1% | | |
| **sc1879** | The same spectral pattern and reflectance response with the 1879 pyroclastic deposit and 1832 scoria deposits. | | |
| **sc1892** | The same spectral pattern with the scoriae deposit in 1832.<br>Refl. response: 9-10% (2007), 4-5% (2009), 4.5-6% (2012)<br>Difference in reflectance response between 2009 and 2012 is 0.2% | | |

**Mongibello Torre del Filosofo 3 Formation (122BC – 1669AD) – MF3**

According to Table 7.1.3, the reflectance responses of the MF3 endmembers vary from 12% to 30% in 2007 image, from 5% to 22% in 2009 image and from 5.5% to 25% in 2012 image. It seems that the MF3 endmembers are characterized by higher reflectance, compared with the MF1 and MF2 formations, although the reflectance does not increase from the most recent to the oldest lava flows. The lowest reflectance responses are observed in 1610 and 1614-24 lava flows and in scoriae deposits. In particular, the 1610 scoriae deposit has lower reflectance than the lava flow of the corresponding date.

All the endmembers extracted from 2007 image are characterized by an absorption in 1-1.12μm, probably due to the presence of iron; though this fact is not observed in scoriae deposits. Also, all endmembers except from the most recent (1646-47 and 1669) reveal an absorption in 1.78μm. Sparse vegetation presence (e.g. lichen colonization) is observed in all endmembers except from the oldest lava flow (1536). The 1536, 1566 and 1669 lava flows are probably affected by alteration, due to reflectance increase in 0.4-0.9μm and in 1.5-1.6 μm ("curved shape") and the decrease in 2.1-2.35μm.

The lava flows, which are affected by the sparse vegetation show more similarities in spectral pattern with the respective endmembers of the 2009 image. The spectral pattern of the 1669 lava flow is similar with the respective endmember of the 2012 image. The 1566 and 1646-47 lava flows reveal the same reflectance responses with the 2012 endmembers, in 0.8μm and 1.5-1.6μm / 2.1-2.3μm, correspondingly. The 1614-24 lava flow and the 1610 scoriae deposit have the same spectral pattern with the respective 2009 and 2012 spectra, while the 1646-47 lava flow spectral pattern is similar only to the 2009 one.

In the 2009 image, all endmembers (lava flows and scoriae deposits) are affected by sparse vegetation, except from the 1669 lava flow. Iron is revealed in every lava flow endmember, except from 1646-47 lava flow. Water absorption is observed in the 1614-24 and 1669 lava flows and in the 1646-47 scoriae deposit. The 1536, 1566 and 1669lava flows in are probably affected by alteration, since their reflectances increase between 0.4-0.9μm, 1.5-1.7μm and decrease in 2.1-2.3μm.

The same endmember spectra, which show sparse vegetation, iron and potential alteration in 2007 and 2009 images, present the same spectral characteristics in the 2012 image. Exceptions are the 1610 and 1646-47 lava flows, where the chlorophyll absorption is not observed.

The difference in reflectance response between the 2009 and the 2012 endmembers varies from 0.5 to 10%. The most characteristic difference is depicted in the 1566 lava flow, while the lowest in the 1610 lava flow, in the spectral area of 0.75-0.9μm. The only endmember, which has the same reflectance response in 2009 and 2012 images, is the 1610 scoriae deposit, in 1.12-2.35μm. It seems that the endmembers in MF3 formation can be discriminated better, according to their spectral pattern, compared with the endmembers in MF1 and MF2 formations. Also, their reflectance response temporal change is distinguished better, compared with the endmembers in MF1 and MF2 formations.

***Table 7.1.3: The description of the characteristics of each MF3 endmember of the 2007, 2009 and 2012 datasets. The description of the similarities and the differences in spectral pattern and reflectance response between the images are also provided.***

| | **2007** | **2009** | **2012** |
|---|---|---|---|
| **1536** | Refl. response: 28%<br>**0.4-0.9μm:** Continuous reflectance increase<br>**1.1-1.2μm:** Absorption Potential iron presence<br>**1.5-1.6μm:** refl. increase (curved shape)<br>**1.78μm:** Absorption<br>**2.1-2.35μm:** refl. decrease<br>Potential alteration presence | Refl. response: 18%<br>**0.7μm:** absorption + red edge (vegetation presence)<br>**1.1-1.2μm:** Absorption Potential iron presence<br>**1.5-1.6μm:** refl. increase (curved shape)<br>**2.1-2.35μm:** refl. decrease<br>Potential alteration presence<br>**0.75-0.9μm**: the same refl. values with 2012<br>**1-2.35μm:** difference refl. values by 2%, compared with 2012 | Refl. response: 16%<br>**0.7μm:** absorption<br>**1.1-1.2μm:** Absorption Potential iron presence<br>**1.5-1.6μm:** refl. increase (curved shape)<br>**2.1-2.35μm:** refl. decrease<br>Potential alteration presence |
| **1566** | Refl. response: 30%<br>**0.7μm:** absorption + red edge (vegetation presence) | Refl. response: 15%<br>**0.7μm:** absorption + red edge (vegetation presence) | Refl. response: 25%<br>**0.7μm:** absorption + red edge (vegetation presence)<br>**0.4-0.9μm:** Continuous |

| | | | |
|---|---|---|---|
| | **0.4-0.9μm:** Continuous reflectance increase<br>**1.1-1.2μm:** Absorption Potential iron presence<br>**1.5-1.6μm:** refl. increase (curved shape)<br>**1.78μm:** Absorption<br>**2.1-2.35μm:** refl. decrease<br>Potential alteration presence<br>**0.8μm:** The same refl. response with 2012<br>5% reflectance difference with 2012 in the whole spectrum range | **0.4-0.9μm:** Continuous reflectance increase<br>**1.1-1.2μm:** Absorption Potential iron presence<br>**1.5-1.6μm:** refl. increase (curved shape)<br>**2.1-2.35μm:** refl. decrease<br>Potential alteration presence<br>10% reflectance difference with 2012 in the whole spectrum range | reflectance increase<br>**1.1-1.2μm:** Absorption Potential iron presence<br>**1.5-1.6μm:** refl. increase (curved shape)<br>**2.1-2.35μm:** refl. decrease<br>Potential alteration presence |
| **1610** | Refl. response: 15%<br>**0.7μm:** absorption + red edge (vegetation presence)<br>**1.1-1.2μm:** Absorption Potential iron presence<br>**1.5-1.6μm:** refl. increase (curved shape)<br>**1.78μm:** Absorption | Refl. response: 7%<br>**0.7μm:** absorption + red edge (vegetation presence)<br>**1.1-1.2μm:** Absorption Potential iron presence<br>**1.5-1.6μm:** refl. increase (curved shape)<br>**0.75-0.9μm:** refl. difference with 2012 by 0.5%<br>**1-2.35μm:** refl. difference with 2012 by 1% | Refl. response: 9%<br>**1.1-1.2μm:** Absorption Potential iron presence<br>**1.5-1.6μm:** refl. increase (curved shape) |
| **1614-24** | Refl. response: 13-14%<br>**0.7μm:** absorption + red edge (vegetation | Refl. response: 5-6%<br>**0.7μm:** absorption + red edge (vegetation | Refl. response: 9-10%<br>**0.7μm:** absorption<br>**1.1-1.2μm:** Absorption |

| | | | |
|---|---|---|---|
| | presence)<br>**1.1-1.2µm:** Absorption Potential iron presence<br>**1.78µm:** Absorption<br>The same spectral pattern with 2009 and 2012 | presence)<br>**1.1-1.2µm:** Absorption Potential iron presence<br>**1.14µm:** Weak water absorption<br>**1.5-1.6µm:** refl. increase<br>Difference in refl. response by 3% with 2012 | Potential iron presence<br>**1.14µm:** Slight refl. increase (0.1%)<br>**1.5-1.6µm:** refl. increase |
| **1646-47** | Refl. response: 15-17%<br>**0.7µm:** absorption + red edge (vegetation presence)<br>**1.1-1.2µm:** Absorption Potential iron presence<br>**1.5-1.7µm:** refl. increase (curved shape)<br>**1.5-1.6µm & 2.1-2.35µm:** the same refl. response with 2012<br>Similar spectral pattern with 2009 | Refl. response: 8%<br>**0.7µm:** absorption + red edge (vegetation presence)<br>**1.5-1.7µm:** refl. increase (curved shape)<br>Refl. response difference by 7% with 2012 | Refl. response: 13-15%<br>**1.1-1.2µm:** Absorption Potential iron presence<br>**1.5-1.7µm:** refl. increase (curved shape) |
| **1669** | Refl. response: 23-27%<br>**0.7µm:** Absorption<br>**1.1-1.2µm:** Absorption Potential iron presence<br>**1.14µm:** Water absorption<br>**1.5-1.7µm:** refl. increase (curved shape)<br>**1.78µm:** Absorption<br>Similar spectral pattern with 2012 | Refl. response: 17-22%<br>**1.1-1.2µm:** Absorption Potential iron presence<br>**1.14µm:** Water absorption<br>**1.5-1.7µm:** refl. increase (curved shape)<br>**1.78µm:** Absorption<br>**2.1-2.35µm:** Refl. decrease<br>Potential alteration | Refl. response: 13-17%<br>**0.78-0.87µm:** steep slope decrease of the refl. response<br>Potential iron presence<br>**1.1-1.2µm:** Absorption Potential iron presence<br>**1.14µm:** Water absorption<br>**1.5-1.7µm:** refl. increase (curved shape)<br>**1.78µm:** Absorption |

| | | | |
|---|---|---|---|
| | **2.1-2.35μm:** Refl. decrease<br>Potential alteration presence | presence | **2.1-2.35μm:** Refl. decrease<br>Potential alteration presence |
| **sc1610** | Refl. response: 12%<br>**0.7μm:** absorption + red edge (vegetation presence)<br>**1.78μm:** weaker absorption feature<br>Same spectral pattern with 2009 and 2012 | Refl. response: 5.5%<br>**0.7μm:** absorption + red edge (vegetation presence)<br>**0.4-1.12 μm:** Refl. response difference by 0.2% with 2012<br>**1.12-2.35μm:** same reflectance response with 2012 | Refl. response: 5.5%<br>The same spectral pattern with 2007 & 2009 except from the 0.7μm absorption |
| **sc1646-47** | Refl. response: 13%<br>**0.7μm:** absorption + red edge (vegetation presence)<br>**1.78μm:** Absorption | Refl. response: 5%<br>**0.7μm:** absorption + red edge (vegetation presence)<br>**1.14μm:** weaker water absorption feature | Refl. response: 8%<br>**0.7μm:** absorption + red edge (vegetation presence) |

**Ellitico Formation**

The volcanic products of the Ellitico formation are divided into two spectral groups according to their common spectral behavior. The EC24cs, EC24mn, EC24pn, EP22el, EP22fu and EP22ta endmembers are grouped to the first group. The characteristics of this group are the high reflectance values, the potential presence of sparse vegetation (0.7μm absorption and red edge) and alteration (0.4-0.9μm absorption and 1.5-1.75 μm reflectance increase). The second group includes the EP22pa, EP22gc, EPD21a,b, EPG25a,b endmembers, which have much lower reflectance response and potentially are affected by sparse vegetation. The ESC20 endmember's spectral pattern is in general "smooth" and it seems that it isn't affected by any of the above factors.

According to Table 7.1.4, almost all endmembers are characterized by chlorophyll absorption in 0.7μm, which becomes stronger in the older lava flows. Exceptions are the ESC_20 in all the images, the EP_22ta of the 2012 image and the EP_22gc of the 2009 image. Presence of iron feature is observed in the EP_22 and EC_24 endmembers. A particular absorption in 1.78μm is revealed in 2007 endmembers and in the EP_22ta endmember of the 2009 image. Also, the reflectance response in the EP_22 and EC_24 endmembers, except from EP_22gc and EP_22el, increase between 1.5-1.7μm (curved shape) and 2.1-2.3μm probably due to alteration.

The discrimination between spectra volcanic products within the same spectral group is less evident, due to their spectral similarities..Exceptions are the ESC_20, EPD_21b and the EC_24cs endmembers, which reveal the same reflectance responses in the three images.

***Table 7.1.4: The description of the characteristics of each Ellitico endmember of the 2007, 2009 and 2012 datasets. The description of the similarities and the differences in spectral pattern and reflectance response between the images are also provided.***

| | **2007** | **2009** | **2012** |
|---|---|---|---|
| **ESC_20** | Refl. response: 10%<br>**1.78μm:** weaker absorption feature<br>“Smooth” spectral pattern | Refl. response: 5.5%<br>**1.14μm:** weaker absorption feature<br>“Smooth” spectral pattern<br>**0.4-0.7μm:** the same refl. response with 2012<br>**0.7-2.35μm:** Higher refl. response &<br>Difference by 0.5% | Refl. response: 5%<br>“Smooth” spectral pattern |
| **EPD_21a** | Refl. response: 10-12%<br>**0.7μm:** Absorption + weaker red edge (vegetation presence)<br>**1.78μm:** Absorption<br>Same spectral pattern with 2009 and 2012 | Refl. response: 4.8%<br>**0.7μm:** Absorption + weaker red edge (vegetation presence)<br>**1.14μm:** Weak water absorption<br>Difference by 0.2% in overall reflectance | Refl. response: 5%<br>**0.7μm:** Absorption + red edge (vegetation presence) |
| **EPD_21b** | Refl. response: 10% | Refl. response: 5% | Refl. response: 5% |

| | | | |
|---|---|---|---|
| | **0.7µm:** Absorption + red edge (vegetation presence)<br>**1.78µm:** Absorption<br>Same spectral pattern with 2009 and 2012 | **0.7µm:** Absorption + red edge (vegetation presence)<br>Same spectral pattern & refl. response with 2012 | **0.7µm:** Absorption + red edge (vegetation presence) |
| **EP_22ta** | Refl. response: 37%<br>**0.7µm:** Absorption + red edge (vegetation presence)<br>**1.1-1.2µm:** Absorption Potential iron presence<br>**1.5-1.7µm:** refl. increase (curved shape)<br>**1.78µm:** Absorption<br>**2.1-2.35µm:** Refl. decrease<br>Similar spectral pattern with 2009 | Refl. response: 24%<br>**0.7µm:** Absorption + red edge (vegetation presence)<br>**1.1-1.2µm:** Absorption Potential iron presence<br>**1.5-1.7µm:** refl. increase (curved shape)<br>**1.78µm:** Slight absorption<br>**2.1-2.35µm:** Refl. decrease<br>Difference by 5% in overall reflectance, except from the 0.7-0.9µm (2%), comparing with 2012 | Refl. response: 30%<br>**1.1-1.2µm:** Absorption Potential iron presence<br>**1.5-1.7µm:** refl. increase (curved shape)<br>**2.1-2.35µm:** Refl. decrease |
| **EP_22pa** | Refl. response: VNIR (17%), SWIR (15%)<br>**0.7µm:** Absorption + red edge (vegetation presence)<br>**1.1-1.2µm:** Absorption Potential iron presence<br>**1.78µm:** Absorption feature<br>Similar spectral pattern | Refl. response: 6%<br>**0.7µm:** Absorption + weaker red edge (vegetation presence)<br>**1.78µm:** Weak absorption feature<br>Difference by 4% between 0.4-1.3µm, 1% between 1.45-1.78µm and 0.5% between 2.1- | Refl. response: VNIR (10%), SWIR (8%)<br>**0.7µm:** Absorption + red edge (vegetation presence)<br>**1.1-1.2µm:** Weak absorption<br>Potential iron presence |

| | | | |
|---|---|---|---|
| | with 2012 | 2.35μm, comparing with 2012 | |
| **EP_22gc** | Refl. response: 14%<br>**0.7μm:** Absorption + red edge (vegetation presence)<br>**1.1-1.2μm:** Absorption Potential iron presence<br>**1.78μm:** Absorption feature | Refl. response: 4%<br>**1.78μm:** Weak absorption feature<br>Highest reflectance difference by 5.5% in 0.7-1.3μm, comparing with 2012<br>Lowest reflectance difference by 1% in 2.1-2.35μm, comparing with 2012 | Refl. response:10%<br>**0.7μm:** Absorption + red edge (vegetation presence)<br>**1.1-1.2μm:** Absorption Potential iron presence<br>**1.5-1.7μm:** refl. increase (curved shape) |
| **EP_22el** | Refl. response: 30%<br>**0.7μm:** Absorption + red edge (vegetation presence)<br>**1.1-1.2μm:** Absorption Potential iron presence<br>**1.5-1.7μm:** refl. increase (curved shape)<br>**2.1-2.35μm:** Refl. decrease<br>Potential presence of alteration<br>**1.78μm:** Absorption<br>The same spectral pattern with 2009 and 2012 | Refl. response: 22%<br>**0.7μm:** Absorption + red edge (vegetation presence)<br>**1.1-1.2μm:** Absorption Potential iron presence<br>**1.5-1.7μm:** refl. increase (curved shape)<br>**2.1-2.35μm:** Refl. decrease<br>Potential presence of alteration<br>Difference by ~5% in overall reflectance, comparing with 2012 | Refl. response: 17%<br>**0.7μm:** Absorption + red edge (vegetation presence)<br>**1.1-1.2μm:** Absorption Potential iron presence<br>**1.5-1.7μm:** refl. increase (curved shape)<br>**2.1-2.35μm:** Refl. decrease<br>Potential presence of alteration |
| **EP_22fu** | The same spectral pattern with EP_22el.<br>Refl. response: 2007 (35%), 2009 (30%), 2012 (27%)<br><u>Difference:</u><br>0.7-0.9μm: The same reflectance response in 2009 and 2012 | | |
| **EC_24pn** | The same spectral pattern with EP_22el & EP_22fu | | |

<table>
<tr><td></td><td colspan="3">Refl. response: 2007 (35%), 2009 (34%), 2012 (24%)<br><u>Difference:</u><br>0.7-1.3μm: Slight refl. difference (0.2%) between 2007 and 2012<br>2.1-2.35μm: Refl. difference by 1%, between 2009 and 2012</td></tr>
<tr><td>EC_24mn</td><td colspan="3">The same spectral pattern with EP_22el<br>Refl. response: 2007 (36%), 2009 (22%), 2012 (29%)</td></tr>
<tr><td>EC_24cs</td><td colspan="3">The same spectral pattern with EP_22el, EP_22fu, EC_24pn & EC_24mn<br>Refl. response: 2007 (35%), 2009 (34%), 2012 (24%)<br><u>Difference:</u><br>0.4-0.9μm & 2.1-2.35μm: The same refl. response in 2009 and 2012</td></tr>
<tr><td>EPG_25a</td><td>Refl. response: 14%<br>0.7μm: Absorption + red edge (vegetation presence)<br>1.78μm: Absorption<br>The same spectral pattern with 2009 and 2012</td><td>Refl. response: 5%<br>0.7μm: Absorption + red edge (vegetation presence)</td><td>Refl. response: 7%<br>0.7μm: Absorption + red edge (vegetation presence)</td></tr>
<tr><td>EPG_25b</td><td colspan="3">The same spectral pattern with EPG_25a<br>Refl. response: 2007 (14.5%), 2009 (6%), 2012 (9.5%)<br><u>Difference:</u><br>Difference by less than 1% in overall reflectance (especially in 2.1-2.35μm), between 2009 and 2012</td></tr>
</table>

Finally, our ongoing study will include, first the implementation of linear spectral unmixing algorithms, in order to investigate the possibility to discriminate the difference volcanic products. Secondly, the examination of the differences in spectral responses in the north and south region of the crater.

## 7.2. SAR Data Analysis

Investigating the mean backscatter coefficient values, which acquired from ascending and descending SAR images in single and cross polarization, of each volcanic product, we primarily conclude that:

- The vertical single polarization reveals always higher backscatter coefficient values in every volcanic formation, regardless the satellite acquisition geometry.
- Investigating the temporal change in the backscatter coefficient, we ascertain that in ascending acquisition geometry in VV and VH backscatter coefficient values increase from the oldest lava flow (Ellitico formation) to the most recent (MF1 formation), while the opposite occurs in descending pass.
- The variation of the backscatter coefficient values of each formation doesn't depend on their chronological categorization.
- The combination of the intense local topography (slopes more than $30^o$) with the satellite acquisition geometry creates the shadowing and foreshortening distortions, which affect the backscatter coefficient values of various volcanic products.

**Mongibello Torre del Filosofo 1 Formation (1971-2007) – MF1**

The MF1 lava flows are described by higher backscatter coefficient values in ascending pass, regardless the polarization. Investigating the spatial location of the 1999 lava flow, which reveals the highest sigma0 values, we assume that one potential reason, which increases the backscatter coefficient values, is the combination of the local topography (high slopes, more than $30^o$) and the satellite acquisition geometry (foreshortening distortion), (Figure 7.2.1). In descending pass, the highest backscatter coefficient values are revealed in the middle of the MF1 time period, while this fact is contradictory since according to Dierking and Haack (1998) study, which claim that recent lava flows are characterized by higher $\sigma^0$ values.

Although, it is not significant, how the surface changes over time and its contribution to the backscatter coefficient. Thus, we cannot be conclusive about the ability of the backscatter signal to discriminate the different volcanic products, according to the surface change in Mt. Etna.

Pyroclastic and scoriae volcanic products are characterized by lower backscatter coefficient values in comparison with lava flows, in both polarizations and in satellite orbits. The pyroclastic products, except from the 1999-01, reveal almost the same sigma0 values in VH polarization, in ascending and descending satellite acquisitions. The scoriae deposits present a decrease in the backscatter coefficient values from the oldest volcanic product (2001) to the most recent (2012), in both polarization and acquisition geometries.

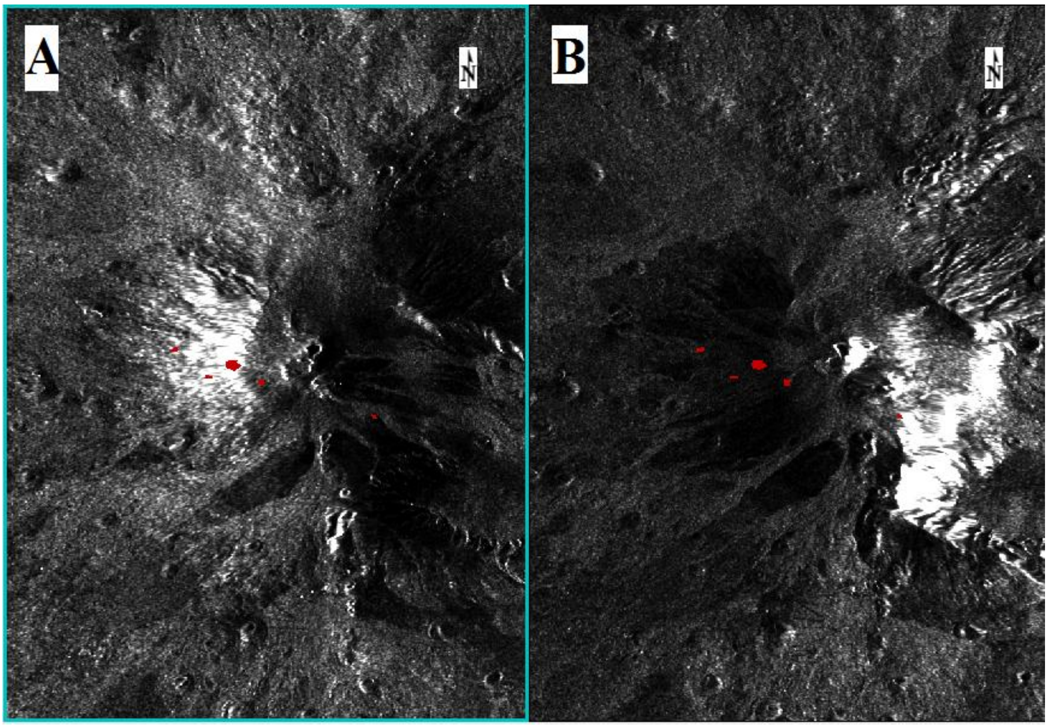


*Figure 7.2.1: The spatial location of the 1999 lava flow samples in the ascending (A) the descending (B) acquisition geometry in VV polarization.*

**Mongibello Torre del Filosofo 2 Formation (1669-1971) – MF2**

The MF2 lava flows are characterized by higher backscatter coefficient values in ascending acquisition geometry and in VV polarization. The backscatter coefficient values decreases from the oldest lava flow to the most recent, while the value trend is the same in both polarizations, but not in the satellite passes.

Investigating the spatial location of the 1735-36/58-59 lava flow, which reveals the highest sigma0 values in ascending pass, we assume that the combination of the local topography and the acquisition geometry (foreshortening distortion), contribute in the alteration of the backscatter value. Using the same approach in the descending pass, we see that the backscatter coefficient values of the 1735-36/58-59 lava flow maybe are affected by the shadowing distortion, (Figure 7.2.2).

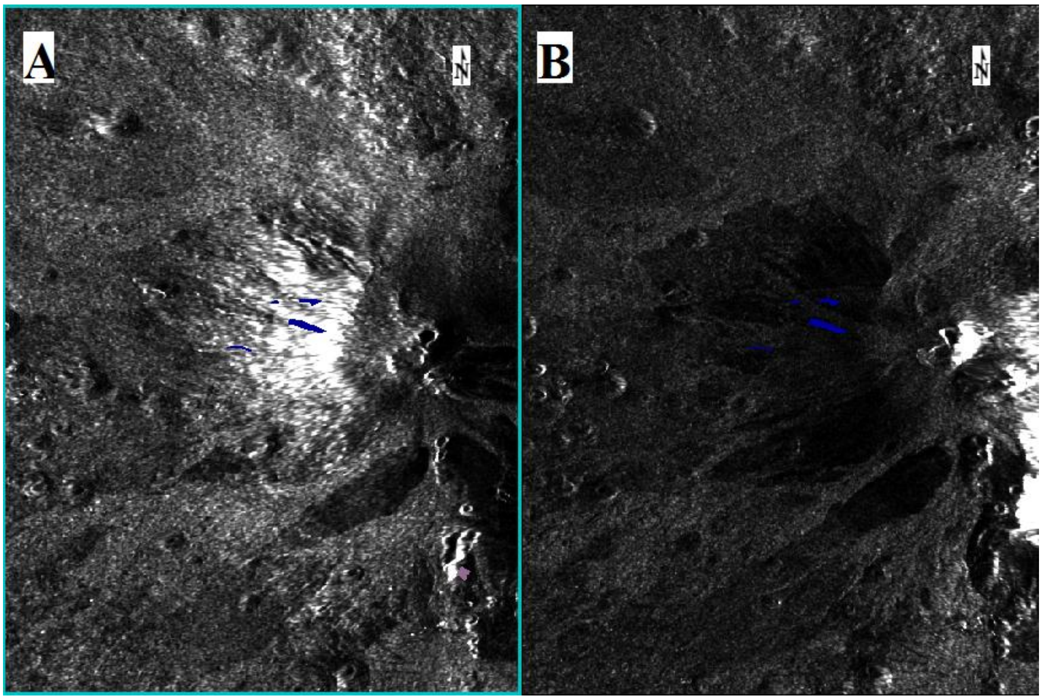


***Figure 7.2.2: The spatial location of the 1735-36/58-59 lava flow samples in the ascending (A) the descending (B) acquisition geometry in VV polarization***.

Moreover, we assumed that the backscatter coefficient values, which describe the 1766 lava flow, maybe affected by the shadowing distortion. In particular, the 1766 lava flow is characterized by the lowest sigma0 values, compared with the other volcanic products, in both ascending (0.046 dB) and descending (0.088 dB) acquisition geometry. In Figure 7.2.3, we can see that the area, where the lava of 1766 is located, is at a lower altitude (1848m) from the two volcanic cones (1948m), which are located in front of the lava flow. Thus, we hypothesize that in ascending pass the terrain of this cones seems more intense in ascending pass than in descending pass and this probably prevents the transmition of the backscatter signal to this location. Lastly, lava deposits recorded in 1910, 1911 and 1923 are identified by higher $\sigma 0$, as a potential result of the coarser surface.

Pyroclastic deposits are characterized by lower backscatter coefficient values in both acquisition geometries and polarizations. The backscatter coefficient values of the volcanic products are equal in descending and ascending acquisition geometries. In scoriae deposits, the sigma0 values decrease from the older to the younger, with an exception in the 1892 volcanic product.

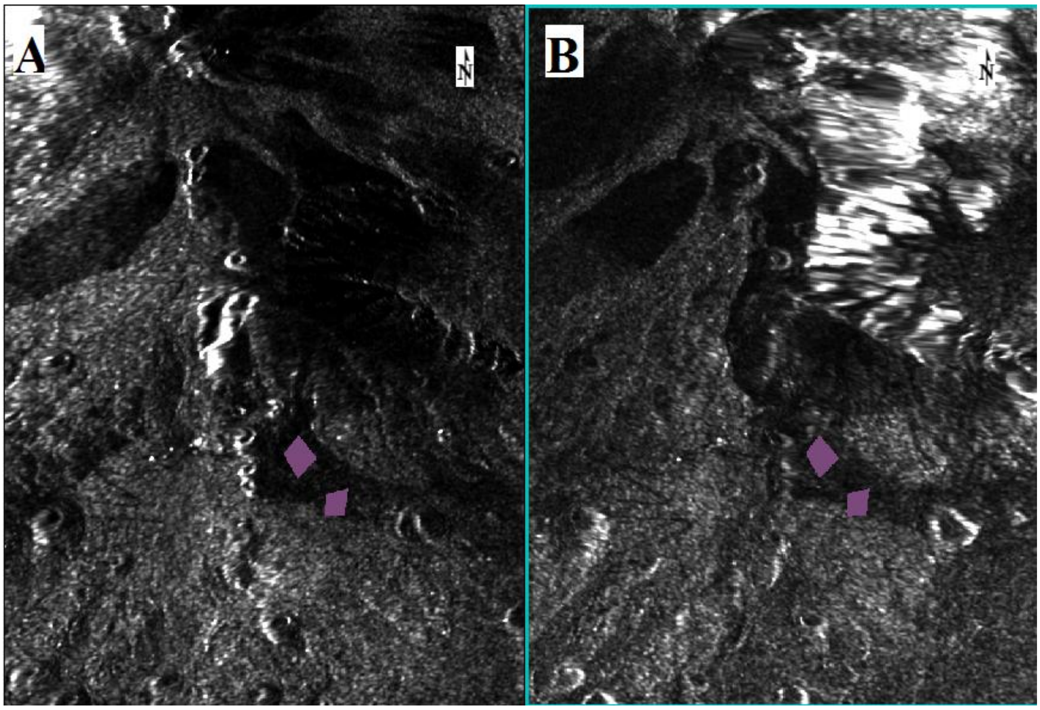


***Figure 7.2.3: The spatial location of the 1766 lava flow samples in the ascending (A) the descending (B) acquisition geometry in VV polarization.***

**Mongibello Torre del Filosofo 3 Formation (122BC – 1669AD) – MF3**

The backscatter coefficient values of the MF3 formation are not always higher in ascending acquisition geometry, as it was depicted in MF1 and MF2 formations. It seems that the most of the volcanic products are located in lower slopes ($15^o$-$30^o$) and this could potentially diminish the topographic effects to the backscatter coefficient values (Figure 7.2.4). Also, the ascending image reveals, mainly higher backscatter coefficient values and thus we assume that it is able to discriminate in a more effective way the volcanic formations.

The mean backscatter coefficient values in descending pass and VV polarization increase from the oldest volcanic product to the most recent, while the opposite occurs to the ascending vv, vh and descending vh. According to Spinetti et al (2009) and Dierking and Haack (1998) studies, pahoehoe lava flows (e.g. the 1614-24 lava flows) are described with lower backscatter coefficient values. This fact is not proved in our study. In particular, the 1614-24 lava flow reveals the highest sigma0 values in ascending pass.

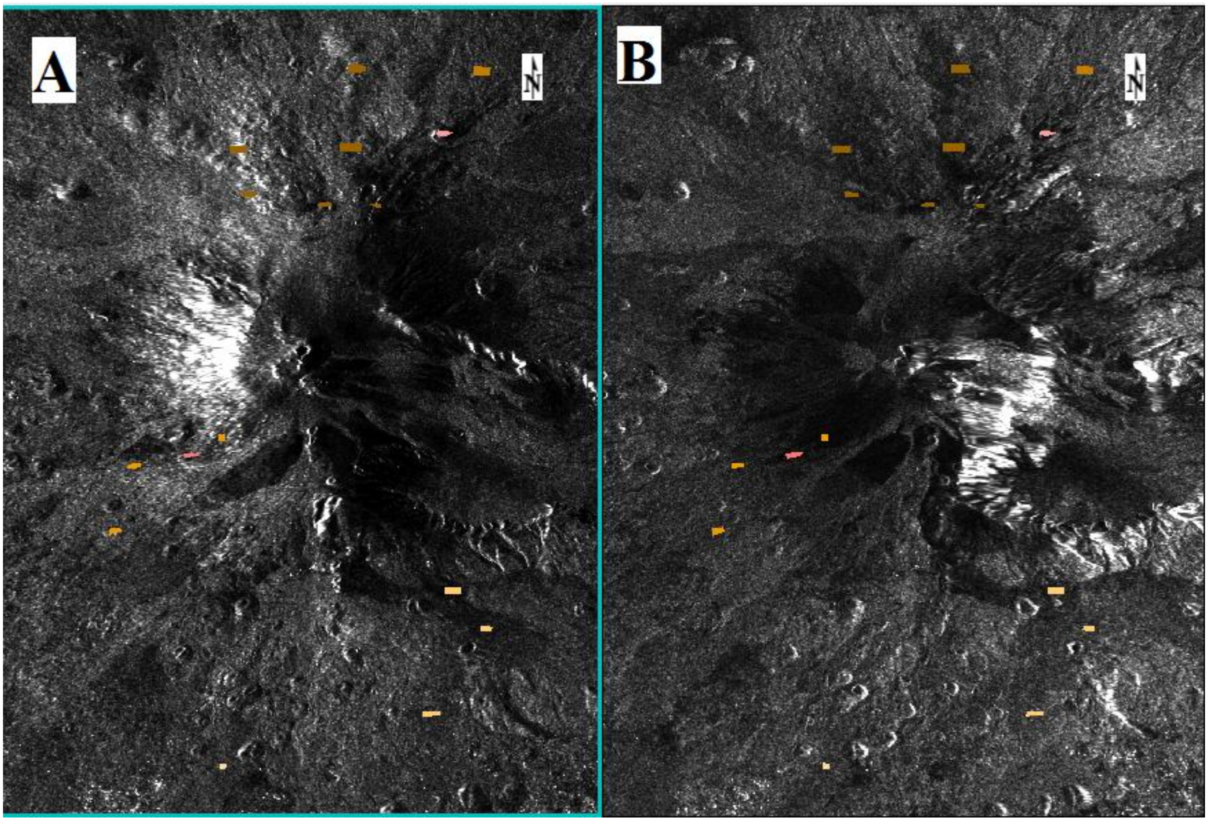

*Figure 7.2.4: The spatial location of the MF3 volcanic products in ascending (A) and descending (B) pass in VV polarization.*

**Ellitico Formation**

In Ellitico formation the highest backscatter coefficient values are revealed in the descending pass. The backscatter coefficient values increase with a linear trend from the EC24 volcanic products to the ESC20 in descending pass, while in descending pass the trend is almost stable with minor variations.

The Ellitico volcanic products are mainly located behind the NW, W ridges of the Valle del Dove, (Figure 7.2.5). Thus, we hypothesize that the backscatter coefficient values in ascending pass are lower than in descending pass, because the backscatter signal is potentially affected by the topography and the satellite acquisition geometry. The backscatter coefficient values in descending pass are also affected by this effect but to a lesser extent.

The EP_22ta reveal high sigma0 values in VV polarization in both acquisition geometries. A potential cause of this phenomenon is the contribution of more than one land cover types in the backscatter coefficient, because the sample of this volcanic product is located close to an urban area.

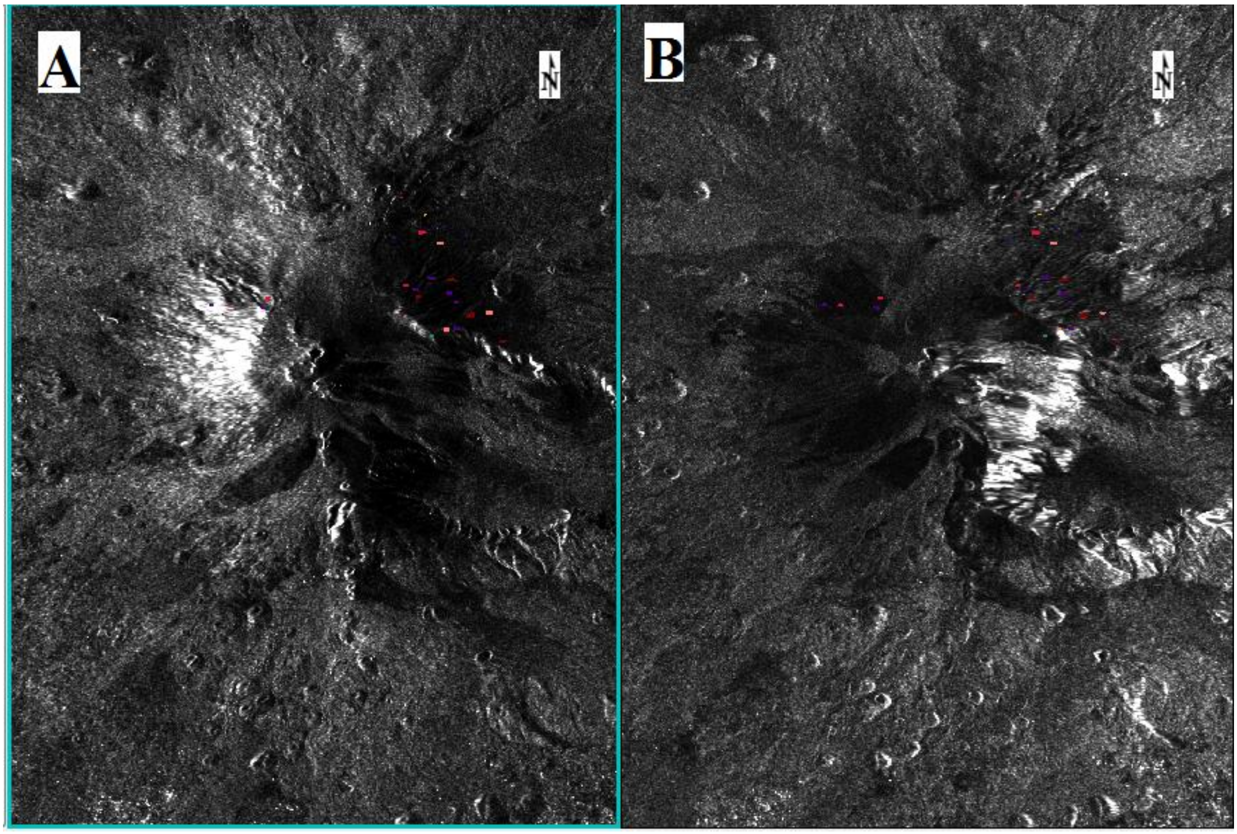


***Figure 7.2.5: The spatial location of the Ellitico volcanic products in ascending (A) and descending (B) pass in VV polarization***

## Correlation between the Backscatter Coefficient ($\sigma^0$) and the Topographic Variables

According to the Tables 7.2.1-2, we assume that the topography and the backscatter coefficient don't reveal a strong linear correlation, because almost all the correlation coefficient values depict a moderate or weak correlation and some of them reveal no correlation.

An exception to that conclusion are the correlation coefficient values between the $\sigma_{VV}0$ in (i) ascending (0.69) and descending (-0.85) pass in the MF3 formation, with the aspect, (ii) the descending σVV0 (-0.61) and MF3 σVH0 (-0.64) in the MF2 formation with the slope and (iii) ascending σVV0 (0.60) and MF3 σVH0 (-0.64) in the MF1 formation, with the slope. Also, we ascertain that almost all the descending correlation coefficient values are negative, while in the opposite occurs in ascending pass. Finally, correlation coefficient values between the backscatter coefficient in ascending and descending pass and slope are equal in both polarizations, in MF3 and Ellitico volcanic formations.

*Table 7.2.1: Correlation Statistics between Polarizations in Descending, Ascending pass and Aspect of each volcanic formation.*

| | MF1 Formation | | MF2 Formation | | MF3 Formation | | Ellitico Formation | |
|---|---|---|---|---|---|---|---|---|
| | VV | VH | VV | VH | VV | VH | VV | VH |
| **Descending** | -0,43 | -0,24 | -0,57 | -0,46 | -0,85 | -0,60 | -0,24 | -0,08 |
| **Ascending** | 0,27 | 0,30 | 0,52 | -0,01 | 0,69 | 0,22 | 0,42 | 0,22 |

*Table 7.2.2: Correlation Statistics between Polarizations in Descending, Ascending pass and Slope of each volcanic formation.*

| | MF1 Formation | | MF2 Formation | | MF3 Formation | | Ellitico Formation | |
|---|---|---|---|---|---|---|---|---|
| | VV | VH | VV | VH | VV | VH | VV | VH |
| **Descending** | -0,24 | -0,40 | -0,61 | -0,58 | -0,25 | -0,64 | 0,04 | -0,48 |
| **Ascending** | 0,60 | 0,49 | 0,39 | 0,21 | -0,25 | -0,64 | 0,04 | -0,48 |

## 7.3. Temporal Surface Change Analysis

Regardless the local topography (aspect and slope) and satellite acquisition geometries, the VV polarization give higher mean values in every lava flow, compared with VH polarization. Also, the mean backscatter coefficient values present higher variance in VV, in every formation, while the opposite occurs in the VH and especially in the descending pass.

In ascending pass the single vertical polarization shows higher backscatter coefficient values, with the maximum variance. However, it seems that the $\sigma_{VH}^{0}$ values maybe are able to discriminate the volcanic formations in a more effective way, (Figure 7.3.1). The backscatter coefficient values in cross polarization decrease from the recent formation to the oldest. Consequently, in descending pass, the volcanic formations could be discriminate in a more effective way in single polarization and lesser in cross. Likewise, a decreasing trend is detected from the younger to the oldest volcanic formation, regardless the satellite orbit.

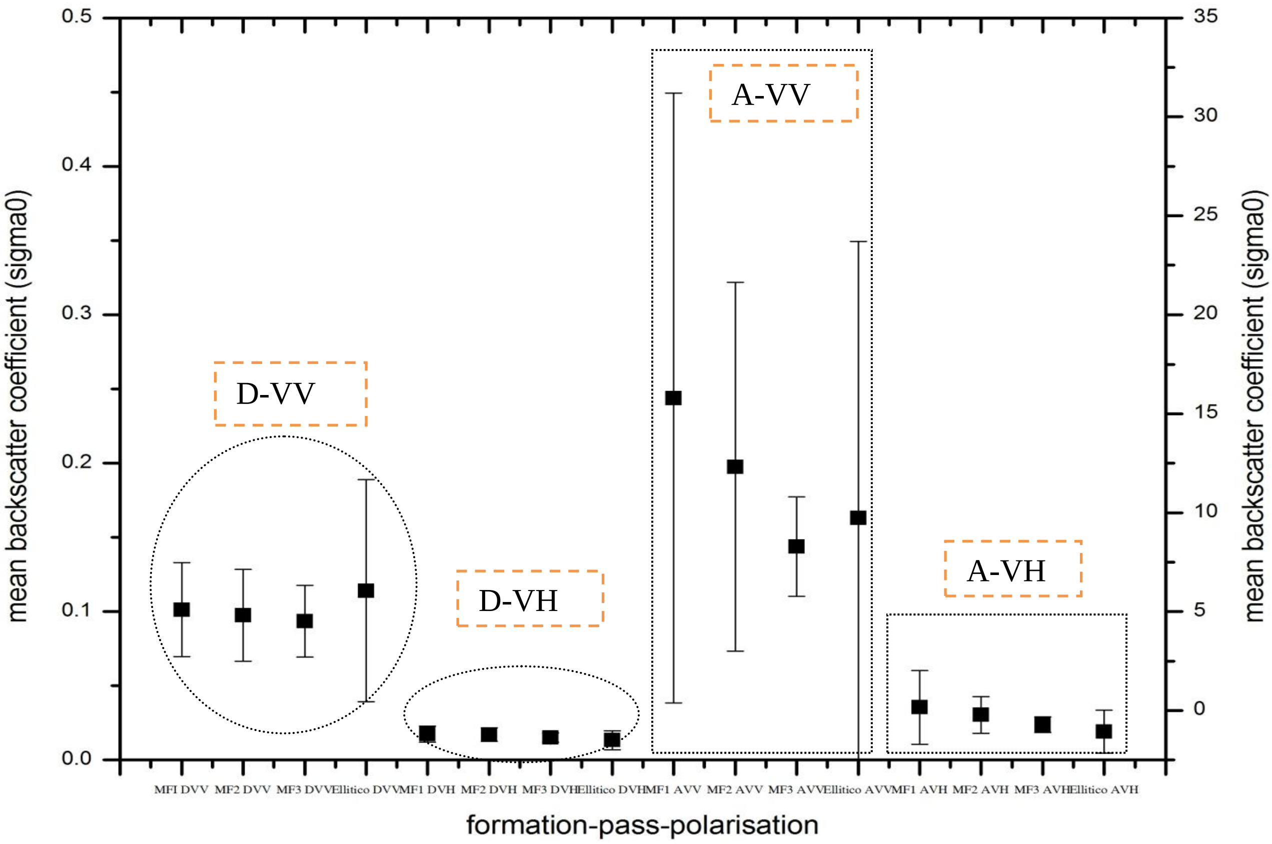


***Figure 7.3.1: Mean backscatter coefficient for the 4 formations from left to right: MF1, MF2, MF3 and Ellitico. D corresponds to Descending pass, A corresponds to Ascending pass.***

According to the Table 7.3.1, in descending pass, MF1 volcanic formation in both single and cross polarizations reveal the maximum topographic categories, while the categories existence decrease by the following order MF1> MF2> Ellitico> MF3. Ellitico formation presents the most topographic categories, when the backscatter coefficient values decrease, whereas its presence decreased according to the following order: Ellitico> MF2> MF1> MF3. In general MF2 and MF3 formations are characterized by the moderate backscatter coefficient values, comparing with MF1 and Ellitico formations.

On the other hand, the ascending mode depicts the opposite results in comparison with the descending mode, id est. more maximum sigma0 values in Ellitico, especially in VV polarization, while they decrease like below: Ellitico> MF2> MF1> MF3. Also, it should be pointed it out that when the frequency of the maximum values in VV polarization decreased, in VH polarization increased. Lastly, Ellitico formation had the most categories of minimum σ0 values, while their appearance decreased from the oldest to the most recent (Ellitico> MF3> MF2> MF1).

*Table 7.3.1: The topographic characteristics, where minimum and maximum backscatter coefficient values were observed, in each volcanic formation.*

| | **Ellitico** | | **MF3** | | **MF2** | | **MF1** | |
|---|---|---|---|---|---|---|---|---|
| | DESCENDING | | | | | | | |
| | **VV** | **VH** | **VV** | **VH** | **VV** | **VH** | **VV** | **VH** |
| $\sigma^0 \uparrow$ | 15-90 | 45-180 | 45-180 | 45-360 | 15-180 | 15-180 | 15-270 | 15-90 |
| | 30-90 | | | | 30-360 | 30-90 | 15-360 | 15-270 |
| | 45-90 | | | | 45-270 | 30-270 | 30-90 | 15-360 |
| | | | | | | 45-270 | 30-180 | 30-90 |
| | | | | | | | 30-270 | 30-360 |
| | | | | | | | | |
| $\sigma^0 \downarrow$ | 15-270 | 15-90 | 15-90 | ---- | 30-180 | 30-180 | 15-180 | 15-180 |
| | 30-270 | 15-270 | | | 45-90 | 45-90 | | |
| | 30-360 | 15-360 | | | 45-180 | 45-360 | | |
| | 45-270 | 30-270 | | | | | | |
| | 45-360 | 30-360 | | | | | | |
| | | 45-270 | | | | | | |
| | | 45-360 | | | | | | |
| | **ASCENDING** | | | | | | | |
| | **VV** | **VH** | **VV** | **VH** | **VV** | **VH** | **VV** | **VH** |
| $\sigma^0 \uparrow$ | 15-90 | 15-90 | 15-180 | 15-180 | 15-270 | 15-270 | 15-90 | 15-270 |
| | 15-180 | 30-90 | 15-360 | 15-360 | 30-90 | 30-90 | 45-180 | 15-360 |
| | 15-270 | 45-90 | 30-180 | 30-180 | 45-90 | 45-90 | | 30-180 |
| | 15-360 | | | | | 45-270 | | 30-270 |
| | 30-90 | | | | | | | |
| | 45-90 | | | | | | | |
| | 45-180 | | | | | | | |
| | | | | | | | | |
| $\sigma^0 \downarrow$ | 30-270 | 15-270 | 30-270 | 30-270 | 30-360 | 45-360 | ---- | 15-180 |
| | 30-360 | 30-270 | 45-270 | 45-270 | 45-270 | | | |
| | 45-270 | 30-360 | 45-360 | | | | | |
| | 45-360 | 45-270 | | | | | | |

| | | | | | | | | |
|---|---|---|---|---|---|---|---|---|
| | | 45-360 | | | | | | |

According to the Table 7.3.2, we could probably claim that:

- The topographic categories that present the highest backscatter coefficient values show that potentially the backscatter signal is more affected by the roughness and less by the topography/viewing angle relation.
- The Ellitico formation, in VV and VH polarization, is predominated by greater slopes (30-45).
- The highest and lowest sigma0 values are depicted in East ($90^o$) and South ($180^o$) aspect orientations.
- The backscatter coefficient values are differentiated very much in the MF3 (both polarizations) and in MF1-MF2 (single vertical polarization).
- In MF2 formation, the minimum and maximum backscatter coefficient values in cross polarization, are observed in the highest slopes ($30^o$-$45^o$) and in North, East and West orientations.
- In MF1 formation, in VH polarization, we detect that maximum and minimum values are revealed in lower slopes ($15^o$-$30^o$), in North-South aspect.

According to the topography; backscatter values are more affected by the roughness in Ellitico, in higher slopes ($30^o$-$45^o$) and East aspect. On the other hand, sigma0 values influenced more by the topography than by the rugosity in MF3, MF2 and MF1 formations. Maybe, roughness affects more the North and South slopes orientations**.**

***Table 7.3.2: Topographic categories (slope, aspect), which were identified by maximum $\sigma^0$ values, regardless the satellite orbits.***

| | **Ellitico** | | **MF3** | | **MF2** | | **MF1** | |
|---|---|---|---|---|---|---|---|---|
| | **Regardless Ascending/Descending pass** | | | | | | | |
| | **VV** | **VH** | **VV** | **VH** | **VV** | **VH** | **VV** | **VH** |
| | 15-90 | 45-180 | ---- | ---- | ---- | 30-90 | ---- | 15-270 |
| **$\sigma^0$ ↑** | 30-90 | 45-180 | | | | 45-270 | | 15-360 |
| | 45-90 | | | | | | | 30-90 |
| | | | | | | | | 30 (180-360) |

| | | | | | | | | |
|---|---|---|---|---|---|---|---|---|
| | | | | | | | | 30-270 |
| | | | | | | | | |
| **$\sigma^0$ ↓** | 30-270 | 15-270 | ----- | ----- | ----- | 45-360 | ---- | 15-180 |
| | 30-360 | 30-270 | | | | | | |
| | 45-270 | 30-360 | | | | | | |
| | 45-360 | 45-270 | | | | | | |
| | | 45-360 | | | | | | |

In our ongoing study, further investigations will include; (i) the estimation of the spatial locations, where satellite distortions occur and exclude them from the whole procedure, (ii) the estimation of the surface roughness and the correlation coefficient calculation with the backscatter coefficient (iii) the fusion of the spectral reflectance and polarimetric backscatter in order to investigate their capabilities in volcanic products discrimination and (iv) the application of advanced polarimetric techniques.

## Chapter 8: Conclusion

This study presents the primary results of spectral analysis of hyperspectral (EO-1 Hyperion) data and polarimetric backscatter coefficient analysis of SAR (Sentinel 1A) data, of volcanic products (lava flow, pyroclastic and scoria deposits), which are categorized into for classes according to their recorded date, on Mt. Etna. Our main conclusions are as follows:

In hyperspectral data analysis:

Hyperion was able to identify the temporal changes on the volcanic products, between the three datasets, according to their reflectance response and spectral pattern. However, potentially it is difficult to discriminate accurately each volcanic product, in every dataset, because of their similar spectral pattern and reflectance response. Endmembers' spectral curves are an average of the contribution of different surfaces contained in an area (i.e. pixel) of 30m, which indicates that mixed pixel will occur. The reflectance response increase from the youngest volcanic formation (MF1) to the oldest (Ellitico). However, the reflectance response isn't always increased, according to the recorded age of the volcanic products.

The endmembers of the MF1 formation reveal a weak absorption in 0.4-0.5μm. The difference in reflectance response, between 2009 and 2012 images is ~1%. The reflectance response doesn't increase from the recent to the old lava flows, because some of them present the same spectral pattern and reflectance magnitude. Absorptions in 2.1 and 2.3μm are located in the same endmembers of 2007 and 2009 images. The 2009 endmembers are characterized by a water and chlorophyll absorptions in 1.14μm and 0.7μm, correspondingly. The lava deposits endmembers extracted from 2007 and 2012 images present similarities in their spectral pattern. The 2001 and 2002 scoria endmembers extracted from 2009 and 2012 images present some similarities in the spectral pattern.

In the three datasets, the highest reflectance responses correspond to the middle ages of the MF2 lava flows and the lowest reflectances to both the oldest and most recent lavas. The difference in reflectance response between 2009 and 2012 endmembers is ~2%. In 2007 image, absorption in 1.78μm is observed as in MF1 endmembers. Chlorophyll absorption (0.7μm) and potential lichen cover (2.3μm absorption) are depicted in various endmembers of the three images. The endmembers of 2007 image, which are characterized by the above description, have similar spectral pattern. Water absorption (1.14μm) is revealed in the 2007 and 2009 endmembers.

Potential iron absorption (1-1.3μm) is revealed in all endmembers in 2007, in pyroclastic products in 2009 and in 1927-28/32-33, 1780, 1787, 1792, 1886, 1911, 1947 and 1960-64 lava flows and in the 1879 pyroclastic deposit, in the 2012 image. Continuous reflectance increase in 0.4-0.9μm, 1.5-1.6μm and 2-2.35μm is observed probably due to alteration in the same lava flows spectra in the three data images. The difference in reflectance response between the 2009 and 2012 endmembers varies from less than 0.1% to 3%. The spectral patterns are similar in the three images, except from the lava flows, which may be affected by alteration.

The MF3 endmembers reflectance response doesn't increase from the most recent to the oldest lava flows. The lowest reflectance responses are observed in 1610 and 1614-24 lava flows and in scoriae deposits. All the lava flow endmembers extracted from 2007 image are characterized by absorption in 1-1.3μm (potential iron presence) and 1.78μm. Sparse vegetation is revealed in the three datasets, but more frequently in 2009 image. Reflectance increase in 0.4-0.9μm and in 1.5-1.6 μm ("curved shape") and the decrease in 2.1-2.35μm is observed in the three datasets (potential alteration presence). The difference in reflectance response between the 2009 and the 2012 endmembers varies from 0.5 to 10%. The 1610 scoriae deposit have the same reflectance response in 1.12-2.35μm, in 2009 and 2012 images. The MF3 endmembers can be discriminated better according to their spectral pattern and reflectance response.

In Ellitico formation, almost all endmembers are characterized by chlorophyll absorption in 0.7μm, which becomes stronger in the older lava flows. Exceptions are the ESC_20 in all the images, the EP_22ta of the 2012 image and the EP_22gc of the 2009 image. Presence of iron feature is observed in the EP_22 and EC_24 endmembers. A particular absorption in 1.78μm is revealed in 2007 endmembers and in the EP_22ta endmember of the 2009 image. Alteration effect probably occurs in EP_22 and EC_24 endmembers. The discrimination between spectra volcanic products within the same spectral group is less evident, due to their spectral similarities.

The endmembers derived from 2007 image have always higher reflectance responses, probably due to sensor's artifacts. Reflectance response of the endmembers of the 2009 image is usually lower than in 2012, while this is mainly observed in 1.45-1.78μm spectral region. Although, there are some particular endmembers in every formation that reveal the same of higher reflectance response in 2009 image, compared with the 2012 image. The most characteristic temporal changes, according to the reflectance response are depicted in SWIR region, while in VNIR spectral region occur changes according to the spectral pattern of the volcanic products.

Pyroclastic and scoriae deposits always reveal lower reflectance response, compared with the lava flows. Various endmembers are characterized by some specific absorptions, which depict the potential presence of vegetation (e.g. lichen colonization), atmospheric residuals (water vapor), iron and magnesium. The chlorophyll and water vapor absorptions are revealed more in the endmembers of the 2009 image. The iron and magnesium presence is depicted more in 2007 and 2012's endmembers. The scoria deposits in MF3 formation don't reveal any presence of iron oxides or magnesium. According to the above observations, the absorptions in 0.9-1.3μm and 2.3μm potentially occur due to traces of olivine and/or pyroxene (clinopyroxenes) compositions, which are generally typical compositions of basaltic lavas, such as the Mt. Etna lava flows. Alteration presence potentially occurs in MF2, MF3 and Ellitico formations and more often in the endmembers extracted from the 2007 and 2012 images.

In SAR data analysis:

The vertical single polarization reveals always higher backscatter coefficient values in every volcanic formation, regardless the satellite acquisition geometry. In ascending acquisition geometry and in both polarizations, the backscatter coefficient values increase from the oldest lava flow (Ellitico formation) to the most recent (MF1 formation), while the opposite occurs in descending pass.

The MF1 and MF2 formations reveal higher backscatter coefficient values in ascending pass. This fact isn't observed always in MF3 formation. In Ellitico formation the highest backscatter coefficient values are identified by descending pass. The backscatter coefficient values of each volcanic product don't increase, according to their chronological categorization. Pyroclastic and scoriae volcanic products are characterized by lower backscatter coefficient values in comparison with lava flows, in both polarizations and in satellite orbits.

The combination of the intense local topography (slopes more than $30^{o}$) with the satellite acquisition geometry potential creates shadowing and foreshortening distortions, which affect the backscatter coefficient values of various volcanic products.

The topography variables don't show a linear correlation with the backscatter coefficient, except from the $\sigma_{VV}0$ in (i) ascending (0.69) and descending (-0.85) pass in the MF3 formation, with the aspect, (ii) the descending σVV0 (-0.61) and MF3 σVH0 (-0.64) in the MF2 formation with the slope and (iii) ascending σVV0 (0.60) and MF3 σVH0 (-0.64) in the MF1 formation, with the slope. The correlation coefficient values with ascending image and the topographic variables are positive, while the opposite usually occurs in descending. The correlation coefficient values between the backscatter coefficient in ascending and descending pass and the slope are equal in both polarizations, in MF3 and Ellitico volcanic formations.

The backscatter values are more affected by the roughness in Ellitico, in higher slopes ($30^{o}$-$45^{o}$) and East aspect. The backscatter coefficient values of the MF1, MF2 and MF3 formations are influenced more by the topography than by the rugosity. Maybe, roughness affects more the North and South slopes orientations**.** We could probably infer that lava flows recorded in different dates are differentiated in a more effective way in VH polarization and in descending pass, due to the lower variance in their values. Also, the backscatter signal is increased from the oldest to the youngest formations almost linearly. Finally, it is not significant, how the surface changes over time and its contribution to the backscatter coefficient. Thus, we cannot be conclusive about the ability of the backscatter signal to discriminate the different volcanic products, according to the surface change in Mt. Etna.

## References

Abbott, E.A.; Gillespie, A.R.; Kahle, A.B. (2013) *Thermal-infrared imaging of weathering and alteration changes on the surfaces of basalt flows, Hawai'i, USA*. Int. J. Remote Sens. Vol: 34, pp: 1–24

Acocella, V., Neri, M., (2003). *What makes flank eruptions? The 2001 Etna eruption and the possible triggering mechanisms*. Bull. Volcanol. 65, 517–529, doi:10.1007/s00445-003-0280-3. Science Direct, Vol: 78, pp: 85-114

Ager, C.M.; Milton, N.M, (1987), *Spectral reflectance of lichens and their effects on the reflectance of rock substrates.* Geophysics Vol: 52, pp: 898–906.

Allard P, Behncke B, D' Amico S, Neri M, Gambino S, (2006), *Mount Etna 1993–2005: Anatomy of an evolving eruptive cycle,*

Alparone S, Andronico D, Lodato L, Sgroi T, (2003) *Relationship between tremor and volcanic activity during the Southeast Crater eruption on Mount Etna in early 2000*. J. Geophysics. Res. Vol: 108, pp: 2241. http://dx.doi.org/10.1029/2002JB001866.

Amici S. & Pieri D. (2010), *Spectral analysis of aster and Hyperion data for geological classification of volcano Teide,* IGARSS (Conference paper), pp: 1-5, DOI: 10.1109/IGARSS.2010.5652063

Amici S., Piscini A., Neri M., (2014), *Reflectance Spectra Measurements of Mt. Etna: A Comparison with Multispectral/Hyperspectral Satellite*, Scientific Research, Vol: 3, pp: 235-240, http://dx.doi.org/10.4236/ars.2014.34016

Armienti, P., Pareschi, M.T., Pompilio, M., (1997). *Lava textures and time scales of magma storage at Mt. Etna (Italy).* Acta Vulcanol. Vol: 9, pp: 1–5.

Arsenault H. H., April G., (1976) *Properties of Speckle Integrated with a Finite Aperture and Logarithmically Transformed*, J. Opt. Soc. Am., Vol. 66, pp. (1160-1163)

Bailey, J.E., A.J.L. Harris, J. Dehn, S. Calvari and S.K. Rowland (2006). *The changing morphology of an open lava channel on Mt. Etna*, B. Volcanol., Vol: 68, pp: 497-515.

Barry P. & Hyperion Performance Analysis and Team Lead (2001), *EO-1/ Hyperion Science Data User's Guide, Level 1_B*, TRW Space, Defense & Information Systems, pp. (6-15)

Behncke, B., Neri, M., (2003a). *The July–August 2001 eruption of Mt. Etna (Sicily).* Bull. Volcanol. Vol: 65, pp: 461–476. doi:10.1007/s00445- 003-0274-1.

Behncke, B., Neri, M., (2003b). *Cycles and trends in the recent eruptive behavior of Mt. Etna (Italy)*. Can. J. Earth Sci. Vol: 40, pp: 1405–1411. doi:10.1139/E03-052.

Behncke, B., Neri, M., Nagay, A., (2005). *Lava flow hazard at Mount Etna (Italy): new data from a GIS-based study.* In: Manga, M., Ventura, G. (Eds.), Kinematics and Dynamics of Lava Flows, Geol. Soc. Am. Spec. Pap. Vol: 396, pp: 189–209, doi:10.1130/ 2005.2396(13).

Behncke, B., Neri, M., Pecora, E., Zanon, V., (2006) *The exceptional activity and growth of the Southeast Crater, Mount Etna (Italy), between 1996 and 2001*. Bull. Volcanol. 69, 149–173. http://dx.doi.org/10.1007/s00445-006-0061-x.

Behncke, B., Calvari, S., Giammanco, S., Neri, M., Pinkterton, H., (2008) *Pyroclastic density currents resulting from the interaction of basaltic magma with hydrothermally altered rock: an example from the 2006 summit eruptions of Mount Etna*, Italy. Bull. Volcanol. 70, 1249–1268. http://dx.doi.org/10.1007/s00445-008-0200-7.

Behncke B, Branca S, Corsaro R.A, De Deni E, Miraglia L, Proietti C, (2014) *The 2011–2012 summit activity of Mount Etna: Birth, growth and products of the new SE crater*, Journal of Volcanology and Geothermal Research, Vol: 270, pp: 10-21, http://dx.doi.org/10.1016/j.jvolgeores.2013.11.012

Benedetti, M. (2003*) Chemical weathering of basaltic lava flows undergoing extreme climatic conditions: The water geochemistry record*. Chem. Geol. Vol: 201, pp: 1–17.

Berk A, Bernstein, L.S, & Robertson, D.C, (1989), *MODTRAN: A moderate resolution model for LOWTRAN7 (GL-TR-89-0122),* Hanscom AFB, Bedford, MA: Air Force Geophysics Laboratory. Retrieved from www.dtic.mil/dtic/tr/fulltext/u2/a214337.pdf

Branca S, Coltelli M, Groppelli G and Lentini F, (2011) Geological Map of Etna volcano, 1:50,000 scale, Ital.J.Geosci., Vol: 130 (3), pp: 265-291

Branca S, Coltelli M, Groppelli G, Lentini F, (2011) Geological evolution of a complex basaltic stratovolcano, Ital.J.Geosci. Vol: 130 (3), pp: 306-317

Burgers, K., Fessehatsion, Y., Rahmani, S., (2009), *A Comparative Analysis of Dimension Reduction Algorithms on Hyperspectral Data*, Jia Yin Seo edn., pp. 4-6

Calvari, S., Coltelli, M., Müller, W., Pompilio, M., Scribano, V., (1994) *Eruptive history of South-Eastern Crater of Mount Etna, from 1971 to 1994*. Acta Vulcanol. Vol: 5, pp: 11–14.

Calvari, S., Neri, M., Pinkerton, H., (2002) *Effusion rate estimations during the 1999 summit eruption on Mount Etna, and growth of two distinct lava flow fields*. J. Volcanol. Geotherm. Res. 119, 107–123.

Carmichael, R.S., (1982) *Handbook of Physical Properties of Rocks,* CRC Press Inc., Boca Roton, FL.

Chein-I Chang (2003). *Hyperspectral Imaging: Techniques for Spectral Detection and Classification*. Springer Science & Business Media. ISBN 978-0-306-47483-5.

Chester, D.K., Duncan, A.M., Guest, J.E., Kilburn, C.R.J., (1985). *Mount Etna: The Anatomy of a Volcano*. Chapmann and Hall, pp: 404, London (ISBN-13: 978-0804713085).

Clark, R. N. and Roush, T. L. (1984) *Reflectance spectroscopy: Quantitative analysis techniques for remote sensing applications,* Journal of Geophysical Research: Solid Earth, 89(B7), 6329–6340. doi:10.1029/JB089iB07p06329

Corsaro, R.A., Pompilio, M., (2004*). Dynamics of magmas at Mount Etna*. In: Bonaccorso, A., Calvari, S., Coltelli, M., Del Negro, C., Falsaperla, S. (Eds.), Mt. Etna: Volcano Laboratory. Geophysical Monograph Series, Vol: 143. pp. 91–110.

Curlander J. C., McDonough R. N. (1992) *Synthetic Aperture Radar: Systems and Signal Processing,* Willey Encyclopedia of Electrical and Electronics Engineering, ISBN: 978-0-471-85770-9

Datt, B., McVicar, T. R., Van Niel, T. G., Jupp, D. L. B., Pearlman, J. S. (2003). *Preprocessing EO-1 Hyperion hyperspectral data to support the application of agricultural indexes*. IEEE Transactions on Geoscience and Remote Sensing, 41(6 PART I), pp. 1246-1259.

Datt B. & Jupp D.L.B., (2004) *Hyperion Data Processing Workshop, Hands-On Processing Instructions,* CSIRO Office of Space Science & Applications Earth Observation Centre, Canberra

De Beaumont E. (1836) - Recherché sur la structure et sur l’origine du Mount Etna. A. Mines Carbur. Paris, ser. 3, 9, 175-216, 575-630.

Di Figlia, M.G.; Bellanca, A.; Neri, R.; Stefansson, A. (2007) *Chemical weathering of volcanic rocks at the island of Pantelleria, Italy: Information from soil profile and soil solution investigations*. Chem. Geol. Vol: 246, pp: 1–18.

Dierking W. & Haack H. (1998) *L-band polarimetric SAR-signatures of lava flows in the Northern Volcanic Zone, Iceland*, IEEE Xplore (Conference paper), pp: 1-4, DOI: 10.1109/IGARSS.1998.691402

Dietterich, H.R.; Poland, M.P.; Schmidt, D.A.; Cashman, K.V.; Sherrod, D.R.; Espinosa, A.T. (2012) *Tracking lava flow emplacement on the east rift zone of Klauea, Hawaii, with synthetic aperture radar coherence*. Geochem. Geophys. Geosyst., Vol: 13, pp: 1–17.

Elvidge, Christopher D. (1990). *Visible and near infrared reflectance characteristics of dry plant materials,* International Journal of Remote Sensing, Vol: 11 (10), pp: 1775–1795. doi: 10.1080/01431169008955129

Favalli M, Tarquini S & Fornaciai A, (2011), *DOWNFLOW code and LIDAR technology for lava flow analysis and hazard assessment at Mount Etna,* Annals of Geophysics, Vol: 54 (5), pp: 552-567, doi: 10.4401/ag-5339

Ferretti A., Monti-Guarnieri A., Prati C., Rocca F, Massonet D, (2007) *InSAR Principles: Guidelines for SAR Interferometry Processing and Interpretation*. The Netherlands: ESA Publications, ISBN 92-9092-233-8.

Ferretti A., (2014), *Satellite InSAR Data: Reservoir Monitoring from Space,* European Association of Geoscientists & Engineers, pp: (13-31) ISBN Number: 978-90-73834-71-2

Gaddis L. R., (1992) *Lava flow characterization at Pisgah volcanic field, California, with multiparameter imaging radar,* Geol. Soc. Am. 13ull., Vol: 104, pp: 695-703.

Garduño VH, Neri M, Pasquarè G, Borgia A, Tibaldi A, (1997) *Geology of the NE-rift of Mount Etna (Sicily, Italy)*: Acta Vulcanologica, Vol: 9, pp: 91-100

Gemmellaro C. (1958) - *La Vulcanologia dell 'Etna. Tipografia dell'Accademia Gioenia, Catania*, pp: 266.

Goodman, J.W. (1976*). Some fundamental properties of speckle,* The Journal of the Optical Society of America, Vol: 66(11), pp. 1145-1150

Goetz, A.F.H., Vane, G., Solomon, J.E., & Rock, B.N. (1985). *Imaging spectrometry for earth remote sensing*, Science, Vol: 228 (4704), pp: 1147–1153. doi:10.1126/science.228.4704.1147

Goetz, A.F.H. (1992). *Imaging spectrometry: Sensors and data analysis.* In Proceedings of the International Geoscience and Remote Sensing Symposium IGARSS (pp. 547-548). Houston, TX: IEEE

Gonzalez, R., and R. Woods, (1993), *Digital image processing.* Reading, Massachusetts, Addison-Wesley Publishing Company, pp: 148-56.

Grahn H & Geladi P. (2007). *Techniques and Applications of Hyperspectral Image Analysis.* John Wiley & Sons. ISBN 978-0-470-01087-7.

Green A, Berman M, Switzer P, (1988). *A transformation for ordering multispectral data in terms of image quality with implications for noise removal*, IEEE Trans Geosci Remote Sens, 26(1) (65–74)

Guest, J.E., Murray, J.B., (1979). *An analysis of hazard from Mount Etna volcano*. J. Geol. Soc. (Lond) Vol: 136, pp: 347–354.

Handayani L.D, Trisasongko B.H, Tjahjono B, (2015) *Geomorphology analysis of lava flow of Mt. Guntur in West Java using Synthetic Aperture Radar (SAR) with fully polarimetry*, Science Direct, Vol: 24, pp: 303-307

Head, E.M.; Maclean, A.L.; Carn, S.A. (2013) *Mapping lava flows from Nyamuragira volcano (1967–2011) with satellite data and automated classification methods.* Geomat. Nat. Hazards Risk, Vol: 4, pp: 119–144.

Hellman, M.J., Ramsey, M.S., (2004). *Analysis of hot springs and associated deposits in Yellowstone National Park using ASTER and AVIRIS remote sensing.* J. Volcanol. Geotherm. Res. 135, 195–219.

Hughes, J.W., Guest, J.W., Duncan, A.M., (1990). *Changing styles of effusive eruption on Mount Etna since AD 1600*. In: Ryan, M.P. (Ed.), Magma Transport and Storage. John Wiley & Sons, New York, pp: 385–406.

Jarecke P. & Yokoyama K., (2000). *Radiometric calibration of the Hyperion imaging spectrometer instrument from primary standards to end-to-end calibration* Proceedings Optical Science and Technology Symposium, Earth Observing Systems V, SPIE 1435, pp. 1-9.

Jolliffe, I.T., (2002), *Principal Component Analysis*, Second edn., UK: Springer, pp. 1-6.

Kahle, A.B.; Gillespie, A.R.; Abbott, E.A.; Abrams, M.J.;Walker, R.E.; Hoover, G.; Lockwood, J.P. (1988) *Relative dating of Hawaiian lava flows using multispectral thermal infrared images: A new tool for geologic mapping of young volcanic terranes*. J. Afr. Earth Sci. Vol: 93, pp: 15239–15251.

Kanakaki S. (2016), Amazon Rainforest Deforestation Study using SAR Polarimetry methods (Master Thesis), Harokopio University of Athens, Department of Geography, pp. (41).

Kawishwar P. (2007)*“Atmospheric Correction Models for Retrievals of Calibrated Spectral Profiles from Hyperion EO-1 Data,”* Master Thesis of Science in Geo-information Science and Earth Observation, International Institute For Geo-Information Science And Earth Observation, Enschede, The Netherlands.

Karagiannopoulou C, Sykioti O, Parcharidis I, Briole P, (2016) *Lava flow mapping and change detection in the Mt. Etna Volcano between 2009-2012 using Hyperion hyperspectral imagery*, Living Planet ESA (Conference Paper), pp: 1-8, DOI: 10.13140/RG.2.1.2829.0169

Kaufmann, Y. J., A. E. Wald, L. A. Remer, B.-C. Gao, R.-R. Li, and L. Flynn, (1997). *The MODIS 2.1-μm Channel-Correlation with Visible Reflectance for Use in Remote Sensing of Aerosol*. IEEE Transactions on Geoscience and Remote Sensing. Vol. 35, pp. 1286-1298.

Kerola D.X., Bruegge C.J., Gross H.N., Helmlinger M.C. (2009*) On-Orbit Calibration of the EO-1 Hyperion and Advanced Land Imager (ALI) Sensors Using the LED Spectrometer (LSpec) Automated Facility*, IEEE Transactions on Geoscience and Remote Sensing 47(4), pp. 1244-1255.

Kieffer G, (1975) *Sur l’ existence d’ une “riftzone” ‘a l’ Etna*: Comptes Rendus de l’ Academie des Sciences Paris, ser. D, Vol: 280, pp: 263-266

Kilburn, C.R.J. and R.M.C. Lopes (1988). *The growth of a’a lava flow fields at Mount Etna, Sicily*, J. Geophys. Res., Vol: 93 (B12), pp: 14759-14772.

Kriegler F.J., Malila W.A., Nalepka R.F. & Richardson W, (1969). *Preprocessing transformations and their effects on multispectral recognition*, in: Proceedings of the Sixth International Symposium on Remote Sensing of Environment, University of Michigan, Ann Arbor, MI, p. 97-131

Lautze, N.C., A.J.L. Harris, J.E. Bailey, M. Ripepe, S. Calvari, J. Dehn and S. Rowland (2004). *Pulsed lava effusion at Mount Etna during 2001*, J. Volcanol. Geoth. Res., Vol: 137, pp: 231-246.

Lee, J.S, Pottier L, (2009), *Polarimetric Radar Imaging: from Basics to Applications*. Boca Raton: CRC Press, Taylor & Francis Group, ISBN 978-1-4200-5497-2.

Li L., Solana C., Canters F., Chan J.C-W, Kervyn M., (2015) *Impact of Environmental Factors on the Spectral Characteristics of Lava Surfaces: Field Spectrometry of Basaltic Lava Flows on Tenerife, Canary Islands, Spain*, Remote Sensing, Vol: 7, pp: 1-27, doi:10.3390/rs71215864

Li, L.; Canters, F.; Solana, C.; Ma, W.; Chen, L.; Kervyn, M. (2015) *Discriminating lava flows of different age within Nyamuragira's volcanic field using spectral mixture analysis*. Int. J. Appl. Earth Obs. Geoinf. Vol: 40, pp: 1–10.

Lillesand T. M. & Kiefer R. W (1999), *Remote Sensing and Image Interpretation,* 4th Edition, John Wiley & Sons, ISBN 10: 0471255157 ISBN 13: 9780471255154

Lillesand, T. M., Kiefer, R. W., Chipman, J. W. (2008) *Remote Sensing and Image Interpretation*. Hoboken: John Wiley & Sons, ISBN: 978-471-15227-7.

Lim J. S., Nawab H., (1981) *Techniques for Speckle Noise Removal,* Opt. Engineering, Vol. 20, pp. (472-480)

Lombardo V. & Buongiorno M.F, (2003), *Temperature distribution analysis of July 2001 Mt. Etna eruption observed by the airborne hyperspectral sensor MIVIS*, Annals of Geophysics, Vol: 46 (6), pp: 1-12,

Lu G., Fei B. (2013) *'Medical hyperspectral imaging: a review'*, Biomedical Optics, 19(1), pp. 3-5.

Lyell C. (1859) - *On the structure of lavas which have consolidated on steep slopes; with remarks on the mode of origin of Mt. Etna, and on the theory of "Center of Elevation*". Phill. Trans. Roy Soc., pp: 703-785.

Manolakis D, Marden D, Kerekes J & Shaw G, (2001), *On the Statistics of Hyperspectral Imaging Data*, SPIE Proceedings, Vol: 4381, pp: 1-9

Mansourpour M, Rajabi MA, Blais JAR. (2006) *Effects and performance of speckle noise reduction filters on active radar and SAR images*. Proceedings of the ISPRS Ankara Workshop 2006, Ankara, Turkey

Martinez P, Perez P.M, Plaza A, Aguilar P.L, Cantero M.C & Plaza J, (2006), *Endmember extraction algorithms from hyperspectral images*, Annals of Geophysics, Vol: 49 (1), pp: 1-9

Matthew, M. W., S. M. Adler-Golden, A. Berk, S. C. Richtsmeier, R. Y. Levine, L. S. Bernstein, P. K. Acharya, G. P. Anderson, G. W. Felde, M. P. Hoke, A. Ratkowski, H.-H. Burke, R. D. Kaiser, and D. P. Miller, (2000). *Status of Atmospheric Correction Using a MODTRAN4-based Algorithm. SPIE Proceedings, Algorithms for Multispectral, Hyperspectral, and Ultraspectral Imagery VI.* Vol: 4049, pp. 199-207.

Mazzarini, F., Pareschi, M.T., Favalli, M., Isola, I., Tarquini, S., Boschi, E., (2005). *Morphology of basaltic lava channels during the Mt. Etna September 2004 eruption from airborne laser altimeter data*. Geophys. Res. Lett. Vol: 32, L04305, doi:10.1029/2004GL021815.

Moreira A., Prats-Iraola P., Younis M., Krieger G, Hajnsek I, Papathanasiou K. P, (2013), A Tutorial on Synthetic Aperture Radar, IEEE Geoscience and remote sensing magazine, Germany, pp. (6-7), doi: 0.1109/MGRS.2013.2248301

Münch B, Trtik P, Marone F. & Stampanoni M., (2009) *Stripe and ring artifact removal with combined wavelet-Fourier filtering*, Optics Express, 17(10), pp. 8567-8591.

Murray, J.B., (1980). *Changes in the North–East Crater region in 1976–78*. UK research on Mount Etna, 1977–1979. Roy. Soc. 37–42.

Neri, M., Acocella, V., (2006). *The 2004–05 Etna eruption: implications for flank deformation and structural behavior of the volcano.* J. Volcanol. Geotherm. Res. 158, 195–206, doi:10.1016/j.jvolgeores.2006.04.022.

Neri, M., Behncke, B., Burton, M., Giammanco, S., Pecora, E., Privitera, E., Reitano, D (2006) *Continuous soil radon monitoring during the July 2006 Etna eruption.* Geophys. Res. Lett. 33, L24316, doi:10.1029/2006GL028394.

Neri, M., Guglielmino, F., Rust, D., (2007) Flank instability on Mount Etna: radon, radar interferometry and geodetic data from the southern boundary of the unstable sector. J. Geophys. Res. 112, doi:10.1029/2006JB004756.

Neri, M., Mazzarini, F., Tarquini, S., Bisson, M., Isola, I., Behncke, B., Pareschi, M.T., (2008). *The changing face of Mount Etna's summit area documented with LiDAR technology*. Geophys. Res. Lett. 35, L09305. http://dx.doi.org/10.1029/2008GL033740.

Ockert. January 23, 2011. What are the differences between horizontally polarized and vertically polarized signals? techbaron. http://techbaron.com/what-are-the-differences-b PCIGeomatics. 2015. http://www.pcigeomatics.com/geomatica help/concepts/spw_c/spw3n128.html, last site visit: 22/9/15

Olsen, R. C. (2014), *Remote sensing from air and space*, (2nd Ed.) Bellingham, WA: SPIE Press.

Richards, J. A., & Jia X, (2013), *Remote sensing digital image analysis: An introduction*, (5th Ed.) Berlin, Germany: Springer.

Önder K. & Doğan A. (2013) *"Quantitative and comparative examination of the spectral features characteristics of the surface reflectance information retrieved from the atmospherically corrected images of Hyperion,"* Journal of Applied Remote Sensing, 7 (1) 73528.

Patanè, D., Aiuppa, A., Aloisi, M., Behncke, B., Cannata, A., Coltelli, M., Di Grazia, G., Gambino, S., Gurrieri, S., Mattia, M., Salerno, G., (2013). *Insights into magma and fluid transfer at Mount Etna by a multi-parametric approach: a model of the events leading to the 2011 eruptive cycle*. J. Geophys. Res. 118, 1–21. http://dx.doi.org/10.1002/jgrb.50248.

Ponte, G., (1920). *Il cratere centrale dell'Etna. Suoi cambiamenti e sue eruzioni*. Atti Accademia Gioenia Scienze Naturali Catania, ser V 12, Mem. III, pp. 1–12.

Rees,W.G.; Tutubalina, O.V.; Golubeva, E.I. (2004) *Reflectance spectra of subarctic lichens between 400 and 2400 nm*. Remote Sens. Environ. Vol: 90, pp: 281–292.

Rodarmel G. & Shan J, (2002) *Principal Component Analysis for Hyperspectral Image Classification*, Surveying and Land Information Systems, Vol. 62 (2), 2002, pp.115-000

Rollin, E.; Milton, E.; Roche, P. (1994), *The influence of weathering and lichen cover on the reflectance spectra of granitic rocks*. Remote Sens. Environ. Vol: 50, pp: 194–199.

Rothery, D.A.; Lefevre, R.H. (1985) *The causes of age dependent changes in the spectral response of lavas, Craters of the Moon, Idaho, U.S.A.* Int. J. Remote Sens., Vol: 6, pp: 1483–1489.

Rouse, J. W., R. H. Haas, J. A. Schell, and D. W. Deering (1973) *'Monitoring vegetation systems in the Great Plains with ERTS'*, Third ERTS Symposium, NASA SP-351 I, 309-317.

Salvaggio C, Miller C, Bauer R., Lewis P. (2001), *Infrared field spectra collection protocol*, (Ver 1.0). Fairfax, VA: Spectral Information Technology Applications Center. Retrieved from http://dirs.cis.rit.edu/instrument_protocols/Field_IR_Protocol.pdf

Scheffler D & Karrasch (2013), *Preprocessing of Hyperspectral Images a Comparative Study of Destriping Algorithms for EO-1 Hyperion*, SPIE proceeding, Vol: 8892, 88920H, pp: 1-15, doi: 10.1117/12.2028733

Schurmer, J.H., (2003), *Air Force Research Laboratories Technology Horizons*, pp. 253

Sgavetti M, Pompilio L & Meli S, (2006) Reflectance spectroscopy (0.3–2.5 μm) at various scales for bulk-rock identification, Geosphere, Vol: 2 (3), pp: 142–160; doi:10.1130/GES00039.1

Shanthi I. & Valarmathi M.L. (2013) *SAR image despeckling using possibilistic fuzzy C-means clustering and edge detection in bandelet domain*, Springer, Vol: 23 (Supp 1), pp: 279-291, doi:10.1007/s00521-013-1394-y

Shaw G.A. & Burke H.H.K, (2003). *Spectral imaging for remote sensing.* Lincoln Laboratory Journal, 14(1), pp: 3–28. Retrieved from https://www.ll.mit.edu/publications/journal/pdf/vol14_no1/14_1remotesensing.pdf

Sentinel-1 Team (2013), *Sentinel-1 User Handbook Documentation*, https://sentinel.esa.int/

Simard M, Grandi GD, Saatchi S, Mayaux P, (2002) *Mapping tropical coastal vegetation using JERS-1 and ERS-1 radar data with a decision tree classifier*. International Journal of Remote Sensing. Vol: 23 pp: 1461-1474.

Sletten Mark A., Mc Laughlin David J. (1999) *Radar Polarimetry*, Willey Encyclopedia of Electrical and Electronics Engineering, pp: 1-15, DOI: 10.1002/047134608X.W2032

Solikhin A, Pinel V, Vandemeulebrouck J, Thouret J-C, Hendrasto M, (2015), *Mapping the 2010 Merapi pyroclastic deposits using dual-polarization Synthetic Aperture Radar (SAR) data*, Remote Sensing of Environment, Vol: 158, pp: 180-192, http://dx.doi.org/10.1016/j.rse.2014.11.002

Spinetti C., Neri M., Salvatori R., Buongiorno M. F., (2009), *Spectral properties of volcanic materials from hyperspectral field and satellite data compared with LiDAR data at Mt. Etna, International journal of applied earth observation and geoinformation*, 347(11), (142-154), doi: 10.1016/j.jag.2009.01.001

Stevens N.F, Wadge G, Williams C.A, Morley J.G, Muller J.P, Murray J.B, Upton M, (2001), Surface movements of emplaced lava flows measured by Synthetic Aperture Radar Interferometry, Journal of Geophysical research, Vol (106), No (B6), pp: 1-21, Paper number 2000JB900425. 0148-0227/01/2000JB900425509.00

Tanguy, J.-C., Condomines, M., Kieffer, G., (1997) Evolution of the Mount Etna magma: constraints on the present feeding system and eruptive mechanism. J. Volcanol. Geotherm. Res. Vol: 75, pp: 221–250.

Tarquini, S.; Favalli, M.; Mazzarini, F.; Isola, I.; Fornaciai, A. (2012) *Morphometric analysis of lava flow units: Case study over LIDAR-derived topography at Mount Etna, Italy*. J. Volcanol. Geotherm. Res. Vol: 235–236, pp: 11–22.

Tjahjono B, Syafril AHA, Panuju DR, Kasno A, Trisasongko BH, Heidina F, (2009) *Pemantauan lahan sawah menggunakan citra Alos AVNIR-2*. Jurnal Ilmiah Geomatika. 15 (2) pp: 1-8.

Trisasongko BH, (2009) Tropical *mangrove mapping using fully-polarimetric radar data*. ITB Journal of Science. Vol: 41(A), pp: 98-109.

Van der Meer, F. D., & S. M. de Jong, (2011), *Imaging spectrometry: Basic principles and prospective applications*, (Vol. 4). Dordrecht, Netherlands: Springer.

Vanko Bc. J. (2015) *Monitoring Landslides changes using Satellite Radar Imagery*, (Master thesis), Slovak university of technology in Bratislava faculty of Civil Engineering, pp. (16-23)

Vieux BE, Bedient BP, Mazroi E, (2002) *Real-time urban runoff simulation using radar rainfall and physics-based distributed modeling for site-specific forecasts. Di dalam: Simulation using Radar Rainfall and Physics-Based Distributed Modeling*. Proceedings of Symposium 10th International Conference on Urban Drainage, Copenhagen Denmark, pp: 1-8

Waltershausen W.S. (1880) - *Der Aetna.* Vol. (1 & 2), Engelmann, Leipzig.

Weeks R, Smith M, Pak K, Gillespie A. (1997) *Inversion of SIR-C and AIRSAR data for the roughness of geological surfaces*. Remote Sensing of Environment; Vol: 59, pp: 383-396.

Weissel JK, Czuchiewski KR, Kim Y, (2004) *Synthetic aperture radar (SAR)-based mapping of volcanic flows: Manam Island, Papua New Guinea.* Natural Hazard and Earth System Science. Vol: 4, pp: 339-346.

Wondie M, Teketat D, Melesse A.M, Schneider W, (2012) *Relationship between Topographic Variables and Land Cover in the Simen Mountains National Park, a World Heritage Site in Northern Ethiopia*, International Journal of Remote Sensing Applications, Vol: 2 (2), pp: 36-43

Xiao J, Li J, Moody A, (2003) *A detail-preserving and flexible adaptive filter for speckle suppression in SAR imagery*, International Journal of Remote Sensing, Vol: 24 (12), pp: 2451-2465, DOI: 10.1080/01431160210154885

Yamasaki, S.; Sawada, R.; Ozawa, A.; Tagami, T.;Watanabe, Y.; Takahashi, E. (2011) *Unspiked K-Ar dating of Koolau lavas, Hawaii: Evaluation of the influence of weathering/alteration on age determinations*. Chem. Geol. Vol: 287, pp: 41–53

## Internet Sources:

http://latex-community.org/forum/viewtopic.php?t=24290

https://www.harrisgeospatial.com

http://www.ingv.it/it/

https://volcano.si.edu/volcano.cfm?vn=211060

http://glovis.usgs.gov/

https://scihub.copernicus.eu/

http://www.spectral.com

http://modtran5.com

https://www.esrl.noaa.gov/gmd/ccgg/trends/global.html

http://aeronet.gsfc.nasa.gov

http://webhelp.esri.com/arcgisdesktop/9.3/index.cfm?TopicName=welcome